DESIGN, SYNTHESIS AND BIO-EVALUATION OF ANTICANCER

RUTHENIUM(II) COMPLEXES WITH APPLICATIONS IN PHOTOACTIVATED

CHEMOTHERAPY AND CHEMOTHERAPY

A Dissertation

by

SAYAN SAHA

Submitted to the Office of Graduate and Professional Studies of
Texas A&M University
in partial fulfillment of the requirements for the degree of

DOCTOR OF PHILOSOPHY

Chair of Committee,	Kim R. Dunbar
Committee Members,	Marcetta Y. Darensbourg
	François P. Gabbaï
	Robert C. Burghardt
Head of Department,	Simon W. North

December 2019

Major Subject: Chemistry

ABSTRACT

The serendipitous discovery of cisplatin marks a milestone achievement in the field of medicinal inorganic chemistry and spearheaded the development of anticancer metallotherapeutics. Ruthenium (Ru) compounds hold great promise as a potential alternative to platinum (Pt) drugs with improved therapeutic efficacy and different anticancer mechanisms in addition to reduced dose-limiting side-effects. Several Ru metallodrugs are being investigated in clinical trials for their potential to treat cancer malignancies and to stop solid tumor metastasis. Photodynamic therapy (PDT) is an alternative to traditional cancer chemotherapy with more localizing in action. In this modality, a photosensitizer is irradiated with visible light to generate toxic singlet oxygen ($^1O_2$) inside the cellular environment leading to irreversible cell death. To circumvent the oxygen dependence, a new promising field of therapeutics is under development referred to as photoactivated chemotherapy (PCT) in which a pro-drug, when irradiated with light, induces cytotoxic behavior by releasing caged toxins. Ru(II) complexes that exhibit visible light accessible excited states are increasingly being pursued as photocaging motifs in PCT.

In an effort to expand the Ru(II) photocage architecture, a new class of partially solvated dinuclear Ru(II) complexes was developed in which two metal centers are bridged by pyrazine and quinoxaline-based ligands which enhance their absorption in the lower energies of the visible spectrum and near-infrared region which is in the therapeutic window (600-900 nm) for applications as PCT agents. The bridged compounds exhibit moderate photodissociation ability but no phototoxicity properties were detected with

visible light irradiation, a fact attributed to high positive charge (+4) and low solubility in the media. To reduce overall positive charge and improve photodissociation, a mononuclear Ru(II) photocage architecture with an unusual bidentate coordination mode of 6-phenyl-2,2′-bipyridine (pbpy) ligand was explored wherein the phenyl ring is directed towards the Ru center to exert steric strain thus enhancing caged ligand dissociation upon irradiation. In fact, this coordination motif generates enough steric congestion to facilitate the dissociation of the caged ligand even in absence of light and as a consequence, is able to covalently bind to DNA and potentially damage the DNA helical structure at higher concentrations.

Finally, to investigate the enhancement of cytotoxic behavior due to cyclometallation, a new series of organometallic Ru(II) compounds was developed with the pbpy ligand and their lipophilicities carefully tuned by choosing suitable ancillary ligand environments that immensely alter their anticancer efficacy. All four compounds are highly toxic against human lung adenocarcinoma (A549) cells with sub-micromolar LC_{50} values and induce apoptosis via the mitochondrial dysfunctional pathway to trigger programmed cell death upon activation of caspase3/7. It was discovered that intracellular ROS generation partially facilitates cell death through ROS mediated apoptosis.

Overall, the research reported in this dissertation constitutes the successful establishment of new avenues into Ru-based anticancer drug design for potential applications in PCT and chemotherapy.

DEDICATION

To my parents, *Dr. Arogya Varam Saha* and *Dr. Nivedita Saha*,

Thank you for all your support and encouragement to achieve my destiny called ***Ph.D.***

ACKNOWLEDGEMENTS

The guidance, encouragement and friendship of several people during my graduate career here at Texas A&M University have been indispensable for the research work presented in this dissertation. I am truly grateful to my research advisor, Professor Kim R. Dunbar for her guidance, mentoring and support all these years. Her passion and love for science continuously encouraged me to give my best effort and push the boundary of my knowledge to explore new chemistry. Thank you for trusting in me when I started in the group in 2013 and helping me to grow as an independent chemist to pursue different areas of chemistry with such freedom. Your teaching and mentoring skills have assisted me to improvise during my class and become a successful teaching assistant. Your relentless effort to improve my problem-solving skills as well as communicating ideas will prepare me for my future endeavor.

I would like to thank Professor Claudia Turro, Professor Jean-Philippe Pellois, Professor Robert C. Burghardt and Professor Rola Barhoumi Mouneimne for giving me the opportunity to collaborate with them. Their willingness to help me with invaluable advice has been a key to the success of my work. Specially I would like to acknowledge Dr. Mouneimne for helping me immensely with the bio-evaluation and microscopy work along with providing me constructive feedback when discussing my research projects. I also want to thank my committee members Professor Marcetta Y. Darensbourg, Professor François P. Gabbaï and Professor Robert C. Burghardt for their support during my studies.

which I will cherish for the rest of my life. I want to thank Dr. Dipanjan Saha and Anamitra Debnath for being the other two musketeers in our group.

I would like to thank my whole family and friends back in India for their support. I am grateful to my uncle Sujit Saha and aunt Sujata Saha for their constant love and support away from home. I would like to thank Dr. Bhaskar Dutta and Dr. Nandita Chaudhuri at College Station for making me feel closer to home which helped me to survive my tough times.

Finally, I want to thank my parents, Dr. Arogya Varam Saha and Dr. Nivedita Saha for all their sacrifices in life to see my success. I could not have achieved my destiny without their support and encouragement throughout my entire life. My dad, who was an inorganic chemist and a great teacher, is my sole inspiration to pursue a career in chemistry. It is my immense pleasure to dedicate my dissertation work to both of you.

CONTRIBUTORS AND FUNDING SOURCES

Contributors

This work was supervised by a dissertation committee consisting of Professor Kim R. Dunbar of the Department of Chemistry as Chair with Professor Marcetta Y. Darensbourg, Professor François P. Gabbaï of the Department of Chemistry and Professor Robert C. Burghardt of the College of Veterinary Medicine and Biomedical Sciences as Committee Members.

The bio-evaluation study conducted in Chapter II and Chapter III was performed in collaboration with Professor Jean-Philippe Pellois in the Department of Biochemistry and Biophysics at Texas A&M University in assistance with Ryan P. Coll and Ellen Song from Dunbar group. The *in vitro* cellular studies discussed in Chapter IV were performed in collaboration with Professor Robert C. Burghardt and Professor Rola Barhoumi Mouneimne in the College of Veterinary Medicine & Biomedical Sciences at Texas A&M University. The live cell imaging using confocal microscope was accomplished with the help of Dr. Mouneimne. Some of the crystal structures described in this dissertation were refined with the help of Dr. Brian S. Dolinar and Haomiao Xie.

Part of the synthesis and characterization work depicted in Chapter II have been published in collaboration with Professor Claudia Turro in the Department of Chemistry and Biochemistry at The Ohio State University in Albani, B. A.; Peña, B.; Saha, S.; White, J. K.; Schaeffer, A. M.; Dunbar, K. R.; Turro, C. *Chem. Commun.* **2015,** *51*, 16522.

The Laboratory for Molecular Simulation, the X-ray Diffraction Laboratory and NMR Facility in the Department of Chemistry have provided the necessary software, computer time and instrument time. The Chemistry Mass Spectrometry Laboratory in the Department of Chemistry have measured the sample and provided high quality data.

All other work and data analysis conducted as part of this dissertation was completed by the student independently.

Funding Sources

TABLE OF CONTENTS

LIST OF FIGURES

Page

xvii

xx

LIST OF TABLES

CHAPTER I

INTRODUCTION

Cancer Statistics: Worldwide and United States

Cancer is a group of diseases characterized by uncontrolled cellular growth with potential to invade or spread to other parts of the body resulting in death. Cancer can be caused by different factors which are not limited to intrinsic factors such as inherited genetic mutations or immune system defects but also include external factors such as alcohol consumption and tobacco smoking, physical inactivity and high body mass index, infectious organisms, environmental chemicals/ carcinogens, radiation *etc*.[1] These risk factors can act simultaneously or in sequence to initiate and augment cancer cell growth. The abnormal gene expression in cancerous cells can cause imbalance between cell proliferation and cell death leading to the formation of tumors that can eventually spread into other tissues and organs through the blood and lymph systems, a process known as metastasis.[2,3] Owing to diagnosis tools and modern cancer therapies that can detect cancer at very early stages, and even cure it in the case of some specific cancer types, the mortality rate has decreased 27% from 1991 to 2016.[1]

Cancer is the second leading cause of death globally with an estimated 9.6 million deaths in 2018 according to the World Health Organization (WHO). One in six deaths are accounted for by cancer. The most common causes of cancer deaths are lung, colorectal, stomach, liver and breast cancers worldwide.[4] According to the American Cancer Society,

1

cancer is the second most common cause of death in the United States (US) after heart diseases with more than 1.7 million new cases of cancer expected to be diagnosed in 2019 with an estimated death toll of 606,880. The risk of occurrence of cancer is higher for older people with 80% of all cancer cases diagnosed in people of age 55 or older. The 2019 report on Cancer Facts & Figures released by American Cancer Society[1] states that prostate cancer in men and breast cancer in women are the most common type of cancer occurrences in each gender category with an estimated 174,650 (20%) and 268,600 (30%) cases respectively, whereas, lung and bronchial cancers are responsible for the highest number of cancer related deaths in the US in both gender categories (24% for men and 23% for women). The 5-year relative survival rates vary by cancer types with pancreatic cancer (9%), liver cancer (19%), lung and bronchial cancer (20%) and esophageal cancer (21%) having the lowest survival rates in the US during the 2008-2014 period.[1]

Cancer is clearly a worldwide problem and a major health issue in the United States and will continue to elicit enormous global research efforts across several disciplines to gain a better understanding of cancer biology with aims of providing faster and more accurate cancer diagnoses and improved treatments for patients. In this regard, chemistry is at the forefront of cancer drug research and continues to provide innovative solutions for the treatment of cancer through the development of more effective and safer chemotherapeutic drugs.

Cisplatin and Pt-based Chemotherapeutics

The field of medicinal inorganic chemistry witnessed a major milestone after the serendipitous discovery of cisplatin (cis-$[Pt(NH_3)_2Cl_2$, Figure 1.1) by Rosenberg *et al.* in 1965 followed by its approval by the United States Food and Drug Administration (FDA) in 1978 due to its remarkable antiproliferative properties.[5-6] Although it was initially approved to specifically treat metastatic ovarian and testicular cancer with high cure rates, it has also been used to treat bladder, melanoma, lymphomas, cervical, non-small cell lung cancer (NSCLC) and small cell lung cancer (SCLC).[7-8] When cisplatin enters the bloodstream, the high chloride concentration (100 mM) in the blood prevents the hydrolysis of coordinated chloride, but, after being transported inside the cell, the lower intracellular chloride concentration (4-20 mM) facilitates rapid hydrolysis of one or both chloride ligands to form the aquated species which can covalently bind to purine DNA bases to form both intra- and inter-strand DNA crosslinks.[7, 9-13] Cisplatin binds more strongly to the N7 position of guanine over adenine and forms a variety of DNA adducts. In particular, 1,2-GpG intra-strand adducts are known to significantly bend and unwind the DNA helical structure leading to obstruction of replication and transcription processes which trigger various signal transduction pathways leading to cell cycle arrest and programmed cell death/apoptosis.[7-8, 11-14]
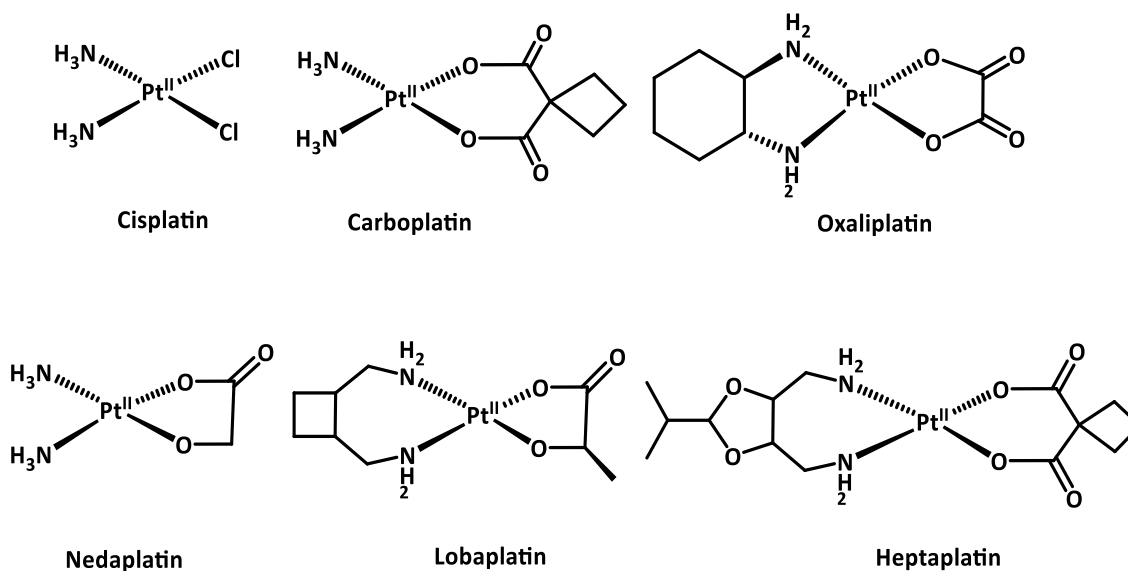
Figure 1.1. The platinum-based anticancer drugs approved for cancer chemotherapy.

In spite of its success and high cure rates, cisplatin suffers from severe dose-limiting side effects due to lack of specificity arising from indiscriminate cellular uptake by both healthy and cancerous cells. The side effects include acute nephrotoxicity, neurotoxicity, hepatotoxicity, ototoxicity, myelosuppression or bone marrow suppression, toxicity to gastrointestinal tract among others.[8] Subsequently, the second generation Pt-based drug carboplatin (Figure 1.1) was developed and approved by FDA in 1989 which is effective against cisplatin resistant ovarian cancer. Carboplatin is essentially devoid of nephrotoxicity and it is less toxic to the gastrointestinal tract and less neurotoxic compared to cisplatin,[7] but one of the major impediments with both drugs is development of acquired tumor resistance during the course of therapy along with intrinsic resistance to some tumors. Major mechanisms of drug resistance include decreased membrane transport/cellular uptake of the drugs, increased cytoplasmic detoxification, improved

4

DNA damage recognition and repair together with increased tolerance to DNA damage.[7-8] Tumor resistance exhibited by ovarian cancer can be related to downregulation of copper transporter-1 (CTR1) expression by cisplatin, which is the major plasma-membrane transporter of cisplatin, leading its reduced influx. Also, levels of cytoplasmic thiol-containing species such as glutathione determine the efficacy of the drug.[7]

Further improvements were implemented in the next generation of Pt-based drugs to circumvent some of the detrimental side effects and to overcome one or more resistance mechanisms. After cisplatin's approval in the late 70s, many platinum-based drugs have entered clinical trials but only two drugs, *viz.*, carboplatin and oxaliplatin have gained global approval in addition to nedaplatin, lobaplatin and heptaplatin (Figure 1.1) which are approved in Japan, China and South Korea respectively.[8, 11-13] Oxaliplatin, approved in 2002 by FDA, is able to overcome acquired tumor resistance in some cancers due to the fact that its uptake is less dependent on CTR1 and the oxaliplatin-DNA adduct is less recognizable by DNA repair enzymes as oxaliplatin-induced DNA crosslinks differ in structure. Oxaliplatin in combination with 5-fluorouracil and folinic acid is used as the first line of chemotherapeutic treatment of cisplatin-resistant metastatic colon cancers.[7, 11]

Many researchers are continuously improving the effectiveness of platinum drugs by introducing complex functionalization around the general square planar framework shared by the approved Pt(II) based drugs.[15] For example, sugar conjugation can target glucose receptors, steroid conjugation can target selective steroid receptors (like estrogen, testosterone, bile acid) on the cancer cells, whereas, folic acid and peptide conjugated Pt(II) complexes target specific tumor types overexpressing folate receptors and specific

proteins.[11, 15] Other than traditional Pt(II) complexes, octahedral Pt(IV) complexes are also being evaluated for their antiproliferative properties and satraplatin, a Pt(IV) drug that can be administered orally, is currently in clinical trials. Overall, Pt(IV) complexes are kinetically more stable to ligand dissociation than Pt(II) complexes with ease of tunability.[7-8, 11, 15] More recently nano delivery of both Pt(II) and Pt(IV) drugs encapsulated inside liposomes, co-polymers, polymeric micelles, carbon nanotubes and even metal organic framework (MOF) have been pursued to improve their cellular uptake as well as efficacy.[11, 16-17]

Non-Platinum Metallodrugs as Cancer Chemotherapeutics

To circumvent the drawbacks associated with traditional Pt-based chemotherapeutic drugs, scientists are striving to find alternative metal based anticancer drugs with more selectivity, lower systemic toxicity and different mechanisms of action. In this vein, ruthenium and gallium based metallodrugs are the most promising ones entering into clinical trials. Two Ru(III) compounds, *viz.*, [H_2im][*trans*-RuCl$_4$(S-dmso)(Him)] (**NAMI-A**; Him = imidazole, dmso = dimethylsulfoxide)[13] and [H_2ind][*trans*-RuCl$_4$(Hind)$_2$] (**KP1019**; Hind = indazole) (Figure 1.2), are the first Ru-based metallodrugs to enter into human clinical trials.[12, 18-21] More recently, the sodium salt of KP1019 (**NKP1339**) (Figure 1.2) with improved water solubility and similar anticancer efficacy as KP1019 has been studied successfully in a phase I clinical trial against solid tumor.[22] It was hypothesized that Ru(III) compounds are reduced to Ru(II)

species facilitated by the reducing environment of the tumor cells which is believed to be the active component.[13] The only gallium based metallodrug developed by Keppler *et al.*, namely, tris(8-hydroxyquinolinato)gallium(III) or more well-known as KP46 (Figure 1.2) contains a chelating ligand 8-hydroxyquinoline, which itself has anticancer properties. An oral formulation of KP46 (NKP2235) was evaluated in phase I clinical trials with the outcome being promising tolerability and preliminary evidence of clinical activity against renal cell carcinoma.[12, 23-24] Other transition metal complexes that are actively being evaluated for their promising antiproliferative properties includes titanium, iron, copper, palladium, rhodium, osmium, iridium and gold complexes.[13-14]

Redox active transition metal complexes of Pt^{IV} or Ru^{III} possessing multiple oxidation states under physiological condition have already being explored in clinical trials as prodrugs which generate active Pt^{II} and Ru^{II} drugs in the reducing environment of tumors. With similar concepts in mind, more recently other redox active metal complexes of Co^{III}, Fe^{III}, Os^{II}, Ir^{III} along with Pt^{IV} and Ru^{III} have been reported to exhibit redox-mediated anticancer activity. These metal complexes can introduce artificial oxidative or reductive stress inside the cell through generation of reactive oxygen species (ROS) and trigger apoptosis through various pathways which can increase selectivity and combat drug resistance.[25]
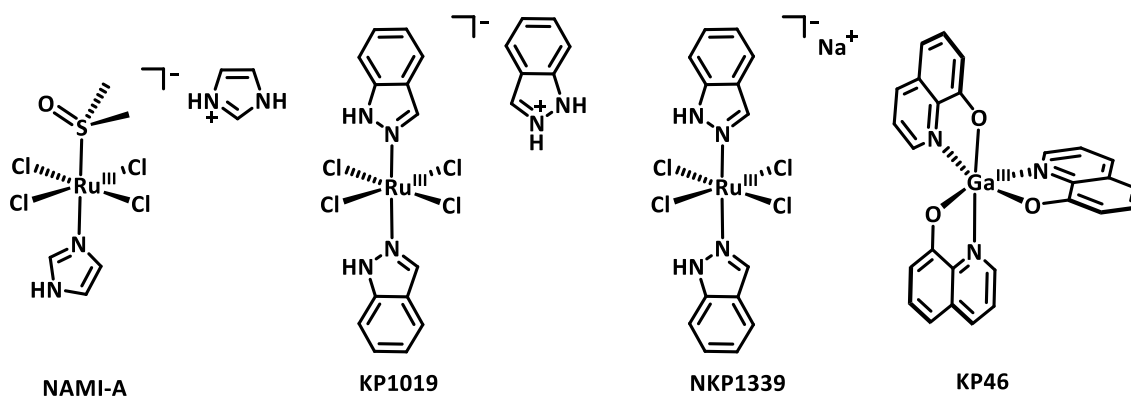
Figure 1.2. Promising non-platinum metallodrugs in clinical trials for cancer chemotherapy.

Emergence and Success of Ruthenium Metallodrugs

Ruthenium metallodrugs are emerging as the most promising alternatives to Pt-based chemotherapeutic agents given the initial success of three Ru(III) complexes, namely, NAMI-A, KP1019 and NKP1339 (Figure 1.2), which have been evaluated favorably in clinical trials. Although the structures of NAMI-A and KP1019 are quite similar, their mechanism of action and anticancer efficacy are different. NAMI-A, developed by Alessio *et al.*, is not very cytotoxic *in vitro* but this is the only metal based compound developed in last 30 years which has been intensely investigated for its ability to inhibit solid tumor metastases such as metastatic lung cancer.[18, 26-27] Sava *et al.* have studied NAMI-A in combination with conventional anticancer chemotherapy drugs including doxorubicin, gemcitabine, 5-fluorouracil, paclitaxel etc.[28] Despite its impressive efficacy against solid tumor metastases, NAMI-A was withdrawn from the human clinical trial after it failed in phase I/II study in combination with gemcitabine in patients with

8

NSCLC.[25, 29] In contrast, KP1019, developed by Keppler *et al.*, is specifically effective against cisplatin resistant colorectal tumors and, more recently, the water soluble drug NKP1339 with similar anticancer efficacy has also been studied successfully in a phase I clinical trial against solid tumors.[19-22] Both compounds possess high tumor targeting potential based on their strong binding to serum proteins like albumin and transferrin. The redox activity of these compounds can disrupt cellular redox balance which induces G2/M cell cycle arrest and blockage of DNA synthesis leading to induction of apoptosis via a mitochondrial pathway.[19, 22] It is hypothesized that all three compounds with Ru(III) centers act as prodrugs and are activated upon reduction to Ru(II) inside the reductive tumor environment. The Ru(II) drug, which is more susceptible to ligand exchange than Ru(III), facilitates the hydrolysis of Ru-Cl bond to interact with cellular targets.[22, 30]

As evidenced from the clinical results, ruthenium metallodrugs exhibit lower systemic toxicities with higher efficacies against some cisplatin resistant cancer cells. Major advantages associated with Ru coordination complexes for their favorable clinical applications are as follows[31-33] –

- Ruthenium forms thermodynamically stable coordination compounds with slow ligand exchange rates which enable them to reach the biological targets without being modified.

- Multiple oxidation states can be attained under physiological pH which can also be explored for a prodrug approach along with redox-mediated anticancer activity.

- Ruthenium is capable of mimicking iron in the active sites of different carrier proteins, such as transferrin (a major iron transporter protein present in plasma and other body fluids), for its transportation through the body thus exhibiting less systemic toxicity.

- Ruthenium coordination complexes can be tuned and modified easily for the desired chemotherapeutic properties leading to higher efficacies.

The initial success of Ru(III) compounds in the clinical trial sparked the development of new Ru coordination complexes as potential chemotherapeutic agents. Among them, the most successful lead compounds belong to the family of organometallic Ru-arene half sandwich complexes investigated by Sadler *et al.* and Dyson *et al.* Although the structures of the "piano stool" shaped organometallic compounds (Figure 1.3a and b) are quite similar, their anticancer properties are very different.[34] The design of Ru^{II} arene ethylenediamine (en) derivatives, [(arene)Ru(en)Cl]$^{+}$ (Figure 3.1a), developed by the Sadler group possess different functional features. For example, the arene moiety aids in intercalation of DNA along with stabilizing the Ru(II) oxidation state, the en ligand improves water solubility and H-bonding recognition and the Cl^{-} ligand can dissociate to provide a binding site for DNA.[35-36] Although DNA is a major target for this family of derivatives, the mechanism of DNA binding is different than traditional cisplatin. These complexes exhibit high affinity to thiol containing proteins such as glutathione which, upon oxidation, form reactive sulfenate intermediates that react with the guanine N7 of DNA.[25, 34, 37] The compounds induce apoptosis through inhibition of DNA synthesis, activation of p53, G0/G1 cell cycle arrest and nuclear fragmentation.[14]
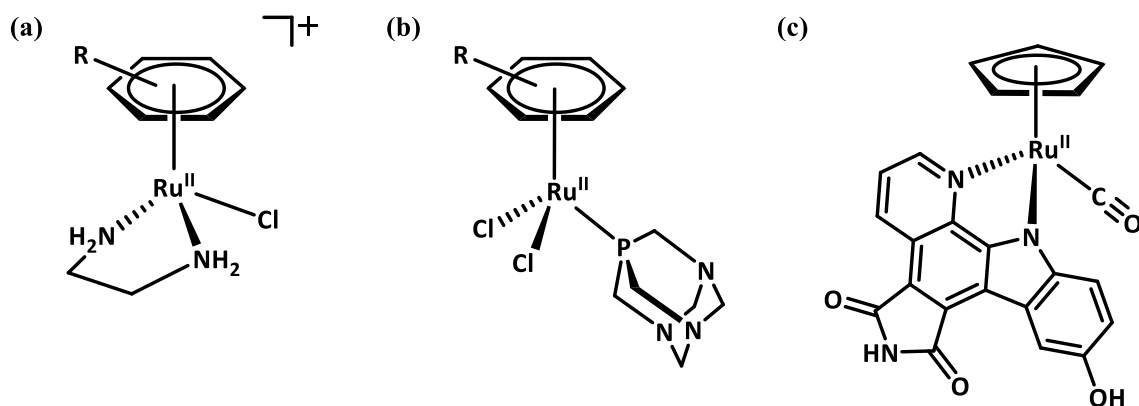
Figure 1.3. Promising ruthenium half-sandwich complexes (a) Ru[II] arene ethylenediamine derivatives, (b) RAPTA derivatives, and (c) Ru[II] arene complex with a tethered kinase inhibitor.

Ruthenium-arene-PTA (PTA= 1,3,5-triaza-7-phosphaadamantane) complexes, commonly known as RAPTA derivatives (Figure 1.3b), developed by Dyson group operate by a different mode of action.[38-39] Similar to NAMI-A, this family of compounds also lack *in vitro* cytotoxicity but exhibit promising antimetastatic activity through the inhibition of angiogenesis.[14] RAPTA compounds preferentially form adducts with enzymes and serum proteins rather than DNA as shown in different studies.[34, 39] RAPTA-C (arene = p-cymene) exhibits cell growth inhibition *in vivo* against Ehrlich ascites carcinoma by triggering G2/M phase arrest and induces apoptosis through the mitochondrial pathway facilitated by release of cytochrome c and activation of caspases.[14] Many more derivatives of the RAPTA family were developed over the years with diverse anticancer properties and selectivities.[39] More recently, Dyson *et al.,* in collaboration with the Gasser and Renfrew groups, modified the RAPTA-C structure by replacing chlorides with azide ligands which renders the compound photoactive and potentially useful in photoactivated chemotherapy (PCT).[40] One approach to improve the selectivity of the

organometallic ruthenium half-sandwich complexes is by introducing known enzyme inhibitor motifs into the ligand architecture to target tumors overexpressing those enzymes. For example, a family of organometallic ruthenium compounds was developed by Meggers *et al.* by incorporating the well-known protein kinase inhibitor staurosporine motif in the ligand design (Figure 1.3c).[41-43] Specifically, this complex inhibits glycogen synthase kinase 3β (GSK3β) to activate p53 and induces apoptosis *via* the intrinsic mitochondrial pathway.[43]

Researchers are continuing to use innovative approaches to design novel ruthenium compounds with improved efficacy and selectivity by focusing on specific tumor targets and specific cell organelles. Due to the well-established synthetic chemistry of ruthenium, extensive effort is being directed at the development of mononuclear as well as multinuclear coordinatively saturated and substitutionally inert Ru(II) polypyridyl complexes as anticancer drug candidates.[15, 33, 44-46] Since covalent binding to DNA is not possible for these types of metal complexes, they exert cytotoxic behavior by different mechanisms than cisplatin. These complexes can interact with DNA electrostatically or by intercalation.[33, 44] Also, they can accumulate inside mitochondria due their cationic nature as well as with several other organelles including the nucleus, lysosomes, endoplasmic reticulum (ER) etc.[46] Complexes targeting both enzymes and proteins overexpressed in certain types of cancers have also been designed for their selective accumulation inside the tumors.[15, 46] A number of these Ru(II) complexes generate oxidative stress inside the cell due to cellular ROS generation.[46] Apart from homometallic polynuclear Ru complexes, several heterometallic multinuclear complexes of Ru have

been developed with Pt, Ti, Fe, Au, Co as anticancer agents.[33, 45, 47] Also, these Ru polypyridyl complexes are increasingly utilized in photodynamic therapy (PDT) and PCT applications which will be discussed in the following sections.[46, 48-49] Cyclometallated ruthenium compounds, a class of Ru-based oraganometallic complexes, are also being explored for both chemotherapeutic and PCT application which is discussed in Chapter 4 of this dissertation.[46] On a more recent approach, Ru(II)-based nanomaterial vehicle systems are developed with Se and Au nanoparticles, carbon nanotubes, silica composites, biocompatible polymers for improved delivery of the compounds into tumor cells.[46, 50]

Numerous cellular studies, both *in vitro* and *in vivo*, were reported in the literature. Overall, the general trend observed is that the higher the lipophilicity of the complex, the more cytotoxic it is due to greater cellular uptake. So the strategy of introducing lipophilic moieties on the ligands to improve cellular uptake is very common in the design of novel Ru complexes.[33] The mechanism of cell death induced by Ru(II) anticancer compounds can involve apoptosis, necrosis and autophagy or a combination of multiple mechanisms. Apoptosis, which is the desired mechanism of programmed cell death (PCD), can be activated through two pathways, *viz.*, intrinsic and extrinsic pathways. The intrinsic pathway, also known as mitochondria-mediated pathway, can be activated by DNA damage, oxidative stress and ER stress. These stimuli induce mitochondrial release of cytochrome c which signals activation apoptotic proteases like caspases and regulated other proteins involved in apoptotic cell death.[14, 46]

Photodynamic Therapy (PDT) Modality

Until now, cancer chemotherapy heavily relies on Pt-based chemotherapeutic drugs despite of their detrimental dose-limiting side effects. Among several cancer therapies available, PDT proved to be a successful non-invasive therapeutic modality for the treatment of melanoma and several dermatological diseases.[51] The approach of PDT involves low systemic toxicity due to its highly localized and selective mode of action.[52] In PDT, light (both visible and infra-red) is used as a tool to activate a pro-drug, known as photosensitizer (PS), to generate or release toxic species inside the cell leading to cellular death. PDT gives more spatial and temporal control over the drug and is suited for the treatment of endoscopically accessible tumors such as lung, bladder, advanced head and neck, gastrointestinal, esophageal, prostate, gynecological related cancer other than skin related conditions.[51-54] For the optimal tissue penetration, the therapeutic window considered for PDT is 600 – 900 nm as lower energy light penetrates deeper inside the tissue.[53, 55-56]
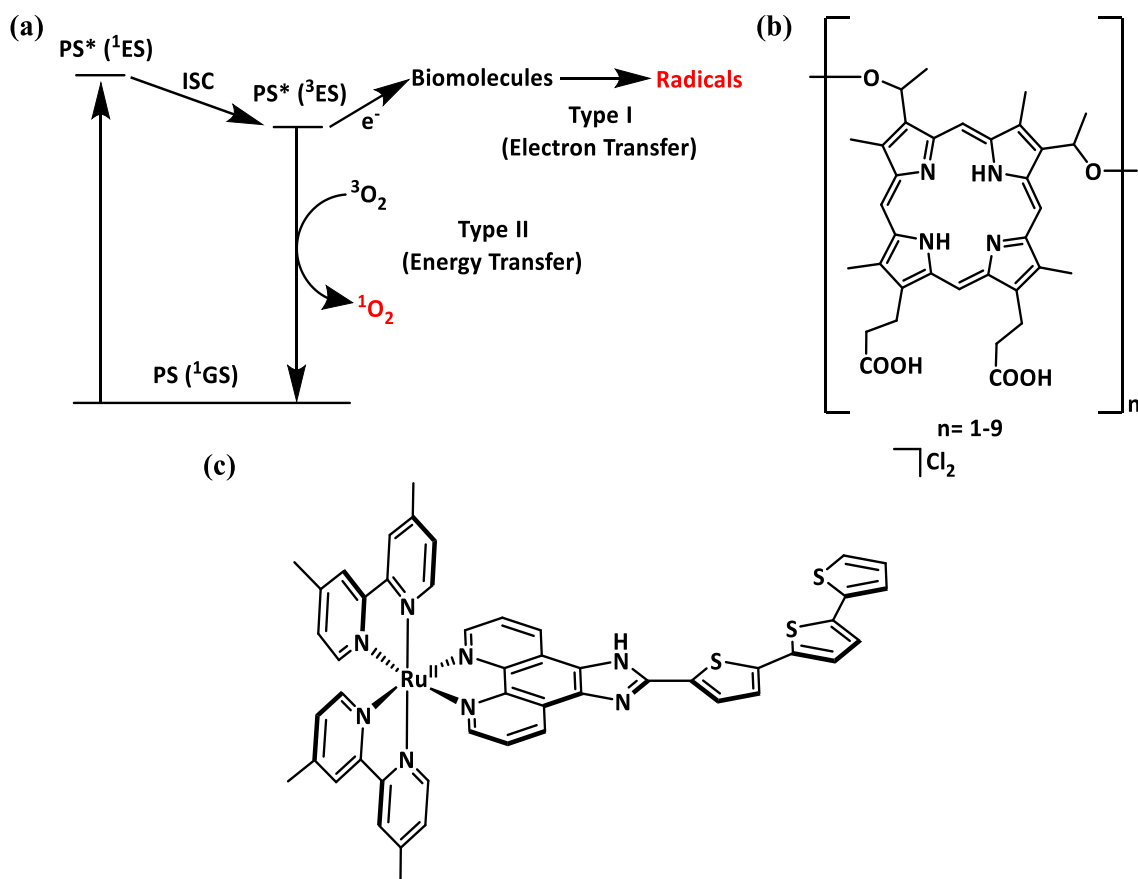
Figure 1.4. (a) Jablonski diagram showing type I and type II photoreactions, (b) chemical structure of porfimer sodium or, Photofrin®, and (c) chemical structure of TLD1433.

In PDT, after injecting the PS directly into the tumor or in the bloodstream, PS is selectively accumulated in the tumor cells over the period and then the PS is activated by laser directed through fiber optics or light-emitting diode (LED). Upon irradiation with a specific wavelength of light, the PS in its singlet ground state (^{1}GS) is promoted to its singlet excited state (^{1}ES) which quickly populates more stable triplet excited state (^{3}ES) due to intersystem crossing (ISC). With a long lived ^{3}ES, the PS can either facilitate excited state electron transfer to cellular biomolecules like proteins[49] to generate free radicals (H_2O_2, superoxide radical, hydroxide radical) inside the cell (Type I PDT) or, can

transfer the energy to molecular oxygen [triplet oxygen ($^3O_2$)] to generate extremely reactive and highly cytotoxic singlet oxygen ($^1O_2$) inside the cell (Type II PDT), both causing irreversible cellular damage leading to cell death (Figure 1.4a).[49, 53, 57] PDT can kill the tumor cell directly in addition to vascular damage and immune response.[51-52]

Hematoporphyrin and its oligomeric mixture, better known as porfimer sodium or, Photofrin® (Figure 1.4b) is considered to be the gold standard in PDT and was approved by FDA in 1995 for the treatment of esophageal cancer and NSCLC. Photofrin® suffers from major drawbacks like unknown composition, low molar absorption coefficient (3000 $M^{-1}cm^{-1}$) at 630 nm (excitation wavelength), low quantum yield of oxygen sensitization (~ 20%) and prolonged photosensitivity (4-6 weeks) in patients after treatment.[51-52, 58] To improve the efficacy in the therapeutic window, substituted porphyrins, chlorins, phthalocyanines based PDT agents with strong absorbance in red region of visible light are evaluated in the clinical trials.[53, 57] Also to facilitate ISC, heavy metal ions are introduced in the tetrapyrrolic core of parent PDT photosensitizers as increased spin-orbit coupling favors ISC with almost unit efficiency. Three metal-based PDT agents with Lu^{III} (Lutex), Pd^{II} (WST11) and Sn^{IV} (Purlytin) are currently in clinical investigations.[49, 57] Several new approaches are underway to improve drug penetration with improved drug delivery systems.[59]

TLD1433 (Figure 1.4c), the first Ru-based photosensitizer that entered human clinical trials and is currently being investigated for non-muscle invasive bladder cancer, was developed by McFarland *et al*. TLD1433 was selected from a group of Ru(II)-dyads that incorporate α-oligothiophenes as a part of a structure activity relationship (SAR)

study. The complex is non-toxic in the dark with low micromolar EC_{50} values upon irradiation. The intense luminescence arising from the emissive ^{3}MLCT (triplet metal-to-ligand charge transfer) states can be utilized to localize the compound inside the tumor cell or when bound to DNA. Whereas, a population of much longer-lived α-terthienyl based ^{3}IL (triplet intra-ligand) states result in potent toxicity of the compound with generation of both $^1O_2$ and radical cations. So, it is hypothesized that TLD1433 acts by both type I and type II mechanisms.[57] TLD1433 absorbs at 525 nm which is far blue shifted from the approved therapeutic PDT window. To red-shift the absorption band, McFarland *et al*. have recently introduced cyclometallated α-oligothiophene ligands to form cyclometallated Ru(II)-complexes.[60-61] Multiple Ru(II) centers are also incorporated in the porphyrin structure[48] and other supramolecular motifs along with several Ru(II) nanomaterial systems are developed with polymers, metal-organic frameworks, carbon-nanotubes etc. for improved delivery of Ru-based sensitizers inside tumors with improved efficacy.[62-63]

One of the major disadvantages associated with PDT is its major reliance on O_2 dependent mechanisms (Type II PDT) which involve sensitization of cellular oxygen to generate lethal $^1O_2$ to kill tumors. As a result, PDT proves to be ineffective against the most aggressive and drug resistant hypoxic (oxygen poor) tumors. To circumvent this impediment, PDT agents need to be modified such that they destroy cancer cells by O_2 independent pathways in addition to singlet oxygen or other reactive oxygen species.[48]

Photoactivated Chemotherapy (PCT) Modality

PCT, a new field of therapeutics, was developed to overcome the limitations associated with traditional PDT by moving away from the oxygen dependent pathway.[64] In PCT, the light activation of otherwise inert transition metal complexes can generate cytotoxic species in a controlled manner with complete spatiotemporal control similar to PDT. Unlike most PDT agents, PCT agents exploit different mechanisms to induce cell death; these include photoinduced ligand dissociation, DNA crosslinking, uncaging biologically active molecules/drugs, and excited state oxidation of cellular components among others.[48-49] Some PCT complexes can additionally produce singlet oxygen upon irradiation due to the presence of specific ligand systems, giving rise to dual action therapeutics.[65-67] Numerous photoactivatable transition metal compounds including those containing Pt(II), Pt(IV), Ru(II), Rh(III), Ir(III), Re(I), Mn(I), Co(III) metal ions are being investigated as PCT agents.[49, 56, 64, 68-69]

Coordination complexes of Ru(II) are increasingly being pursued as PCT agents due to their well-studied and diverse photophysical and photochemical properties and the fact that they absorb strongly in the visible region due to intense MLCT transitions and possess long-lived excited states.[68] In this approach, coordinated ligand/drug/inhibitor molecules are released inside the tumor cells upon light irradiation, a strategy referred to as "photo-uncaging".[46, 48, 64, 68, 70] Additionally, in some Ru(II) complexes the resulting coordinatively unsaturated metal fragment is capable of binding to proteins and DNA giving rise to dual-action properties.[71-76] Another dual action approach targets some Ru

compounds with sterically bulky extended polypyridine ligands possessing low-lying π^* orbitals that generate $^1O_2$ and undergo ligand photodissociation triggered by light, thus combining both PDT and PCT pathways of cell death.[65-67]
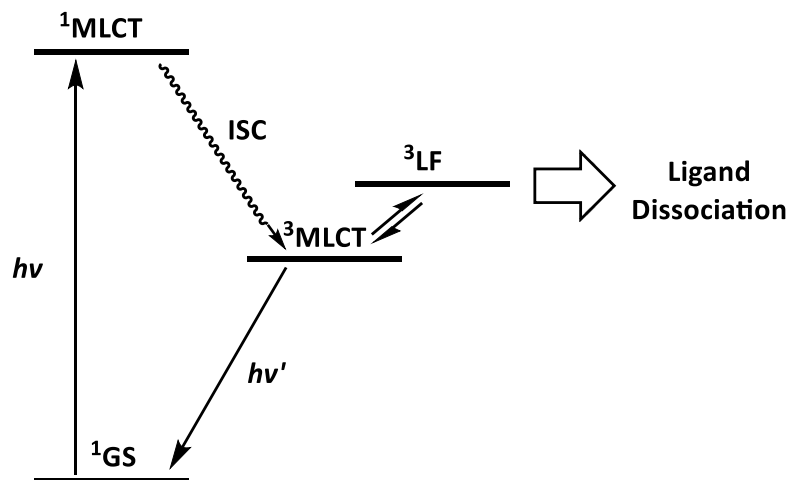
Figure 1.5. Jablonski diagram showing the mechanism of ligand photodissociation.

Absorption of visible light by Ru(II) complexes leads to excitation from the ground state to the corresponding ^{1}MLCT (singlet metal-to-ligand charge transfer) state which undergoes fast ISC to populate the ^{3}MLCT state. This the ^{3}MLCT state can either decay *via* radiative (also known as luminescence) or non-radiative processes (thermal relaxation) to the ground state or can thermally populate the reactive ^{3}LF (triplet ligand field) state possessing Ru–L(σ^*) character (L= ligand). The population of the ^{3}LF state weakens the metal-ligand bond thus promoting photoinduced ligand dissociation (Figure 1.5).[77-80] The quantum yield of ligand photodissociation relies on the thermal accessibility of the ^{3}LF state from ^{3}MLCT.[81] The introduction of distortion in the metal coordination sphere can

lower the energy of the dissociative ^{3}LF state making it more thermally accessible which leads to an enhancement of ligand dissociation.[75] Incorporation of sterically bulky ligands induces distortion that leads to increased quantum yields of ligand photodissociation.[77, 81-83] This concept is being increasingly pursued in the design of new Ru(II) photocage architectures.[70, 84-87]

Development of Polypyridyl Ru(II) Photocage Architectures: Design and Mechanism of Action

The concept of "photocaging" was introduced in the late 1970s by organic chemists including Engels or Kaplan who designed photocaged cAMP (cyclic adenosine monophosphate) and photocaged ATP (adenosine triphosphate) where the phosphate group is protected by photocleavable nitrobenzyl group.[88-89] At that time, UV light was used for deprotection purposes as well as biological functions. Later some of the pioneering work by Etchenique *et al.* led to the development of the field of Ru(II)-based photocage design to release bioactive molecules upon irradiation with visible blue light suitable for biological studies. The Etchenique group demonstrated the release of caged neurotransmitters and neuromodulators such as 4-aminopyridine, serotonin, γ-aminobutyric acid (GABA) along with several amino acids.[90-92] Several groups have employed innovative approaches to design novel Ru(II) photocages with improved quantum yields of photodissociation along with bathochromic shifting of the absorption band of the complexes near the therapeutic window (600-900 nm).

Photocages Designed by the Turro and Dunbar Groups

Pioneering research by Turro *et al.* involved excited state ligand photodissociation phenomena associated with Ru(II) complexes to design their initial photocages. These researchers employed selective and step-wise photocleavage of L (L = NH$_3$, NCCH$_3$) in [Ru(bpy)$_2$(L)$_2$]$^{2+}$ (bpy = 2,2′-bipyridine) using blue light to generate [Ru(bpy)$_2$(H$_2$O)$_2$]$^{2+}$ as the active species which can bind to 9-ethylguanine (9-EtG) and photocleave DNA.[93-94] Later this group introduced the bioactive 5-cyanouracil (5-CNU) analog of the anticancer drug 5-fluorouracil in photocage design to synthesize **1** and **2** (Figure 1.6). Both complexes exhibit photorelease of 5-CNU when irradiated with blue light ($\lambda \geq 400$ nm) and the resulting coordinatively unsaturated metal fragment can subsequently bind to plasmid DNA. Additionally, **2** has the potential to kill HeLa cells upon irradiation as determined by a SYTOX green assay.[72-73] To integrate dual action cell death mechanism, the extended dppn ligand (dppn = benzo[*i*]dipyrido[3,2- a:2′,3′-c]phenazine), well-known to generate ^{1}O$_2$ from its low-lying π* orbitals, was introduced into the design of **3** (Figure 1.6). This complex is capable of both ^{1}O$_2$ production (quantum yield of 0.72) and excited state ligand exchange when irradiated with $\lambda \geq 400$ nm. Compound **3** is essentially non-toxic in the dark, but, when irradiated with 466 nm LED light, it is highly phototoxic with an IC$_{50}$ value in the nanomolar range (470 nM) and a phototoxicity index (PI) value of ~ 711 against HeLa cells.[95] To red-shift the excitation wavelength, the Dunbar group, in

collaboration with the Turro group, introduced the cyclometallated phpy ligand
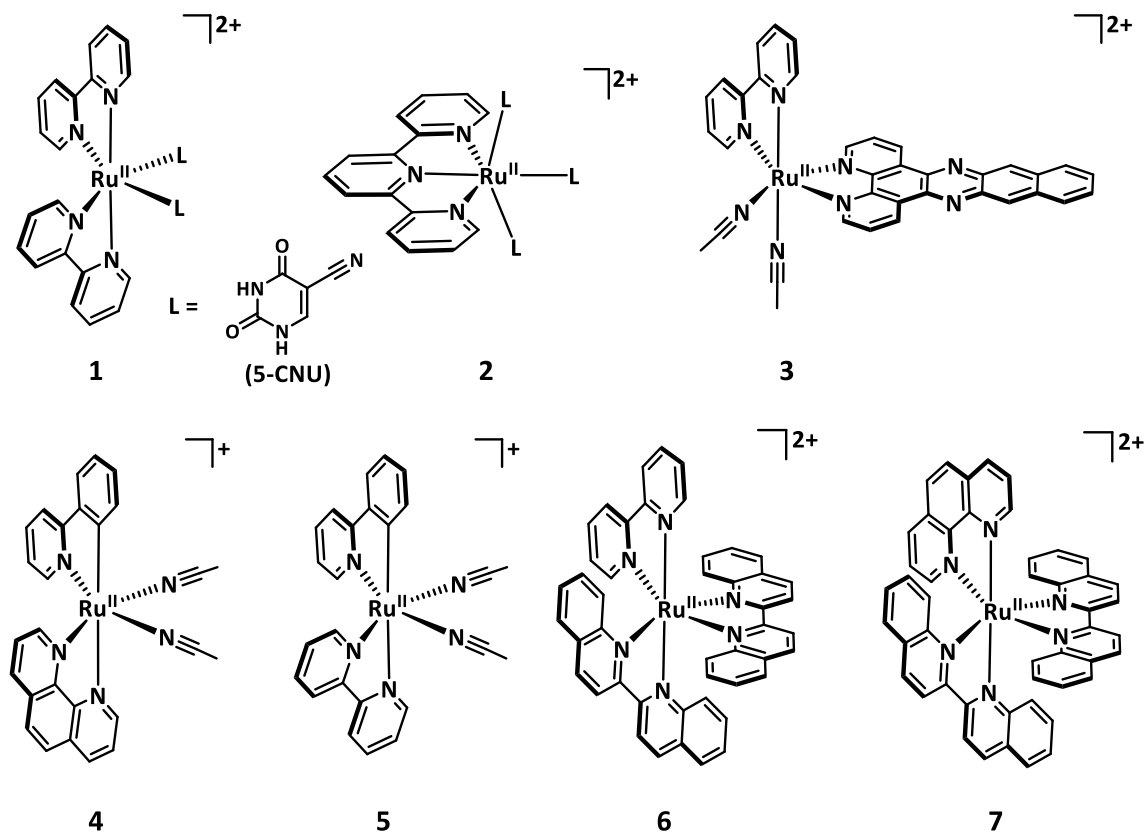
Figure 1.6. Ru(II) photocages designed by Turro and Dunbar *et al.*

(deprotonated 2-phenylpyridine) and biq ligand (biq = 2,2′-biquinoline) to synthesize **4-7** (Figure 1.6).[96-98] The phpy ligand destabilizes the HOMO upon cyclometallation whereas the biq ligand possesses low energy π^* LUMO orbitals which leads to a bathochromic shift of the absorptions. Compound **4** is more potent than **5** with a 14-fold enhancement of toxicity upon irradiation with 690 nm light against OVCAR-5 cells along with DNA binding.[98] This study showcased the role of glutathione (GSH) in enhancing ligand substitution both in the dark and upon irradiation.[96] Besides red-shifting the MLCT band in **6** and **7**, one biq ligand dissociates when irradiated with 630 nm light to generate the

potentially cytotoxic bis-aqua species, *viz.*, [Ru(bpy/phen)(biq)(H$_2$O)$_2$]$^{2+}$ (phen = 1,10-phenanthroline) which binds to plasmid DNA in a manner similar to cisplatin.[97] The Turro group also employed different sterically bulky ligand architectures to improve ligand photodissociation and introduced π-extended as well as σ-donating ligands to red-shift the excitation wavelength into the therapeutic window to design novel Ru(II) photocage platforms for potential PCT applications.[66, 77-78, 80, 86, 99-103] Incorporation of the dppn motif into the ligand architecture can generate ^{1}O$_2$ thus engendering dual action.[65-66, 86, 100] In a recent study, the Glazer group demonstrated that, instead of pyridyl-based photocleavable ligands, diazine-based ligands are excellent choices for the development of light activated dual action PCT agents.[76]

Photocages Designed by the Kodanko and Turro Groups

Cysteine protease enzymes play a critical role in the invasion and metastasis of cancer therefore the inhibition of cysteine proteases inside the tumor can prevent enzyme-substrate interactions to achieve anticancer effects. Some nitrile containing cysteine protease inhibitors can cease the enzyme activity through covalent interactions between the nitrile "warhead" with the active site thiolate moiety.[70] The Kodanko and Turro groups designed several nitrile containing cysteine protease inhibitors and tethered them covalently to [Ru(bpy)$_2$] fragment to synthesize [Ru(bpy)$_2$(L)$_2$]$^{2+}$ complexes **8**-**10** (Figure 1.7).[70, 74, 104] The inhibitors are stable when caged to the metal fragment in the absence of light and only exhibit inhibitory effects upon exposure to light (λ > 395 nm) due to their

photorelease, which provide complete spatiotemporal control over enzyme inhibition. Irradiation of **8** results in an ~ 32-fold enhancement of the inhibition of cysteine protease papain compared to dark and control experiments performed with $[Ru(bpy)_2(NCCH_3)_2]^{2+}$ showed lack of any inhibition which rules out the possibility of inhibition through the photoreleased metal fragment. The inhibition of human cathepsin B, L, K exhibited by **8** is also enhanced by light along with inhibition of significant cathepsin B activity being observed with human cell lysate from DU145 and hBMSC cells.[70, 74] Compounds **9** and **10** represent the structural modification of **8** and are more potent at inhibiting cathepsin K (CTSK) compared to **8**. Inhibition of human CTSK is augmented by 35-fold and 88-fold for **9** and **10** respectively upon light exposure.[70, 104] Compound **10** exhibits strong inhibition of CTSK activity in 3D tumor spheroids engineered to overexpress CTSK from prostate carcinoma cells lines.[105] The Turro group introduced the CTSK inhibitor Cbz-Leu-NHCH$_2$CN into a Ru(II) photocage architecture containing the dppn ligand to synthesize **12** with dual photochemotherapeutic properties. They compared the effect of $^1O_2$ generated by **12** with its bpy-analog **11** (Figure 1.7). Both compounds are stable in the dark and effectively release the caged inhibitor upon light ($\lambda \geq 450$ nm) exposure with additional generation of $^1O_2$ by **12** which is responsible for the DNA photocleavage observed in the gel electrophoresis ($\lambda_{irr} \geq 395$ nm, 5 min) experiment.[67]
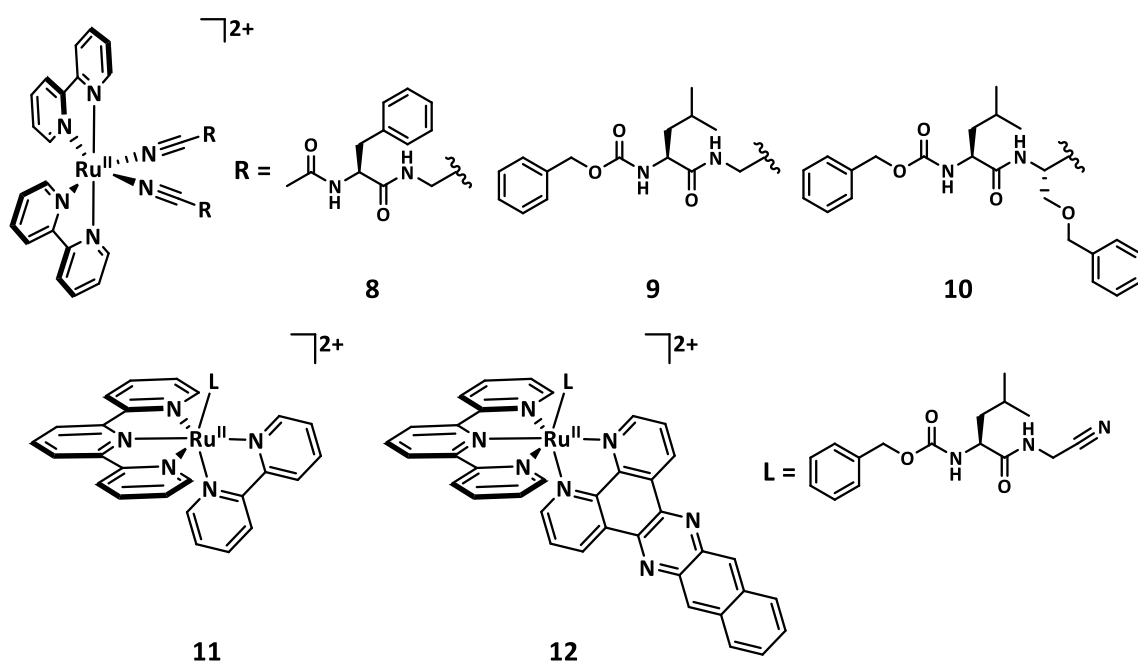
Figure 1.7. Ru(II) photocages with coordinated nitrile-functionalized cysteine protease inhibitors designed by Kodanko and Turro *et al.*

After successfully implementing the inhibition of cysteine protease in a controlled manner using a photocleavable nitrile-functionalized inhibitor coordinated to Ru(II) photocages, Kodanko *et al.* developed a new class of pyridyl-functionalized epoxysuccinyl-based cathepsin L (CTSL) inhibitors by modifying well-known CLIK inhibitors.[70, 84] Epoxysuccinyl-based CLIK-148 and CLIK-181 are known to effectively deactivate CTSL through the irreversible nucleophilic attack of the epoxy ring by the active thiolate moiety at the enzyme active site.[70, 84] This group used [Ru(tpy)(dmbpy)(L)]$^{2+}$ (tpy = 2,2′;6′,2″-terpyridine; dmbpy = 6,6′-dimethyl-2,2′-bipyridine, L = CTSL inhibitor) cage instead to enhance the pyridyl-based ligand photodissociation and synthesized **13** and **14** (Figure 1.8). The quantum yield of pyridyl-based ligand release is significantly lower than their nitrile-analog. To address this issue,

the sterically bulky dmbpy ligand was incorporated in the cage architecture to improve the quantum efficiency of inhibitor release. Compound **13** is stable in the dark but inhibits CTSL activity without light exposure suggesting that the epoxy ring on the bound inhibitor is sufficiently sterically open to undergo irreversible nucleophilic attack prior to cleavage of the Ru-N bond in the presence of light. In contrast, **14** is not very stable in the dark with ~ 30% enzyme activity being suppressed within an hour of incubation. In both compounds, however, improved CTSL inhibition was observed in the presence of visible light, an indication of enhanced inhibition due to photocleavage of the inhibitor.[70, 84] More recently,
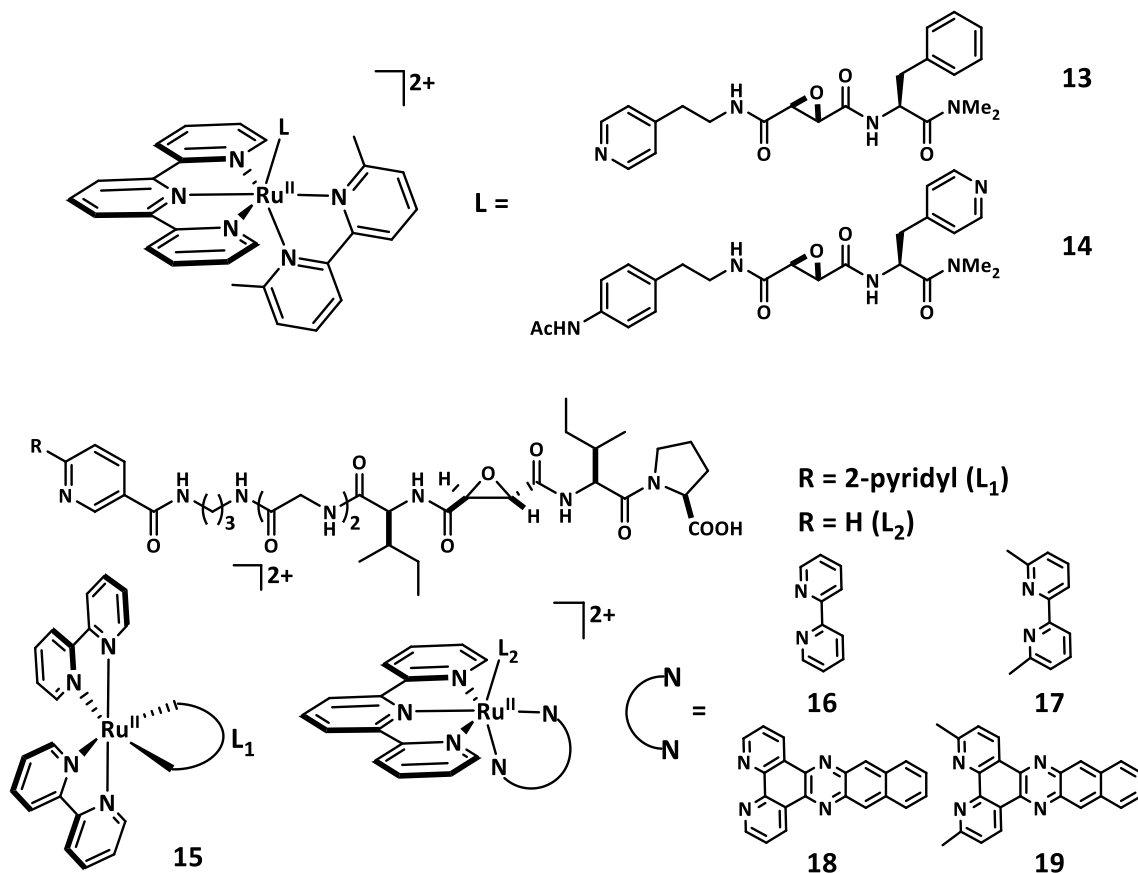
Figure 1.8. Ru(II) photocages with coordinated pyridyl and 2,2′-bipyridyl-functionalized cysteine protease inhibitors designed by Kodanko and Turro *et al.*

26

they designed bipyridyl and pyridyl-functionalized epoxysuccinyl inhibitors for cathepsin B (CTSB), a cysteine protease associated with invasive and metastatic behavior of tumors.[85] Complex **15** containing the emissive $[Ru(bpy)_3]^{2+}$ core was designed to track subcellular localization of complex-inhibitor conjugate whereas, (**16**-**19**) were designed to undergo photodissociation of the inhibitor along with generation of $^1O_2$ from coordinated dppn/dmdppn ligands for **18**-**19** (dmdppn = 3,6-dimethylbenzo[*i*]dipyrido[3,2-a:2′,3′-c]phenazine) to engender dual action (Figure 1.8).[85] These results were confirmed by photochemical studies and all compounds (**15**-**19**) irreversibly inhibit CTSB. Compounds **16**-**19** were evaluated against MDA-MB-231 triple-negative human breast cancer and MCF-10A breast epithelial cells in 2D and 3D cultures for their efficacy at proteolysis and cell viability under both dark and light conditions. Compounds **15**-**19** potentially inhibit dye-quenched collagen degradation to prevent metastatic behavior and only **19** causes efficient cell death under irradiated condition, consistent with its dual action properties.[85]

Photocages Designed by the Bonnet Group

Bonnet's group selected thioether-based photocleavable ligands with bio-relevant moieties attached to them which ensures the stability of the molecules in the dark[106] and also aids in cell penetration for improved efficacy. Once inside the cell, upon light exposure, the compounds can release the bioactive ligands along with the mono-aqua Ru(II)-fragment, either or both of which can potentially exhibit cytotoxic action.[107] These researchers also coordinated N-acetyl-L-methionine and D-biotin to the well-known

[Ru(tpy)(bpy)] fragment to synthesize **20** and **21** (Figure 1.9).[107] Their precursor [Ru(tpy)(bpy)Cl]$^+$ is highly susceptible to facile hydrolysis (90% conversion) within 4 h but, in contrast, **20** is stable for more than 3 weeks and **21** hydrolyses only 3% after 3 days in the absence of light. Both **20** and **21** demonstrate spontaneous thioether ligand dissociation in aqueous solution when irradiated with blue light ($\lambda = 452$ nm) to generate [Ru(tpy)(bpy)(H$_2$O)]$^{2+}$ **(Ru-aqua)**.[107] This exceptional stability of ruthenium-thioether photocages inspired Bonnet *et al.* to explore different thioether photocages for their potential PCT properties.[108-110] Cholesterol itself is a lipophilic molecule and by tethering them to a Ru complex can dramatically alter the partition coefficient (log P).[111-112] Thus to improve lipophilicity and enhance cellular uptake of Ru(II) photocages, they designed a thioether-cholesterol ligand to synthesize **22** (Figure 1.9).[108] The compound is stable in the dark in cell-growth medium but when irradiated with blue-light ($\lambda = 455$ nm, 10.5 mW/cm^2), it dissociates to form a free thioether-cholesterol ligand and **Ru-aqua**. When evaluated against six human cancer cell lines (A375, A431, A549, MCF-7, MDA-MB-231 and U87MG), the free ligand and **Ru-aqua** are found to be non-toxic but, unexpectedly, the amphiphilic **22** is potentially cytotoxic similar to cisplatin against all cell lines in the dark (EC$_{50}$ = 5-6.5 µM). Irradiation with blue light ($\lambda = 450$ nm, 6.3 J/cm^2) has little effect on phototoxicity compared to its dark toxicity after 6 h of incubation but increases by a factor of 2 when incubated for 24 h or longer. When unusual cytotoxicity

of **22** in the dark was investigated, it was found that, at lower than critical aggregate
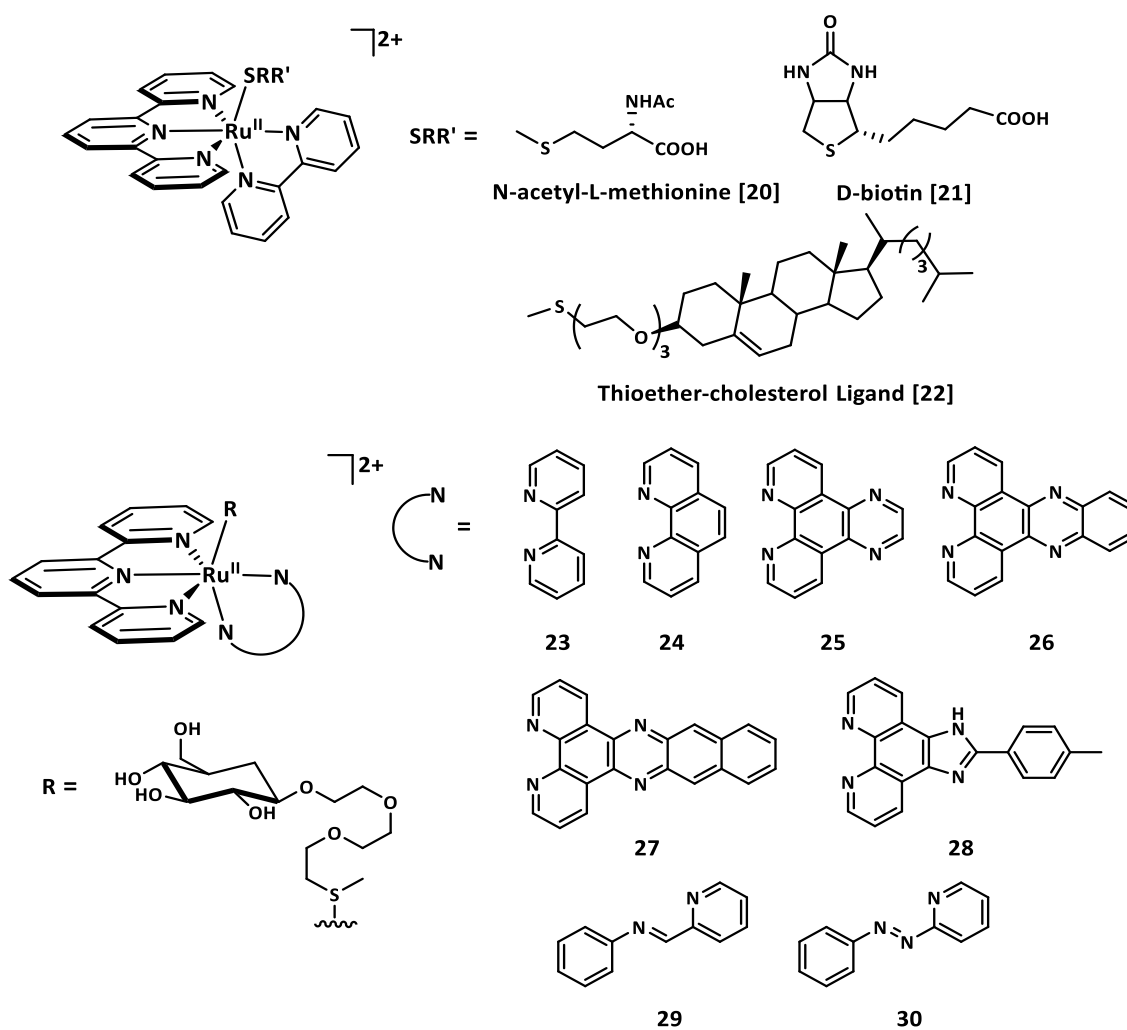
Figure 1.9. Ru(II) photocages with thioether-functionalized photocleavable ligands designed by Bonnet *et al.*

concentration (CDC), it remains a monomer and penetrates the cell membrane due to

intrinsic lipophilicity at higher incubation times. As a result, when light is shone on the

cells after long incubation times, **22** can photorelease the metal fragment [Ru(tpy)(bpy)],

which can interact with cellular biomolecules *in situ* to display enhanced cytotoxicity upon

irradiation. At concentrations higher than CDC (> 3-5 µM), **22** forms supramolecular

aggregates that induce non-apoptotic cell death by permeating cell membranes and extracting lipids and membrane proteins.[108] In another ligand design, the group incorporated a D-glucose decorated thioether ligand and tethered it to the [Ru(tpy)(NN)] fragment (NN = diimine ligands with varying lipophilicity) to synthesize compounds **23**-**30** (Figure 1.9) which improved their water solubility.[109] All compounds are stable in the dark as expected and only **23**-**29** display ligand exchange in aqueous solution with blue light irradiation. Compound **27** with the dppn-ligand generates $^1O_2$ (quantum yield of $^1O_2$ ~ 71%). When all the compounds were evaluated *in vitro* against A549 and MCF-7 cell lines, only **26** and **27** showed phototoxicities with **27** being the most toxic in the series (PI= 26 against A549 cells and PI= 11 against MCF-7 cells). All of the compounds are moderately lipophilic (low negative value of log P) and particularly **26**-**28** accumulate inside A549 cells. The authors concluded that increased cellular uptake does not always lead to increased phototoxicity.[109] Compound **27** was further explored with both D and L-glucose conjugated thioether ligands and both enantiomers exhibit mild but different cytotoxic properties in A549 and MCF-7 cancer cells in the dark. When exposed to low doses of light (λ= 454 nm), both are highly phototoxic with sub-micromolar EC_{50} values ($EC_{50} < 1$ µM). The compounds are localized inside the mitochondria and, when irradiated, they both kill the cells following dual modes of action, *viz.*, ligand photodissociation (PCT) and $^1O_2$ generation (PDT).[110]

One of the limitations associated with thioether-based photocages is that they are activated with blue light ($\lambda = 450$ nm) which lacks tissue penetrability and the rate of ligand dissociation is slower at lower energies of light due lack of any absorption. To

improve visible light absorption, they tethered the rhodamine B moiety (λ_{max} = 555 nm) to the tpy ligand with a suitable linker which enhanced the rate of excited state ligand dissociation using yellow light (λ = 570 nm).[113]
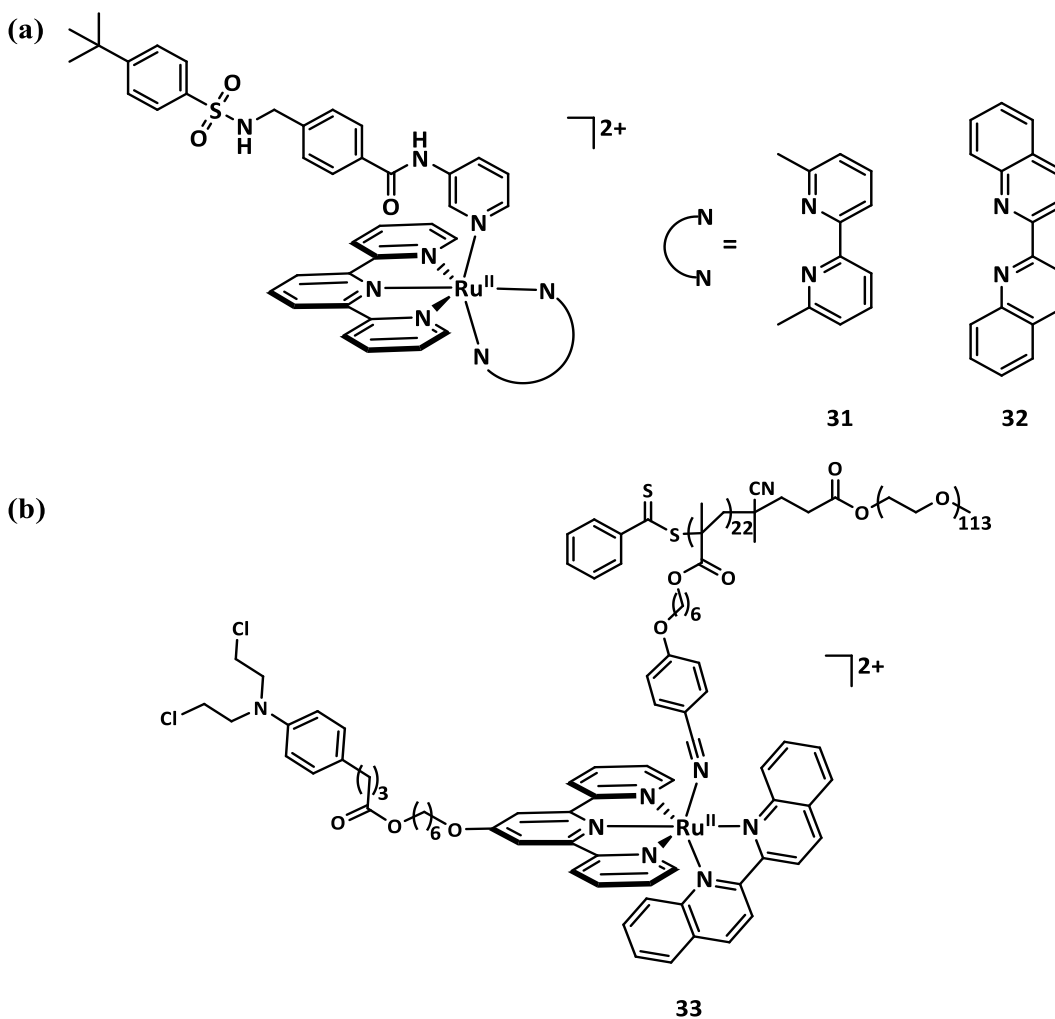
Figure 1.10. (a) Sterically distorted Ru(II) photocages with the pyridyl-functionalized NAMPT inhibitor ligand designed by Bonnet *et al.*, (b) Ru(II) containing block copolymer [PEG-*b*-P(CPH-*co*-RuCHL)] with the Ru-drug conjugate as a photocleavable moiety designed by Bonnet and Wu *et al.*

Nicotinamide phosphoribosyltransferase (NAMPT), a key enzyme in NAD^{+} (oxidized nicotinamide adenine dinucleotide) biosynthesis pathway, is often abnormally

upregulated in cancer cells. Inhibition of NAMPT leads to reduced intracellular NAD^+

levels which can induce apoptosis in cancer cells. This makes NAMPT inhibition a

potential chemotherapeutic target.[114] Using the photocaging scaffold designed by Turro *et*

al.[77], the Bonnet group incorporated a pyridyl-based nicotinamide

phosphoribosyltransferase (NAMPT) inhibitor STF-31 into compounds **31** and **32** (Figure

1.10). The dmbpy and biq ligands introduce steric distortion which facilitates the

photorelease of the inhibitor at a low dose (21 J/cm^2) of red light (λ = 625 nm).

Additionally, the presence of the biq ligand red-shifts the MLCT band from 473 nm in **31**

to 531 nm in **32**. The latter compound exhibits an 18-fold increase in inhibition potency

upon red light activation with the NAMPT activity assay. It also displays a 3 to 4-fold

enhancement in phototoxicity against both A431 and A549 cells upon red-light irradiation

(628 nm, 20.6 J/cm^2) under both hypoxic and normoxic conditions, making it suitable as

a PCT agent.[114] More recently, the Bonnet group in collaboration Wu *et al.* developed Ru-

containing block copolymers PEG-*b*-P(CPH-*co*-RuCHL) (**33**) for PCT applications in

hypoxic tumor environments (Figure 1.10). The block copolymer self-assembles into

micelles which can be efficiently taken up by cancer cells. The design of the photocage

incorporated in the polymer motif contains the Ru-drug conjugate (CHL-Ru) similar to

32, which was shown to be photocleaved inside the cell upon red-light irradiation (λ = 656

nm, 60 J/cm^2) and inhibits tumor cell growth under hypoxia against HeLa cells.[115]

Compound **33** was also tested *in vivo* in a tumor-bearing mouse model which

demonstrated efficient tumor growth inhibition with red light exposure (λ = 660 nm, 360

J/cm^2). The novel polymer micelles do not induce any toxic side effects to mice during treatment and demonstrate good biocompatibility.[115]

Apart from designing novel Ru(II) photocage platforms for PCT applications, Bonnet's group has designed an innovative LED irradiation system for photochemical and photobiological evaluation of PDT and PCT pharmaceuticals *in vitro* against human cancer cell lines. The LED system is equipped with 3 different visible light sources, *viz.*, blue light (λ = 455 nm, 10.5 mW/cm^2), green light (λ = 520 nm, 20.9 mW/cm^2) and red light (λ = 630 nm, 34.4 mW/cm^2). Given the known power of the LED lamps, the light dose during evaluation can be controlled very easily.[116]

Photocages Designed by the Renfrew Group

Renfrew *et al.* revisited the concept of photoinduced drug delivery in PCT by incorporating several anticancer drugs into Ru(II) photocage architectures and releasing them with suitable visible light exposure in a controlled manner (Figure 1.11). The Econazole (Ec, imidazole-based drug in **34** and **35**) is currently being investigated for oral and intravenous applications for the treatment of cancer, tuberculosis and leishmania. Despite exhibiting promising activity *in vitro*, the drug administration has proven to be ineffective due to its poor pharmacokinetics, rapid metabolism, and ability to bind to proteins in the blood stream. When coordinated to a metal, the prodrug lacks activity and its efficacy can be controlled with proper light dose upon releasing the drug molecule.[117] The compounds **34** and **35** were prepared which contain one and two equivalents of bound

Ec ligands respectively (Figure 1.11). Although **34** is susceptible to hydrolysis in the dark,

35 is stable under physiological condition in the absence of light and are luminescent in

nature which was used to determine localization in the cytoplasm rather than the nucleus

of DLD-1 cells. Between the two compounds, only **35** releases one equivalent of Ec when

irradiated with green light ($\lambda = 520$ nm, 1 h, 53 J/cm^2) and loses its luminescence. It is

highly phototoxic when irradiated with green light ($\lambda = 520$ nm, 15 min, 13.3 J/cm^2)

against several human cancer cells (MCF-7, LNCaP, PC-3, DLD-1) with PI values ranging

from (10–34).[117] 6-mercaptopurine (6-MP), an inhibitor of purine synthesis, is widely used

to treat acute leukemia and currently in phase 3 clinical trial against advanced breast

cancer in combination with methotrexate. Several dose limiting toxic side effects along

with poor pharmacokinetics are associated with 6-MP, which also exhibits low solubility

in water. Coordination of 6-MP to Ru can improve its solubility and also reduce other side

effects and the drug can be released with light irradiation inside the cell.[118] Inspired by the

structurally strained tris-chelated Ru(II) photocage architectures pioneered by Glazer *et

al.*,[75, 119] the Renfrew group synthesized (**36**-**38**) with the bidentate 6-MP ligand with the

objective of enhancing the photorelease of the drug with sterically bulky dmbpy and biq

ligand upon visible light irradiation (Figure 1.11). Only **36** exhibits ejection of 6-MP upon

blue light irradiation ($\lambda = 465$ nm), whereas **37** ejects the bulky dmbpy ligand instead of

6-MP with both blue and green light ($\lambda = 520$ nm) irradiation as shown previously in

literature[71, 119] and **38** remains stable in the presence of blue, green or red light ($\lambda = 520$

nm) exposure. In contrast to their expectation, only **37** displays binding to DNA upon

irradiation with blue light. When evaluated against MCF-7 breast carcinoma cells, both

34
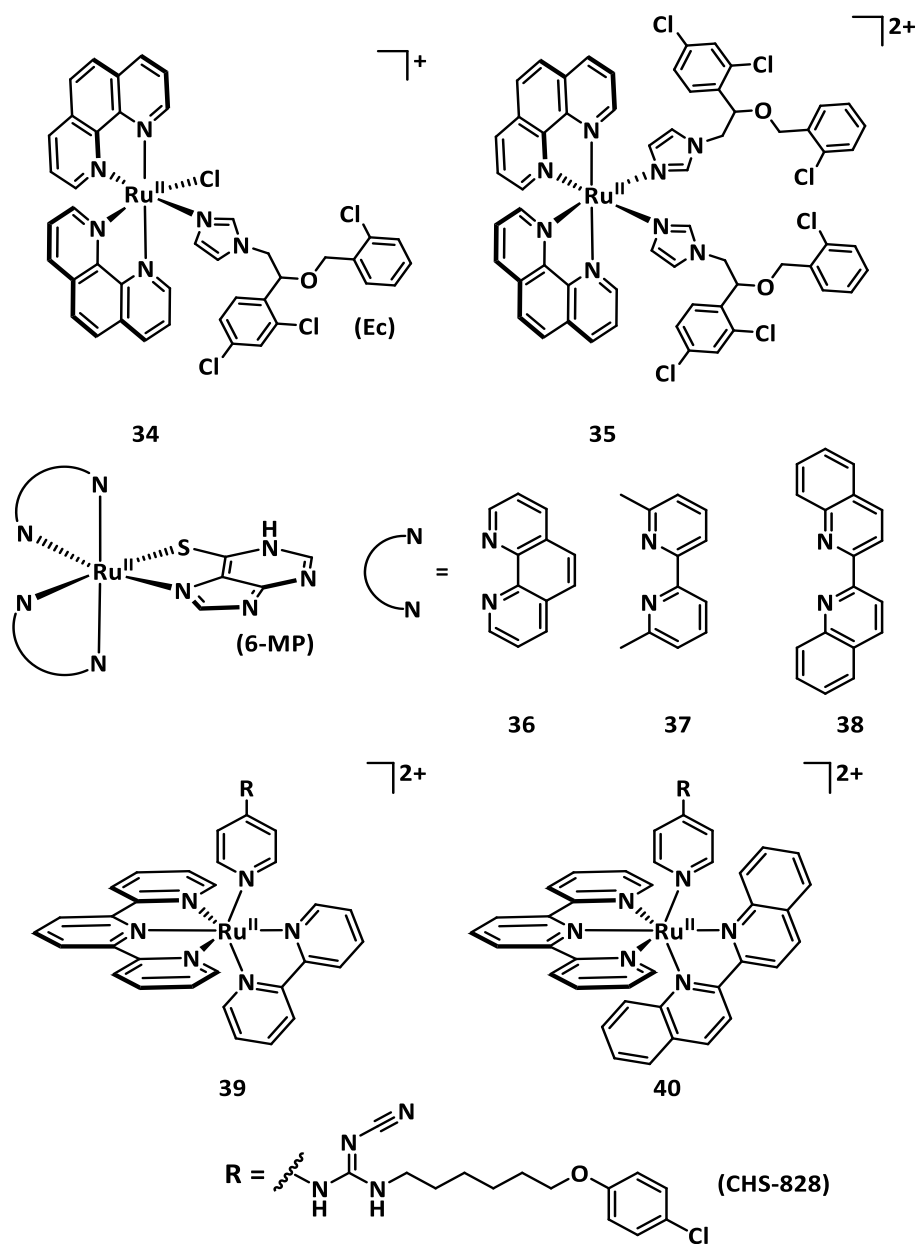
Figure 1.11. Ru(II) photocages with photocleavable anticancer drugs as ligands designed by Renfrew *et al.*

36 and **37** exhibits high IC$_{50}$ values (> 70 µM) in the dark and upon irradiation with only

36 demonstrating enhanced phototoxic effect (PI = 1.4). In contrast, **38** is highly cytotoxic

in both the dark and upon irradiation with essentially no difference and it exhibits similar

toxicity profiles as the free drug 6-MP which makes it suitable as a chemotherapeutic substitute for 6-MP.[118]

NAMPT inhibition is a potential chemotherapeutic target for different cancers. Earlier work by Bonnet *et al.* involved a red light activated ruthenium-caged NAMPT inhibitor which is highly phototoxic in hypoxic cancer cells.[114] The Renfrew group choose a different pyridyl-based NAMPT inhibitor, *viz.*, CHS-828 [N-(6-(4-chlorophenoxy)hexyl)-N′-cyano-N″-4-pyridyl guanidine] (Figure 1.11) for their studies with similar photocaging architectures as shown in **39** and **40** (Figure 1.11).[120] Both are water soluble and stable in the absence of light, but, when irradiated with blue light ($\lambda =$ 465 nm) in aqueous solution, they release the inhibitor to form the corresponding aqua complex $[Ru(tpy)(NN)(H_2O)]^{2+}$ (NN = bpy, biq). By complexation, the solubility of CHS-828 is improved which also improves its bioavailability. Both complexes are efficiently taken up by A549 cells (with selective accumulation in mitochondria) due to the bound inhibitor which improves their overall lipophilicity compared to their pyridine analogues. Both **39** and **40** are highly cytotoxic in the dark as well as upon irradiation against both A549 and MCF-7 cells, but enhancement of cytotoxicity is observed for both compounds when a minimal dose of blue light ($\lambda =$ 465 nm, 30 min, 8.5 J/cm^2) is applied (PI = 9.5 and 4.4 against A549 cells and PI = 10.2 and 4.5 against MCF-7 cells respectively for **39** and **40**). Additionally, a marked increase in ROS levels and mitochondrial depolarization is also observed upon irradiation which is consistent with photo-uncaging of the inhibitor.[120]

The pioneering work by Glazer *et al.* involves the design of sterically strained tris-chelated Ru(II) complexes as potential photocage architectures. This family of complexes is another classic example of photoinduced ligand dissociation due to the thermal population of the reactive ^{3}LF state possessing Ru–L(σ*) character (L= ligand) accessed from ^{3}MLCT state. The introduction of steric strain into the molecule can lower the energy of the dissociative ^{3}LF state making it more thermally accessible which leads to an enhancement of ligand dissociation. The concept behind developing these structurally strained PCT complexes involves photoejection of one ligand upon irradiation to form a bis-aqua intermediate which can subsequently bind to DNA or other biomolecules to exhibit cytotoxic behavior.[48, 68]

To exploit this concept, Glazer *et al.* have introduced methyl substituents on one of the polypyridyl ligands to synthesize geometrically distorted photocages **42** and **43** and compared their properties with the unstrained complex **41** (Figure 1.12).[119] All three complexes are stable in the dark, and, when irradiated with blue light (λ > 450 nm, 200 W), only the methylated ligands, *viz.*, dmbpy ligand in **42** and dmdpq (7,10-dimethylpyrazino[2,3-f][1,10]phenanthroline) ligand in **43**, are photocleaved to form bis-aqua species which can be potentially cytotoxic in a manner similar to cisplatin. The complexes exhibit lack of DNA binding with pUC19 plasmid DNA in the dark but **41** produces DNA photocleavage, **42** exhibits only DNA photobinding when irradiated (λ > 450 nm, 1 h, 200 W), while **43** displays both modes of action. When they were evaluated

37
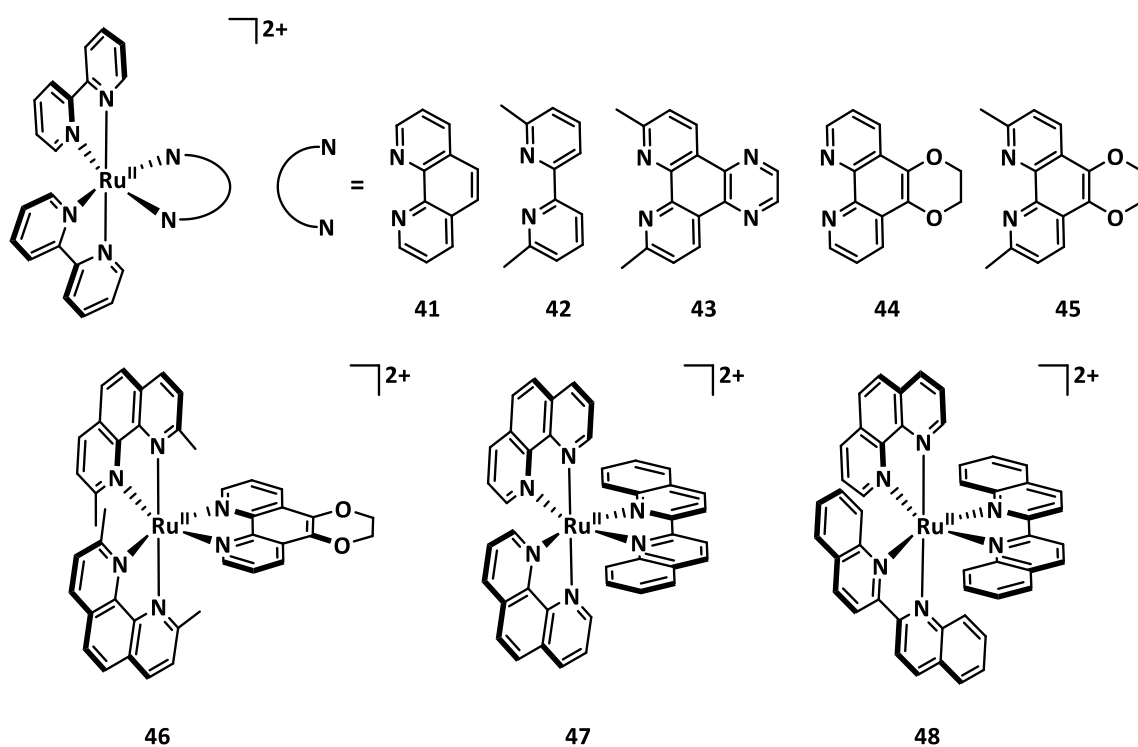
Figure 1.12. Sterically strained tris-chelated Ru(II) photocages with photocleavable diimine ligands designed by Glazer *et al.*

for their *in vitro* phototoxicity against HL60 and A549 cells, no dark toxicity was detected for the complexes ($IC_{50} > 100$ µM) but when irradiated with blue light ($\lambda > 450$ nm, 3 min, 410 W), both **42** and **43** display much higher phototoxicity behavior compared to **41** as evidenced from enhanced PI values for both cells. Both structurally strained complexes demonstrate enhanced photocytotoxicity against A549 spheroids mimicking *in vitro* tumor environment. It is worth noting, however, that unlike for cisplatin, glutathione (GSH) has no deleterious effect on the ligand dissociation or DNA binding ability of these complexes.[119] The same methylation strategy was applied with Ru(II) complexes bearing the dop (2,3-dihydro-1,4-dioxino[2,3-f]-1,10-phenanthroline) ligand to design (**44-46**) (Figure 1.12).[121] As anticipated, upon irradiation with visible light ($\lambda > 400$ nm, 200 W),

both **45** and **46** selectively eject one methylated ligand and the rate of photoejection is 10-times faster in the more strained molecule **46** compared to **45**. Photocleavage results in the formation of similar bis-aqua complexes which is responsible for their photobinding behavior with pUC19 plasmid DNA. While **44** shows single strand breakage in pUC19, likely from $^1O_2$ production, **46** exhibits covalent binding and **45** displays a combination of both mechanisms. All three complexes are phototoxic when exposed to visible light ($\lambda >$ 400 nm, 3 min, 410 W) against HL60 cells and the PI increases drastically with increasing distortion of the Ru complexes in this series with **46** exhibiting one of the largest PI values of 1880.[121]

Following similar distortion strategies, the Glazer group introduced the biq ligand to design **47** and **48**, which also bathochromically shifts the absorption maxima of the complexes closer to the therapeutic window with extended absorptions beyond 700 nm (Figure 1.12).[75] Photodissociation experiments performed with blue ($\lambda >$ 400 nm), green ($\lambda >$ 450 nm), red ($\lambda >$ 600 nm) and near IR light ($\lambda >$ 650 nm) indicate selective ejection of one biq ligand from each complex with rapid dissociation being observed with blue and green light irradiation and relatively slower dissociation with red and near IR light. Both complexes induce reduction in pUC19 plasmid DNA mobility upon irradiation consistent with photobinding behavior with light exposure. The *in vitro* evaluation of the compounds against HL60 cells revealed enhanced phototoxicity upon light irradiation with **48** having the best phototoxicity profile with (PI)$_{blue}$ being greater than (PI)$_{red}$, which is consistent with the energies of the visible light.[75] These tris-chelated geometrically strained Ru(II) photocages hold promise as potential PCT agents and have been explored by other

groups.[97, 118] It is noted, however, that in a recent study, Bonnet's group has demonstrated that neither of the photoproducts generated by these types of photocages can be responsible for their overall phototoxicity behavior.[71]

Photocages Designed by the Gasser Group

Gasser *et al.* has demonstrated an innovative approach in designing a novel Ru(II) photocage (**49**) where a potentially cytotoxic Ru(II) complex (**50**) is inactivated due to the presence of a photo-labile protecting group (PLPG), which upon irradiation with suitable light (λ = 350 nm) can photocleave PLPG to generate cytotoxic precursor complex **50** inside the cell which exert anticancer activity (Figure 1.13).[69, 122] In a previous report, the group has studied the intrinsic cytotoxic behavior associated to complex **50** which is comparable to cisplatin in several human cancer cells. Colocalization study in HeLa cells showed that **50** accumulates inside mitochondria and induces late apoptosis following mitochondrial dysfunctional pathway.[123] But the toxicity is greatly suppressed upon caging by PLPG group which is evident from the IC$_{50}$ (> 100 µM) value of **49** in the dark. The cytotoxicity is regained after photodissociation upon irradiation with UVA light (λ = 350 nm, 10 min, 2.58 J/cm^2) which is similar in values as shown by **50**.[122-123] Confocal studies demonstrated re-localization of caged complex (**49**) from cytoplasm and nucleoli to mitochondria after the light exposure, consistent with complex **50**.[122] Following similar protection strategies, the Gasser group has recently designed new Ru(II) photocages with a photocleavable *o*-nitrobenzyl moiety as PLPG. Additionally, targeting peptides were

tethered to the structure for selectivity purposes. Targeting peptides are selected depending on the type of cancer being treated and the type of peptide receptors being overexpressed on the cancer cell membrane.[124] Although photocages designed using PLPG group strategy exhibit spatiotemporal control, a major drawback associated with this family of photocages is their activation using UV light which, itself, is known to damage cells. So, for their successful implementation as PCT agents, suitable PLPG groups must be chosen that can be photocleaved using lower energy visible or near-infrared light.[48, 69]
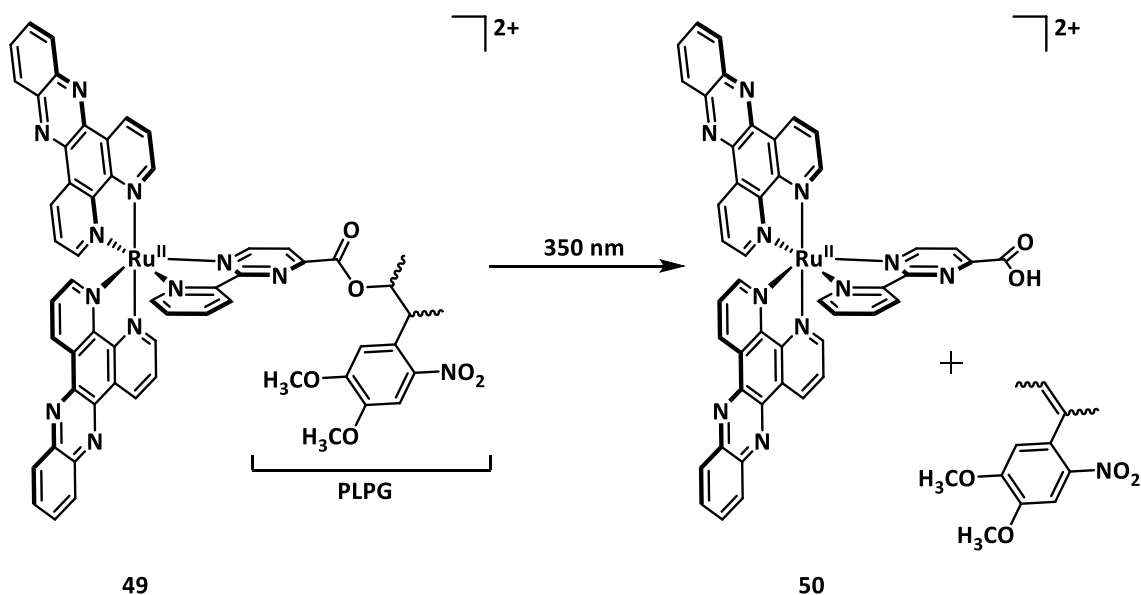
Figure 1.13. Ru(II) photocage protected by PLPG group designed by Gasser *et al.*

In summary, several new strategies of designing Ru(II) photocages discussed above reveal that architectural design of photocages with suitable ligand platforms plays a major role in determining their mechanism of action and thus their success as PCT agents. Incorporating steric distortion around the metal center improves the

41

photodissociation of the ligand but excessive distortion can lead to instability of the molecule in the absence of light. Therefore, the selection of a suitable bulky ligand is also crucial for the efficacy of the compounds. Moreover, the energy of light being used for their activation determines their successful implementation as PCT agents. Although most Ru(II) polypyridyl complexes absorb strongly in the visible region below 500 nm, the absorption in the therapeutic window (600-900 nm) is rather weak which can be improved in several ways as described. Finally, cellular uptake of these photocages can be improved by introducing more lipophilic moieties to the metal coordination sphere, and selectivity can be imparted by tethering specific functionalities to target various cancers. Overall, it can be concluded that the PCT modality holds great potential as a mainstream cancer therapy in addition to PDT.

CHAPTER II

PARTIALLY SOLVATED DINUCLEAR RUTHENIUM(II) PHOTOCAGES WITH

RED-SHIFTED ^{1}MLCT ABSORPTION*

Introduction

Since the serendipitous discovery of cisplatin over six decades ago, research on the topic of platinum based anticancer drugs has been an extremely active field.[5, 9, 11] In spite of their proven efficacy, however, platinum chemotherapeutic compounds suffer from lack of selectivity and exhibit severe side effects due to systemic toxicities.[7] Among the promising candidates for non-platinum metal-based cancer therapies are ruthenium compounds that exhibit lower toxicities and higher activities towards Pt-drug resistant cancer cells.[15, 22, 33, 46] Of specific relevance to the topic of our research in this area is the investigation of ruthenium compounds with reactive excited states for applications in PDT and PCT.[57, 62] In these modalities, a pro-drug is administered and the tumor is selectively irradiated which destroys the cells in the cancerous tissue but leaves healthy cells intact. Due to the associated spatiotemporal control over the drug activation, both techniques are promising non-invasive strategies for the treatment of endoscopically accessible tumors.[53]

Unlike PDT, whose mechanism of action relies on the production of singlet oxygen and requires a supply of oxygen inside the tumor, PCT is a dual action approach that exploits oxygen-independent pathways.[64, 68, 124] In this approach, metal caged drug/inhibitor ligands are released inside tumor cells upon irradiation,[48, 70, 74, 86, 120] which, along with the resulting coordinatively unsaturated metal complex, are available to bind to proteins and DNA.[71-73, 76, 118-119] Mononuclear Ru(II) photocages are typically composed of Ru(II) centers coordinated to electron withdrawing planar diimine-based ancillary ligands along with photolabile biologically active molecules containing different functionalities (nitrile, pyridyl, thioethereal, pyrazolyl functionalities) that absorb strongly in the near ultraviolet to blue spectrum of visible light.[70, 104, 110, 117-118, 125] To tune the ligand environment and improve the quantum yield of ligand photodissociation, non-planar multidentate ligand architectures as well as sterically bulky diimine-ligands possessing low lying π^*-orbitals have also been incorporated.[66, 75, 87, 103, 126] These improved design strategies result in red-shifted [1]MLCT band thus absorbing long wavelength visible light ($\lambda > 500$ nm). For optimal tissue penetration, however, effective PCT agents need to absorb red/near IR light ($\lambda > 620$ nm), but there are only a few Ru-based systems capable of releasing small caged molecules upon irradiation in the 650 nm range.[75, 99, 102, 114-115, 127-128]

In an effort to further red-shift the absorption maxima of Ru(II) photocage complexes, Turro *et al.,* introduced new ancillary ligand platforms that consist of electron donating anionic acetylacetonate (acac)-based ligand systems along with the highly conjugated 2,6-di(quinoline-2-yl)pyridine (dqpy) ligand. Acetylacetonate ligands are

strong π-donor ligands that serve to destabilize the HOMO while the dqpy ligand with its extended conjugation lowers the LUMO energy: both effects synergistically contribute to a much-diminished HOMO-LUMO gap (ΔE). The result of this tuning is evident from the electronic absorption maximum of 770 nm for $[Ru(dqpy)(acac)(CH_3CN)]^+$ which allows for activation using near-IR photons.[99]

A different approach to red-shifting the [1]MLCT band of Ru based photocages is to bridge two Ru(II) units with suitable bridging ligands with lower π^*-orbitals (LUMO) which results in a bathochromic shift of the [1]MLCT band by ~ (70-80) nm.[129-131] In this vein, the current research between our group and the Turro group involves the use of the bridging architecture to prepare a partially solvated bimetallic Ru(II) photocage with the tridentate tppz ligand, *viz.*, $[\{Ru^{II}(NCCH_3)_3\}_2(\mu\text{-tppz})](PF_6)_4$ (**1**, tppz = tetra-2-pyridinylpyrazine), which is the first dinuclear Ru(II) photocage structure capable of photoinduced ligand exchange at both metal centers.[128] To increase the number of coordinated CH_3CN molecules on each Ru center, we also introduced a bis-bidentate dpq-ligand with low lying π^*-orbitals to design $[\{Ru^{II}(NCCH_3)_4\}_2(\mu\text{-dpq})](PF_6)_4$ (**2**, dpq = 2,3-di(pyridin-2-yl)quinoxaline). It was reasoned that introduction of extended conjugation on the bridging ligand can further stabilize its π^* orbital (LUMO) resulting in an even more bathochromic shift of [1]MLCT band.[132] To test this hypothesis the bis-bidentate dpb ligand was incorporated into the cation in $[\{Ru^{II}(NCCH_3)_4\}_2(\mu\text{-dpb})](PF_6)_4$ (**3**, dpb = 2,3-di(pyridin-2-yl)benzo[*g*]quinoxaline) (Figure 2.1). The compounds were characterized by ^{1}H NMR spectroscopy, elemental analyses and single crystal x-ray crystallography (**1** and **2**). The electronic properties were investigated using electronic absorption spectroscopy

and cyclic voltammetry and experimental observations were verified by DFT calculations. The compounds also were evaluated for their phototoxic properties against the HeLa human cervical carcinoma cell line.
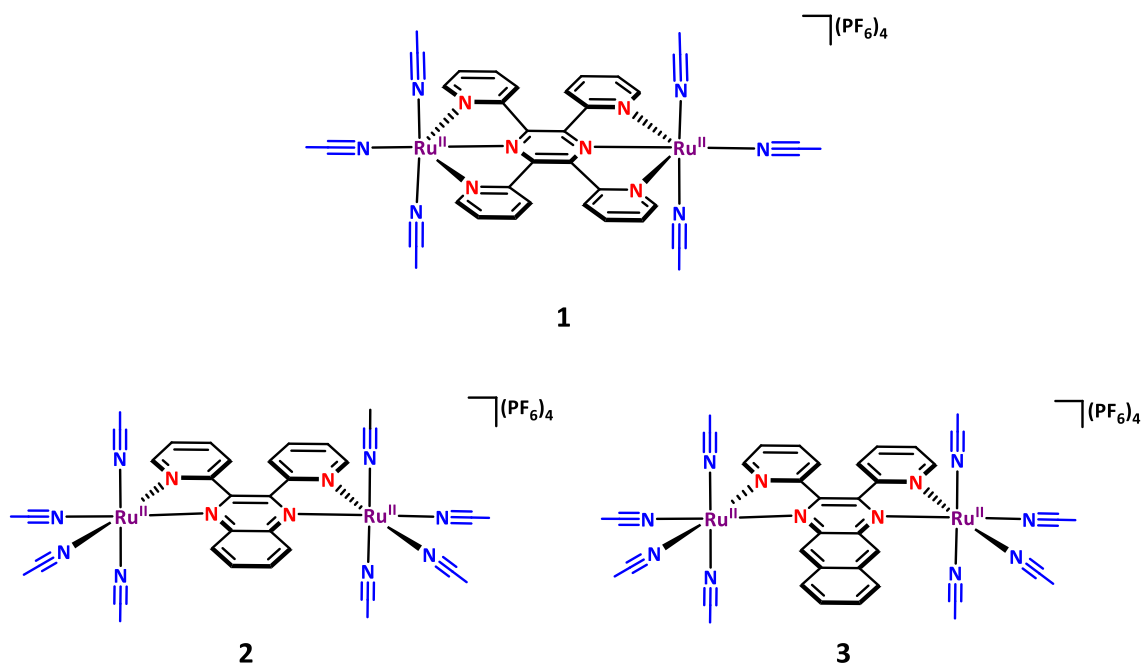
Figure 2.1 Schematic structures of solvated dinuclear Ru(II) photocages in this work.

Experimental Section

General Methods

Standard Schlenk-line techniques were used in a N_2 atmosphere for the preparation of Compounds **2** and **3**. Solvents were of reagent grade quality. Ethanol (KOPTEP, 200 proof), acetonitrile (EMD Chemicals) and diethyl ether (EMD Chemicals) were used as received without further purification. $RuCl_3 \cdot xH_2O$ (Pressure Chemicals Co.), tetra-2-pyridylpyrazine (tppz) (Sigma Aldrich), ascorbic acid (Alfa Aesar) and KPF_6 (Alfa Aesar) were purchased and used as received. The ligands 2,3-di(pyridin-2-yl)quinoxaline (dpq)[133] and 2,3-di(pyridin-2-yl)benzo[*g*]quinoxaline (dpb)[134] and the precursor [(η^6-benzene)Ru(NCCH_3)_3](PF_6)_2[135] were synthesized by following previous literature procedures.

Instrumentations

The ^{1}H NMR spectra were recorded on a Mercury 300 MHz spectrometer. Chemical shifts are reported in δ (ppm) and coupling constants (J) in hertz (Hz). The residual solvent peak (δ =1.94 ppm for CD_3CN) was used as an internal reference. Elemental analyses were performed by Atlantic Microlab, Inc. (Norcross, GA). Absorption spectra were recorded in acetonitrile on a Shimadzu UVPC-3001 spectrophotometer at room temperature. Electrochemical measurements were performed

under anaerobic conditions (N_2 atmosphere) with an HCH Electrochemical Analyzer model CH 1620A using a BAS Pt disk working electrode, Pt wire auxiliary electrode, Ag/AgCl (3M KCl$_{aq}$) reference electrode and 0.1 (M) tetra-n-butylammonium hexafluorophosphate ([^{n}Bu$_4$N](PF$_6$)) in dry acetonitrile as a supporting electrolyte and a100 mV/s scan rate. The concentration of the Ru complexes for the electrochemical experiments was ~1 mM. Ferrocene was used as an internal standard and exhibited an $E_{1/2}$ value of +0.43 V vs Ag/AgCl for the Fc$^+$/Fc couple under the same experimental conditions. The $E_{1/2}$ of the Ru complexes was referenced vs NHE (Normal hydrogen electrode) using the following expression: $E_{1/2}$ vs NHE = [($E_{1/2}$ vs Ag/AgCl of Ru complex) + (0.64 − 0.43)] V, where 0.64 V = $E_{1/2}$ [Fc$^+$/Fc] vs NHE and 0.43 V = $E_{1/2}$ [Fc$^+$/Fc] vs Ag/AgCl.

Synthetic Details

[{Ru^{II}(NCCH$_3$)$_3$}$_2$(µ-tppz)](PF$_6$)$_4$ (1). A suspension of [(η^6-benzene)Ru(NCCH$_3$)$_3$](PF$_6$)$_2$ (0.111 g, 0.19 mmol) and tppz (0.037 mg, 0.10 mmol) was heated to reflux in an acetonitrile:ethanol mixture (1:10) for 6 h. The resulting dark purple suspension was filtered while hot and the isolated solid was washed with warm ethanol (3 x 15 mL) followed by copious amounts of diethyl ether and air-dried. The desired product was obtained as dark purple solid. Yield: 0.083 g (62%). ^{1}H NMR (300 MHz, CD$_3$CN): δ 9.15 (d, 4H, ^3J = 5.5 Hz, H$_1$), 8.82 (d, 4H, ^3J = 8.0 Hz, H$_4$), 8.21 (ddd, 4H, ^3J = 8.0 Hz, ^3J = 8.0 Hz, ^4J = 1.5 Hz, H$_3$), 7.96 (ddd, 4H, ^3J = 7.5 Hz, ^3J = 5.5 Hz, ^4J = 1.0 Hz, H$_2$), 2.88 (s, 6H,

CH$_3$CN$_{eq}$), 2.02 (s, 12H, CH$_3$CN$_{ax}$). Anal. Calcd. for C$_{36}$H$_{34}$F$_{24}$N$_{12}$P$_4$Ru$_2$•2H$_2$O: C, 29.76; H, 2.64; N, 11.57. Found: C, 29.70; H, 2.66; N, 11.61. Dark purple needles suitable for X-ray diffraction were obtained by the slow diffusion of diethyl ether into a dilute solution of **1** in acetonitrile at room temperature.[128]

[{Ru^{II}(NCCH$_3$)$_4$}$_2$(μ-dpq)](PF$_6$)$_4$ (2). A dark brown solution of RuCl$_3$•3H$_2$O (460 mg, 1.76 mmol) and dpq (250 mg, 0.88 mmol) was heated to reflux in ethanol (25 mL) for 6 h. After 2 h, the color of the solution changed to dark green and a precipitate formed. The dark green solid was collected by filtration, washed with chilled ethanol (2 x 5 mL), and air-dried. The filtrate was concentrated and kept in an ice bath for 30 min to obtain more precipitate which was isolated as mentioned above. In the next step, a solution of AgNO$_3$ (536 mg, 3.75 mmol) in an acetonitrile:water mixture (10 mL, 3:2) was added to a suspension of the dark green intermediate (460 mg, 0.62 mmol assuming the formula Ru^{III}$_2$Cl$_6$(H$_2$O)$_2$(μ-dpq)) and ascorbic acid (450 mg, 2.50 mmol) in an acetonitrile:water mixture (10 mL, 3:2). With refluxing, the initial dark green color gradually changed to dark purple. The mixture was refluxed overnight under a N$_2$ atmosphere and the final dark purple solution was slowly filtered through Celite® to remove AgCl precipitate and the filtrate was reduced to dryness under reduced pressure. The residue was dissolved in a minimum volume of warm water and KPF$_6$(aq) (3.75 mmol in 6 mL of water) was added dropwise to obtain a dark purple precipitate which was collected by vacuum filtration and washed with copious amounts of water and diethyl ether (3x10 ml). The product was obtained as a dark purple powder. Yield: 777 mg (89%). ^{1}H NMR (300 MHz, CD$_3$CN): δ 9.26 (dd, 2H, ^3J = 5.7 Hz, ^4J = 1.5 Hz, H$_1$), 8.79 (dd, 2H, ^3J = 6.7 Hz, ^4J = 3.3 Hz, H$_5$),

8.48 (d, 2H, ^3J = 8.1 Hz, H$_4$), 8.24 (dd, 2H, ^3J = 6.7 Hz, ^4J = 3.3 Hz, H$_6$), 8.05 (ddd, 2H,

^3J = 8.2 Hz, ^3J = 7.5 Hz, ^4J = 1.5 Hz, H$_3$), 7.80 (ddd, 2H, ^3J = 7.6 Hz, ^3J = 5.7 Hz, ^4J = 1.5

Hz, H$_2$), 2.76 (s, 6H, CH$_3$CN$_{eq}$), 2.64 (s, 6H, CH$_3$CN$_{eq}$), 2.28 (s, 6H, CH$_3$CN$_{ax}$), 2.13 (s,

6H, CH$_3$CN$_{ax}$). Anal. Calcd. for C$_{34}$H$_{36}$F$_{24}$N$_{12}$P$_4$Ru$_2$•2H$_2$O: C, 28.54; H, 2.82; N, 11.75.

Found: C, 28.71; H, 2.88; N, 11.28. Dark purple needles suitable for X-ray diffraction

were obtained by slow diffusion of diethyl ether into a dilute solution of **2** in acetonitrile

at room temperature.

[{Ru^{II}(NCCH$_3$)$_4$}$_2$(μ-dpb)](PF$_6$)$_4$ (3). This compound was synthesized in a manner

similar to **1** by replacing the dpq with dpb. RuCl$_3$•3H$_2$O (391 mg, 1.5 mmol) and dpb (250

mg, 0.75 mmol) were refluxed in ethanol (20 ml) for 6 h to yield a dark green solid (453

mg) which was isolated as described above. A solution of AgNO$_3$ (129 mg, 0.762 mmol)

in an acetonitrile:water mixture (10 mL, 3:2) was then added to a suspension of the dark

green intermediate (100 mg, 0.127 mmol assuming the formula Ru^{III}$_2$Cl$_6$(H$_2$O)$_2$(μ-dpb))

and ascorbic acid (101 mg, 0.571 mmol) in an acetonitrile:water mixture (10 mL, 3:2).

The mixture was refluxed overnight under a N$_2$ atmosphere during time the initial dark

green color changed to dark purple. Compound **2** was isolated as a (PF$_6$)$^-$ salt. Yield: 150

mg (82%). ^{1}H NMR (300 MHz, CD$_3$CN): δ 9.38 (s, 2H, H$_5$), 9.31 (ddd, 2H, ^3J = 5.7 Hz,

^4J = 1.5 Hz, ^5J = 0.9 Hz, H$_1$), 8.48 (dd, 2H, ^3J = 6.5 Hz, ^4J = 3.3 Hz, H$_6$), 8.43 (dd, 2H, ^3J

= 8.3 Hz, ^4J = 0.9 Hz, H$_4$), 8.07 (ddd, 2H, ^3J = 7.8 Hz, ^3J = 7.5 Hz, ^4J = 1.5 Hz, H$_3$), 7.92

(dd, 2H, ^3J = 6.5 Hz, ^4J = 3.3 Hz, H$_7$), 7.82 (ddd, 2H, ^3J = 7.8 Hz, ^3J = 5.7 Hz, ^4J = 1.5/1.2

Hz, H$_2$), 2.80 (s, 6H, CH$_3$CN$_{eq}$), 2.71 (s, 6H, CH$_3$CN$_{eq}$), 2.25 (s, 6H, CH$_3$CN$_{ax}$), 2.15 (s,

6H, CH₃CN$_{ax}$). Anal. Calcd. for $C_{38}H_{38}F_{24}N_{12}P_4Ru_2 \cdot 2H_2O$: C, 30.82; H, 2.86; N, 11.35. Found: C, 30.94; H, 2.83; N, 11.09.

X-Ray Crystallography

Single crystals of compound **1** and **2** were obtained by slow diffusion of diethyl ether into a dilute acetonitrile solution of the compound at room temperature. X-ray data were collected at 110 K on a Bruker APEX II CCD X-ray diffractometer (Bruker-AXS, 2014) equipped with a graphite monochromated MoKα radiation source (λ = 0.71073 Å). The data were integrated in the Bruker SAINT software package (SAINT v8.34A, Bruker, 2013).[136] The absorption correction (SADABS)[137] was applied based on fitting a function to the empirical transmission surface as sampled by multiple equivalent measurements (SADABS-2012/1, Bruker, 2012). Solution and refinement of the crystal structure was carried out using the ShelX (2013) suite of programs [138-139] and the graphical interface OLEX 2.[140] All non-hydrogen atoms were refined with anisotropic displacement parameters using full-matrix least-squares techniques on F^2. Hydrogen atoms were fixed to parent atoms and refined using the riding model. Idealized geometries were used to model disordered $(PF_6)^-$ anions.[141] Despite numerous attempts, a satisfactory model for the disordered solvent diethyl ether molecule was not able to be obtained for **2**. The corresponding electron density was removed using the SQEEZE algorithm of PLATON.[142] The total solvent accessible volume (SAV) per unit cell was found to be 454

Å^3 and the number of electrons occupied inside the SAV per unit cell is 87 which correspond to two molecules of diethyl ether (84 electrons).

Structural Optimization and TDDFT Calculation

The crystal structures of **1** and **2** were used as initial coordinates for the structural optimization of all three compounds in the gas phase with the Gaussian 09 program package[143] using the Becke's three -parameter exchange correlation functional and the Lee Yang and Parr correlation functional (B3LYP).[144,145] The Stuttgart RSC 1997 effective core potential (ECP) basis set[146] was used for the Ru atom and the 6-311G* basis set[147-148] was used for C, N and H atoms. The solvent phase geometry optimizations were performed by using self-consistent reaction field (SCRF) calculations with an SMD model (Truhlar's model)[149] in acetonitrile to incorporate solvent polarization effects with subsequent frequency analysis. The molecular orbitals (MOs) were plotted with Ampac GUI 9 (Semichem, Inc; www.semichem.com) with an isovalue of 0.04. Fragment contributions to the MOs were calculated using the Chemissian v4.60 software (www.chemissian.com). Time-dependent density functional theory (TDDFT) calculations were performed on the solvent optimized structures to compute electronic transitions from singlet ground states to singlet excited states using the SMD model with acetonitrile as the solvent.

Cell Culture Studies

The HeLa human cervical carcinoma cell line was obtained from the American type culture collection, cell line CCL-2 (ATCC CCL-2). Dulbecco's modified Eagle medium [DMEM] (Corning), Dulbecco's phosphate-buffered saline [DPBS] (VWR), trypsin (ThermoFisher), dimethyl sulfoxide [DMSO] (Sigma Aldrich), resazurin (Sigma Aldrich), Leibovitz's L-15 Medium (ThermoFisher) were purchased from the vendors and used as received. HeLa cells were cultured in DMEM supplemented with 10% fetal bovine serum [FBS] (Fisher) and $1\times$ penicillin/streptomycin [P/S] (Fisher). Cell cultures were incubated in a humidified atmosphere containing 5% CO_2 at 37°C and were approximately 80% confluent at the time of analysis.

In vitro *Phototoxicity Evaluation*

HeLa cells were plated in 96 well plates and preincubated in a humidified incubator containing 5% CO_2 at 37°C for 24 h. The compounds were dissolved in PBS buffer with 0.5% DMSO and the cells were treated with different concentrations of the compounds ranging from (0 – 200 µM). The "Light" plate was incubated for 90 minutes followed by irradiation inside a broad band visible light chamber for 1 h and then placed in the incubator for additional 22.5 h for a total of 24 h incubation. The "Dark" plate was incubated for 24 h in the same incubator without irradiation. The next day, the media was aspirated from each well and the cells were washed with PBS buffer followed by addition

53

of resazurin solution (in PBS buffer) and L-15 media under limited light conditions. After this treatment, both plates were incubated for 2 h and emission was measured using an Omega plate reader at 585 nm. Emission intensity is directly proportional the number of viable cells. Two experiments were conducted on different days with each experiment having 8 replicates per concentration. Phototoxicity was measured by the PI value which is defined as the ratio of $(LC_{50})_{dark}$ to $(LC_{50})_{irradiated}$. An ideal photochemotherapeutic (PCT) agent should have PI >> 1.

Results and Discussion

Synthesis and Characterization

All three ligands have been used as bridging ligands in coordination chemistry reactions to synthesize numerous coordinatively saturated and substitutionally inert polynuclear Ru(II)-polypyridyl compounds.[129-132, 150-151] For the first time, we used these bridging ligands to prepare partially solvated dinuclear Ru(II)-compounds for photocaging applications.[128] Two different synthetic routes were employed to successfully synthesize all three compounds with high purities. For compound **1**, a more selective Ru(II) starting material, viz. $[(\eta^6\text{-benzene})Ru(NCCH_3)_3](PF_6)_2$ with a piano stool geometry was used. A (2:1) mixture of Ru(II) starting material:tppz ligand was refluxed in acetonitrile:ethanol mixture (1:10) for 6 h which resulted in the formation of the desired compound as a dark purple insoluble solid which was isolated by filtration followed by recrystallization (Figure 2.2). The purity of the compound was confirmed by ^{1}H NMR spectroscopy and elemental analyses. Protons on each peripheral pyridyl ring are magnetically inequivalent, with four peaks being observed between (7.5-9.5) ppm, which is consistent with C_{2v} molecular symmetry. Also, two singlet peaks at $\delta = 2.02$ ppm and 2.88 ppm are observed which correspond to coordinated acetonitrile molecules directed along the axial and equatorial plane of the central pyrazine ring respectively (see Figure 2.2 for proton numbering scheme).[128] The assignment of axial acetonitrile (CH_3CN_{ax}) and equatorial acetonitrile (CH_3CN_{eq}) is also supported by the peak integration ratio of (1:2). Axial

acetonitrile ligands possess shorter Ru-N bonds (Table 2.2) and appear more upfield shifted at 2.88 ppm, similar to mononuclear $[Ru(tpy)(CH_3CN)_3]^{2+}$.[152]

The syntheses of compounds **2** and **3** involved a two-step synthetic route starting from hydrated $RuCl_3$ as the starting material. First, dinuclear Ru(III) precursors were isolated by refluxing a (2:1) mole ratio of $RuCl_3 \cdot 3H_2O$:BL (dpq/ dpb) in ethanol. The resulting dark green intermediates were used in the next step without further purification which involved reduction with excess ascorbic acid (4 eqv.) in an (acetonitrile/water) mixture. Water soluble $AgNO_3$ was used to facilitate the removal of coordinated chloride ions and the product was isolated as $(PF_6)^-$ salt after treatment with aqueous KPF_6 solution. The purity of the compounds was confirmed by ^1H NMR spectroscopy and elemental analyses. The NMR spectra are consistent with C_{2v} molecular symmetry as one-half of the protons on the bridging ligands are magnetically equivalent (Figure 2.2 for proton numbering schemes). Also, four singlet peaks appear between 2-3 ppm that correspond to four magnetically inequivalent acetonitrile molecules on each Ru(II) center. The axial acetonitrile molecules (CH_3CN_{ax}) directed perpendicular to the bridging ligand plane exhibit shorter Ru-N distances and appear more upfield (between 2.1–2.3 ppm). In contrast, the equatorial acetonitrile molecules (CH_3CN_{eq}) with longer Ru-N bond distances resonate between 2.65–2.80 ppm, similar to $[Ru(bpy)(NCCH_3)_4](PF_6)_2$.[153-154] The NMR spectra also confirm that all three complexes possess diamagnetic Ru(II) centers. The integration values of the peaks match the total proton count (**1**, 34H; **2**, 36H; **3**, 38H) for all three compounds, indicating the formation of the desired molecules (Figure 2.3-2.5).
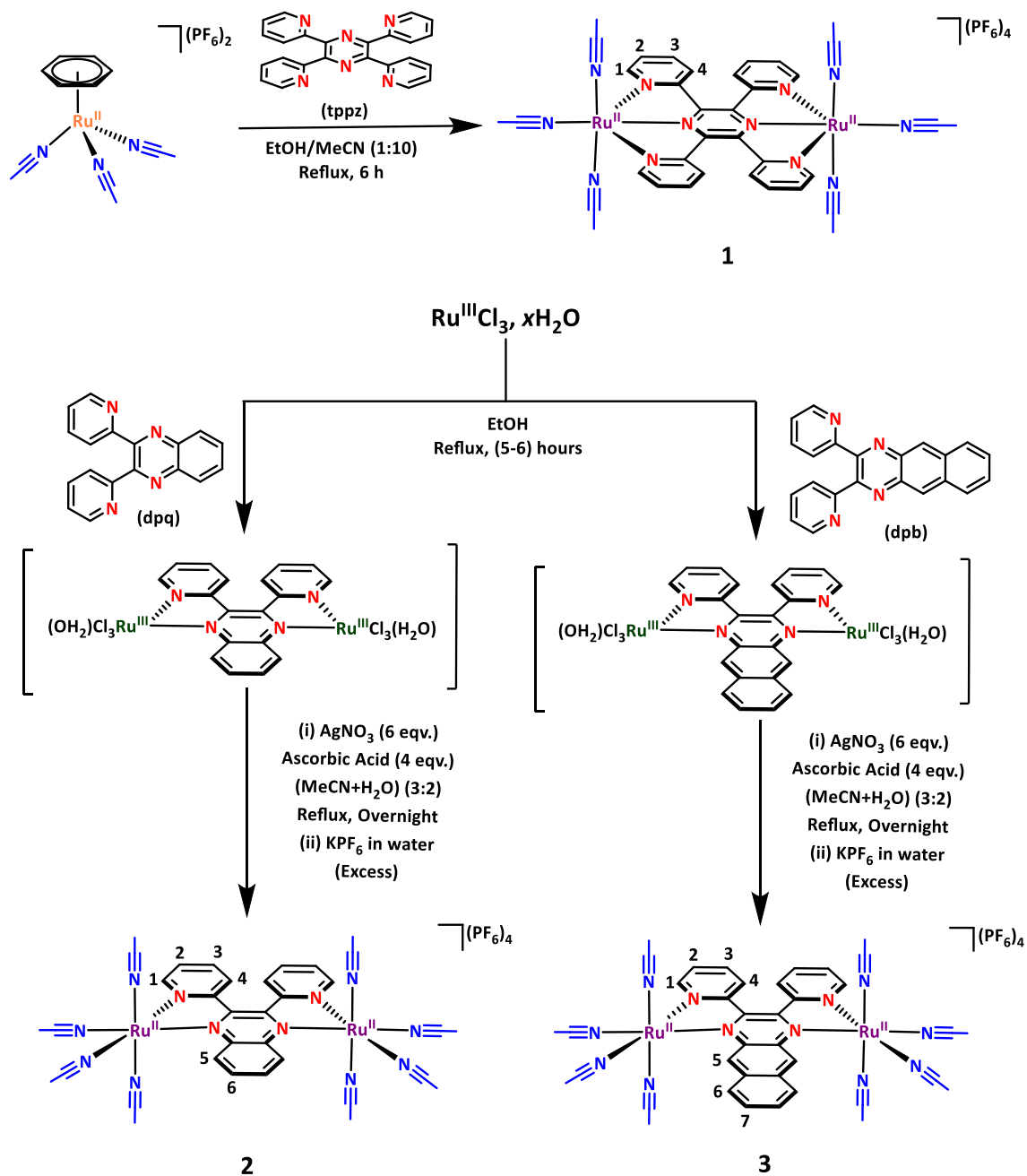
Figure 2.2 Reaction schemes for the synthesis of compounds **1**-**3** (with numbering scheme for proton assignment).

(a)

(b)
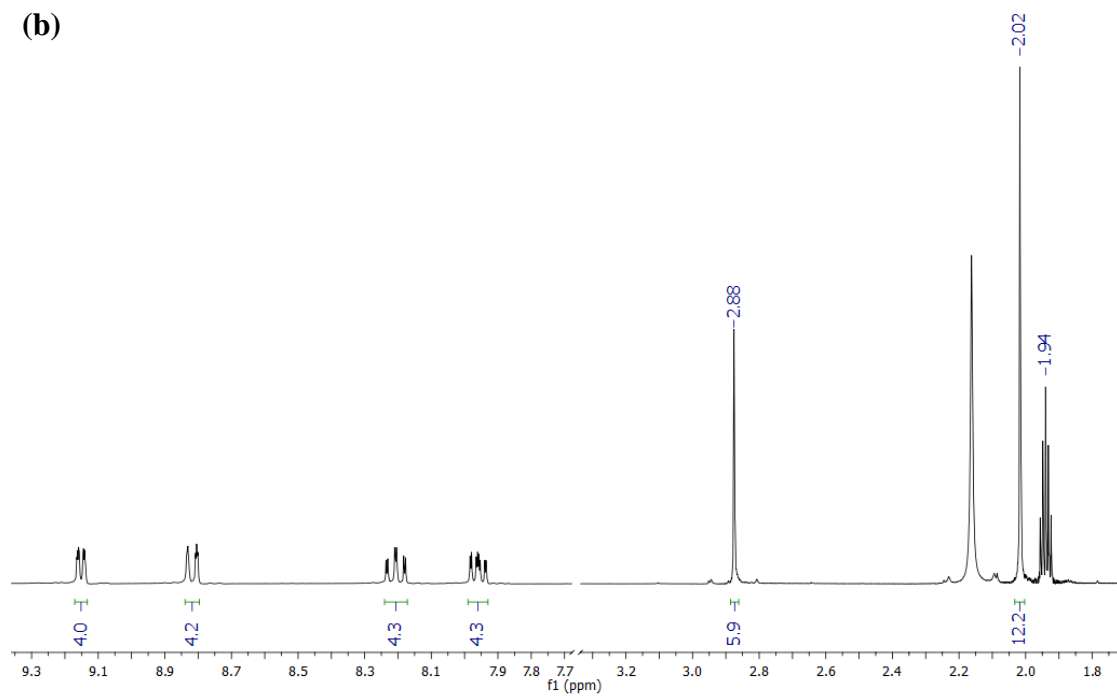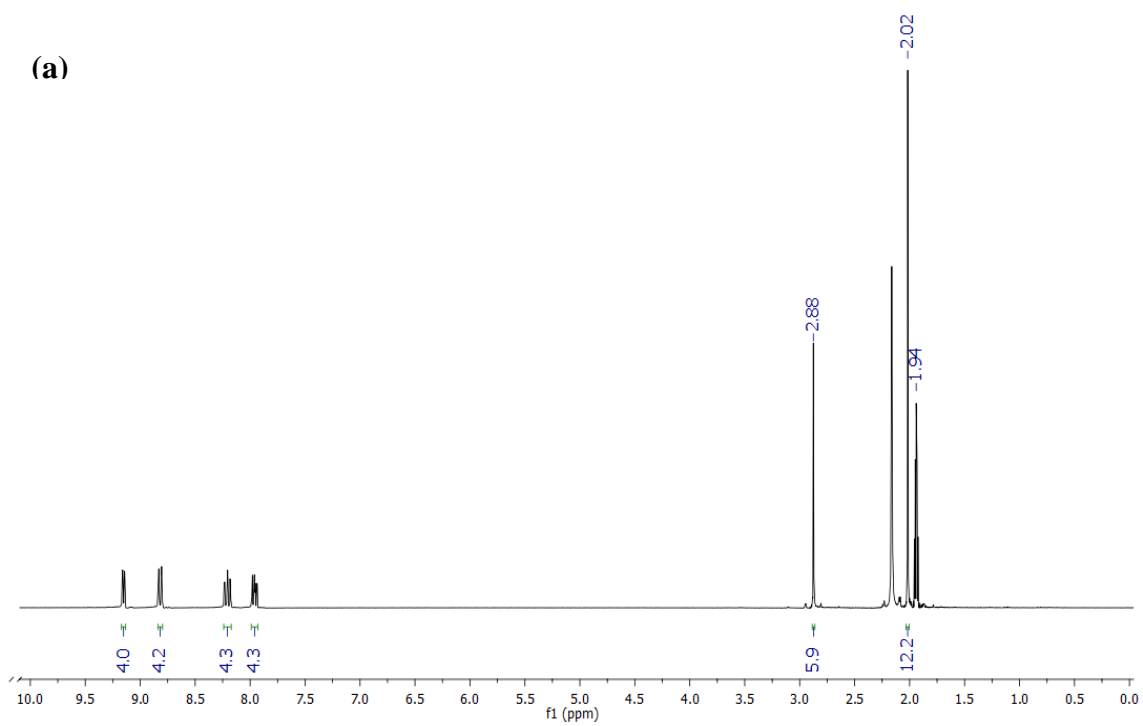
Figure 2.3. ^{1}H NMR spectra (CD$_3$CN, 300 MHz) of compound **1** (a) full spectrum, (b) enlarged. Adapted with permission from reference 128.
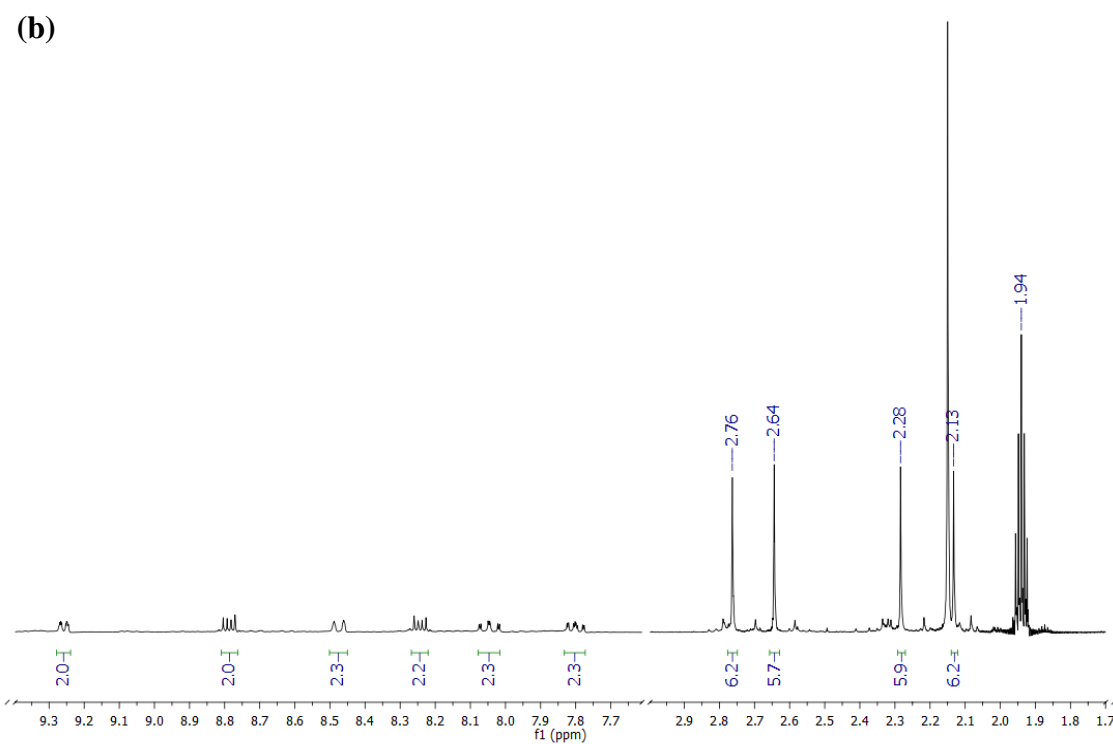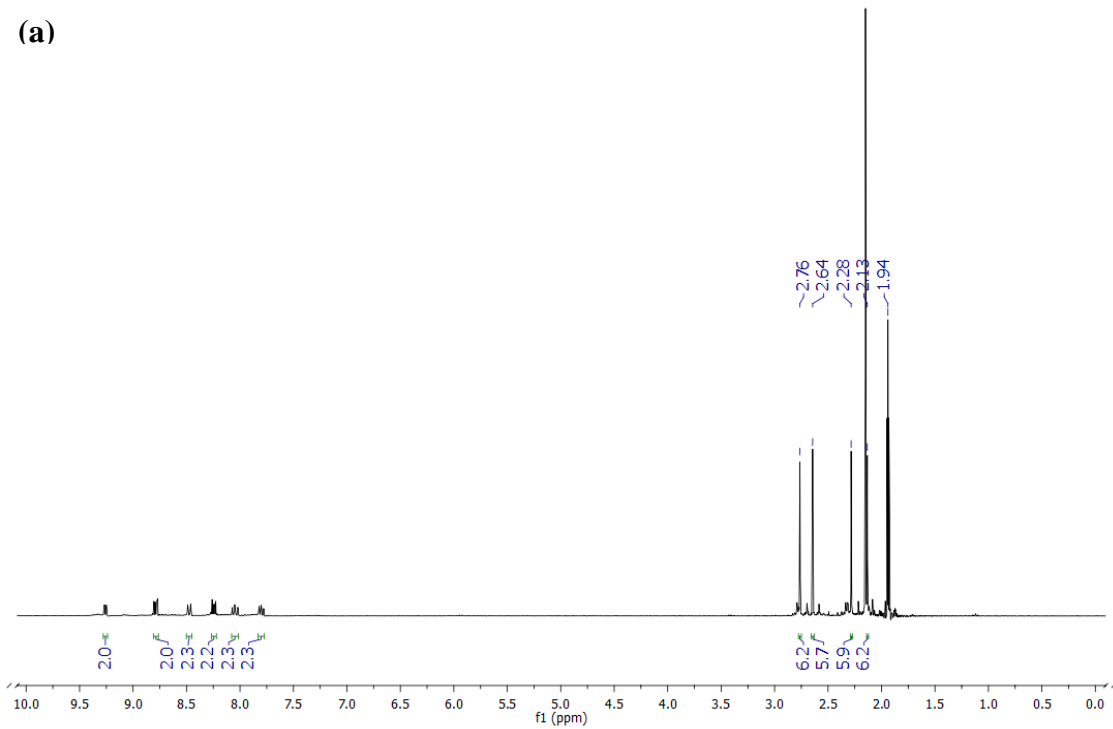
Figure 2.4. ^{1}H NMR spectra (CD$_3$CN, 300 MHz) of compound **2** (a) full spectrum, (b) enlarged.

(a)

(b)
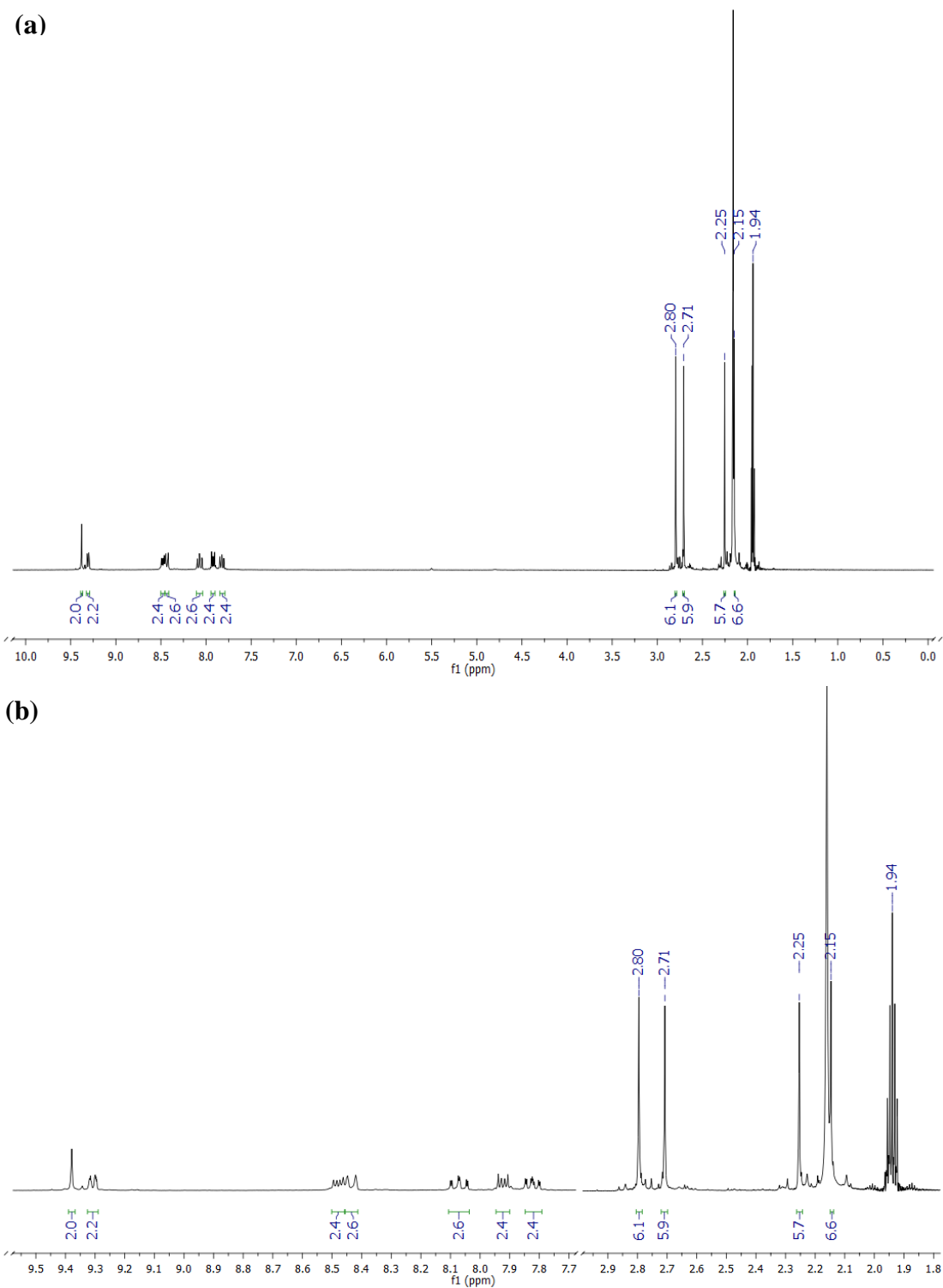
Figure 2.5. ^{1}H NMR spectra (CD$_3$CN, 300 MHz) of compound **3** (a) full spectrum, (b) enlarged.

Crystal Structure Determination

Single crystals suitable for X-ray diffraction were obtained for both **1** and **2** by diffusing diethyl ether into acetonitrile solution of the compounds and the molecular structures are depicted in Figures 2.6 and 2.9. Both of them crystallize in the monoclinic space group *P*2$_1$/c. Crystal data and refinement parameters along with all Ru-N bond distances are compiled in Table (2.1-2.3). The structure of **1** (Figure 2.6) exhibits meridional binding of the tppz ligand. The coordination sphere of each Ru center is surrounded by six N-atoms in a distorted octahedral geometry, which is evident from the Ru-N distances in Table 2.2 which range from 1.948 (3) – 2.064 (3) Å which is in good agreement with other dinuclear polypyridine ruthenium (II) complexes bridged by tppz.[155] The bonds between the Ru(II) ions and the central pyrazine ring N-atoms (Ru1-N1= 1.948 (3) Å and Ru2-N7= 1.961 (3) Å) are shorter than the rest of the Ru-N bonds. Similar short bond distances between Ru and pyrazine ring N-atoms (1.944 – 1.978 Å) have been reported for several dinuclear Ru(II) compounds bridged by tppz.[155-156] Increased back-bonding interaction between the Ru(dπ) and pz (π*) [pz= pyrazine ring] orbitals resulting in shorter Ru-N bonds has been reported for dinuclear Ru(II)-compound bridged by pyrazine ligand.[157] A similar argument explains the shorter Ru-N bonds in **1** which owing to the π-acidic nature of the bridging tppz moiety. Equatorial acetonitrile ligands exhibit longer Ru-N bond distances (2.053 – 2.059 Å) compared to the axial ones (2.007 – 2.029 Å), a trend also noted for the partially solvated [Ru(tpy)(CH$_3$CN)$_3$]$^{2+}$ cation where the equatorial acetonitrile bond is ~ 0.05 Å longer than the axial bonds.[152] The crystal structure

of **1** also reveals a significantly twisted tppz ligand caused by repulsions of the hydrogen atoms at the 3-position of each of the four pyridine rings of the bridging ligand (Figure 2.7). The torsion angles between the planes of the coordinated pyridine rings are 29.5° and 27.3° which is less than the twist angles reported for other dinuclear tppz bridged Ru(II) complexes (36.8° – 54.7°).[128, 155] The twisting of the bridging ligand also is observed in the optimized geometry of **1** in acetonitrile (Figure 2.8) with torsion angles of 26.4° and 26.5°, indicating that the structure is essentially preserved in solution.

The structure of **2** (Figure 2.9) contains two Ru(II) centers, each of which is surrounded by six N-atoms in a pseudo-octahedral geometry with considerable distortion. The Ru-N bond distances range from 2.011 (3) – 2.063 (3) Å (Table 2.3). The distances between Ru and the pyrazine ring N-atoms (Ru1-N2 = 2.063 (3) Å and Ru2-N8 = 2.059 (3) Å) are longer than other Ru-N bonds but are ~ 0.03 Å shorter than the corresponding Ru-N_{pz} distance (2.096 Å) in the mononuclear compound $[Ru(bpy)_2(dpq)](PF_6)_2$, indicating a higher π-acidic character for the bridging dpq ligand in **2**.[158] Also, the equatorial CH_3CN molecules (CH_3CN_{eq}) that are co-planar with the dpq ligand exhibit longer Ru-N bond distances compared to the axial CH_3CN molecules (CH_3CN_{ax}), in agreement with the corresponding metrical parameters for the partially solvated $[Ru(bpy)(NCCH_3)_4]^{2+}$.[153] The bridging dpq ligand adopts a twisted geometry (Figure 2.10) as a result of repulsion between the hydrogen atoms located at the 3-position of the peripheral pyridyl rings as observed in the case of **1**.[128] The torsion angle between the two planes of the coordinated pyridyl rings is 39.1°. Moreover, the optimized geometry of **2** in acetonitrile (Figure 2.11) gave a torsion angle of 35.4° which is close to the torsion angle

value obtained in the solid state, indicating that the structure is essentially preserved in solution. The optimized geometry for **3** in acetonitrile indicated a twisted dpb ligand with a similar torsion angle of 37.4º (Figure 2.12).

Table 2.1. Crystal data and refinement parameters for **1** and **2**.

Compound	1	2
CCDC number	1063936	1912992
Empirical Formula	$C_{38}H_{37}F_{24}N_{13}P_4Ru_2$	$C_{36}H_{39}F_{24}N_{13}P_4Ru_2$
Formula weight	1457.82	1435.82
Temperature, K	110 (2)	110 (2)
Crystal system	Monoclinic	Monoclinic
Space group	$P2_1/c$	$P2_1/c$
Unit cell dimensions	$a = 21.526\ (4)$ Å, $\alpha = 90º$ $b = 16.614\ (3)$ Å, $\beta = 137.293\ (2)º$ $c = 21.937\ (5)$ Å, $\gamma = 90º$	$a = 12.3441\ (17)$ Å, $\alpha = 90º$ $b = 15.196\ (2)$ Å, $\beta = 93.079\ (2)º$ $c = 30.269\ (4)$ Å, $\gamma = 90º$
Volume, Å^3	5321.1 (19)	5669.7 (13)
Z	4	4
Density, g/cm^3	1.820	1.682
Absorption coefficient, mm^{-1}	0.817	0.765
$F(000)$	2880.0	2840.0
Crystal color, morphology	dark purple needle	dark purple needle
Crystal size, mm^3	$0.387 \times 0.078 \times 0.077$	$0.347 \times 0.09 \times 0.074$
Reflections collected	61008	63444
Independent reflections	12228 [$R_{int} = 0.0569$]	12491 [$R_{int} = 0.0406$]
Data/restraints/parameters	12228/0/711	12491/499/842
Goodness-of-fit on F^2	1.025	1.049

Table 2.1. Continued

Compound	1	2
R indices [I>2sigma(I)][a,b]	$R_1 = 0.0526$, $wR_2 = 0.1263$	$R_1 = 0.0493$, $wR_2 = 0.1188$
R indices (all data)	$R_1 = 0.0712$, $wR_2 = 0.1385$	$R_1 = 0.0625$, $wR_2 = 0.1265$
Largest diff. peak/hole, e Å^3	2.23/–1.39	1.21/–0.89

[a] $R1 = \sum||F_o| - |F_c||/[\sum|F_o|]$. [b] $wR2 = [\sum[w(F_o^2 - F_c^2)^2]/\sum[w(F_o^2)^2]]^{1/2}$, $w = 1/\sigma^2(F_o^2) + (aP)^2 + bP$, where $P = [max(0 \text{ or } F_o^2) + 2(F_c^2)]/3$.

Table 2.2. Selected bond distances in (Å) for compound **1**. Adapted with permission from reference 128.

Ru1–N1	1.948 (3)	Ru2–N7	1.961 (3)
Ru1–N2	2.053 (4)	Ru2–N8	2.059 (4)
Ru1–N3	2.056 (4)	Ru2–N9	2.064 (4)
Ru1–N4	2.063 (4)	Ru2–N10	2.055 (4)
Ru1–N5	2.019 (4)	Ru2–N11	2.029 (4)
Ru1–N6	2.017 (4)	Ru2–N12	2.007 (4)
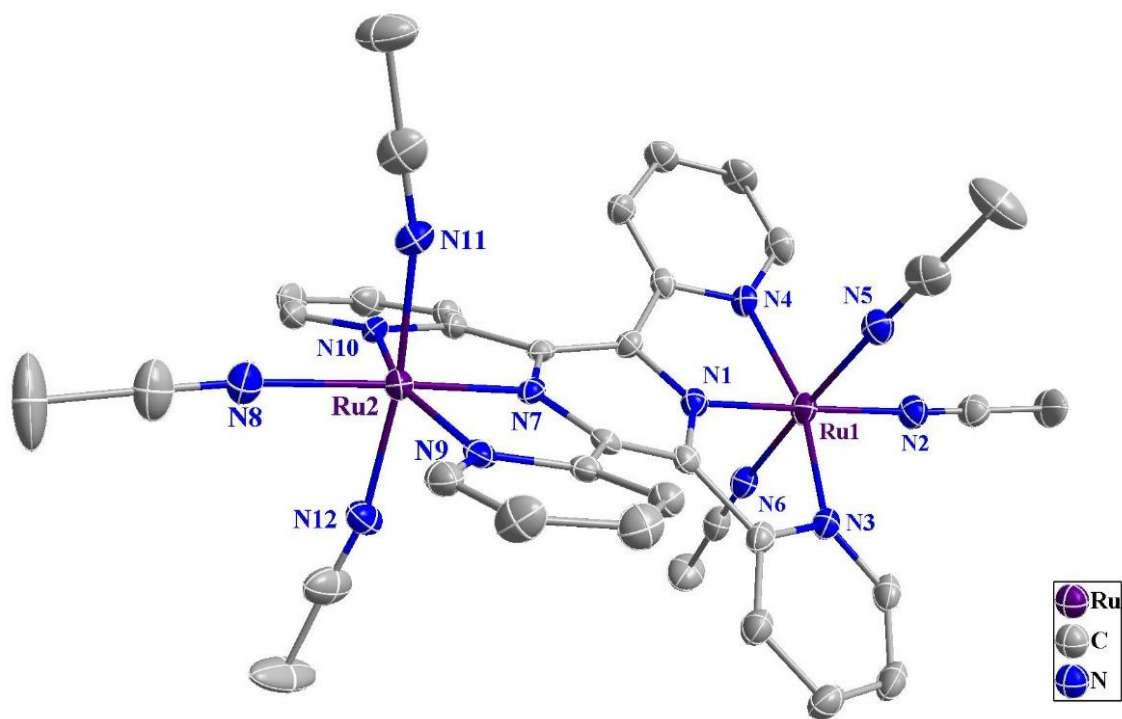
Figure 2.6. Thermal ellipsoid plot (50% probability) for $[\{Ru^{II}(NCCH_3)_3\}_2(\mu\text{-tppz})]^{4+}$ in (**1**). The $(PF_6)^-$ counterions, solvent of crystallization (acetonitrile) and H atoms have been omitted for the sake of clarity. Adapted with permission from reference 128.
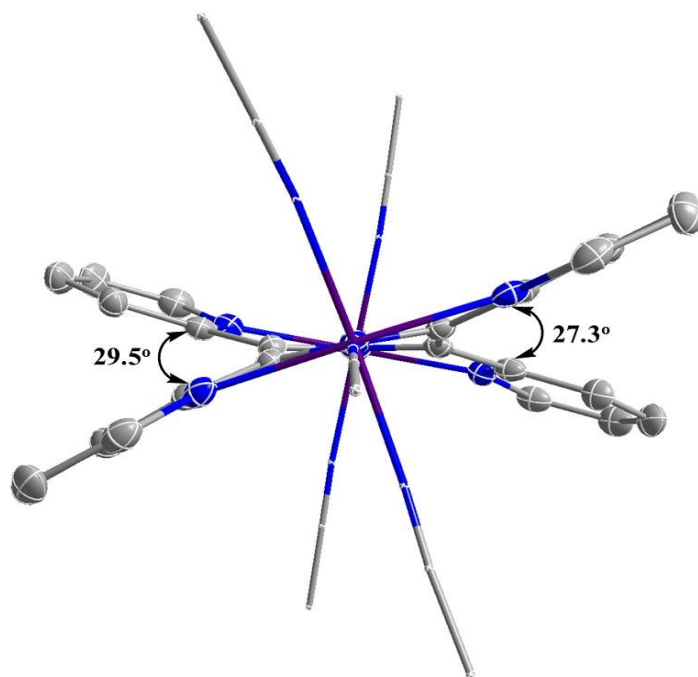
Figure 2.7. Structure of $[\{Ru^{II}(NCCH_3)_3\}_2(\mu\text{-tppz})]^{4+}$ in (**1**) emphasizing the twisted bridging tppz ligand. H atoms have been omitted for the sake of clarity. Adapted with permission from reference 128.
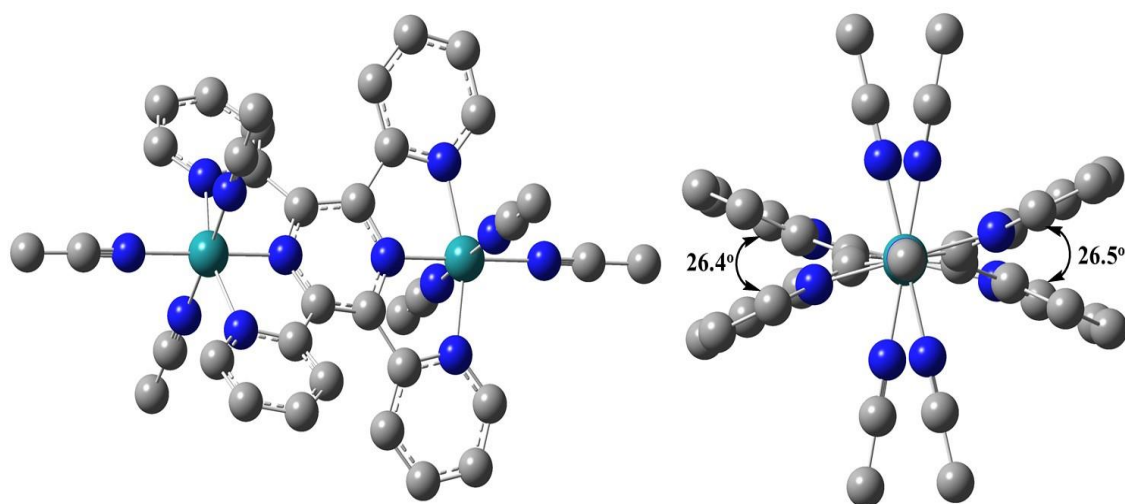
Figure 2.8. Optimized geometry of $[\{Ru^{II}(NCCH_3)_3\}_2(\mu\text{-tppz})]^{4+}$ (**1**) in acetonitrile using the SMD Model showing the twisted bridging tppz ligand. H atoms have been omitted for the sake of clarity.

Table 2.3. Selected bond distances in (Å) for compound **2**.

Ru1–N1	2.011 (3)	Ru2–N7	2.026 (4)
Ru1–N2	2.063 (3)	Ru2–N8	2.059 (3)
Ru1–N3	2.055 (3)	Ru2–N9	2.036 (4)
Ru1–N4	2.041 (3)	Ru2–N10	2.043 (3)
Ru1–N5	2.031 (3)	Ru2–N11	2.017 (3)
Ru1–N6	2.016 (3)	Ru2–N12	2.027 (3)
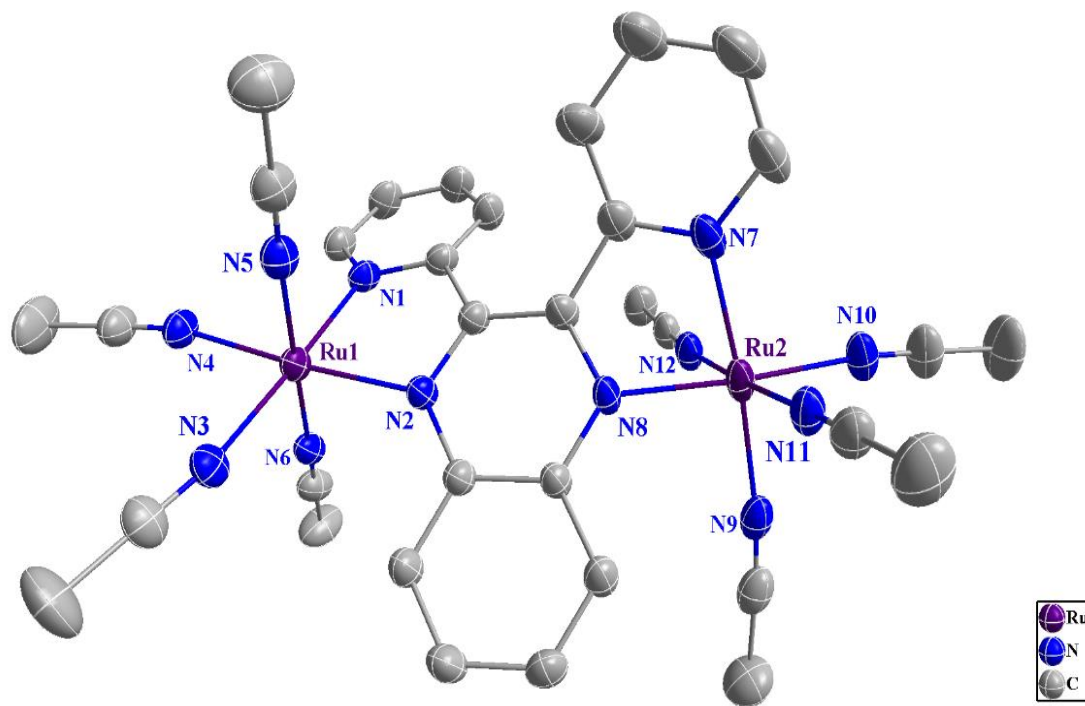
Figure 2.9. Thermal ellipsoid plot (50% probability) for $[\{Ru^{II}(NCCH_3)_4\}_2(\mu\text{-dpq})]^{4+}$ in (**2**). The $(PF_6)^-$ counterions, solvent of crystallization (acetonitrile) and H atoms have been omitted for the sake of clarity.
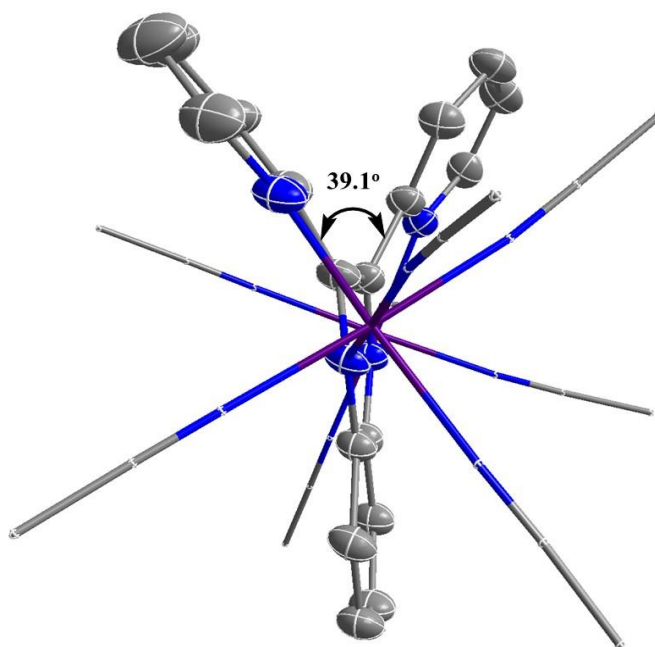
Figure 2.10. Structure of [{Ru^{II}(NCCH$_3$)$_4$}$_2$(μ-dpq)]$^{4+}$ in (**2**) emphasizing the twisted bridging dpq ligand. H atoms have been omitted for the sake of clarity.
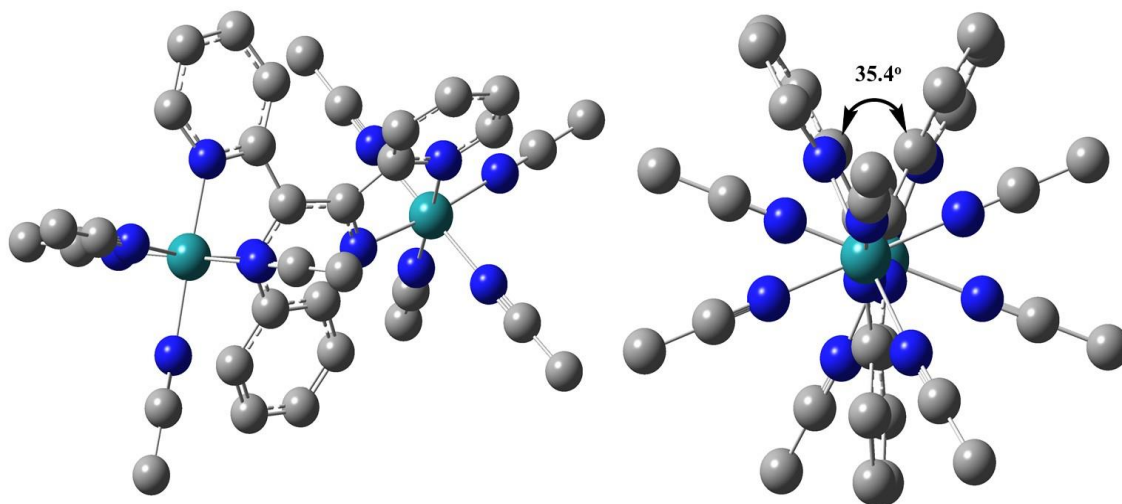
Figure 2.11. Optimized geometry of [{Ru^{II}(NCCH$_3$)$_4$}$_2$(μ-dpq)]$^{4+}$ (**2**) in acetonitrile using the SMD Model showing the twisted bridging dpq ligand. H atoms have been omitted for the sake of clarity.
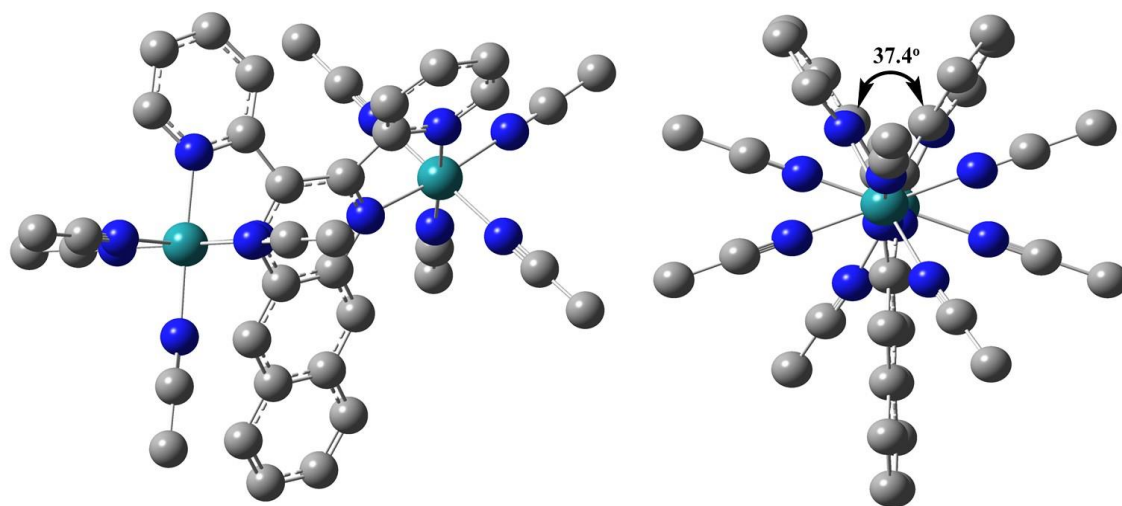
Figure 2.12. Optimized geometry of [{Ru^{II}(NCCH$_3$)$_4$}$_2$(μ-dpb)]$^{4+}$ (**3**) in acetonitrile using the SMD Model showing the twisted bridging dpb ligand. H atoms have been omitted for the sake of clarity.

Electronic Absorption Spectroscopy and Electronic Structure Calculations

Electronic absorption spectra of the compounds in acetonitrile are depicted in Figure 2.13; the absorption data are summarized in Table 2.4. Compound **1** with the bridging tppz ligand exhibits a strong ^{1}MLCT band in the visible region with a maximum at 498 nm ($\varepsilon = 22{,}400$ M^{-1}cm^{-1}). A broad tail with relatively low intensity extends beyond 650 nm. The absorption profile is similar to the related complex [{Ru(tpy)}$_2$(μ-tppz)](PF$_6$)$_4$.[159] The bridging dpq and dpb compounds **2** and 3 possess lower lying π^* orbitals as evidenced by the bathochromic shift of the ^{1}MLCT transition to for **2** and **3** respectively with tails extending beyond 650 nm. These absorptions are red-shifted by 21 nm (**2**) and 51 nm (**3**) compared to **1** (Figure 2.13 inset) which supports the hypothesis that the use of quinoxaline bridging ligands leads to lower energy transitions. In the case of **3**,

69

an additional bathochromic shift of 30 nm is observed due to the introduction of extended

conjugation in the bridging ligand. The intensities of the visible absorption bands are lower

and the bands are broader for **2** and **3**. The ^{1}MLCT transitions of the compounds are

assigned to Ru(dπ)$\rightarrow$BL(π*) which is supported by the calculated TDDFT data compiled

in Tables 2.11-2.13. The absorptions in the UV region of the spectra of **1-3** are due to

singlet ligand centered (^{1}LC) $\pi$$\rightarrow$$\pi$* transitions (Figure 2.12). The low energy absorptions

in the red region of the visible spectra of **1**–**3** is promising for applications as PCT agents.

Table 2.4. Electronic absorption data for **1**–**3** in acetonitrile at RT.

Compound	λ_{max} (nm) ($\varepsilon \times 10^4$ M^{-1} cm^{-1})
[{Ru^{II}(NCCH$_3$)$_3$}$_2$(μ-tppz)](PF$_6$)$_4$ (**1**)	498 (2.24), 382 (4.67), 364 (4.24), 349[a] (2.64), 286 (5.57), 231[a] (4.50)
[{Ru^{II}(NCCH$_3$)$_4$}$_2$(μ-dpq)](PF$_6$)$_4$ (**2**)	600[a] (0.47), 519 (1.10), 386 (1.80), 371[a] (1.45), 314[a] (2.45), 298 (2.82)
[{Ru^{II}(NCCH$_3$)$_4$}$_2$(μ-dpb)](PF$_6$)$_4$ (**3**)	635[a] (0.44), 549 (0.93), 401[a] (1.77), 370 (3.95), 306 (2.31), 254[a] (2.62)

[a] Shoulder.
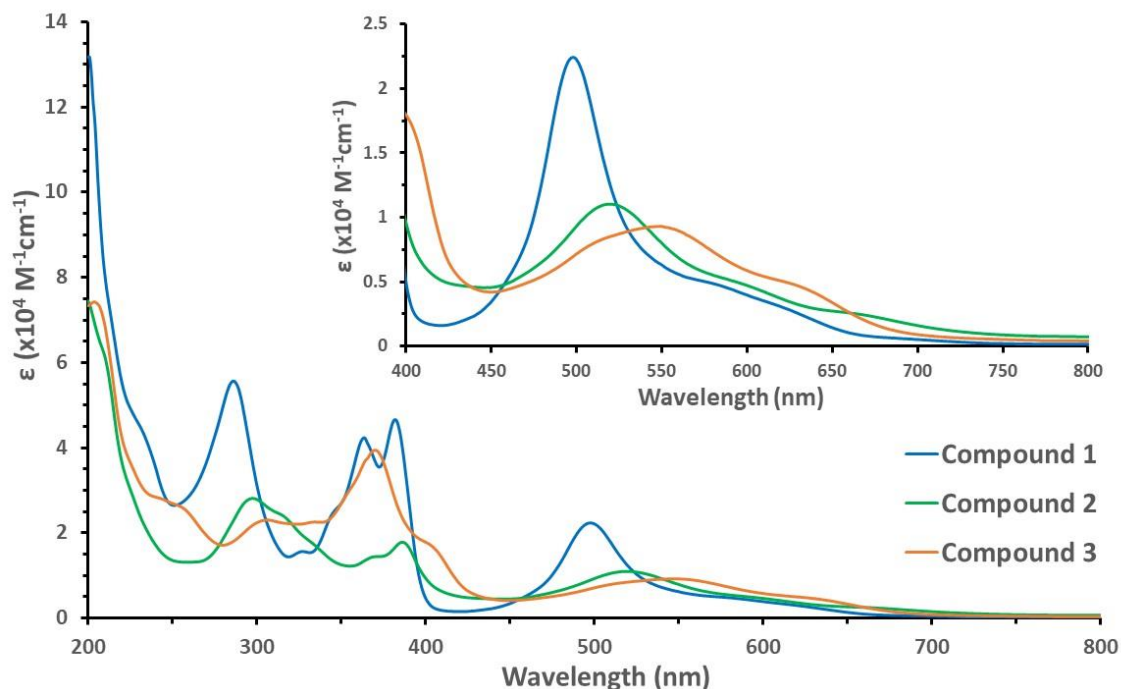
Figure 2.13. Electronic absorption spectra of **1**–**3** in acetonitrile at room temperature. Inset: [1]MLCT absorption of the compounds in the visible region.

The optimized geometries in acetonitrile were analyzed to gain insight into the electronic properties of the molecules. Electron densities and energies of selected MOs along with the percentage contribution of the metal centers and coordinated ligands are tabulated in Table (2.5-2.9). In all three compounds, the (HOMO-2) and (HOMO-1) orbitals are primarily localized on Ru centers and represent the occupied "t_{2g}-type" Ru(dπ) orbitals in a pseudo-octahedral coordination environment. In the case of the HOMO, the electron density is localized on both the bridging ligand (dpb) as well as on the metal centers for **3**, in contrast to **1** and **2** for which the HOMOs are predominantly metal in character. These results indicate that there is mixing of metal and ligand orbitals due to the presence of dpb based low energy π^*-orbitals in **3**. For **1**, the (LUMO+1) is localized on the central pyrazine ring whereas the LUMO and (LUMO+2) to (LUMO+4) orbitals

71

are delocalized over the pyrazine ring and the peripheral pyridyl rings. For **2** and **3**, the LUMO is centered on the quinoxaline moiety of the bridging ligand whereas electron densities on (LUMO+1) to (LUMO+4) are delocalized over the quinoxaline ring and the peripheral pyridyl rings (Table 2.5-2.8). These electronic distributions confirm the conclusion that the low energy ^{1}MLCT transitions occur between Ru(dπ) orbitals to bridging ligand (π^*) orbitals. Compound **3** possesses a lower lying π^* orbital on the dpb ligand due to its extended conjugation, resulting in the overall stabilization of HOMO to (LUMO+4) levels with significant ligand contribution compared to **2**.

Table 2.5. Frontier molecular orbitals (HOMO-2 and HOMO-1) of **1**-**3** (isovalue = 0.04).

[{Ru(NCCH$_3$)$_3$}$_2$(μ-tppz)]$^{4+}$ (1)	[{Ru(NCCH$_3$)$_4$}$_2$(μ-dpq)]$^{4+}$ (2)	[{Ru(NCCH$_3$)$_4$}$_2$(μ-dpb)]$^{4+}$ (3)
HOMO-2	HOMO-2	HOMO-2
HOMO-1	HOMO-1	HOMO-1
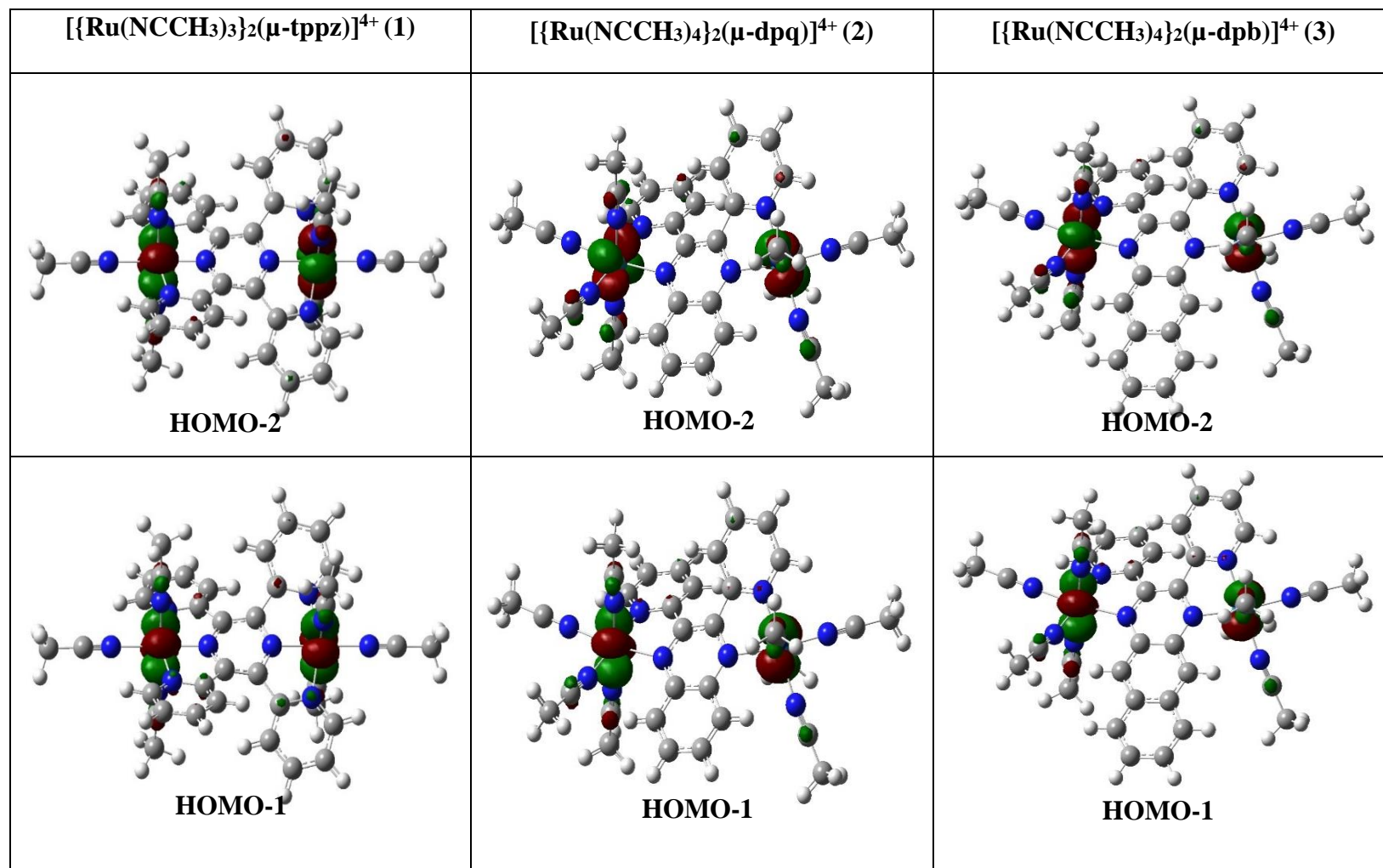
Table 2.6. Frontier molecular orbitals (HOMO and LUMO) of **1**-**3** (isovalue = 0.04).

[{Ru(NCCH₃)₃}₂(μ-tppz)]⁴⁺ (1)	[{Ru(NCCH₃)₄}₂(μ-dpq)]⁴⁺ (2)	[{Ru(NCCH₃)₄}₂(μ-dpb)]⁴⁺ (3)
 HOMO	 **HOMO**	 **HOMO**
 LUMO	 **LUMO**	 **LUMO**
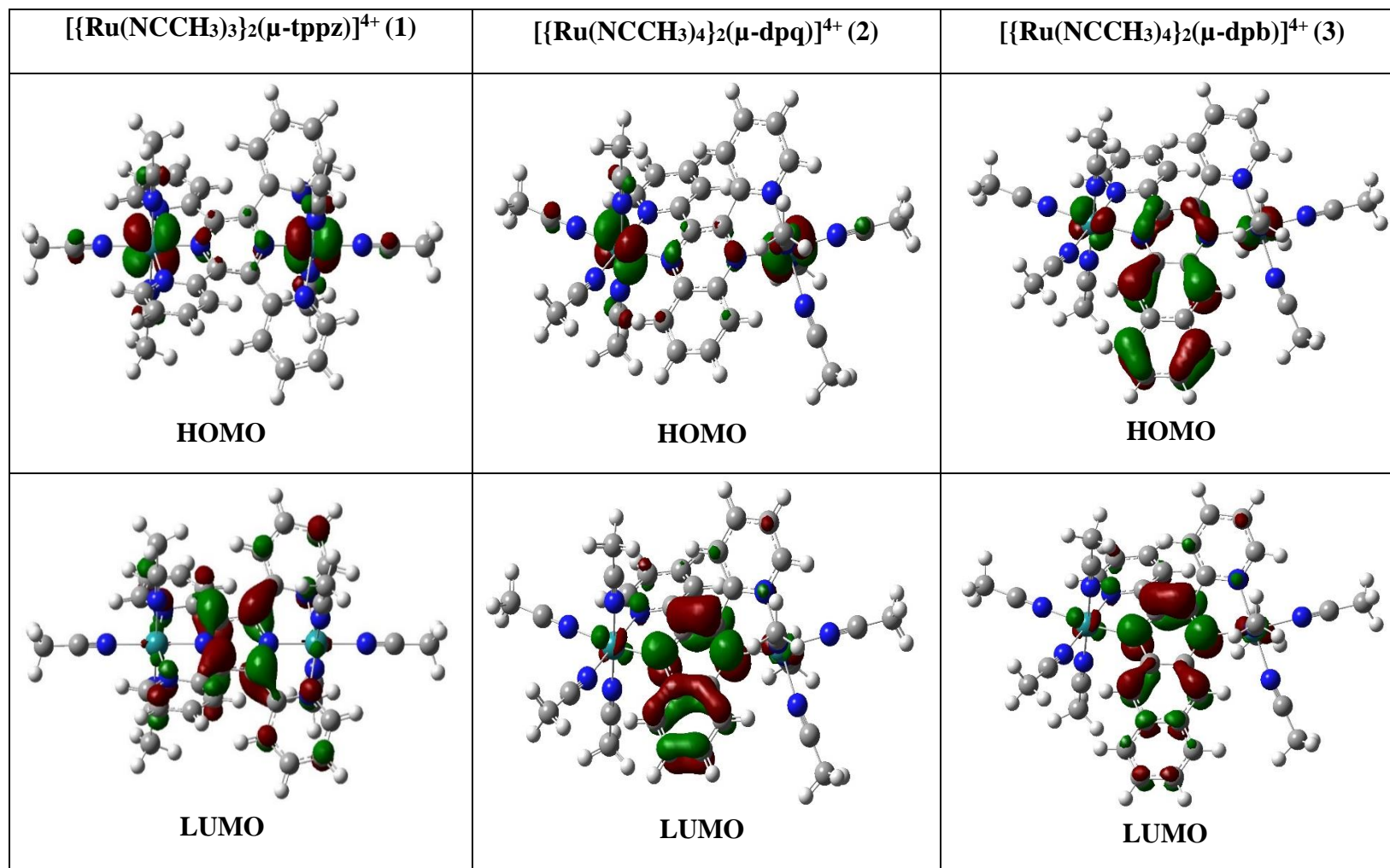
Table 2.7. Frontier molecular orbitals (LUMO+1 and LUMO+2) of **1-3** (isovalue = 0.04).

[{Ru(NCCH$_3$)$_3$}$_2$(μ-tppz)]$^{4+}$ (1)	[{Ru(NCCH$_3$)$_4$}$_2$(μ-dpq)]$^{4+}$ (2)	[{Ru(NCCH$_3$)$_4$}$_2$(μ-dpb)]$^{4+}$ (3)
LUMO+1	**LUMO+1**	**LUMO+1**
LUMO+2	**LUMO+2**	**LUMO+2**
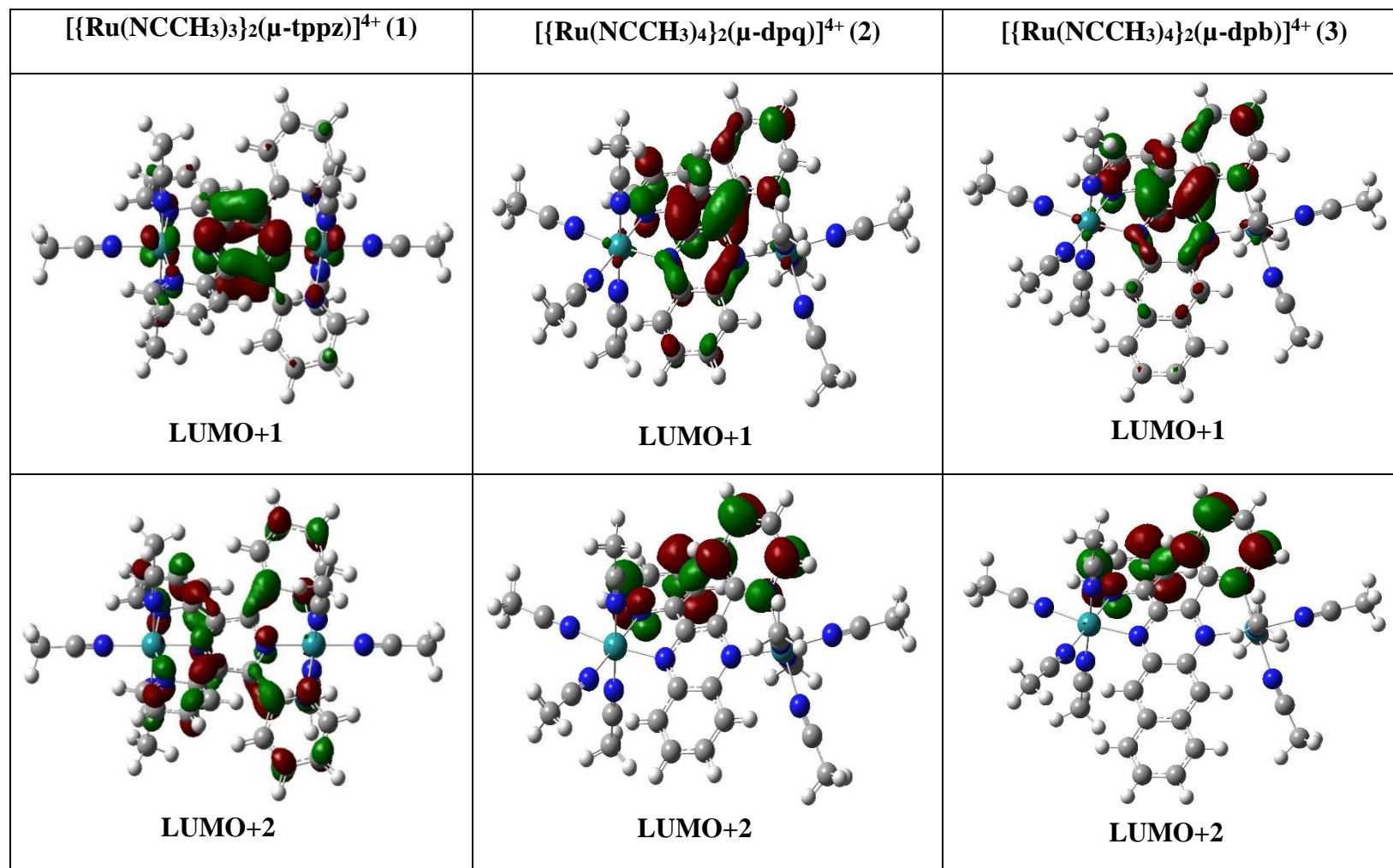
Table 2.8. Frontier molecular orbitals (LUMO+3 and LUMO+4) of **1-3** (isovalue = 0.04).

[{Ru(NCCH$_3$)$_3$}$_2$(μ-tppz)]$^{4+}$ (1)	[{Ru(NCCH$_3$)$_4$}$_2$(μ-dpq)]$^{4+}$ (2)	[{Ru(NCCH$_3$)$_4$}$_2$(μ-dpb)]$^{4+}$ (3)
LUMO+3	LUMO+3	LUMO+3
LUMO+4	LUMO+4	LUMO+4
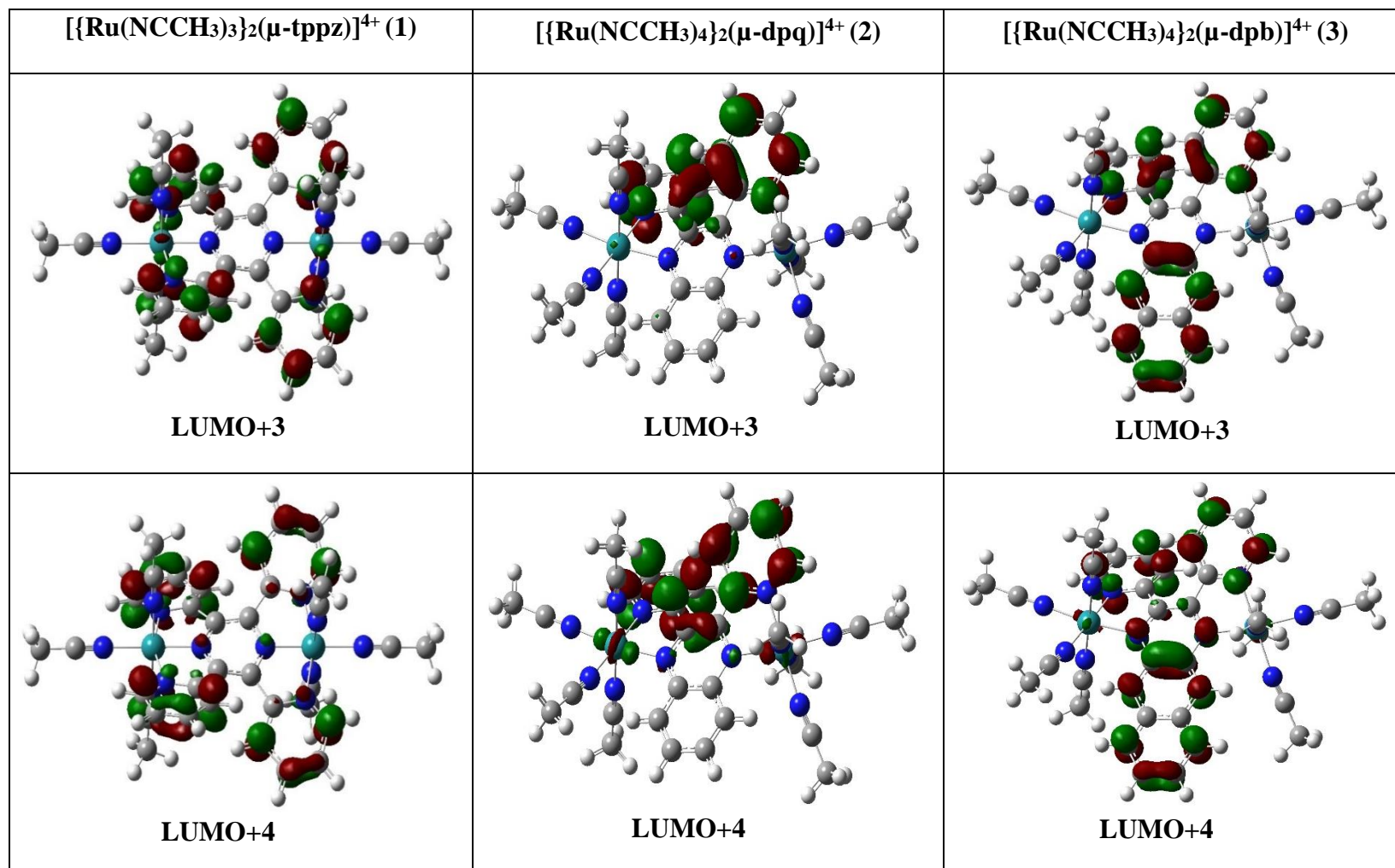
Table 2.9. Percent contribution of selected MOs and corresponding energies (E_{MO}) of **1–3**.

MO	[{Ru(NCCH$_3$)$_3$}$_2$(μ-tppz)]$^{4+}$ (**1**)				[{Ru(NCCH$_3$)$_4$}$_2$(μ-dpq)]$^{4+}$ (**2**)				[{Ru(NCCH$_3$)$_4$}$_2$(μ-dpb)]$^{4+}$ (**3**)			
	% Contribution			E_{MO}	% Contribution			E_{MO}	% Contribution			E_{MO}
	Ru	tppz	CH$_3$CN	(eV)	Ru	dpq	CH$_3$CN	(eV)	Ru	dpb	CH$_3$CN	(eV)
LUMO+4	1	98	1	-1.686	7	88	4	-1.047	4	92	4	-1.425
LUMO+3	5	93	2	-1.728	2	94	4	-1.607	2	95	3	-1.725
LUMO+2	3	94	3	-2.513	2	94	4	-1.876	2	94	4	-1.865
LUMO+1	9	87	4	-3.447	4	94	2	-3.128	4	94	2	-3.059
LUMO	5	94	1	-3.636	8	89	3	-3.638	7	90	3	-3.781
HOMO	74	12	14	-6.462	73	12	15	-6.550	33	60	7	-6.339
HOMO-1	72	17	11	-6.475	75	10	15	-6.629	74	11	15	-6.625
HOMO-2	76	14	10	-6.576	76	9	15	-6.684	74	12	14	-6.666

77

Electrochemical Properties

The redox properties of all three compounds were studied by cyclic voltammetry and differential pulse voltammetry in dry deoxygenated acetonitrile at room temperature. The half-wave redox potential values ($E_{1/2}$) *vs* the Ag/AgCl reference electrode obtained from the cyclic voltammograms were further referenced *vs* NHE for the discussion of results as described in the experimental section and summarized in Table 2.10. Cyclic and differential pulse voltammograms of **1**-**3** are depicted in Figures 2.14 and 2.15. For compound **1**, the oxidation events at the metal centers are quasi-reversible as evidenced by the peak-to-peak separation (ΔE_p) values whereas reductions involving the bridging ligands are all irreversible. The two quasi-reversible oxidation events correspond to sequential one electron oxidation of the two metal centers to generate Ru(II,III) and Ru(III,III) species respectively at $E_{1/2}$ values of 2.17 V and 1.94 V (*vs* NHE). The Ru(II) ions oxidize at different potentials indicating they are electronically coupled through the delocalized tppz ligand. These potentials are more positive by 270 mV and 340 mV compared to [{Ru(tpy)$_2$(μ-tppz)](PF$_6$)$_4$ ($E_{1/2}$ = 1.91 V and 1.60 V *vs* NHE).[159] This fact is attributed to the coordination of π-accepting CH$_3$CN ligands at each metal center which renders it more difficult to oxidize than compounds with the less π-accepting tpy ligands. Multiple irreversible bridging ligand based reductions are observed at negative potentials but the values are shifted to more positive potential due the presence of the CH$_3$CN ligands in the coordination sphere.[129, 159]

In contrast, the Ru(II) based redox events are irreversible for **2** and **3** whereas reductions involving the bridging ligands (dpq, dpb) are mostly quasi-reversible as evidenced from the ΔE_p values. The two irreversible oxidation processes correspond to sequential one electron oxidation from Ru(II) to Ru(III) which occur at different potentials for the two metal centers (Figure 2.15) similar to **1**, an indication of electronic coupling through the bridging ligands. The $E_{1/2}$ values for the Ru$^{III/II}$ reduction couples are nearly the same for the dpq and dpb complexes which is in accord with other dinuclear ruthenium polypyridyl compounds bridged by the same ligands.[132] The oxidation potentials, however, are shifted to positive potentials by more than 0.3 V for **2** and **3** as compared to ruthenium polypyridyl analogues.[132] This finding is attributed to the coordination of CH$_3$CN ligands which render the compound more difficult to oxidize than the less π-accepting polypyridine ligands. The observed reduction processes represent sequential one-electron reductions of the bridging ligands, with both ligands exhibiting two quasi-reversible reduction events followed by an irreversible reduction at potentials less than -1.50 V (Figure 2.14-2.16). The two reductions of the dpq ligand in compound **2** closely match the values of the analogous dinuclear compound [{Ru(bpy)$_2$}$_2$(μ-dpq)](PF$_6$)$_4$ for which the first two electrons enter a LUMO localized on the bridging ligand.[160] Ligand-based reduction potentials are shifted to more positive potentials for the dpb compound **3** as compared to the dpq analogue owing to extended π-conjugation.[130-132]

Table 2.10. Half-wave potentials ($E_{1/2}$) for **1**–**3** in acetonitrile.

Compound	$E_{1/2}$ (V) *vs* NHE ($\Delta E_p = E_{pa}$–E_{pc} in mV)			
	$E_{1/2}$ [Ru$^{3+/2+}$]	$E_{1/2,red1}$	$E_{1/2,red2}$	$E_{1/2,red3}$
[{Ru^{II}(NCCH$_3$)$_3$}$_2$(μ-tppz)](PF$_6$)$_4$ (**1**)	2.17 (89), 1.94 (69)	-0.17[a]	-0.67[a]	-1.27 [a]
[{Ru^{II}(NCCH$_3$)$_4$}$_2$(μ-dpq)](PF$_6$)$_4$ (**2**)	2.28, 2.10 [a]	-0.14 (72)	-0.94 (82)	-1.55 [a,b]
[{Ru^{II}(NCCH$_3$)$_4$}$_2$(μ-dpb)](PF$_6$)$_4$ (**3**)	2.24, 2.04 [a]	-0.002 (79)	-0.70 (74)	-1.51 [a]

[a] irreversible. [b] E_{pc} is reported.
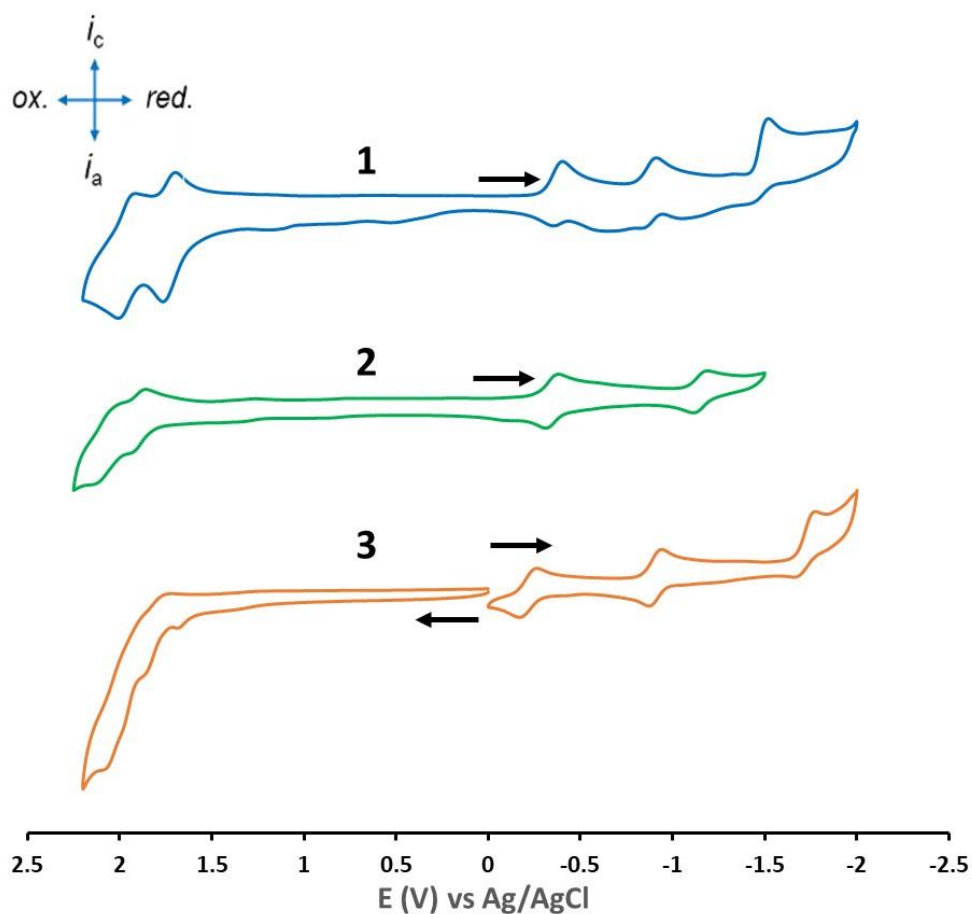
Figure 2.14. Cyclic voltammograms (*vs* Ag/AgCl) of compounds **1**–**3** in dry acetonitrile (0.1 M [^{n}Bu$_4$N](PF$_6$), 100 mV/s scan rate). i_c = cathodic current, i_a = anodic current, ox. = oxidation, red. = reduction. The black arrows indicate the direction of the scan.

80
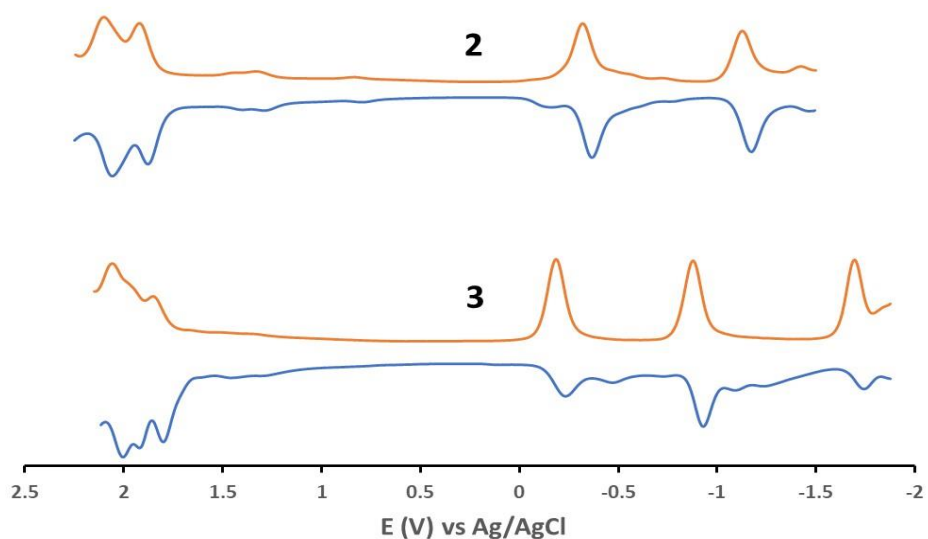
Figure 2.15. Differential pulse voltammograms (*vs* Ag/AgCl) of compounds **2** and **3** in dry acetonitrile displaying both cathodic (orange) and anodic (blue) waves (0.1 M [^{n}Bu$_4$N](PF$_6$), 100 mV/s scan rate).
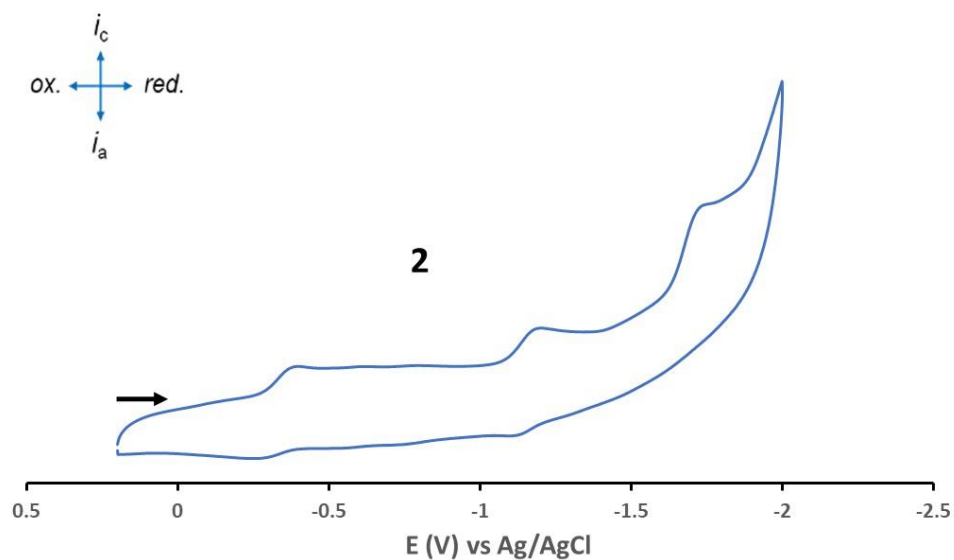
Figure 2.16. Cyclic voltammogram (*vs* Ag/AgCl) of compounds **2** in dry acetonitrile showing the ligand reduction events (0.1 M [^{n}Bu$_4$N](PF$_6$), 100 mV/s scan rate).

TDDFT calculations were performed on the ground state optimized geometry of **1**–**3** in acetonitrile to substantiate the experimental electronic absorption spectra and further interpret visible electronic transitions. The most relevant [1]ES electronic transitions calculated in acetonitrile (using the SMD model[149]) with $\lambda_{calc} \geq 390$ nm are listed in Table (2.11-2.13) along with their extinction coefficients in terms of oscillator strength (f) values, percent transition contributions and nature of transitions. The calculated absorption spectra qualitatively resemble the experimental absorption spectra of the complexes in the visible/near UV region (Figure 2.17) with absorption maxima shifted hypsochromically due to overestimation of orbital energies.[161] The computed singlet excited states in the visible region ($\lambda_{calc} \geq 400$ nm) are predominantly [1]MLCT in nature whereas those in the UV region ($\lambda_{calc} \leq 350$ nm) possess [1]LC ([1]$\pi\pi^*$) character, results that corroborate the experimental assignments. The calculated [1]MLCT transitions occur from Ru(dπ) $\rightarrow$ tppz/dpq/dpb (π^*) orbitals. For compound **1**, the most intense transition at $\lambda_{calc} = 486.6$ nm (f= 0.338) corresponds to the experimental absorption maximum at $\lambda_{exp} = 498$ nm whereas the low energy visible transitions (1-9) constitute the broad shoulder that extends beyond 600 nm. For compound **2**, the most intense transition at $\lambda_{calc} = 512.8$ nm (f= 0.201) corresponds to the experimental absorption maximum at $\lambda_{exp} = 519$ nm whereas both transitions at $\lambda_{calc} = 546.2$ nm (f= 0.004) and 519.8 nm (f= 0.149) correspond to the experimental absorption maxima at $\lambda_{exp} = 549$ nm for compound **3**. The low energy excited

state transitions 1 and 3 represent the extended absorption for both compounds in the near red/red region of the visible spectrum.
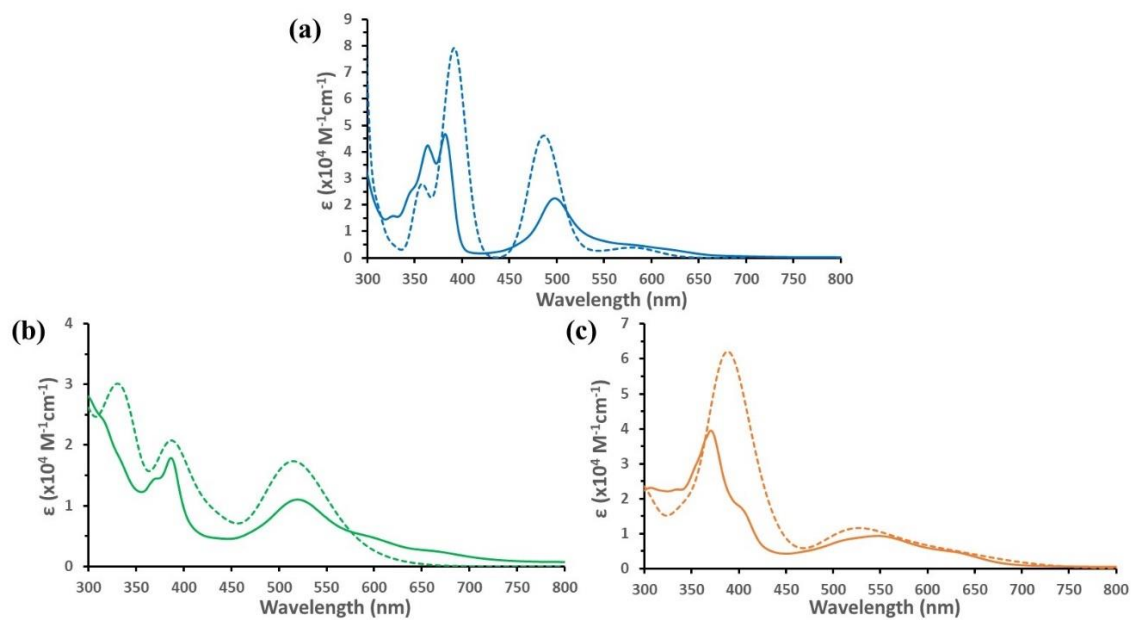
Figure 2.17. Experimental (solid line) and calculated (dotted line) electronic absorption spectra of (a) **1**, (b) **2** and (c) **3** in acetonitrile.

Table 2.11. TDDFT data of **1**.

N^a	λ_{calc} (nm)	f^b	Major Contributions^c	Assignment
1	588.8	0.014	H → L (97%)	MLCT
2	577.7	0.014	H-1 → L (84%), H → L+1 (14%)	MLCT
3	567.9	0.001	H-1 → L+1 (97%), H-2 → L+2 (2%)	MLCT
6	545.3	0.003	H-4 → L (96%)	MLCT
7	541.2	0.004	H-2 → L+1 (95%), H-1 → L+2 (3%)	MLCT
9	530.7	0.006	H-4 → L+1 (88%), H → L+1 (4%), H-1 → L (4%), H-3 → L+2 (4%)	MLCT
10	486.6	0.338	H→ L+1 (78%), H-1 → L (11%), H-4 → L+1 (7%)	MLCT
11	476.0	0.005	H-5 → L (97%)	MLCT
13	394.9	0.440	H-6 → L (98%)	LC

^{a} excited state number, ^{b} oscillator strength, ^{c} percent contribution = 2x(configuration coefficient)^{2}x100%.

Table 2.12. TDDFT data of **2**.

N^a	λ_{calc} (nm)	f^b	Major Contributions^c	Assignment
1	569.5	0.023	H → L (65%), H-2 → L (28%), H-1 → L+1 (5%)	MLCT
3	522.2	0.024	H-4 → L (73%), H-2 → L (17%), H-3 → L+1 (5%), H → L (3%)	MLCT
5	512.8	0.201	H-2 → L (53%), H → L (25%), H-4 → L (20%)	MLCT
6	472.4	0.002	H-5 → L (55%), H → L+1 (39%), H-1 → L (3%)	MLCT
8	434.8	0.082	H-1 → L+1 (93%), H → L (4%)	MLCT
9	426.3	0.005	H-2 → L+1 (91%), H-4 → L+1 (2%), H-1 → L (2%)	MLCT
10	408.3	0.024	H-3 → L+1 (91%), H-4 → L (5%)	MLCT
11	407.4	0.002	H-4 → L+1 (89%), H-3 → L (5%)	MLCT
12	400.8	0.005	H-5 → L+1 (90%), H-7 → L (6%)	MLCT/ LC

^{a} excited state number, ^{b} oscillator strength, ^{c} percent contribution = 2x(configuration coefficient)^{2}x100%.

Table 2.13. TDDFT data of **3**.

N^a	λ_{calc} (nm)	f^b	Major Contributions^c	Assignment
1	628.5	0.050	H → L (84%), H-2 → L (14%)	MLCT
3	572.8	0.033	H-2 → L (82%), H → L (14%)	MLCT
5	546.2	0.004	H-5 → L (94%), H-4 → L+1 (3%)	MLCT
6	519.8	0.149	H-3 → L (96%)	MLCT
8	467.7	0.003	H → L+1 (63%), H-7 → L (20%), H-6 → L (15%)	MLCT/ LC
9	425.1	0.068	H-1 → L+1 (95%), H-2 → L (2%)	MLCT
10	420.4	0.035	H-2 → L+1 (73%), H-7 → L (20%)	MLCT/ LC
11	408.2	0.112	H-3 → L+1 (59%), H-7 → L (21%), H-2 → L+1 (12%), H-5 → L+1 (3%), H → L+1 (2%)	MLCT/ LC
12	400.0	0.014	H-4 → L+1 (92%), H-5 → L (4%)	MLCT

^{a} excited state number, ^{b} oscillator strength, ^{c} percent contribution = 2x(configuration coefficient)^{2}x100%.

In vitro *Phototoxicity Studies*

The *in vitro* cellular studies discussed in this section were performed in collaboration with Dr. Jean-Philippe Pellois (Department of Biochemistry and Biophysics, Texas A&M University). Phototoxicities of the new dinuclear Ru(II) photocages were evaluated against HeLa cells using the resazurin assay, also known as the Alamar Blue assay. The resazurin assay is a simple, rapid and inexpensive protocol for the measurement of mammalian cell viability and is more sensitive than MTT based cell viability assays. Resazurin (7-hydroxy-3-oxo-3H-phenoxazine 10-oxide) is a non-fluorescent and non-toxic cell permeable redox indicator, which can be reduced to strongly fluorescent resorufin (λ_{em} = 585 nm) by viable cells with active metabolism in the presence of NADH

85

(reduced nicotinamide adenine dinucleotide) cofactor (Figure 2.18). The amount of resorufin formed is quantified by measuring the fluorescence intensity using a microplate spectrofluorometer. The fluorescence intensity is directly proportional to the number of living, metabolically active cells and can be correlated with % cell viability.[162] Two plates, *viz.* "Light" and "Dark" plates, were read for each of compound **1**-**3** following the protocol described in the experimental method section. Phototoxicities of the compounds were measured by the phototoxicity index (PI) value which is defined by the ratio of $(LC_{50})_{dark}$ to $(LC_{50})_{irradiated}$. An ideal photochemotherapeutic (PCT) agent is PI >> 1.
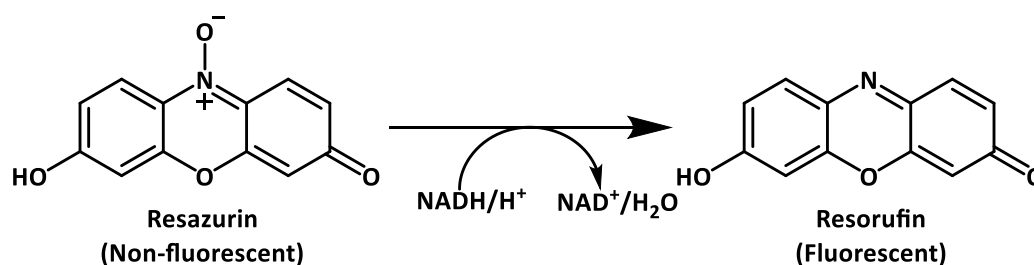
Figure 2.18. Reduction of resazurin to fluorescent resorufin by metabolically active cells.

Compounds **1**-**3** were evaluated for their phototoxicities against HeLa cells determined by LC_{50} values (concentration of compound required to kill 50% of cell population) in the dark $[(LC_{50})_{dark}]$ and under irradiated conditions $[(LC_{50})_{irradiated}]$ determined from % cell viability plots (Figure 2.19). The data are compiled in Table 2.14 along with the corresponding PI values. All three compounds exhibit $LC_{50} >> 200$ µM under both dark and irradiated conditions suggesting a PI value close to ~ 1, an indication that these Ru(II) photocages are inefficient PCT agents.

86

Table 2.14. Phototoxicity data of Compound **1**-**3** against HeLa cells.

Compound	$(LC_{50})_{dark}$[a]	$(LC_{50})_{irradiated}$[a]	PI
$[\{Ru^{II}(NCCH_3)_3\}_2(\mu\text{-tppz})](PF_6)_4$ (**1**)	$\gg 200\ \mu M$	$\gg 200\ \mu M$	~ 1
$[\{Ru^{II}(NCCH_3)_4\}_2(\mu\text{-dpq})](PF_6)_4$ (**2**)	$\gg 200\ \mu M$	$\gg 200\ \mu M$	~ 1
$[\{Ru^{II}(NCCH_3)_4\}_2(\mu\text{-dpb})](PF_6)_4$ (**3**)	$\gg 200\ \mu M$	$\gg 200\ \mu M$	~ 1

[a] Incubation time = 24 h.

Compounds **2** and **3** display weak photodissociation upon irradiation with violet light ($\lambda_{irr} \geq 435$ nm), which is reflected by their high $(LC_{50})_{irradiated}$ values. Also, there are no significant differences between their dark and irradiated toxicities. Compound **1**, which exhibits excellent photodissociation with both violet and red light ($\lambda_{irr} \geq 435$ nm and 610 nm)[128], nevertheless displays a lack of phototoxicity compared to the dark toxicity. It is possible that the low solubility of these Ru(II) photocages in buffer along with their overall high positive charge of +4 results in poor cellular uptake which would account for their high LC_{50} values both in the dark and under irradiated conditions. Similar high LC_{50} values ($LC_{50} > 750\ \mu M$) have been reported for peptide conjugated dinuclear Ru(II) polypyridine compounds bridged by the tppz ligand against human lung cancer cells despite the fact that some of them exhibit binding with oligonucleotides.[155] From these results we can conclude that spontaneous photodissociation does not necessarily lead to an effective Ru(II) photocage design.
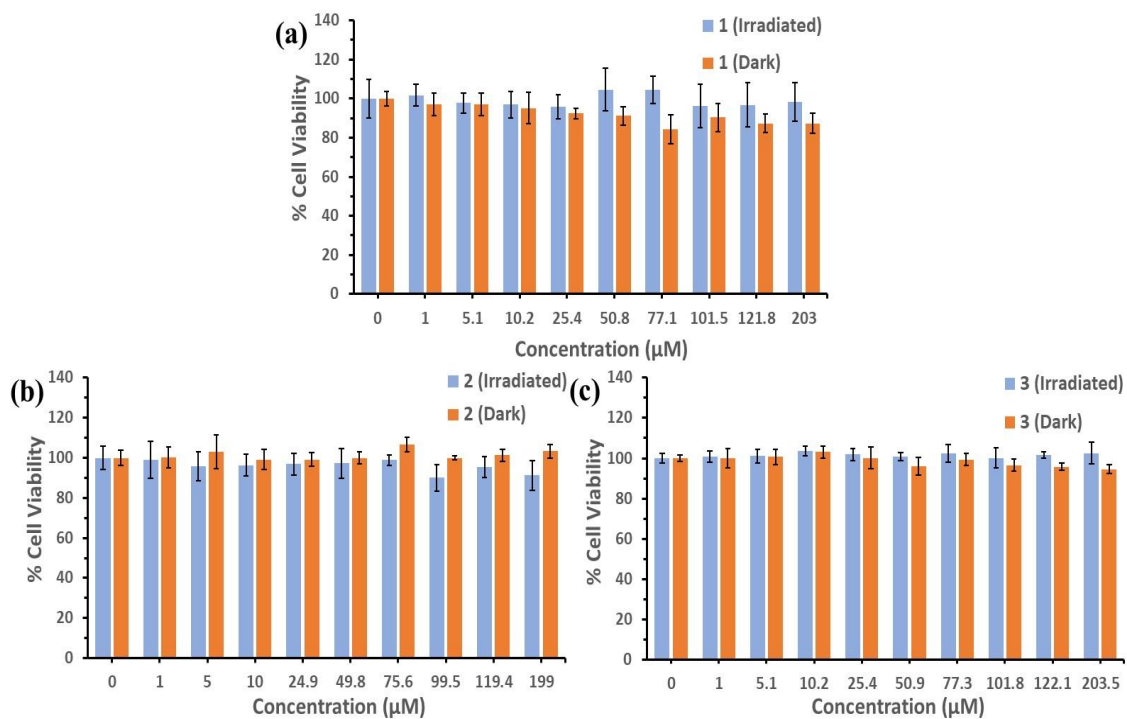
Figure 2.19. Dose-dependent % cell viability graph of (a) **1**, (b) **2** and (c) **3** in the dark and after irradiation.

Conclusions

Three new partially solvated dinuclear Ru(II) photocages were synthesized and their purity was evaluated by ^{1}H NMR spectroscopy, elemental analyses as well as single crystal X-ray crystallography for **1** and **2**. The X-ray structures of **1** and **2** exhibit significant twisting of the bridging ligands which gives rise to a distorted octahedral geometry for each Ru(II) center. The electronic absorption spectra exhibit strong [1]MLCT bands between 490-550 nm which extend into the red region ($\lambda \geq 620$ nm) of the visible spectrum. The spectral properties and assignments were verified by DFT and TDDFT calculations performed on the optimized geometries in acetonitrile. Cyclic voltammograms display two quasi-reversible metal centered oxidation events for **1** in contrast to two irreversible Ru(II) oxidations for **2** and **3**. There are multiple sequential one electron reduction events associated with the bridging ligands. The oxidation potentials are shifted to more positive potentials by ~ 0.3 V compared to analogous bimetallic Ru(II) oligopyridine compounds due to the presence of π-accepting CH_3CN ligands. Compound **1** exhibits spontaneous ligand photodissociation upon irradiation with $\lambda_{irr} \geq 435$ nm and 610 nm. Selective photocleavage of axial versus equatorial acetonitrile ligands was observed by ^{1}H NMR spectroscopy.[128] In contrast, compounds **2** and **3** exhibit only weak photodissociative properties upon photolysis with $\lambda_{irr} \geq 435$ nm. The compounds were evaluated against HeLa cells for their phototoxicities using the resazurin cell viability assay and it was found that they exhibit high LC_{50} values ($LC_{50} \gg 200$ μM) both in the dark and under irradiated conditions. Low solubility of these Ru(II) photocages

in buffer along with a high positive charge (+4) likely suppresses cellular uptake which is reflected in the high LC_{50} values. These results notwithstanding, one could modify the cage design to improve photodissociation as, for example, by installing a bulky polypyridine ancillary ligand which will impose distortion of the coordination environment. In order to improve solubility and increase the likelihood of cell penetration, addition of alkyl side chains on the ancillary ligand and coordination of anionic ligands to lower the overall positive charge are viable options. Although the new compounds do not exhibit promising phototoxic properties for use as PCT agents, the strategy of bridging two Ru(II) centers with pyrazine and quinoxaline based bridging ligands was found to be a viable design strategy for the synthesis of dinuclear Ru(II) photocage prototypes that are capable of absorbing low energy visible light. Efforts to expand on this platform to prepare derivatives with enhanced photochemical and biological properties are clearly warranted.

CHAPTER III

RUTHENIUM(II) PHOTOCAGES WITH THE BULKY 6-PHENYL-2,2′-

BIPYRIDINE LIGAND

Introduction

Photoactivated chemotherapy (PCT) is a chemotherapeutic approach wherein interaction of light with a photochemically active compound can generate toxic species *in situ* thus exhibiting efficacy.[64, 122] Unlike the well-known photodynamic therapy (PDT) approach, for which the mechanism of action relies on the production of singlet oxygen and therefore requires a supply of oxygen inside the tumor, PCT is a dual action approach that exploits oxygen-independent pathways.[64, 68] Coordination complexes of Ru(II) that absorb strongly in both the ultraviolet and visible region and which possess long-lived excited states are being vigorously investigated for PCT properties. In this approach, ruthenium caged drug/inhibitor molecules are released inside the tumor cells upon light irradiation, a strategy referred to as "photo-uncaging". Additionally, the resulting coordinatively unsaturated metal fragment is capable of binding to proteins and DNA giving rise to dual-action properties.[71-76] Another dual action approach targets Ru compounds with sterically bulky extended polypyridine ligands possessing low-lying π^* orbitals that generate singlet oxygen along and undergo ligand photodissociation triggered by light.[65-67]

Absorption of visible light by Ru(II) complexes leads to excitation from the ground state to the corresponding ^{1}MLCT state which undergoes fast intersystem crossing to populate ^{3}MLCT state. This ^{3}MLCT state can either decay via radiative or non-radiative processes to the ground state or can thermally populate the reactive ^{3}LF state possessing Ru–L(σ^*) character (L= ligand). The population of the ^{3}LF state weakens the metal ligand bond thus promoting photoinduced ligand dissociation.[77-79] The quantum yield of ligand photodissociation relies on the thermal accessibility of the ^{3}LF state from ^{3}MLCT.[81] The introduction of distortion in the metal coordination sphere can lower the energy of the dissociative ^{3}LF state making it more thermally accessible which leads to an enhancement of ligand dissociation.[75] Incorporation of sterically bulky ligands can induce distortion that leads to increased quantum yields of ligand photodissociation.[77, 82] This concept is being increasingly pursued in the design of new Ru(II) photocage architectures.[70, 84-87]

Two major architectural features are used in the design of sterically demanding mononuclear Ru(II) photocage structures. The first one involves tris-heteroleptic Ru(II) complexes of the type [Ru(NN)$_2$(LL)]$^{2+}$, where NN = diimine ligands such as bpy, phen ligand and LL = structurally bulky ligands as for example dmbpy, biq ligand. The compounds are stable in the dark and non-toxic, but, upon irradiation, the bulky ligand is selectively photocleaved to generate two photo-products either of which can be responsible for the overall toxicity of the molecules. Additionally, incorporation of biq ligand red-shifts the wavelength of absorption closer to the therapeutic window ($\lambda \geq 600$ nm).[71, 75] The other design consists of the well-studied [Ru(tpy)(N′N′)(L)]$^{2+}$ core where N′N′ = sterically bulky ligands such as dmbpy, biq ligand and L = a photocleavable nitrile/

pyridyl/ thioethereal-functionalized monodentate ligand. Incorporation of sterically bulky ligands facilitates the ligand photodissociation with substantially improved quantum yields compared to parent complexes that lack steric effects.[77, 83, 118] In this vein, Kodanko and Turro *et al.* utilized photocleavable inhibitors to selectively release inside the cell for improved efficacy.[65, 70, 77, 84, 86]

The ligand 6-phenyl-2,2′-bipyridine (pbpy) is versatile and can coordinate to Ru ions either as anionic tridentate chelate (**C^N^N**) to form cyclometallated compound or in a bidentate neutral chelate fashion (**N^N**) by utilizing the bipyridine moiety to form non-cyclometallated compounds.[163-164] Being an unsymmetrical ligand, the bidentate coordination mode can exhibit two structural isomers. In one isomer, the unbound phenyl ring is directed away from the metal center leaving the sixth coordination site sterically free, a conformation that is additionally stabilized by π-stacking interaction between the phenyl ring and the central ring of the other tridentate ligand.[163] In the case of the other isomer, the phenyl ring is directed towards the metal center making the sixth coordination site more sterically strained; this coordination motif is unexplored in the literature for the pbpy ligand. In an effort to further improve the ligand photodissociation, this sterically demanding coordination architecture was used to prepare three new Ru(II) photocages structures of general formula $[Ru(tpy)(pbpy)(L)]^{2+}$ [L= CH_3CN (**2**); Py (**3**); PySNBD (**4**)] (Figure 3.1). Pyridyl based monodentate ligands were introduced in place of acetonitrile to improve the dark stability of the photocages. As both **2** and **3** were found to lack strong emissive properties, a pyridyl functionalized fluorophore (**PySNBD**) ligand was designed and incorporated into the structure.[56, 165] All three compounds were characterized by [1]H

NMR spectroscopy, mass spectrometry, elemental analyses and single crystal X-ray crystallography. The electronic properties were investigated using electronic absorption and emission spectroscopy and the experimental observations were verified by DFT and TDDFT calculations. The compounds were evaluated for their dark stability and DNA binding properties along with DNA photocleavage abilities.
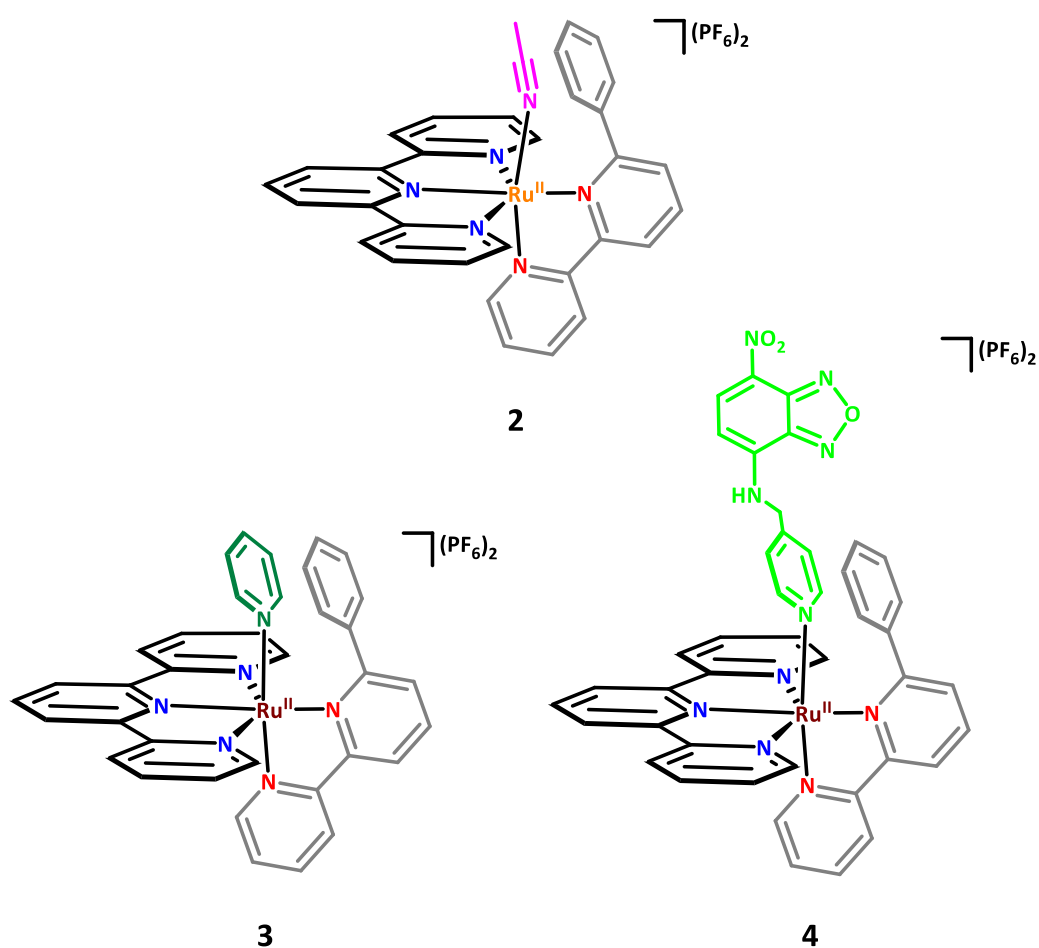
Figure 3.1 Schematic structures of Ru(II) photocages bearing the non-cyclometallated pbpy ligand.

Experimental Section

General Methods

Cyclometallation reactions were conducted using standard Schlenk techniques to maintain anaerobic conditions (N_2 atmosphere). All solvents were of reagent grade quality unless otherwise specified. Methanol, dichloromethane, diethyl ether, acetonitrile, ethyl acetate (Fisher Scientific), ethanol (KOPTEC 200 proof) and pyridine (EMD) were used as received without further purification. Triethyl amine (EMD) was distilled and stored over KOH pellets (EMD). NBD chloride (Alfa Aesar), pyridine-4-ylmethanamine (Ark Pharm.), $NaHCO_3$ (Macron Chemicals), $RuCl_3 \bullet xH_2O$ (Pressure Chemicals Co.), 2,2′:6′,2″-terpyridine (tpy, TCI and Beantown Chemicals), concentrated HCl (Macron Chemicals), and NH_4PF_6 (Sigma Aldrich) were purchased and used as received. The ligands 6-phenyl-2,2′-bipyridine (pbpy),[164] and $[Ru(tpy)Cl_3]$[166] were synthesized by literature methods.

Instrumentations

The ^1H NMR spectra were recorded on an Inova 500 MHz spectrometer. Chemical shifts are reported in δ (ppm) and coupling constants (J) in hertz (Hz). The residual solvent peak was used as an internal reference [δ =2.05 for acetone-d_6, δ =3.31 for CD_3OD, δ =2.50 for dmso-d_6]. Electrospray ionization (ESI) mass spectra were acquired on an

Applied Biosystems PE SCIEX QSTAR mass spectrometer (MDS Sciex). Elemental analyses were performed by Atlantic Microlab, Inc. (Norcross, GA). Absorption spectra were recorded in acetonitrile for **2** and in dry acetone for **3** and **4** on a Shimadzu UVPC-3001 spectrophotometer at room temperature and fluorescence spectra were recorded on a Hitachi F4600 spectrometer (Hitachi Co. Ltd., Japan) with a Xe lamp as the excitation source at room temperature.

Synthetic Details

7-nitro-N-(pyridine-4-ylmethyl)-2,1,3-benzoxadiazole (PySNBD). NBD chloride (4-chloro-7-nitrobenzofurazan) (500 mg, 2.52 mmol) and $NaHCO_3$ (632 mg, 7.52 mmol) were placed in a R.B. flask and treated with 5 mL of MeOH and stirred while pyridine-4-ylmethanamine (271 mg, 2.506 mmol) dissolved in MeOH (5 ml) was added slowly. The initial light-yellow color quickly changed to dark yellow to a brownish hue. The mixture was stirred under reduced light conditions for 14 h with occasional monitoring using TLC. The solution was filtered to remove excess $NaHCO_3$ and the solid was carefully washed with THF. The filtrate was reduced to 8 ml, water (10 ml) was added, and the solution was neutralized with NH_4Cl (aq). The product was extracted with CH_2Cl_2 (200 mL). The organic layer was washed with water and brine, dried over Na_2SO_4 and the reduced to dryness to obtain a dark brown oil. The oil was subjected to column purification (Silica, MeOH/EtOAc, gradient 0% to 5% MeOH) and second bright yellow band was collected. Upon reduction, **PySNBD** was obtained as a reddish brown crystalline solid. Yield: 115

96

mg (17%) ^{1}H NMR (500 MHz, dmso-d$_6$): δ 9.91 (s, 1H), 8.53 (dd, J = 4.5, 1.5 Hz, 2H), 8.48 (d, J = 8.9 Hz, 1H), 7.39 (d, J = 5.9 Hz, 2H), 6.29 (d, J = 4.6 Hz, 1H), 4.78 (s, 2H). ESI-MS(–): Calcd. for [C$_{12}$H$_9$N$_5$O$_3$] ([M–H]$^-$) 270.06. Found: 269.89. Anal. Calcd. for C$_{12}$H$_9$N$_5$O$_3$.0.5(C$_3$H$_6$O): C, 54.00; H, 4.03; N, 23.32. Found: C, 55.31; H, 3.99; N, 23.58. Dark yellow crystalline needles suitable for X-ray diffraction were obtained from the slow evaporation of a solution of **PySNBD** in MeOH.

[Ru(tpy)(pbpy)](Cl) (1). This compound was synthesized in higher yields by modifying a previously reported method.[163] [Ru(tpy)Cl$_3$] (257 mg, 0.583 mmol) and pbpy (136 mg, 0.583 mmol) were added to a Schlenk flask and treated with 32 mL of an EtOH:H$_2$O (3:1) mixture. Excess Et$_3$N (1 mL) was added to the mixture under N$_2$ which was refluxed for 15 h during which time the initial dark brown color slowly changed to dark purple. After cooling to room temperature, the solution was filtered through Celite® to remove unreacted [Ru(tpy)Cl$_3$] and the filtrate was reduced to dryness. The residue was purified by flash column chromatography (Silica, MeOH/CH$_2$Cl$_2$, gradient 0% to 10% MeOH) and the dark purple band that was collected was reduced to ca. 10 mL. Upon addition of a hexanes/diethyl ether mixture, a microcrystalline dark purple (almost black) solid was observed to form and the flask was stored in the refrigerator at 0°C for 1 h. The solid was collected by filtration, washed with hexanes and diethyl ether and vacuum dried. Yield: 222 mg (63%). ^{1}H NMR (500 MHz, CD$_3$OD): δ 8.73 (d, J = 8.1 Hz, 2H), 8.57 (d, J = 8.2 Hz, 1H), 8.54 – 8.50 (m, 3H), 8.29 (d, J = 8.0 Hz, 1H), 8.12 – 8.06 (m, 2H), 7.88 (td, J = 8.1, 1.5 Hz, 1H), 7.82 (d, J = 7.1 Hz, 1H), 7.76 (td, J = 8.3, 1.4 Hz, 2H), 7.45 (d, J = 5.2 Hz, 1H), 7.42 (d, J = 5.6 Hz, 2H), 7.12 – 7.06 (m, 3H), 6.73 – 6.69 (m, 1H), 6.47 (td, J =

7.4, 1.1 Hz, 1H), 5.67 (d, J = 7.4 Hz, 1H). ESI-MS(+): Calcd. for $[C_{31}H_{22}N_5Ru]^+$ ([M –

Cl]$^+$) 566.09. Found: 566.05.

[Ru(tpy)(pbpy)(CH₃CN)](PF₆)₂ (2). [Ru(tpy)(pbpy)](Cl) **(1)** (40 mg, 0.067 mmol) was

placed in a Schlenk flask followed by the addition of 10 mL of an EtOH:H₂O (1:1) mixture

and excess MeCN (2 mL). A quantitative volume of concentrated HCl (6 µL) was added

and the reaction mixture was refluxed under N₂ under reduced light conditions for 6 h.

The initial dark purple color of **1** changed to dark bright orange during the reaction. After

6 h, the solution was cooled to RT, filtered to remove any particles and the filtrate was

reduced to 5 mL. Upon addition of 5 mL of aqueous NH₄PF₆ solution, the formation of

bright orange solid was observed and the flask was placed in the refrigerator for 1 hour.

The solution was filtered, washed thoroughly with chilled water and diethyl ether (3x10

mL) and vacuum dried before isolation. Yield: 49 mg (83%). ^{1}H NMR (500 MHz, acetone-

d₆) δ 8.93 (dd, J = 8.1, 1.2 Hz, 1H), 8.76 (d, J = 8.1 Hz, 2H), 8.69 (d, J = 8.1 Hz, 1H), 8.66

(d, J = 8.0 Hz, 2H), 8.50 (t, J = 8.0 Hz, 1H), 8.39 (t, J = 8.1 Hz, 1H), 8.32 (d, J = 4.9 Hz,

2H), 8.17 (td, J = 7.9, 1.5 Hz, 2H), 8.01– 7.96 (m, 2H), 7.90 – 7.85 (m, 2H), 7.64 (d, J =

5.2 Hz, 1H), 7.63 – 7.59 (m, 2H), 7.54 – 7.49 (m, 3H), 7.25 (ddd, J = 7.3, 5.8, 1.2 Hz, 1H),

1.62 (s, 3H). ESI-MS(+): Calcd. for $[C_{31}H_{23}N_5Ru]^{2+}$ ([{M}–(CH₃CN)–2(PF₆)$^-$]$^{2+}$)

283.5493. Found: 283.5489; Calcd. for $[C_{33}H_{26}N_6Ru]^{2+}$ ([{M}–2(PF₆)$^-$]$^{2+}$) 304.0626.

Found: 304.0622; Calcd. for $[C_{33}H_{26}F_6N_6PRu]^+$ ([{M}–(PF₆)$^-$]$^+$) 753.0899. Found:

753.0890. Anal. Calcd. for C₃₃H₂₆F₁₂N₆P₂Ru.H₂O: C, 43.29; H, 3.08; N, 9.18. Found: C,

42.60; H, 3.03; N, 9.06. Dark reddish-orange crystalline needles suitable for X-ray

diffraction were obtained by slow diffusion of diethyl ether into a dilute solution of **2** in (MeCN/toluene).

[Ru(tpy)(pbpy)(Py)](PF₆)₂ (3). A sample of **2** (40 mg, 0.045 mmol) was dissolved in acetone (10 mL) in a Schlenk flask followed by the addition of 2 mL of pyridine. The reaction mixture was stirred at RT for 5 h. The initial dark bright orange color of **2** gradually changed to dark reddish-brown during the reaction. After 5h, the solution was reduced to 2 mL and addition of diethyl ether yielded a microcrystalline dark brown solid which was stored in the refrigerator overnight. The solid was filtered, washed with diethyl ether (3x10 mL) and vacuum dried before isolation. Yield: 42 mg (83%). ^{1}H NMR (500 MHz, acetone-d$_6$) δ 8.98 (dd, J = 8.1, 1.2 Hz, 1H), 8.72 (d, J = 8.2 Hz, 1H), 8.68 – 8.64 (m, 4H), 8.53 – 8.49 (m, 3H), 8.24 – 8.17 (m, 3H), 8.00 – 7.95 (m, 2H), 7.73 – 7.69 (m, 2H), 7.69 – 7.65 (m, 2H), 7.58 (d, J = 5.7 Hz, 1H), 7.39 (tt, J = 7.6, 1.4 Hz, 1H), 7.25 (dd, J = 6.5, 1.3 Hz, 2H), 7.21 (ddd, J = 7.3, 5.8, 1.2 Hz, 1H), 6.97 – 6.91 (m, 3H), 6.72 (dd, J = 7.5, 6.7 Hz, 2H). ESI-MS(+): Calcd. for $[C_{31}H_{23}N_5Ru]^{2+}$ ($[\{M\}-(Py)-2(PF_6)^-]^{2+}$) 283.5493. Found: 283.5489; Calcd. for $[C_{36}H_{28}N_6Ru]^{2+}$ ($[\{M\}-2(PF_6)^-]^{2+}$) 323.0704. Found: 323.0702; Calcd. for $[C_{36}H_{28}F_6N_6PRu]^+$ ($[\{M\}-(PF_6)^-]^+$) 791.1055. Found: 791.1048. Anal. Calcd. for $C_{36}H_{28}F_{12}N_6P_2Ru.0.5(C_5H_5N)$: C, 47.42; H, 3.15; N, 9.34. Found: C, 47.37; H, 3.19; N, 9.32. Dark orange crystalline platelets suitable for X-ray diffraction were obtained by slow diffusion of diethyl ether into a dilute solution of **3** in (acetone/toluene).

[Ru(tpy)(pbpy)(PySNBD)](PF₆)₂ (4). A sample of **2** (76 mg, 0.085 mmol) was dissolved in acetone (12 mL) in a Schlenk flask followed by the addition of **PySNBD** (23 mg, 0.085

mmol). The reaction mixture was stirred at RT for 5h. The initial dark bright orange color gradually changed to dark brown during the reaction. After all of the **PySNBD** ligand had dissolved after 5 h, the solution was filtered to remove y particles and the filtrate was reduced to 2 mL. Addition of diethyl ether yielded an oily material which was dissolved in acetone and once again precipitated with diethyl ether. The dark brown microcrystalline solid that formed was stored in the freezer for 1 hour. The solid was filtered, washed with diethyl ether (3x10 mL) and vacuum dried before isolation. Yield: 82 mg (86%). ^{1}H NMR (500 MHz, acetone-d_6) δ 8.97 (dd, J = 8.1, 1.2 Hz, 1H), 8.71 (d, J = 8.2 Hz, 1H), 8.67–8.63 (m, 4H), 8.53 – 8.47 (m, 4H), 8.23 – 8.17 (m, 3H), 7.99 – 7.93 (m, 2H), 7.72 – 7.67 (m, 2H), 7.66 – 7.62 (m, 2H), 7.57 (d, J = 5.1 Hz, 1H), 7.23 – 7.18 (m, 3H), 7.05 (t, J = 7.4 Hz, 1H), 6.95 (t, J = 7.7 Hz, 2H), 6.81 (d, J = 6.6 Hz, 2H), 6.27 (d, J = 8.4 Hz, 1H), 4.74 (s, 2H). ESI-MS(+): Calcd. for $[C_{31}H_{23}N_5Ru]^{2+}$ ($[\{M\}-(PySNBD)-2(PF_6)^-]^{2+}$) 283.5493. Found: 283.5489; Calcd. for $[C_{43}H_{32}N_{10}O_3Ru]^{2+}$ ($[\{M\}-2(PF_6)^-]^{2+}$) 419.0846. Found: 419.0841; Calcd. for $[C_{43}H_{32}F_6N_{10}O_3PRu]^+$ ($[\{M\}-(PF_6)^-]^+$) 983.1339. Found: 983.1334. Anal. Calcd. for $C_{43}H_{32}F_{12}N_{10}O_3P_2Ru$: C, 45.79; H, 2.86; N, 12.42. Found: C, 45.51; H, 3.06; N, 12.18. Dark orange crystalline platelets suitable for X-ray diffraction were obtained by slow diffusion of diethyl ether into a dilute solution of **4** in (acetone/toluene).

X-Ray Crystallography

Single crystals of **PySNBD** and compounds (**2–4**) were obtained as described in the experimental section. X-ray data of **PySNBD** were collected at 102.9 K on a Bruker D8-QUEST diffractometer equipped with a IμS Mo micro source ($\lambda = 0.71073$ Å) and the data for compound **3** were collected at 100.01 K on a Bruker D8 Venture (Cu Kα Iμs microfocus) ($\lambda = 1.54178$ Å) instrument equipped with a CMOS detector. Single crystals of compound **2** and **4** were diffracted at 110 K on a Bruker APEX II CCD X-ray diffractometer (Bruker-AXS, 2014) equipped with a graphite monochromated MoK$_\alpha$ radiation source ($\lambda = 0.71073$ Å). The data sets were integrated with the Bruker SAINT software package (SAINT v8.34A, Bruker, 2013).[136] The absorption correction was applied based on fitting a function to the empirical transmission surface as sampled by multiple equivalent measurements using SADABS-2012/1 (Bruker, 2012)[137] for **2** and **4** and using TWINABS-2012/1 (Bruker, 2012)[167] for **3**. Solution and refinements of the crystal structures were carried out using the ShelX (2018/3) suite of programs [138-139] and the graphical interface OLEX 2.[140] All non-hydrogen atoms were refined with anisotropic displacement parameters using full-matrix least-squares techniques on F^2. Hydrogen atoms were fixed to parent atoms and refined using the riding model. Crystals of **3** were found to be non-merohedral twins. The crystal chosen for the structural study was refined as a two-domain twin with the twin fractions refining to 75.4% and 24.6%. Idealized geometries were used to model disordered (PF$_6$)$^-$ anions and acetonitrile solvent in **2**,

disordered $(PF_6)^-$ anions, acetone and diethyl ether solvent in **3**, and disordered acetone and diethyl ether solvent in **4**.[141]

Structural Optimization and TDDFT Calculation

The crystal structures of **PySNBD** and (**2**–**4**) were used as initial coordinates for the structural optimization of the compounds in the gas phase with the Gaussian 09 program package[143] using the Becke's three -parameter exchange correlation functional and the Lee Yang and Parr correlation functional (B3LYP).[144,145] The Stuttgart RSC 1997 ECP basis set[146] was used for the Ru atom and the 6-311G* basis set[147-148] was used for C, N and H atoms. The solvent phase geometry optimizations were performed by using SCRF calculations with SMD model (Truhlar's model)[149] in acetonitrile to incorporate solvent polarization effects with subsequent frequency analysis. The MOs were plotted with GaussView 6[168] with an isovalue of 0.04. Fragment contributions to the MOs were calculated using the Chemissian v4.60 software (www.chemissian.com). TDDFT calculations were performed on the solvent optimized structures to compute electronic transitions from singlet ground states to singlet excited states using the SMD model with acetonitrile as the solvent.

Dark Stability Study

All three complexes were evaluated for their stability in the dark in presence of coordinating CD_3CN using ^{1}H NMR spectroscopy on an Inova 500 MHz spectrometer. The residual solvent peak at δ = 1.94 ppm was used as an internal reference. ^{1}H NMR spectra were obtained at variable times for comparison.

DNA Binding Evaluation and DNA Photocleavage Study

DNA binding assays were performed on **2**-**4** with linearized pUC18 plasmid DNA (Thermo Fisher) in the dark using the gel electrophoresis technique. A stock solution of pUC18 plasmid DNA with a final concentration of 30 ng/µL was made in Tris buffer containing (10 mM TrisCl + 1mM EDTA) at pH = 7.5. The compounds were dissolved in MiliQ water (with 2% DMSO) to make the stock solutions for each and then diluted further to achieve the desired working concentrations. The samples of the compounds were prepared in PCR tubes by mixing equal volumes of DNA stock with the desired working concentrations of the compounds (final concentrations of compounds: 2–400 µM range, with equal or less than 1% DMSO). For the control sample, equal volume of DNA stock was mixed with MiliQ water. 1% DMSO, 400 µM pyridine and 400 µM **PySNBD** solutions were prepared similarly as the control sample and served as additional control samples during the evaluation of **2**, **3** and **4** respectively. All samples were incubated in the dark at 37°C for 24 h. After the incubation period, each sample was loaded on the

ethidium bromide (Bio-Rad)-stained agarose gel (Apex Bioresearch Product) with the help of the gel loading dye (Biolabs Inc.). A 1kB DNA ladder (Biolabs Inc.) was loaded on lane 1 followed by two control samples on lane 2 and 3. The compound samples were loaded from the lowest to the highest concentrations on lanes 4-10. After the electrophoresis experiment, the gel was imaged using a Fotodyne™ FOTO/Analyst™ Investigator Eclipse UV Workstation instrument fitted with 2.0 mega pixel camera. Two experiments were conducted on different days with each compound.

DNA photocleavage experiments were performed only on **3** after observing a lack of DNA damage for the other compounds even with 400 µM solutions. For running one gel electrophoresis assay, two sets of samples of **3** with final concentrations of 5 µM, 50 µM, 200 µM were prepared along with two control samples (one without compound and the other with 200 µM of pyridine) as mentioned above. One set of samples of **3** (5 µM, 50 µM, 200 µM) was irradiated with broad visible light ($\lambda_{irr} \geq 395$ nm) using a 300 W Xe arc lamp source (Newport) for 1 h at RT whereas the remaining samples were kept in the dark at RT. Finally, all samples were incubated in the dark at 37°C. Three gel electrophoresis assays were performed similarly as above after t = 0 h (immediately after irradiation), 12 h, and 24 h of incubation. After each electrophoresis experiment, the gel was imaged using a Fotodyne™ FOTO/Analyst™ Investigator Eclipse UV Workstation instrument fitted with 2.0 mega pixel camera. Two experiments were conducted on different days with compound **3**.

Synthesis and Characterization

pbpy ligand can coordinate either as an anionic tridentate chelate (**C^N^N**) to form a cyclometallated compound or as a bidentate neutral chelate (**N^N**) through the bipyridine moiety to form a non-cyclometallated compound.[163-164] The coordination mode of the pbpy ligand is highly solvent dependent. The use of high dielectric solvents such as aqueous MeOH/EtOH or DMF favors the cyclometallation whereas less polar solvents such as n-butanol or acetic acid facilitate the bidentate coordination mode where the unbound phenyl ring is directed away from the metal center.[163] But to facilitate the formation of the other sterically strained isomer where the phenyl ring is directed towards the metal center, reverse cyclometallation reaction is utilized.

To synthesize nitrile-bound photocage **2**, the well-known cyclometallated compound [Ru(tpy)(pbpy)](Cl) (**1**) was used for which the coordinated phenyl ring possesses the desired orientation. The anionic carbon in **1** was protonated with HCl in presence of excess CH_3CN in a refluxing H_2O:EtOH (1:1) mixture. The successive protonation followed by immediate coordination of MeCN preserves the desired stereochemistry of the protonated pbpy ligand with the unbound phenyl ring directed towards the Ru center. The reaction involves a distinct color change from dark purple to dark bright orange. Compound **2** was precipitated with aqueous NH_4PF_6 and isolated as a bright orange powder in 83% yield (Figure 3.2). The photocage architecture of **2** was

further employed to synthesize **3** and **4** by substituting coordinated MeCN with pyridine (Py) and a pyridyl-functionalized fluorophore molecule **PySNBD** respectively. The pyridyl moiety is a good σ-donor and, most importantly, a better π-acceptor than MeCN which favors the substitution reaction even at RT.[77] A sample of **2** was stirred in acetone at RT with excess pyridine to prepare **3**, which was later isolated as a dark brown microcrystalline solid in an 83% yield. Similarly, **4** was synthesized by stirring an acetone solution of **2** with a stoichiometric amount of **PySNBD** at RT and was isolated as a dark brown microcrystalline solid in an 86% yield (Figure 3.2).
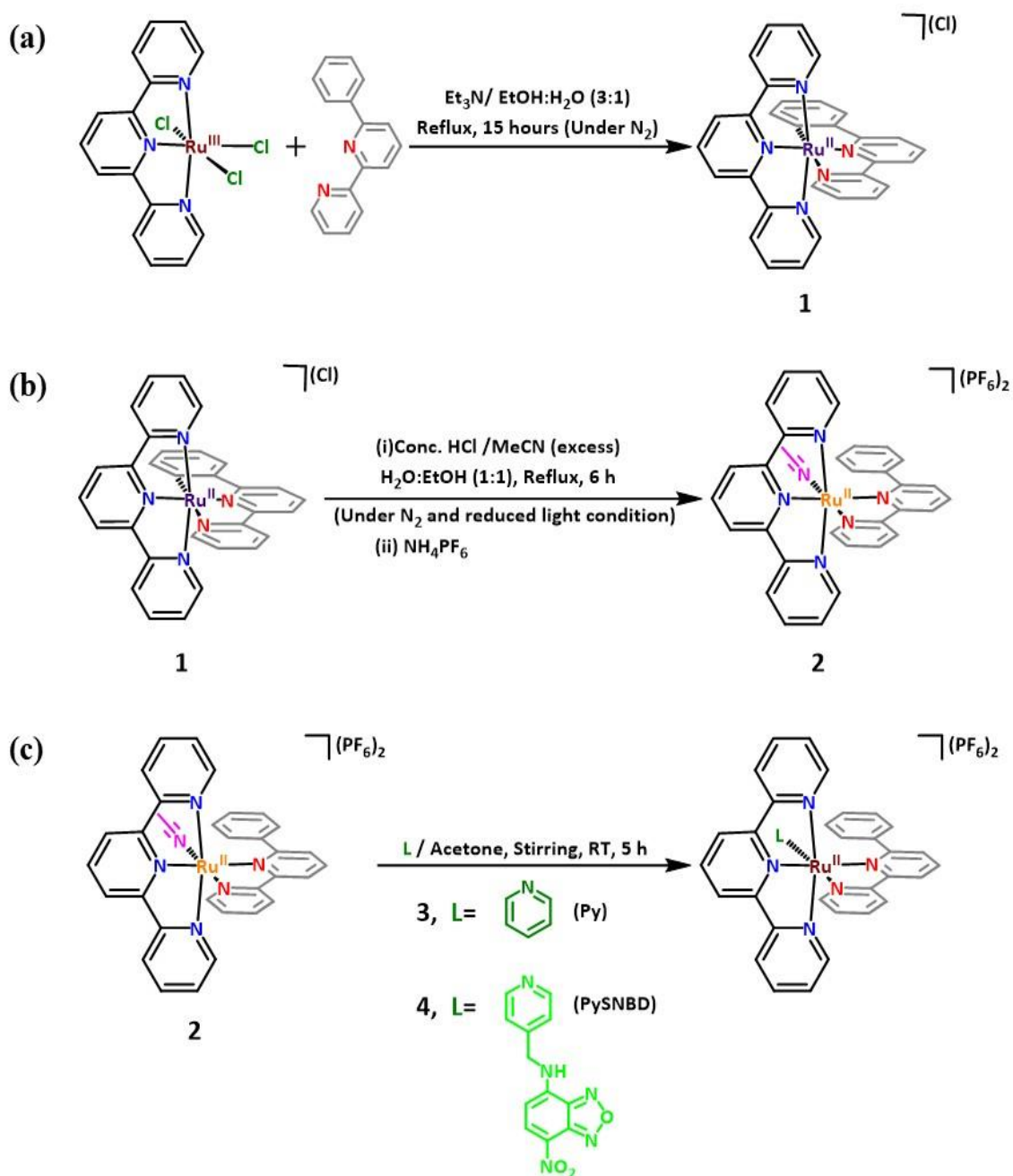
Figure 3.2. Reaction schemes for the synthesis of (a) cyclometallated Ru(II) starting material **1**, (b) nitrile-functionalized Ru(II) photocage **2**, and (c) pyridyl-functionalized Ru(II) photocages **3** and **4**.

The purity of the compounds was confirmed by ^{1}H NMR spectroscopy, ESI mass spectrometry and elemental analyses. The NMR spectra are consistent with C_{2v} molecular symmetry for all three compounds, with a plane of symmetry lying on the plane of the bpy moiety of the pbpy ligand (Figure 3.1). As a result, one-half of the protons on the tpy ligand and the unbound phenyl rings are magnetically equivalent. Importantly, the reverse cyclometallation reaction has a dramatic influence on the resonance of the protons of the [Ru(tpy)(pbpy)] framework. For example, the aryl protons on the unbound phenyl rings of **2**–**4** (Figure 3.5-3.7) are shifted downfield compared to the coordinated phenyl ring protons in **1** (Figure 3.4). Also, the singlet peak of coordinated MeCN in **2** appears at $\delta = 1.62$ ppm which is shifted upfield compared to the literature values between 2-3 ppm.[78, 99, 128] This observation can be explained by the aromatic ring current effect of the unbound phenyl ring which is positioned on top of the coordinated MeCN as evidenced from the crystal structure (Figure 3.11). The NMR spectra also confirm that all four complexes contain a diamagnetic Ru(II) center. The integration values of the peaks match the total proton count (**2**, 26H; **3**, 28H; **4**, 32H) for all compounds, indicating the formation of the desired molecules (Figure 3.5-3.7). In the ESI mass spectra, each molecule exhibits three distinct peaks corresponding to ([{M}–(X)–2(PF$_6$)$^-$]$^{2+}$) [X = CH$_3$CN (**1**); Py (**2**); PySNBD (**3**)], ([{M}–2(PF$_6$)$^-$]$^{2+}$) and ([{M}–(PF$_6$)$^-$]$^+$) species. For all three complexes the ([{M}–(X)–2(PF$_6$)$^-$]$^{2+}$) peak appears at m/z=283.5489 (Figure 3.8-3.10).
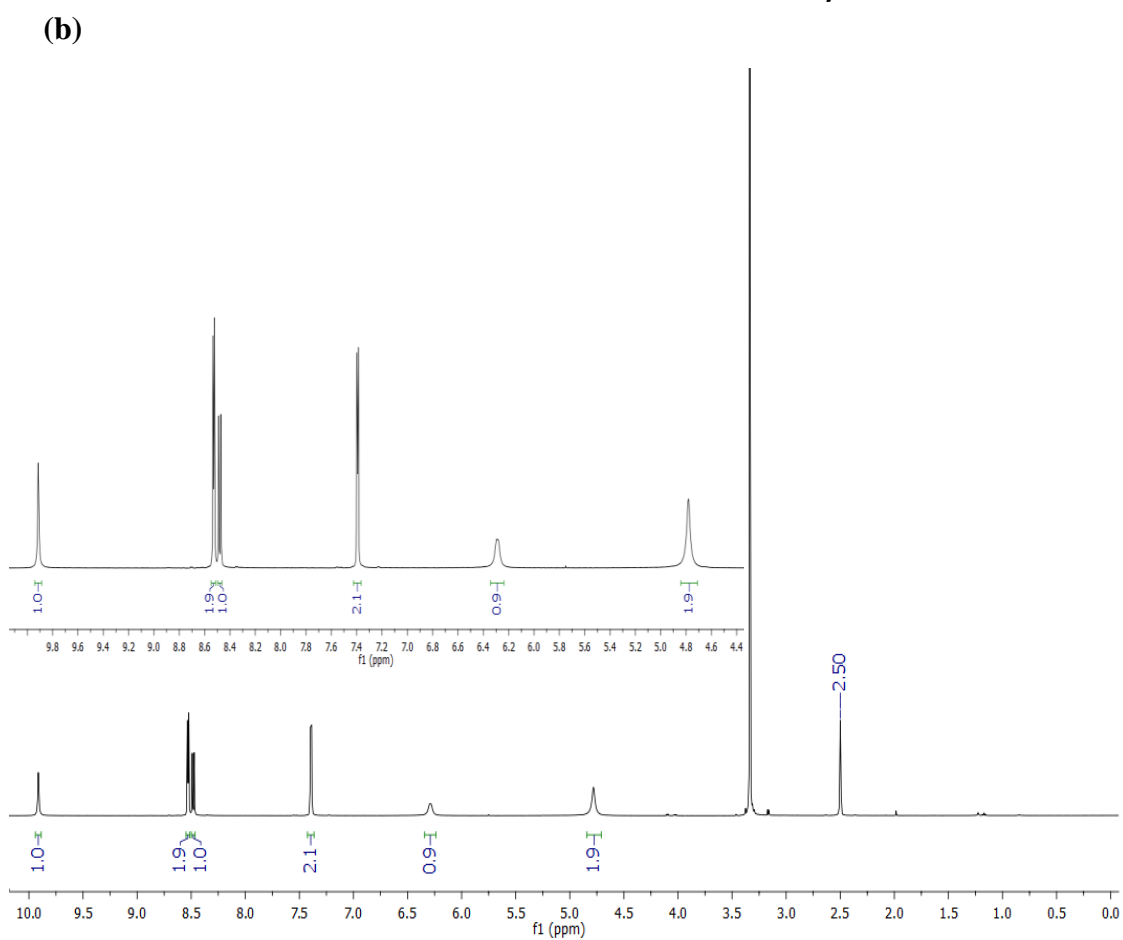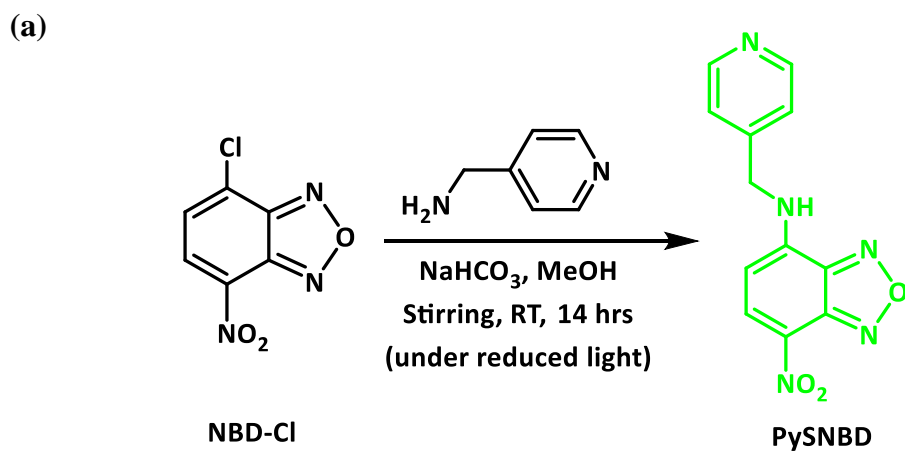
Figure 3.3. (a) Synthetic Scheme and (b) ^{1}H NMR spectra (dmso-d$_6$, 500 MHz) [Inset: enlarged aromatic region] of the **PySNBD** ligand.
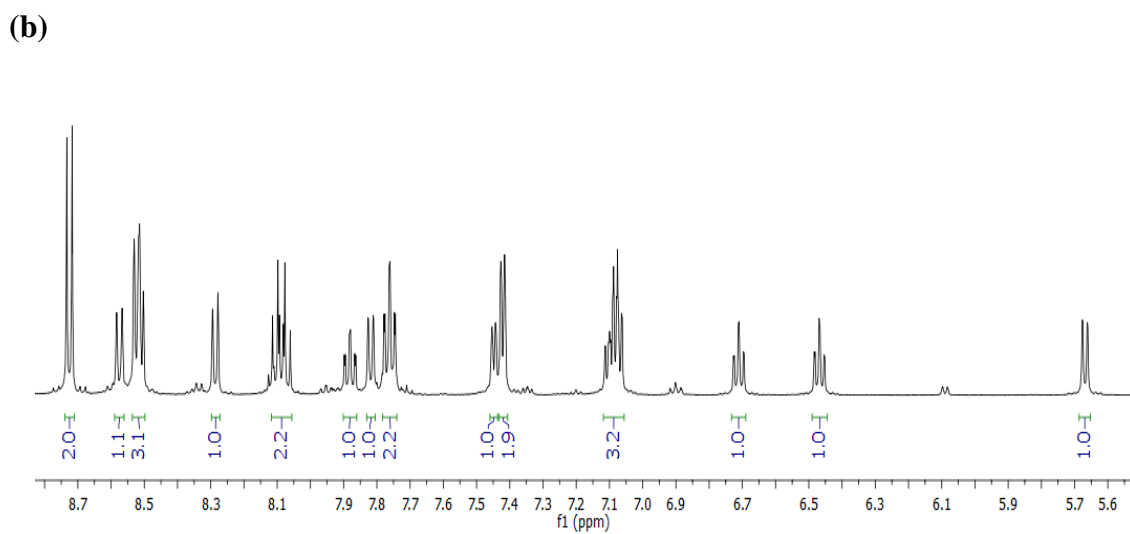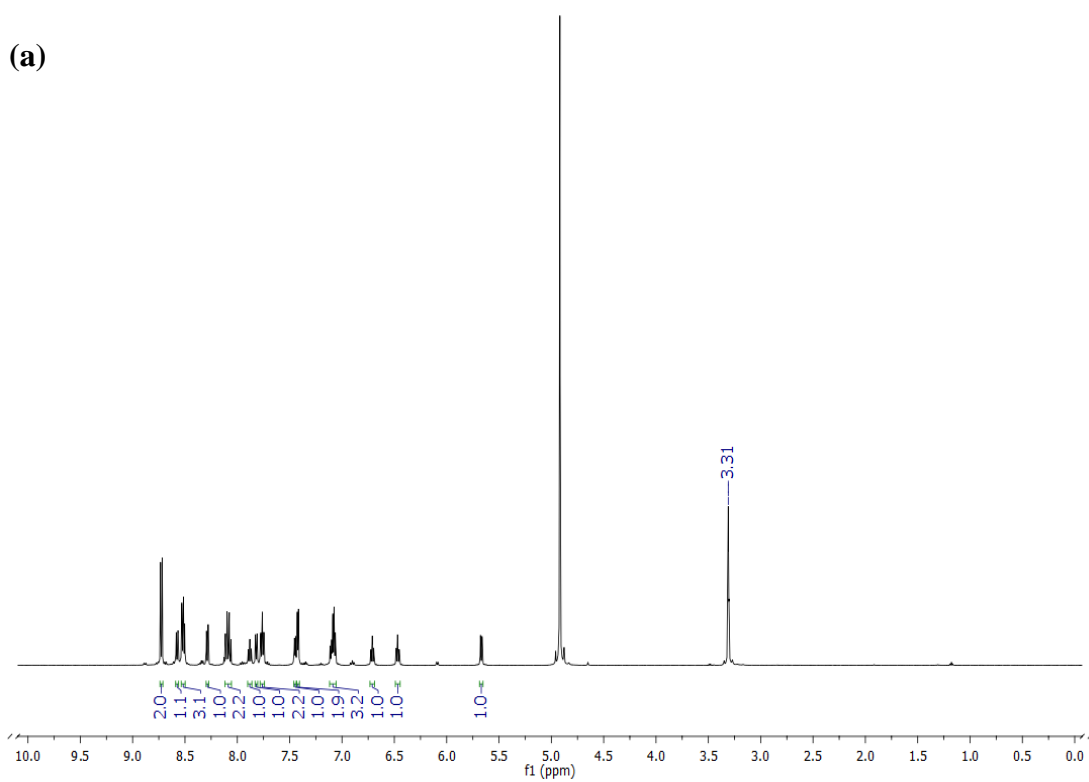
Figure 3.4. ^{1}H NMR spectra (CD$_3$OD, 500 MHz) of compound **1** (a) full spectrum, (b) enlarged aromatic region.

(a)
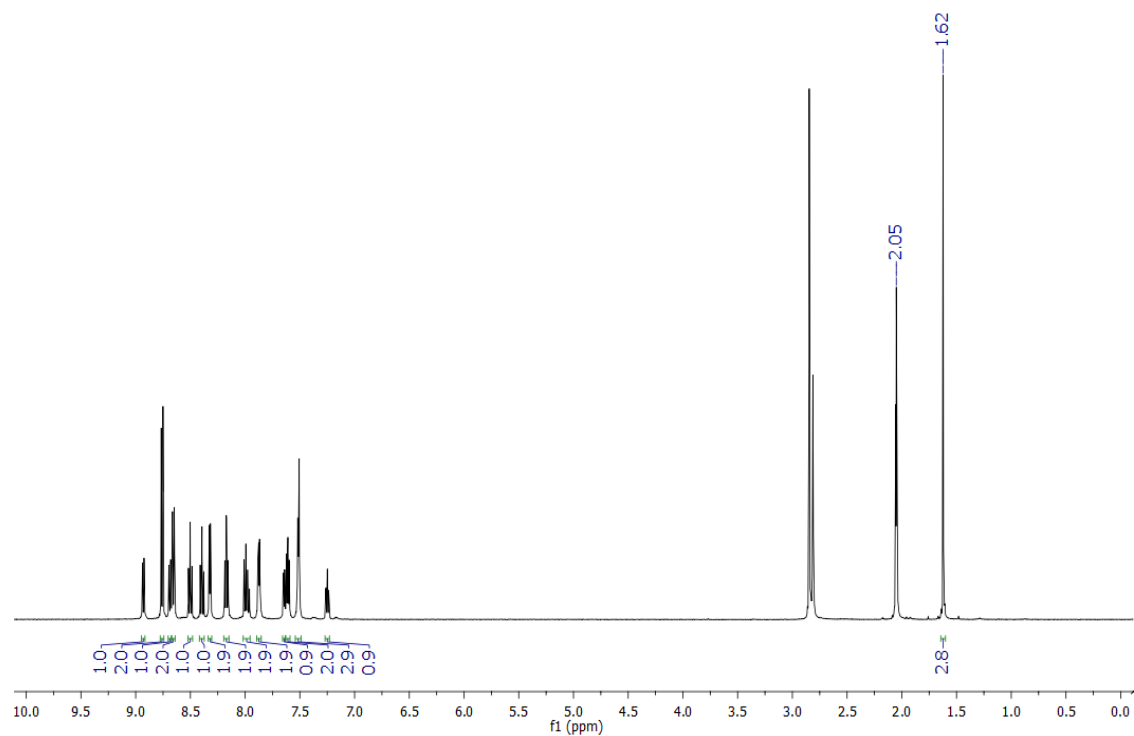
(b)
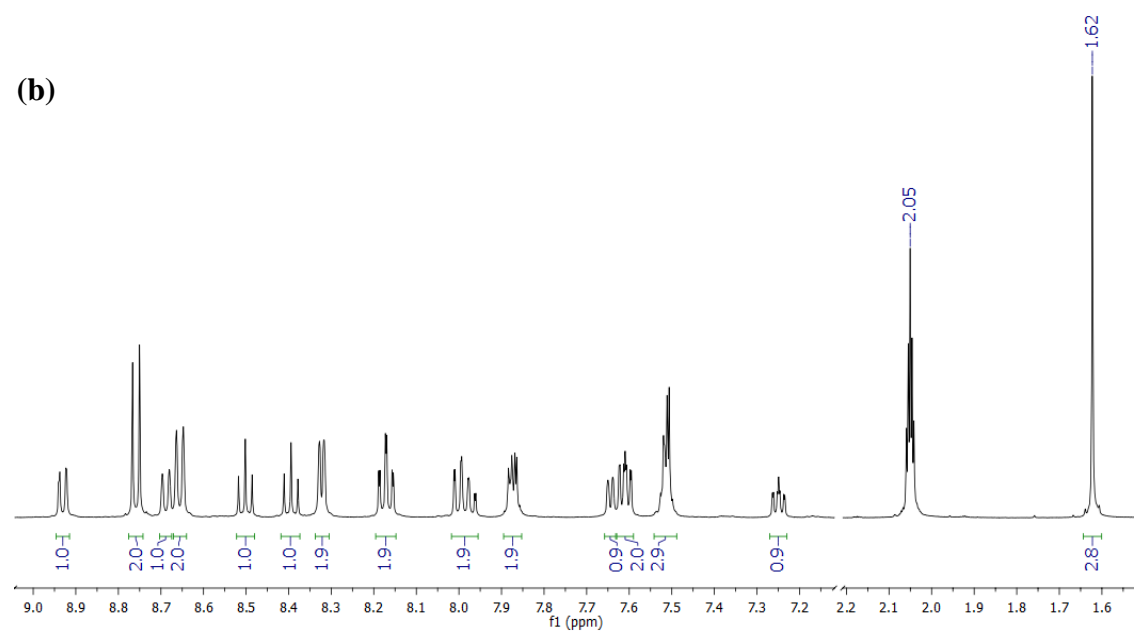
Figure 3.5. ^{1}H NMR spectra (acetone-d$_6$, 500 MHz) of compound **2** (a) full spectrum, (b) enlarged aromatic and aliphatic region.

(a)

(b)
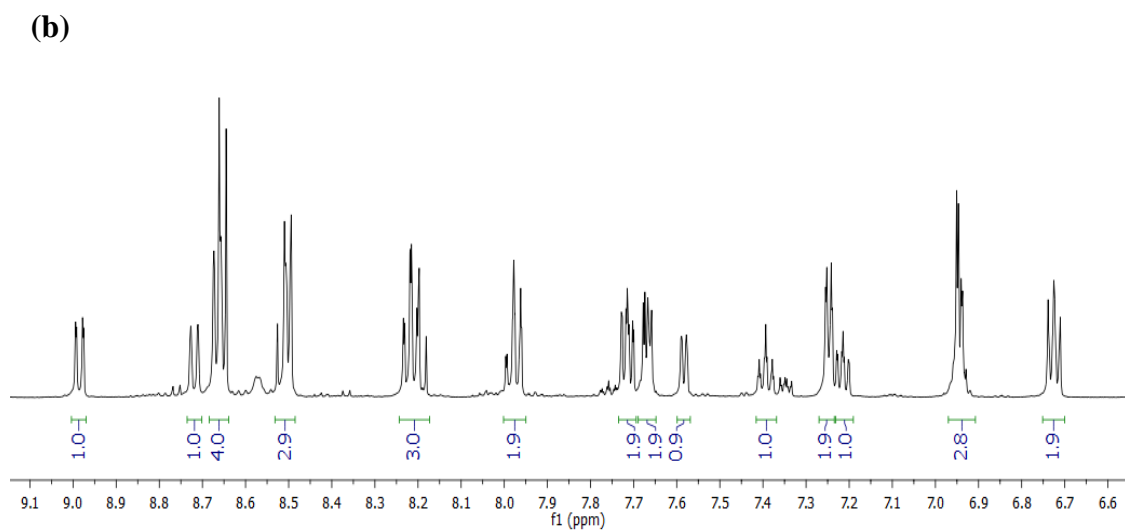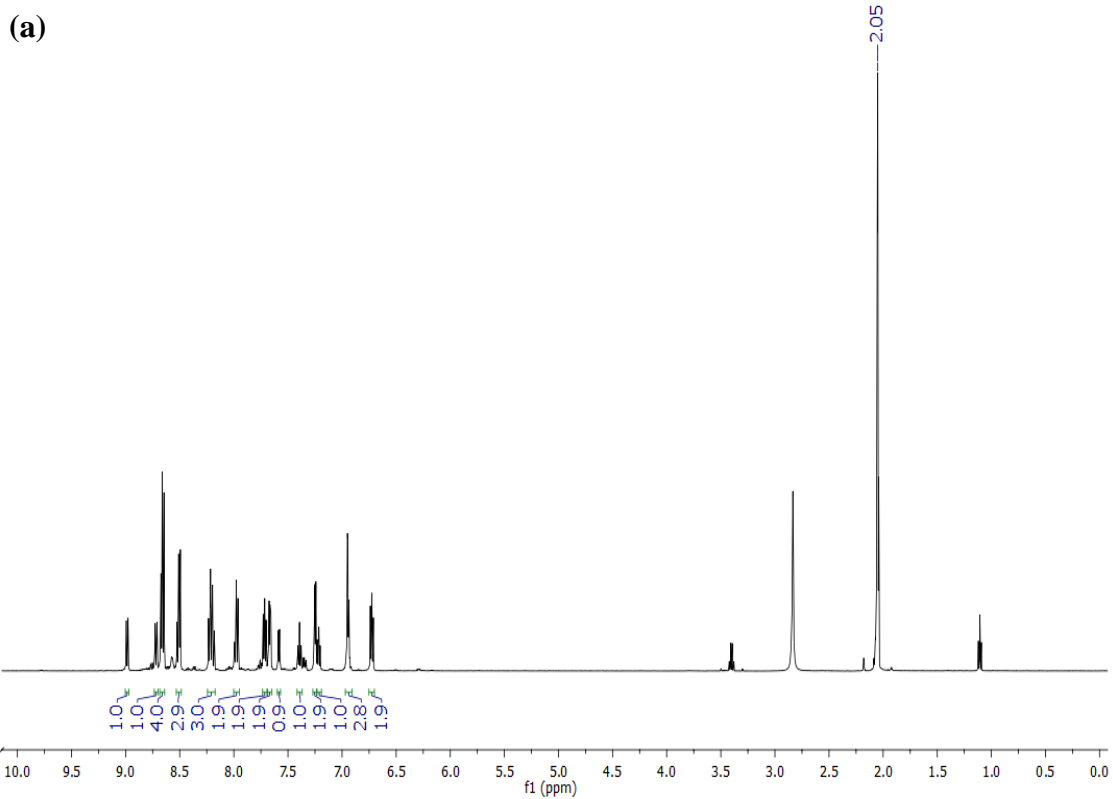
Figure 3.6. ^{1}H NMR spectra (acetone-d$_6$, 500 MHz) of compound **3** (a) full spectrum, (b) enlarged aromatic region.

112

(a)

(b)
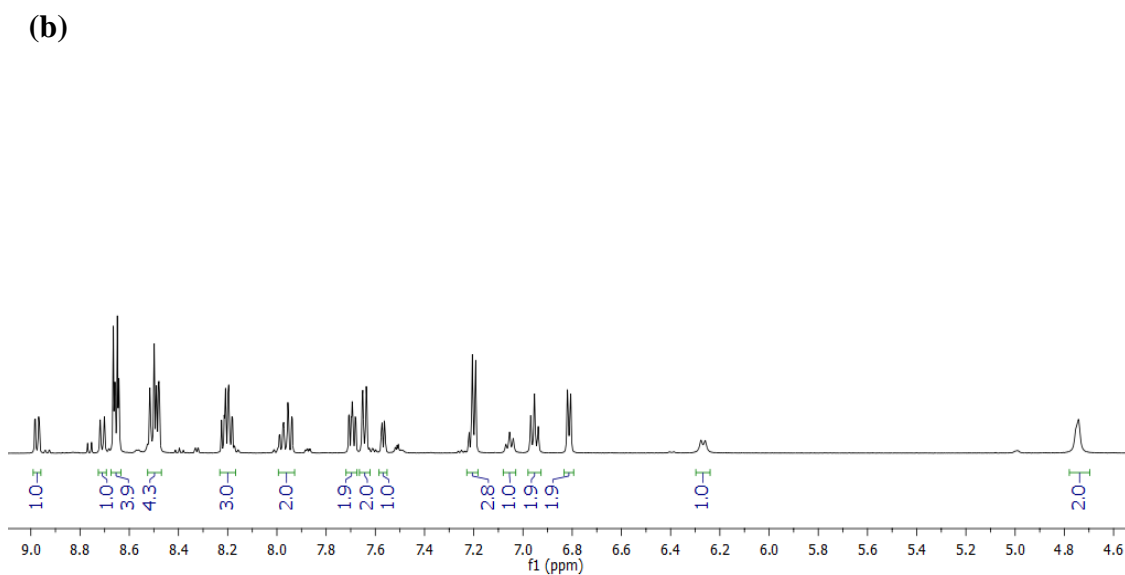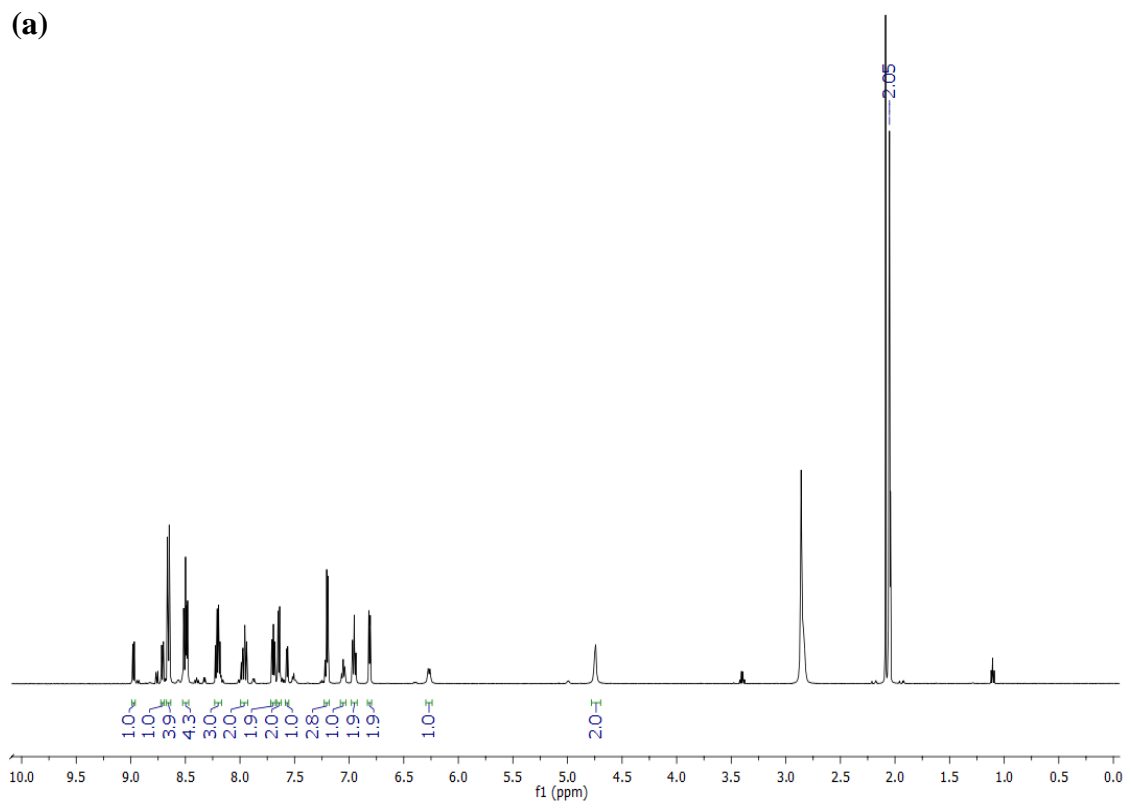
Figure 3.7. ^{1}H NMR spectra (acetone-d_6, 500 MHz) of compound **4** (a) full spectrum, (b) enlarged aromatic region.
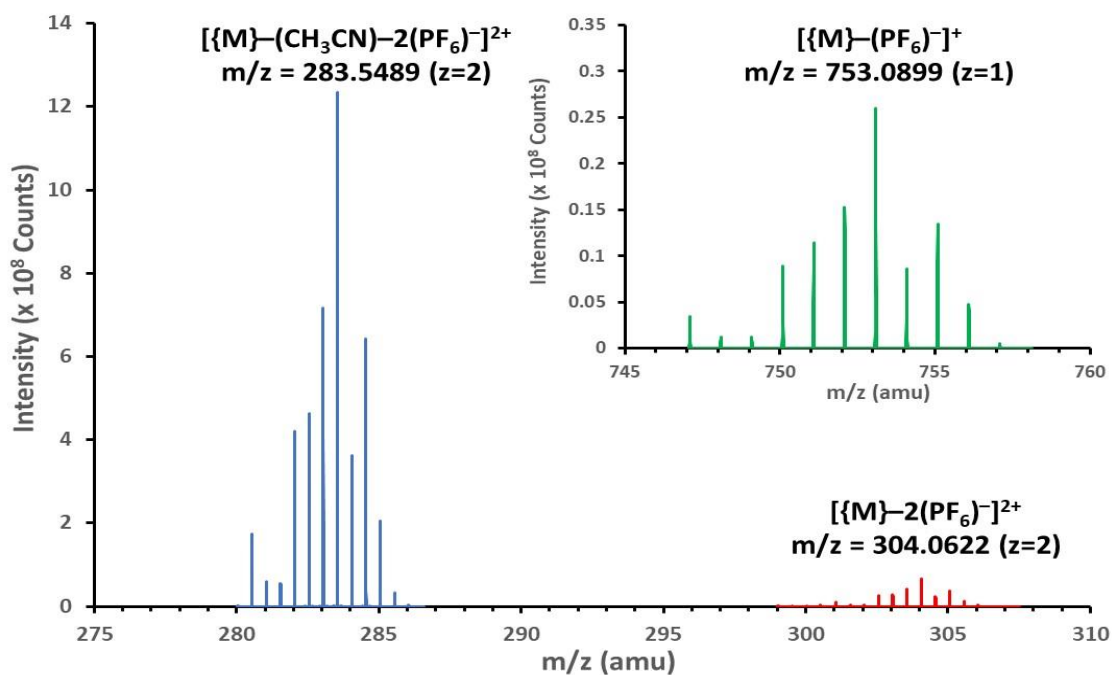
Figure 3.8. (+) ESI-MS of [Ru(tpy)(pbpy)(CH$_3$CN)](PF$_6$)$_2$ (**2**).
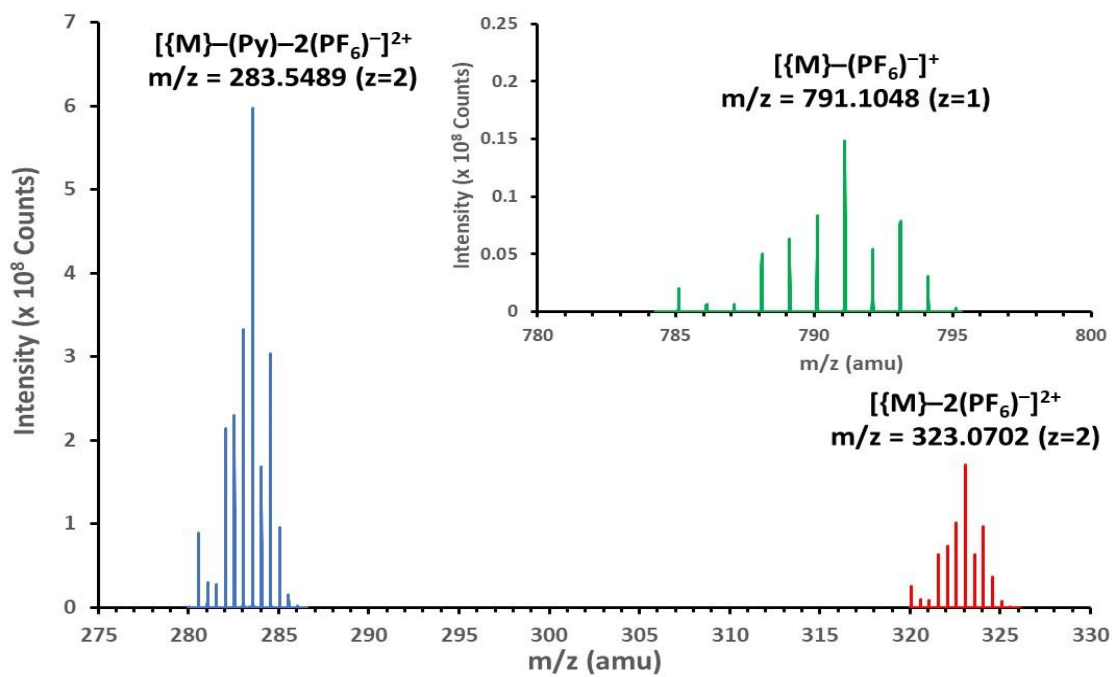
Figure 3.9. (+) ESI-MS of [Ru(tpy)(pbpy)(Py)](PF$_6$)$_2$ (**3**).
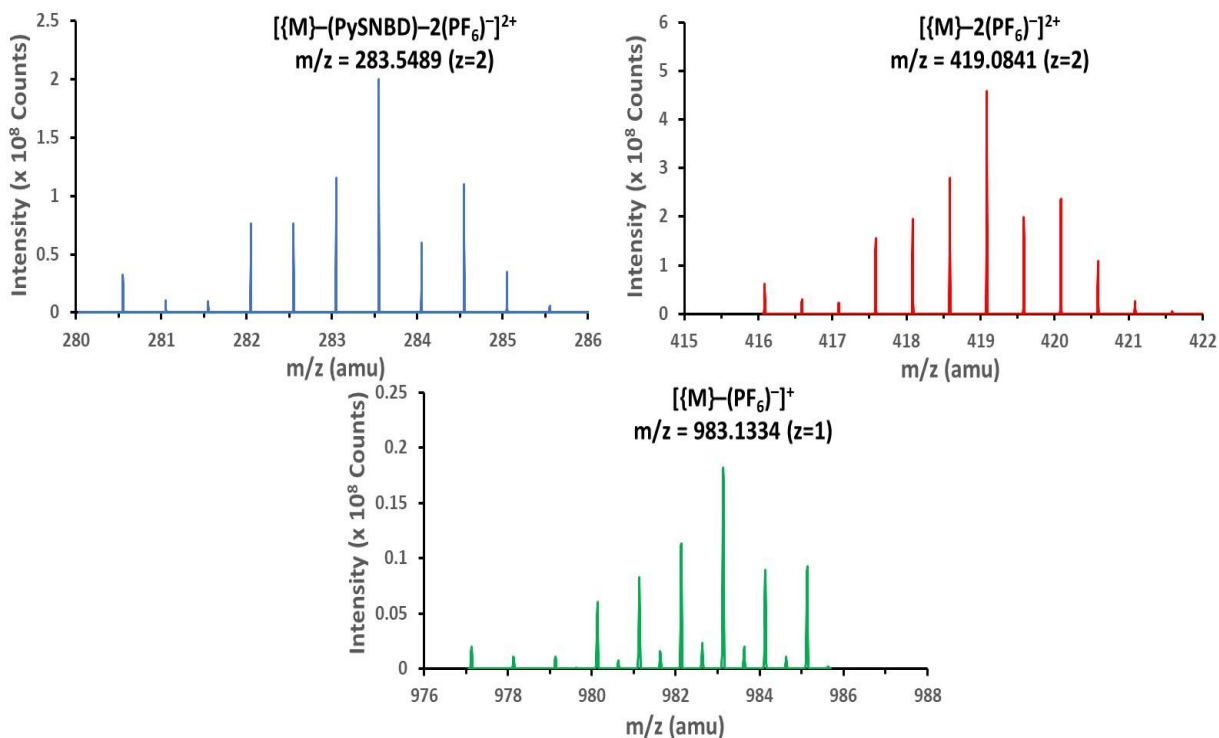
Figure 3.10. (+) ESI-MS of [Ru(tpy)(pbpy)(PySNBD)](PF$_6$)$_2$ (**4**).

Crystal Structure Determination

Single crystals suitable for X-ray diffraction were grown for **2**-**4** along with the **PySNBD** ligand as mentioned in the experimental section; the molecular structures are depicted in Figures 3.11-3.14. All three photocages crystallize in the triclinic *P*−1 space group whereas the **PySNBD** ligand crystallizes in the monoclinic *P*2$_1$/c space group. Crystal data and refinement parameters of **PySNBD** and **2**-**4** are compiled in Tables 3.1 and 3.2. All Ru-N bond distances and some representative bond angles of the complex **2**-**4** are tabulated in Tables 3.3-3.5. All three structures exhibit tridentate chelation of the planar tpy ligand which is nearly orthogonal to the coordinated pbpy ligand, whereas the

115

bidentate pbpy ligand is oriented in the desired conformation with the unbound phenyl ring being positioned towards the metal center, generating structural distortion. The coordination sphere of each Ru center is surrounded by six N atoms in a distorted octahedral geometry as evidenced by the Ru-N distances (Tables 3.3-3.5). The shortest Ru–N bond is the bond between Ru and the central pyridine ring of the tpy ligand (Ru1-N2) with a range of 1.944(3) – 1.958(5) Å, whereas the longest Ru–N bond is between the Ru center and central pyridine ring of the pbpy ligand (Ru1-N5) with a range of 2.128(5) – 2.171(3) Å. The elongated Ru1-N5 bond is consistent with the geometric distortion provided by the bulky pbpy ligand. The peripheral pyridyl rings on the tpy ligand are distal from the metal center with longer Ru-N bonds (more than 2 Å) which results in a contraction of the central Ru-N bond (less than 2 Å). The overall trend of the Ru-N bond distances is in good agreement with sterically demanding and architecturally similar Ru(II) complexes with nitrile/pyridyl functionalities.[77, 82, 169-170]

The crystal structure of **2** is similar to its parent complex [Ru(tpy)(bpy)(NCCH$_3$)]$^{2+}$ and the Ru-N bond distances involving the acetonitrile and tpy ligand are relatively unperturbed in spite of the introduction of steric bulk on the bidentate ligand.[171] There is an elongation of Ru1-N5 bond distance (~ 0.06 Å) as a result of an increase in the N5-Ru1-N6 bond angle by ~ 6° due to the addition of the phenyl substituent on the bpy moiety. This outward tilting of the pbpy ligand to minimize the steric bulk is accompanied by a shortening of the Ru1-N4 distance by ~ 0.01 Å. The CH$_3$CN tilt angle [Ru1-N6-C32 = 168.7(5)°] is close to the parent complex [169.8(8)°].[171] The crystal structure also revealed an eclipsed conformation of the phenyl ring on top of the coordinated acetonitrile (Figure

3.11b) which causes an upfield proton resonance shift of the coordinated acetonitrile. A comparison of the crystal structure of **3** with its bpy analogue, *viz.* [Ru(tpy)(bpy)(Py)]$^{2+}$, revealed that the Ru-N bond distances involving only the tpy ligand remain unaltered. There is a noticeable lengthening of the Ru1-N5 bond distance (~ 0.05 Å) as a result of an increase in the N5-Ru1-N6 bond angle by more than 5° due to the steric effect of pbpy ligand. As in the case of **2**, the outward tilting of the pbpy ligand gives rise to a shorter Ru1-N4 distance which is comparable to its parent complex.[77, 172] Another major structural differences observed due to introduction of the bulky pbpy ligand is the elongation of the Ru-pyridine bond [Ru1-N6 = 2.138(7) Å] along with a tilting of the pyridine ring towards the portion of the tpy ligand bearing the N1 atom which is reflected in the N1-Ru1-N6 bond angle being greater than N3-Ru1-N6 bond angle (Table 3.4). A similar tilting of the pyridine ring was reported for the [Ru(tpy)(dmbpy)(Py)]$^{2+}$ and [Ru(tpy)(biq)(Py)]$^{2+}$ compounds containing bulky bidentate dmbpy and biq ligand. This tilt of the pyridine ring is said to weaken the σ-bonding and π-bonding leading to dissociation of pyridine.[77] Unlike **3**, the crystal structure of **4** exhibits a much longer Ru1-N5 distance of 2.171(3) Å as result of outward tilting of the pbpy ligand with the N5-Ru1-N6 bond angle being 103.12 (10)^o. Moreover, the fluorophore substituent (NBD) on the pyridyl moiety (Figure 3.13) can freely rotate around the C-C bond generating additional steric strain due to repulsion between the NBD substituent and the phenyl ring on pbpy ligand resulting in a longer Ru1-N5 distance. Further elongation of the Ru1-N5 bond leads to a compression of the Ru1-N4 bond distance by ~ 0.03 Å compared to **3**. Also, the **PySNBD** ligand is nearly perpendicular to the tpy plane and tilts slightly towards the N3-atom. Although

117

distorted, both **3** and **4** are additionally stabilized by π-stacking interactions between the

unbound phenyl ring and the pyridyl moiety as shown in Figure 3.12b and 3.13b.

Table 3.1. Crystal data and refinement parameters for **2** and **3**.

Compound	2	3
Empirical Formula	$C_{70.33}H_{55.16}F_{24}N_{14.17}P_4Ru_2$	$C_{40}H_{33.5}F_{11.86}N_6O_{1.25}P_{1.98}Ru$
Formula weight	1880.87	1005.71
Temperature, K	110	100.01
Crystal system	Triclinic	Triclinic
Space group	$P-1$	$P-1$
Unit cell dimensions	$a = 9.2403(5)$ Å, $\alpha = 65.392(3)^o$ $b = 21.3823(12)$ Å, $\beta = 81.361(3)^o$ $c = 21.9092(12)$ Å, $\gamma = 88.921(3)^o$	$a = 10.9051(6)$ Å, $\alpha = 102.4311(11)^o$ $b = 19.8478(10)$ Å, $\beta = 100.5897(11)^o$ $c = 21.3754(11)$ Å, $\gamma = 105.7106(10)^o$
Volume, Å^3	3886.4(4)	4202.6(4)
Z	2	4
Density, g/cm^3	1.607	1.589
Absorption coefficient, mm^{-1}	0.580	4.578
$F(000)$	1881	2023
Crystal color, morphology	light orange, block	dark orange, plate
Crystal size, mm^3	$0.670 \times 0.074 \times 0.062$	$0.304 \times 0.268 \times 0.078$
Reflections collected	60228	15697
Independent reflections	14758 [$R_{int} = 0.0666$]	15697
Data/restraints/parameters	14758/1623/1410	15697/194/1168
Goodness-of-fit on F^2	1.044	1.059
R indices [I>2sigma(I)][a,b]	$R_1 = 0.0691$, $wR_2 = 0.1650$	$R_1 = 0.0866$, $wR_2 = 0.2460$
R indices (all data)	$R_1 = 0.1016$, $wR_2 = 0.1824$	$R_1 = 0.0932$, $wR_2 = 0.2625$
Largest diff. peak/hole, e Å^3	1.45/–1.24	2.03/–1.86

[a] $R1 = \sum||F_o| - |F_c||/[\sum|F_o|]$. [b] $wR2 = [\sum[w(F_o^2 - F_c^2)^2]/\sum[w(F_o^2)^2]]^{1/2}$, $w = 1/\sigma^2 (F_o^2)+(aP)^2+bP$, where $P = [max(0$ or $F_o^2) + 2(F_c^2)]/3$.

Table 3.2. Crystal data and refinement parameters for **PySNBD** and **4**.

Compound	PySNBD	4
Empirical Formula	$C_{12}H_9N_5O_3$	$C_{52.5}H_{52.01}F_{12}N_{10}O_6P_2Ru$
Formula weight	271.24	1310.05
Temperature, K	110	110
Crystal system	Monoclinic	Triclinic
Space group	$P2_1/c$	$P–1$
Unit cell dimensions	$a = 17.9789(8)$ Å, $\alpha = 90°$ $b = 9.8693(5)$ Å, $\beta = 159.682(2)°$ $c = 18.4457(9)$ Å, $\gamma = 90°$	$a = 14.111(5)$ Å, $\alpha = 66.345(4)°$ $b = 14.573(5)$ Å, $\beta = 68.970(4)°$ $c = 15.680(6)$ Å, $\gamma = 79.540(4)°$
Volume, Å^3	1136.50(10)	2754.3(18)
Z	4	2
Density, g/cm^3	1.585	1.580
Absorption coefficient, mm^{-1}	0.119	0.443
F(000)	560	1334
Crystal color, morphology	dark yellow, needle	dark orange, plate
Crystal size, mm^3	$0.208 \times 0.098 \times 0.072$	$0.414 \times 0.122 \times 0.059$
Reflections collected	10120	72038
Independent reflections	2222 [$R_{int} = 0.0662$]	11242 [$R_{int} = 0.0819$]
Data/restraints/parameters	2222/0/181	11242/403/881
Goodness-of-fit on F^2	1.058	1.028
R indices [I>2sigma(I)][a,b]	$R_1 = 0.0434$, $wR_2 = 0.0951$	$R_1 = 0.0469$, $wR_2 = 0.1125$
R indices (all data)	$R_1 = 0.0629$, $wR_2 = 0.1048$	$R_1 = 0.0728$, $wR_2 = 0.1277$
Largest diff. peak/hole, e Å^3	0.23/–0.31	0.66/–0.93

[a] $R1 = \sum||F_o| - |F_c||/[\sum|F_o|]$. [b] $wR2 = [\sum[w(F_o^2 - F_c^2)^2]/\sum[w(F_o^2)^2]]^{1/2}$, $w = 1/\sigma^2 (F_o^2)+(aP)^2+$

bP, where $P = [max(0 \text{ or } F_o^2) + 2(F_c^2)]/3$.

Table 3.3. Selected bond distances and angles for **2**.

Bond distance (Å)		Bond angle (°)	
Ru1–N1	2.065(5)	N1–Ru1–N6	87.7(2)
Ru1–N2	1.958(5)	N3–Ru1–N6	90.76(19)
Ru1–N3	2.068(5)	N1–Ru1–N3	159.4(2)
Ru1–N4	2.030(5)	N4–Ru1–N6	178.6(2)
Ru1–N5	2.128(5)	N5–Ru1–N6	102.09(19)
Ru1–N6	2.037(5)	Ru1–N6–C32	168.7(5)
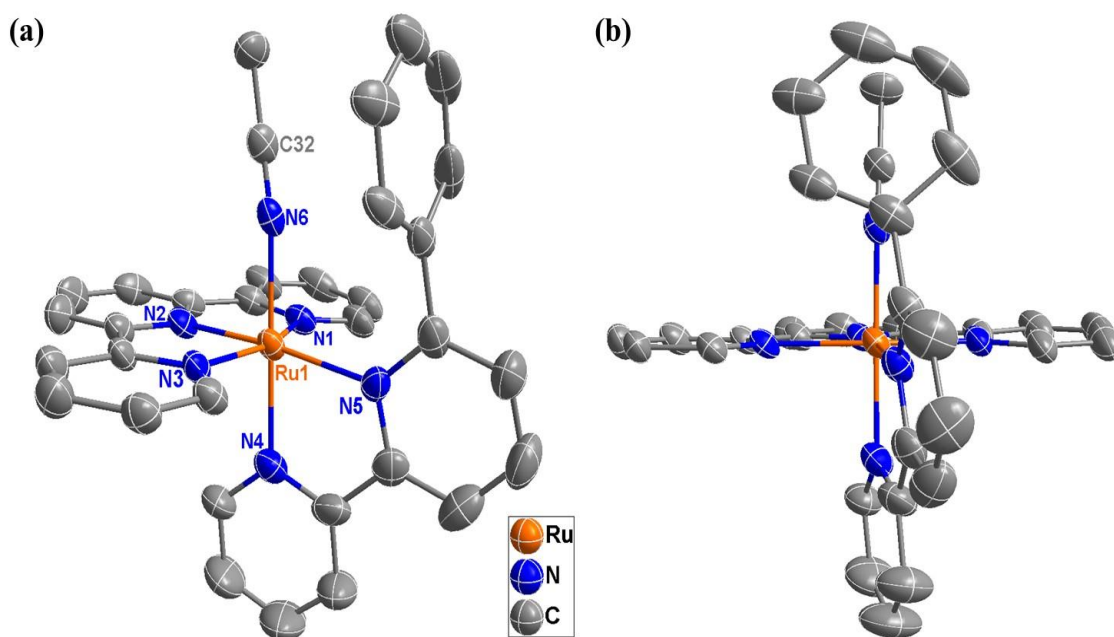
Figure 3.11. (a) Thermal ellipsoid plot at the 50% probability level for the cation $[Ru^{II}(tpy)(pbpy)(NCCH_3)]^{2+}$ in (**2**) and (b) structure emphasizing the eclipsed phenyl ring on top of the coordinated acetonitrile. The $(PF_6)^-$ counterions, solvents of crystallization (acetonitrile) and H atoms have been omitted for the sake of clarity.

Table 3.4. Selected bond distances and angles for **3**.

Bond distance (Å)		Bond angle (°)	
Ru1–N1	2.075(6)	N1–Ru1–N6	88.1(2)
Ru1–N2	1.952(6)	N3–Ru1–N6	95.2(2)
Ru1–N3	2.089(6)	N1–Ru1–N3	158.8(3)
Ru1–N4	2.063(6)	N4–Ru1–N6	176.6(2)
Ru1–N5	2.148(6)	N5–Ru1–N6	100.4(2)
Ru1–N6	2.138(7)	Ru1–N5–C25	130.6(5)
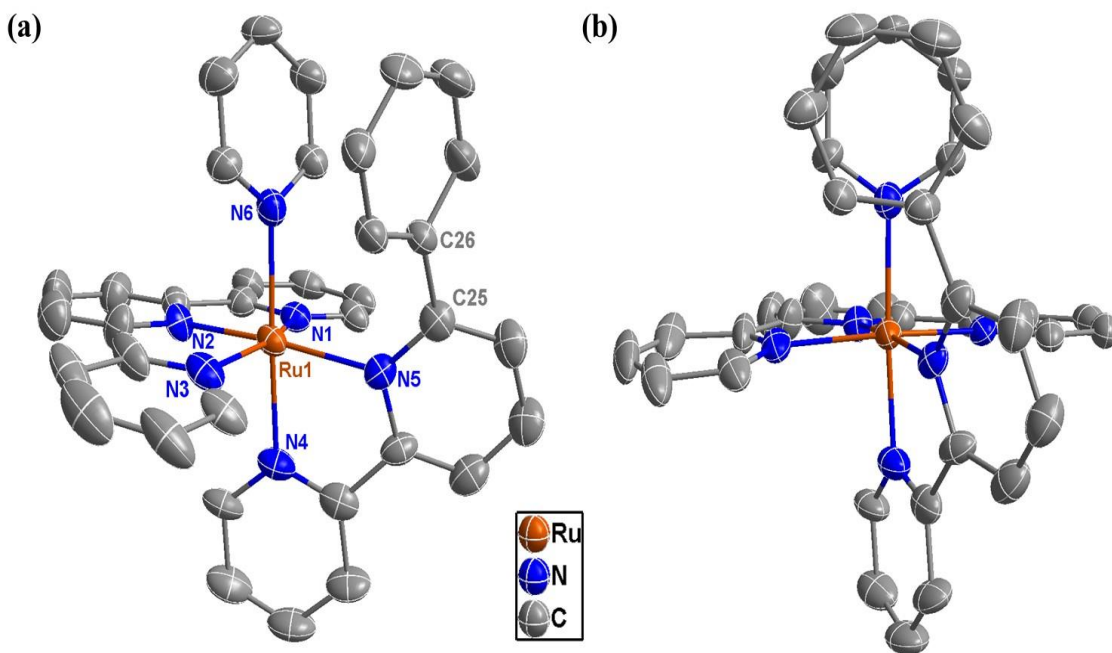
Figure 3.12. (a) Thermal ellipsoid plot at the 50% probability level for the cation $[Ru^{II}(tpy)(pbpy)(Py)]^{2+}$ in (**3**) and (b) structure emphasizing the stabilization through the π-stacking interaction. The $(PF_6)^-$ counterions, solvents of crystallization (acetone, diethyl ether) and H atoms have been omitted for the sake of clarity.

Table 3.5. Selected bond distances and angles for **4**.

Bond distance (Å)		Bond angle (°)	
Ru1–N1	2.064(3)	N1–Ru1–N6	92.73(11)
Ru1–N2	1.944(3)	N3–Ru1–N6	90.07(11)
Ru1–N3	2.061(3)	N1–Ru1–N3	158.88(11)
Ru1–N4	2.037(3)	N4–Ru1–N6	177.43(11)
Ru1–N5	2.171(3)	N5–Ru1–N6	103.12(10)
Ru1–N6	2.115(3)	Ru1–N5–C25	131.6(2)
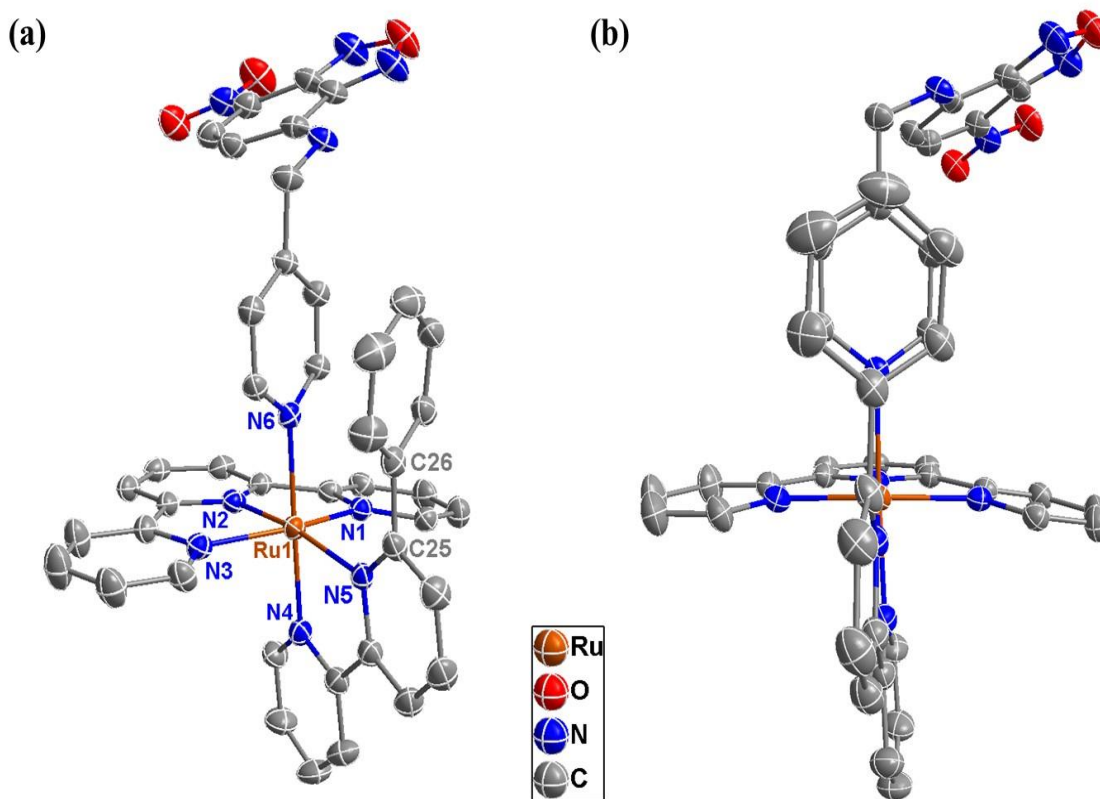
Figure 3.13. (a) Thermal ellipsoid plot at the 50% probability level for the cation $[Ru^{II}(tpy)(pbpy)(PySNBD)]^{2+}$ in (**4**) and (b) structure emphasizing the stabilization through the π-stacking interaction. The $(PF_6)^-$ counterions, solvents of crystallization (acetone, diethyl ether) and H atoms have been omitted for the sake of clarity.
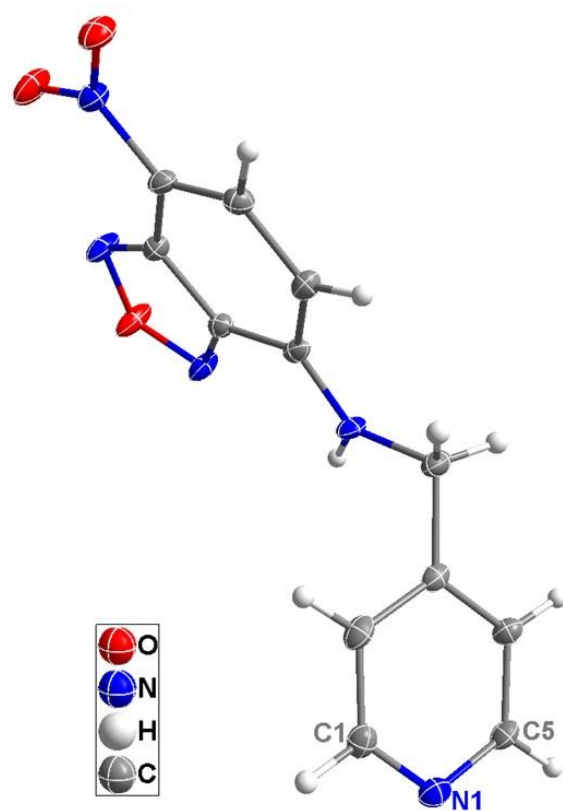
Figure 3.14. Thermal ellipsoid plot at the 50% probability level for the **PySNBD** ligand.

Geometry optimizations of **2**-**4** were performed in both the gas and solvent phases (acetonitrile for **2** and acetone for **3** and **4**). The optimized geometries in the solvent phases are depicted in Figures 3.15-3.17 and are compared with the crystal structures vis-à-vis bond distances; Ru-N bond distances are compiled in Tables 3.6-3.8. From the bond distances, it can be concluded that the structures predicted by the DFT calculations agree well with the structures obtained by crystallography. Solid state Ru-N bond distances involving Ru and the tpy ligand are increased by ~ 0.03 – 0.06 Å in both calculated structures. The elongation of the Ru-N bonds is observed for Ru1-N5 and Ru1-N6 bond which indicates that structural distortion is maintained in both the gas and solvent phase structures. The coordinated monodentate ligands are tilted away from the phenyl ring in all three optimized geometries to alleviate steric repulsion (Figures 3.15-3.17). Furthermore **3** and **4** are stabilized by π-stacking interactions as was observed in their crystal structures (Figures 3.16b and 3.17b).
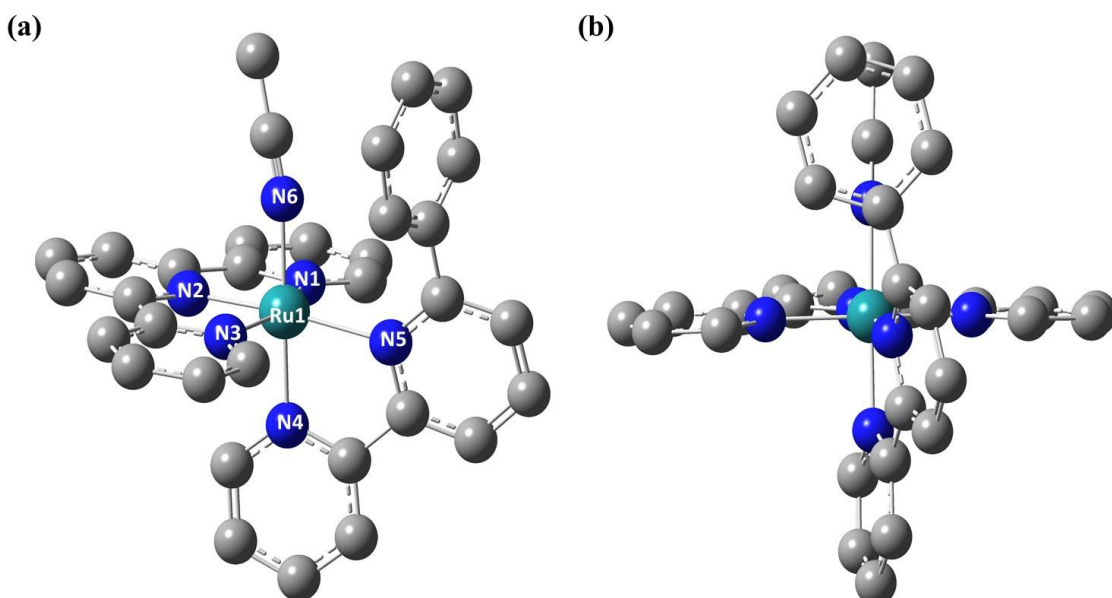
Figure 3.15. (a) Optimized geometry of the cation $[Ru(tpy)(pbpy)(NCCH_3)]^{2+}$ in (**2**) in acetonitrile (using the SMD Model) and (b) structure emphasizing eclipsed phenyl ring on top of coordinated acetonitrile. H atoms have been omitted for the sake of clarity.

Table 3.6. Comparison of bond distances for **2** from the crystal structure and computationally optimized structures.

Selected Bond	Bond Distance (Å) [Crystal Structure]	Bond Distance (Å) [Gas Phase Optimized Structure]	Bond Distance (Å) [Solvent Phase Optimized Structure] [a]
Ru1–N1	2.065(5)	2.121	2.120
Ru1–N2	1.958(5)	1.992	1.992
Ru1–N3	2.068(5)	2.120	2.114
Ru1–N4	2.030(5)	2.082	2.076
Ru1–N5	2.128(5)	2.195	2.189
Ru1–N6	2.037(5)	2.055	2.059

[a] Acetonitrile as solvent.

(a)　　　　　　　　　　　　　**(b)**
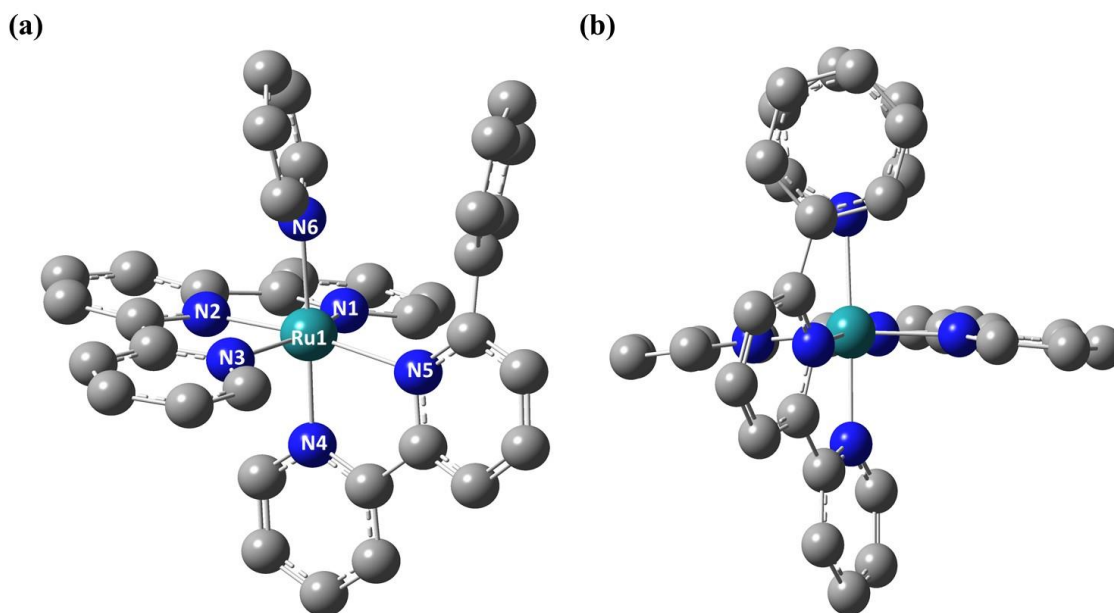
Figure 3.16. (a) Optimized geometry of the cation [Ru(tpy)(pbpy)(Py)]$^{2+}$ in (**3**) in acetone (using the SMD Model) and (b) structure emphasizing the stabilization through the π-stacking interaction. H atoms have been omitted for the sake of clarity.

Table 3.7. Comparison of bond distances for **3** from the crystal structure and computationally optimized structures.

Selected Bond	Bond Distance (Å) [Crystal Structure]	Bond Distance (Å) [Gas Phase Optimized Structure]	Bond Distance (Å) [Solvent Phase Optimized Structure] [a]
Ru1–N1	2.075(6)	2.122	2.120
Ru1–N2	1.952(6)	1.983	1.984
Ru1–N3	2.089(6)	2.118	2.120
Ru1–N4	2.063(6)	2.086	2.078
Ru1–N5	2.148(6)	2.230	2.225
Ru1–N6	2.138(7)	2.190	2.194

[a] Acetone as solvent.

126
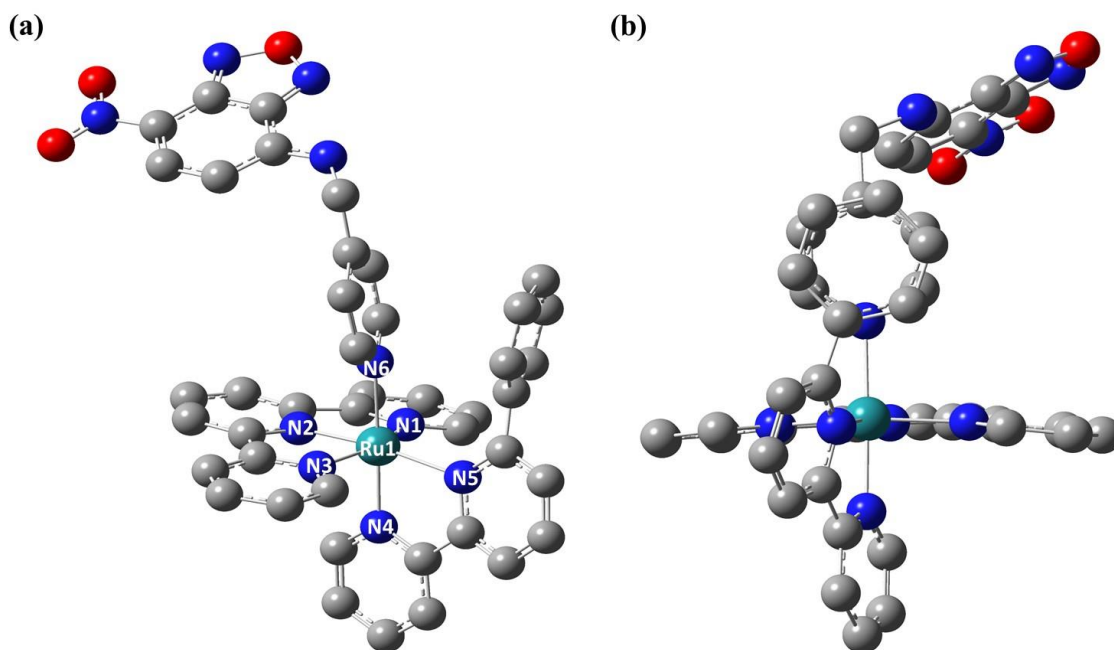
Figure 3.17. (a) Optimized geometry of the cation [Ru(tpy)(pbpy)(PySNBD)]$^{2+}$ in (**4**) in acetone (using the SMD Model) and (b) structure emphasizing the stabilization through the π-stacking interaction. H atoms have been omitted for the sake of clarity.

Table 3.8. Comparison of bond distances for **4** from the crystal structure and computationally optimized structures.

Selected Bond	Bond Distance (Å) [Crystal Structure]	Bond Distance (Å) [Gas Phase Optimized Structure]	Bond Distance (Å) [Solvent Phase Optimized Structure] [a]
Ru1–N1	2.064(3)	2.125	2.118
Ru1–N2	1.944(3)	1.990	1.984
Ru1–N3	2.061(3)	2.122	2.118
Ru1–N4	2.037(3)	2.084	2.078
Ru1–N5	2.171(3)	2.218	2.220
Ru1–N6	2.115(3)	2.193	2.196

[a] Acetone as solvent

Electronic Absorption and Emission Spectroscopy

Electronic absorption spectra of **2** in acetonitrile and **3**-**4** in dry acetone are depicted in Figure 3.18; the absorption data are summarized in Table 3.9. The low-lying electronic transitions in the visible region displayed by **2** and **3** located at 455 nm (ε = 10,000 $M^{-1}cm^{-1}$) and 475 nm (ε = 7,900 $M^{-1}cm^{-1}$) respectively are assigned to ^{1}MLCT transitions from Ru(dπ) $\rightarrow$ L(π*) (L = tpy, pbpy). In contrast, the absorption profile of **4** is identical to that of the free **PySNBD** ligand (Figure 3.19) with absorption maxima centered at 451 nm (ε = 25,400 $M^{-1}cm^{-1}$) and 452 nm (ε = 18,500 $M^{-1}cm^{-1}$) respectively, and, unlike **2** and **3**, the electronic transition is assigned to ^{1}LC $\pi$$\rightarrow$$\pi$* transition centered on the NBD moiety of the **PySNBD** ligand. All three complexes exhibit a broad shoulder surpassing the MLCT maxima which extends beyond 550 nm. The absorption profile of **2** is very similar to its parent complex [Ru(tpy)(bpy)(NCCH$_3$)]$^{2+}$ in MeCN with a visible absorption maximum at 455 nm (ε = 11,000 $M^{-1}cm^{-1}$).[171-172] The visible absorption maximum of **3** is slightly red-shifted (by 7 nm) compared to its parent complex [Ru(tpy)(bpy)(Py)]$^{2+}$ [468 nm (ε = 8,120 $M^{-1}cm^{-1}$)] in acetone. Similar red-shifting was reported for the cation [Ru(tpy)(dmbpy)(Py)]$^{2+}$ due to introduction of steric bulk on the bidentate ligand.[77] Additionally, when MeCN is replaced by Py, the resulting spectrum exhibits a broadening of the absorption peak. The absorption spectrum of **3** also exhibits a weak shoulder at 415 nm (ε = 4,700 $M^{-1}cm^{-1}$), which can be assigned to a Ru(dπ) $\rightarrow$ Py(π*) transition similarly shown for [Ru(tpy)(bpy)(Py)]$^{2+}$.[172] In general, the UV-region

of the spectra primarily consists of intense ^{1}LC $\pi\to\pi^*$ transitions associated with the tpy

and pbpy ligands as observed for their parent complexes (Figure 3.18).[171]

Table 3.9. Electronic absorption spectral data (λ_{abs}) for **2** in acetonitrile and for **3**, **4** and the **PySNBD** ligand in dry acetone. Additionally, emission data (λ_{em}) for **4** and **PySNBD** ligand in dry acetone at RT.

Compound	λ_{abs} (nm) ($\varepsilon \times 10^4$ M^{-1} cm^{-1})	λ_{em} (nm)
[Ru(tpy)(pbpy)(NCCH$_3$)](PF$_6$)$_2$ (**2**)	455 (1.00), 330^a (2.01), 305 (5.06)	ND^b
[Ru(tpy)(pbpy)(Py)](PF$_6$)$_2$ (**3**)	475 (0.79), 415^a (0.47)	ND^b
[Ru(tpy)(pbpy)(PySNBD)](PF$_6$)$_2$ (**4**)	451 (2.54)	522
PySNBD ligand	452 (1.85)	519

^{a} Shoulder. ^{b} Not determined.
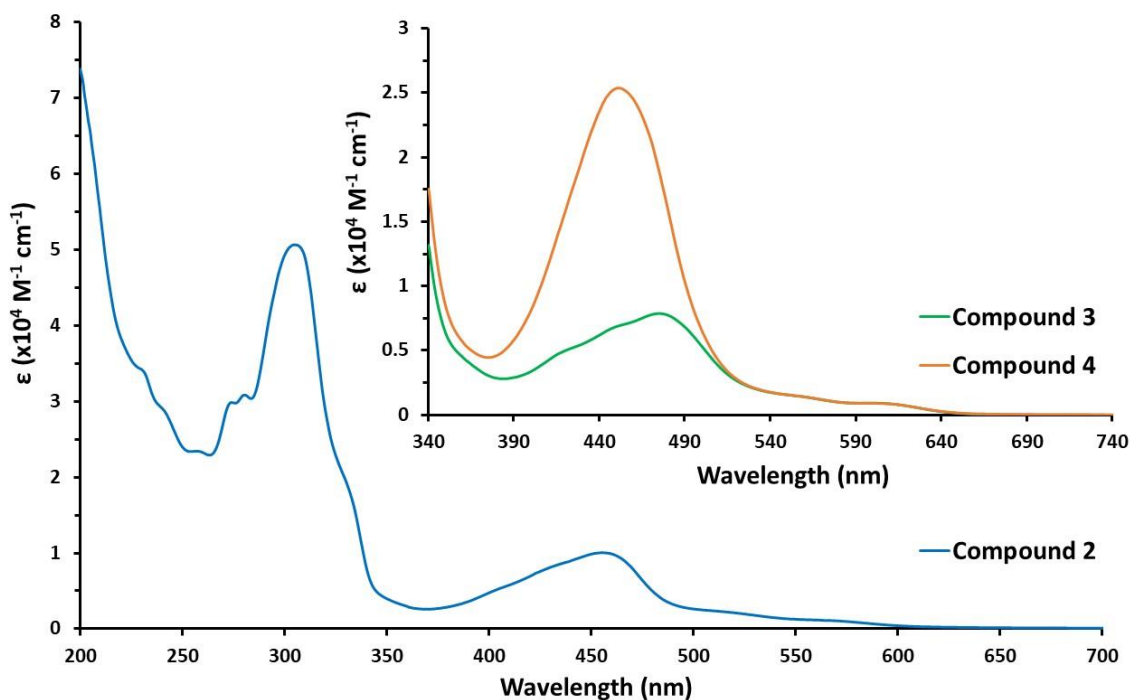
Figure 3.18. Electronic absorption spectra of **2** in acetonitrile at room temperature. Inset: Electronic absorption spectra of **3** and **4** in dry acetone at room temperature.

The absorption-emission spectra of the **PySNBD** ligand along with **4** in dry acetone are depicted in Figure 3.19 and the emission data are summarized in Table 3.9. Due to the fact that the NBD moiety fluoresces very strongly to emit green light when bound to an amine, the **PySNBD** ligand displays a strong emission at 519 nm when excited at 450 nm in acetone at RT. The **PySNBD** ligand has a methylene spacer ($-CH_2-$) between the coordinating 4-pyridyl unit and the NBD fluorophore moiety which prevents any electronic communication between them. As a result, when bound to the Ru(II) center, the emissive property of **4** is retained and the emission spectrum of **4** very much resembles that of the free fluorophore with an emission maximum centered at 522 nm when excited at 450 nm in acetone at RT. Compounds **2** and **3** are not emissive or even weakly emissive at RT and therefore were not investigated. Similar to **2**, the parent complex $[Ru(tpy)(bpy)(NCCH_3)]^{2+}$ is not emissive at RT whereas $[Ru(tpy)(bpy)(Py)]^{2+}$ exhibits weak emission at 604 nm with a lifetime (τ) of 15 ns when excited at 459 nm in CH_2Cl_2 at RT.[171]
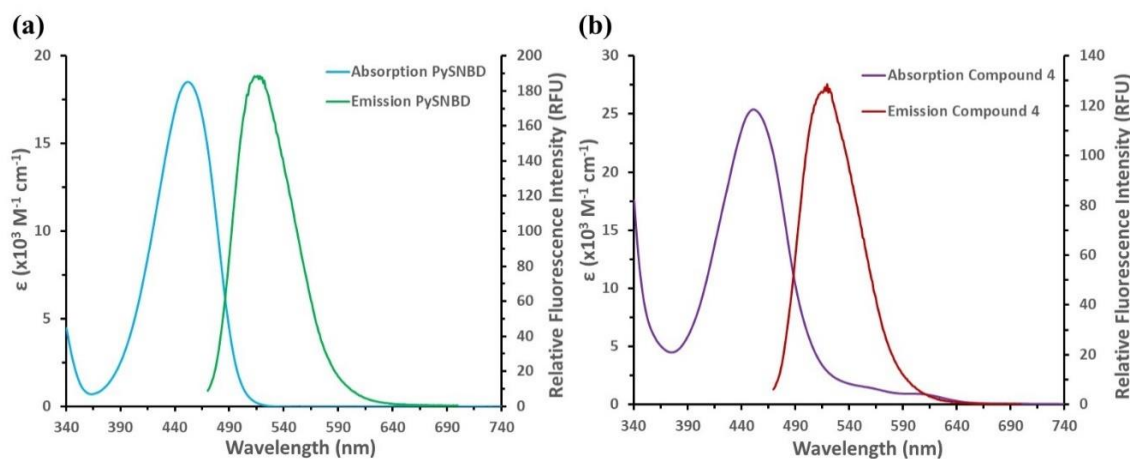
Figure 3.19. Absorption and emission spectra of (a) the **PySNBD** ligand and (b) **4** in dry acetone at room temperature.

Electronic Structure Calculations

The optimized geometries of the complexes in the solvent phase were analyzed to gain further insight into the electronic properties. Electron densities and energies of selected MOs along with the percentage contributions of the metal centers and coordinated ligands are tabulated in Table (3.10-3.14). In diamagnetic Ru(II) mononuclear complexes, the (HOMO-2) to HOMO orbitals typically constitute the occupied "t_{2g}-type" Ru($d\pi$) orbitals in a pseudo-octahedral environment. For **2-4**, the (HOMO-2) to HOMO orbitals are primarily localized on the metal center having similar % contributions of Ru. The (HOMO-2) and (HOMO-1) orbitals are close to being degenerate and are lower in energy than the HOMO for all three complexes. The LUMO to (LUMO+3) orbitals are predominantly localized on both the tridentate tpy ligand and bidentate pbpy ligand for **2** and **3**. In the case of **2**, the (LUMO+4) orbital is delocalized over the π^* orbitals of both the tpy and pbpy ligands with essentially no contribution from coordinated acetonitrile. In

131

contrast, (LUMO+4) has predominant contributions from the π^* orbital of Py (63%) for **3**. Unlike **2** and **3**, complex **4** has LUMO and (LUMO+4) orbitals exclusively localized on the low lying π^* orbital of the NBD moiety of the coordinated **PySNBD** ligand whereas the (LUMO+1) to (LUMO+3) orbitals are delocalized over the tpy and pbpy ligands. Additionally, the (HOMO-3) orbital on **4** is found to be centered exclusively on the π orbital of the NBD moiety which makes any electronic transition from (HOMO-3) to LUMO/(LUMO+4) to be a ligand-centered $\pi \rightarrow \pi^*$ transition which constitutes the absorption maximum in **4**.

Table 3.10. Frontier molecular orbitals (HOMO-2 and HOMO-1) of **2**–**4** (isovalue = 0.04).

[Ru(tpy)(pbpy)(NCCH₃)]²⁺ (2)	[Ru(tpy)(pbpy)(Py)]²⁺ (3)	[Ru(tpy)(pbpy)(PySNBD)]²⁺ (4)
HOMO-2	HOMO-2	HOMO-2
HOMO-1	HOMO-1	HOMO-1
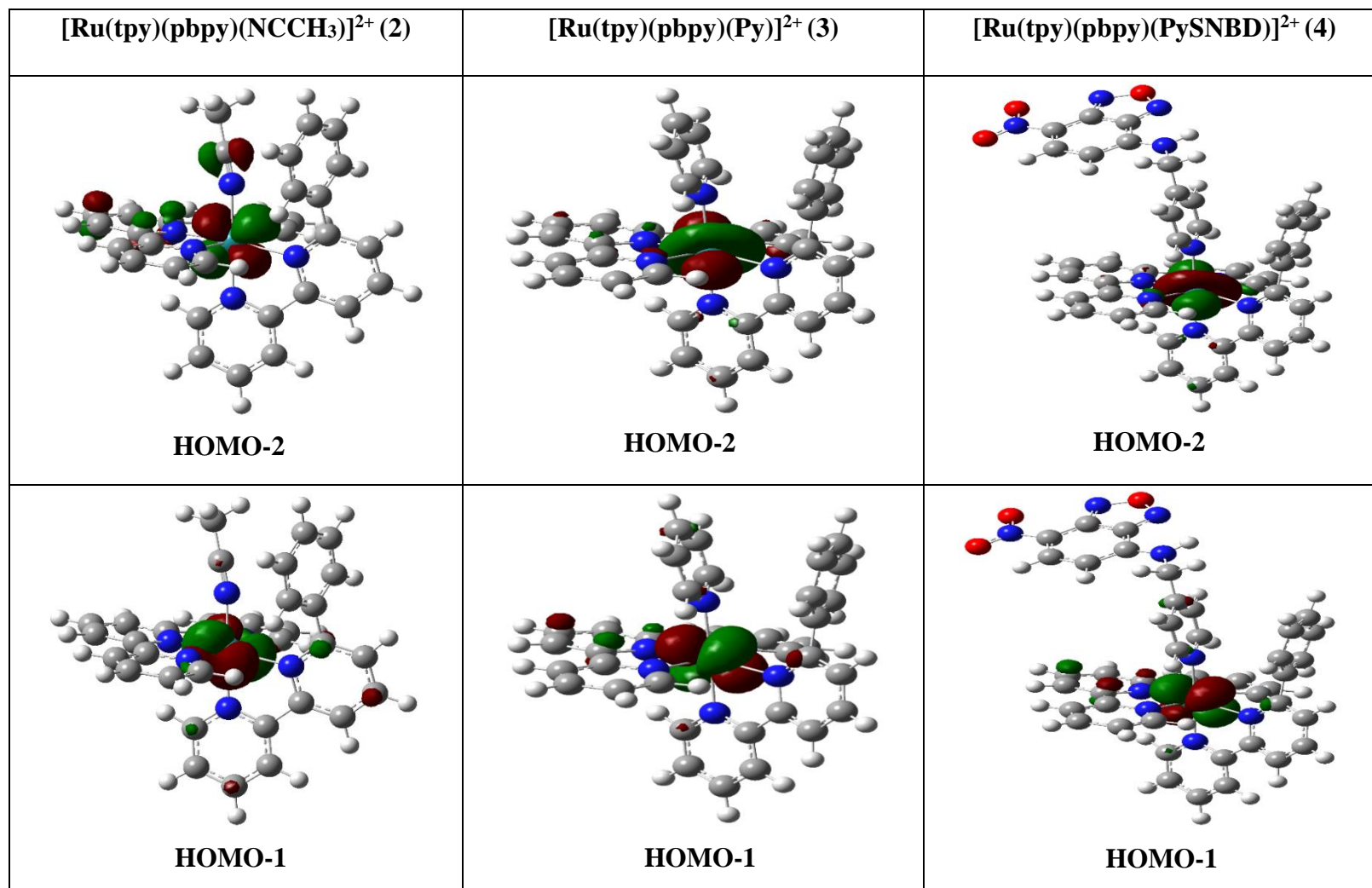
Table 3.11. Frontier molecular orbitals (HOMO and LUMO) of **2**–**4** (isovalue = 0.04).

[Ru(tpy)(pbpy)(NCCH$_3$)]$^{2+}$ (**2**)	[Ru(tpy)(pbpy)(Py)]$^{2+}$ (**3**)	[Ru(tpy)(pbpy)(PySNBD)]$^{2+}$ (**4**)
HOMO	HOMO	HOMO
LUMO	LUMO	LUMO
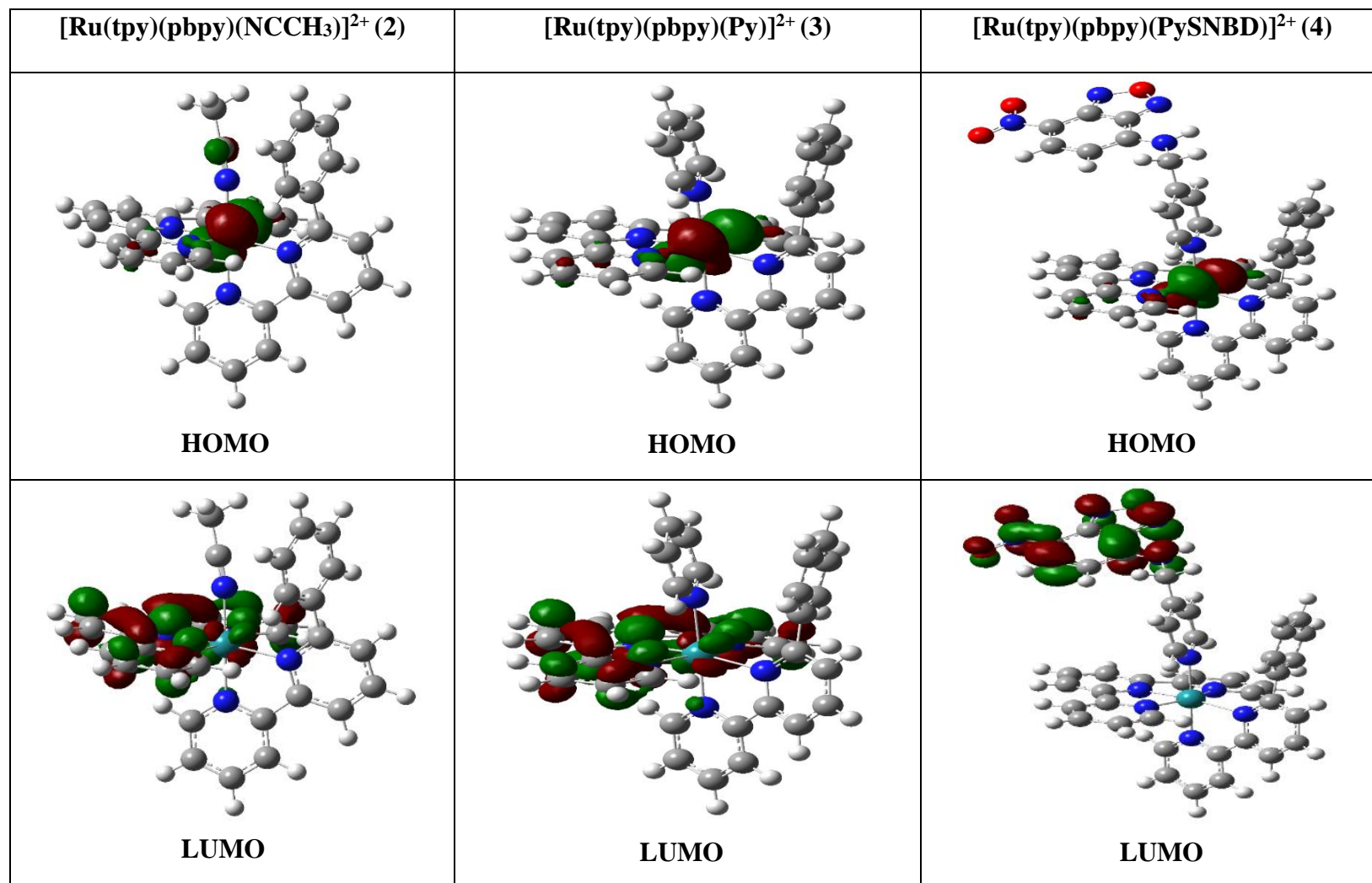
Table 3.12. Frontier molecular orbitals (LUMO+1 and LUMO+2) of **2**–**4** (isovalue = 0.04).

[Ru(tpy)(pbpy)(NCCH₃)]²⁺ (2)	[Ru(tpy)(pbpy)(Py)]²⁺ (3)	[Ru(tpy)(pbpy)(PySNBD)]²⁺ (4)
LUMO+1	LUMO+1	LUMO+1
LUMO+2	LUMO+2	LUMO+2
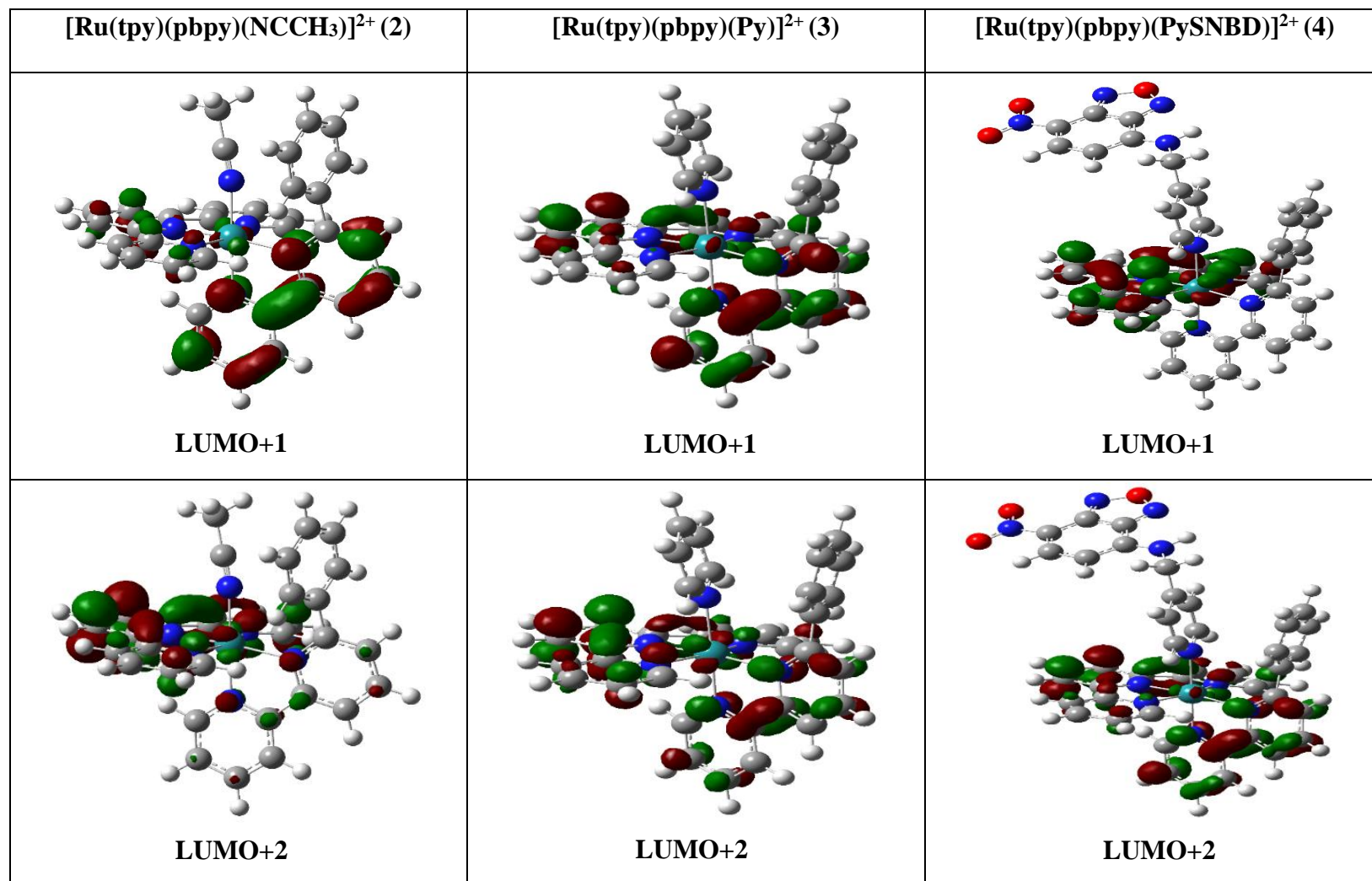
Table 3.13. Frontier molecular orbitals (LUMO+3 and LUMO+4) of **2**–**4** (isovalue = 0.04).

[Ru(tpy)(pbpy)(NCCH₃)]²⁺ (2)	[Ru(tpy)(pbpy)(Py)]²⁺ (3)	[Ru(tpy)(pbpy)(PySNBD)]²⁺ (4)
LUMO+3	LUMO+3	LUMO+3
LUMO+4	LUMO+4	LUMO+4
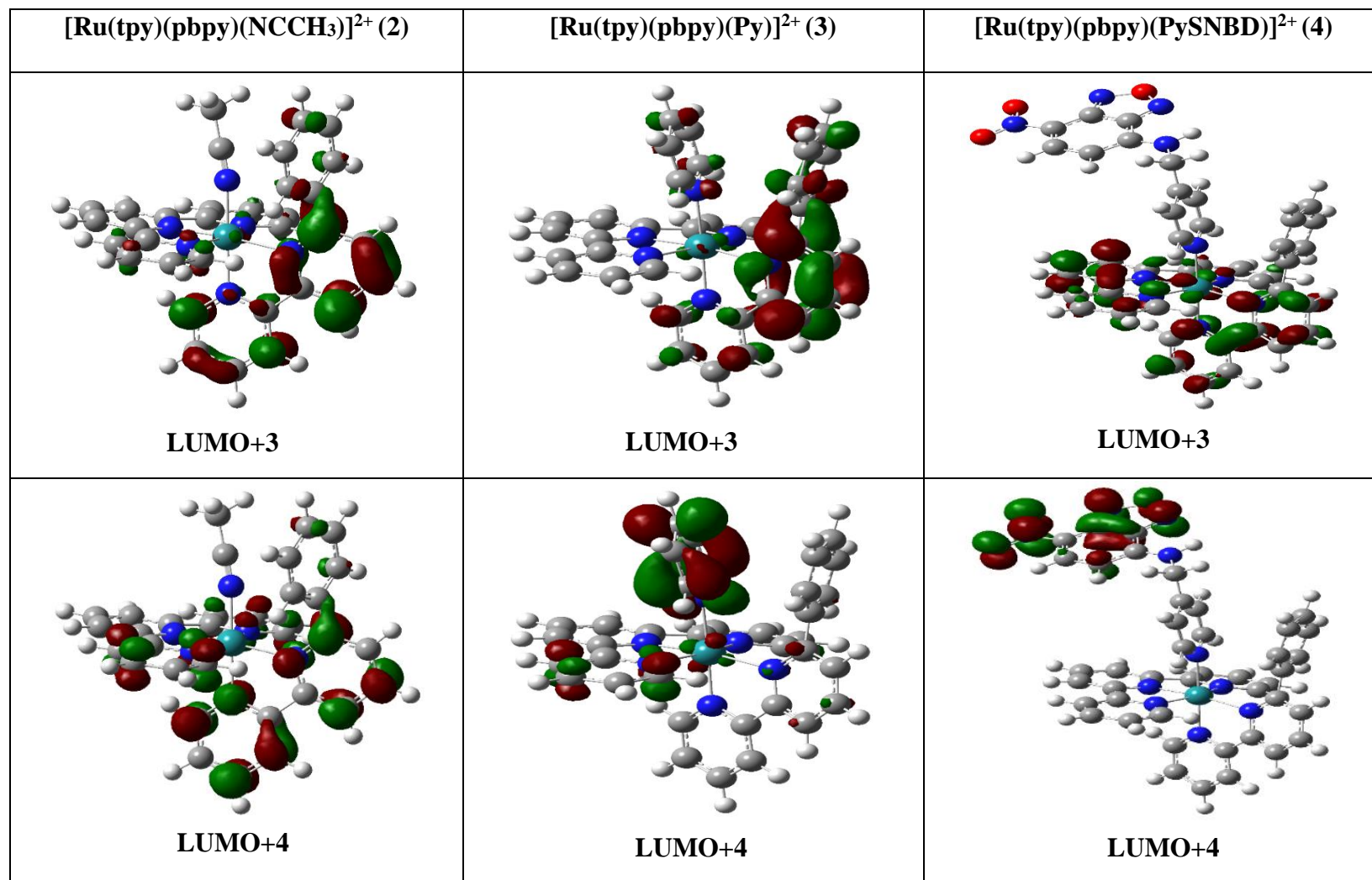
Table 3.14. Percent contributions of selected MOs and corresponding energies (E_{MO}) of **2**–**4**.

MO	[Ru(tpy)(pbpy)(NCCH₃)]²⁺ (2)					[Ru(tpy)(pbpy)(Py)]²⁺ (3)					[Ru(tpy)(pbpy)(PySNBD)]²⁺ (4)				
	% Contributions				E_{MO}	% Contributions				E_{MO}	% Contributions				E_{MO}
	Ru	tpy	pbpy	CH₃CN	(eV)	Ru	tpy	pbpy	Py	(eV)	Ru	tpy	pbpy	PySNBD	(eV)
LUMO+4	1	32	66	1	-1.377	4	19	14	63	-1.570	0	0	0	100	-2.005
LUMO+3	2	15	83	0	-1.553	3	7	80	10	-1.737	5	47	46	2	-2.440
LUMO+2	3	81	16	0	-2.306	4	57	37	2	-2.431	2	51	46	1	-2.460
LUMO+1	3	22	75	0	-2.336	2	41	56	1	-2.445	6	82	9	3	-2.675
LUMO	6	83	10	1	-2.554	6	82	9	3	-2.663	0	0	0	100	-3.061
HOMO	74	16	7	3	-5.847	74	17	6	3	-5.844	74	17	6	3	-5.862
HOMO-1	72	17	10	1	-6.018	72	15	9	4	-6.038	72	14	9	5	-6.043
HOMO-2	73	12	10	5	-6.086	73	15	10	2	-6.090	73	16	9	2	-6.100

TDDFT Calculations

TDDFT calculations were performed on the ground state optimized geometries of **2** in acetonitrile and of **3**–**4** in acetone to substantiate the experimental absorption spectra and to further interpret the visible electronic transitions. The most relevant ^{1}ES electronic transitions calculated in the solvent phase (using the SMD model[149]) with $\lambda_{\text{calc}} \geq 400$ nm are listed in Table (3.15-3.17) along with their extinction coefficients in terms of oscillator strength (f) values, percent transition contributions, and the nature of the transitions. The calculated absorption spectra qualitatively resemble the experimental absorption spectra of the complexes in the visible/near UV region (Figure 3.20) with visible absorption maxima shifted hypsochromically due to overestimation of orbital energies.[161] The calculated singlet excited states in the visible region ($\lambda_{\text{calc}} \geq 400$ nm) are almost exclusively ^{1}MLCT in nature whereas those in the UV region ($\lambda_{\text{calc}} \leq 400$ nm) possess mainly ^{1}LC ($^1\pi\pi^*$) character, results that corroborate the experimental assignments. The calculated ^{1}MLCT transitions occur from Ru(dπ) $\rightarrow$ L(π^*) (L = tpy, pbpy) orbitals for all three compounds. For **2**, the most intense visible transition at $\lambda_{\text{calc}} = 439.4$ nm (f= 0.062) corresponds to the experimental absorption maximum at $\lambda_{\text{exp}} = 455$ nm and the transitions (1-9) compose the broad visible band with weak shoulders that extend beyond 550 nm. Compound **3** similarly displays a red-shifted transition at $\lambda_{\text{calc}} = 457.8$ nm (f = 0.058) compared to **2** which corresponds to the experimental absorption maximum at $\lambda_{\text{exp}} = 475$ nm. Furthermore, the weak shoulder observed for **3** at $\lambda_{\text{exp}} = 415$ nm corresponds to transition 10 found at $\lambda_{\text{calc}} = 371.6$ nm (f= 0.006). This transition with partial contributions

138

from H → (L+4) [37%] can be assigned to Ru(dπ) → Py(π*) orbitals as the (LUMO+4) orbital possesses Py(π*) character (Table 3.13). Similar to **2**, the transitions (1-9) calculated for **3** constitute the broad visible band with weak shoulders that extend beyond 550 nm. Unlike **2** and **3**, compound **4** exhibits a very strong transition at $\lambda_{calc} = 419.5$ nm (f= 0.275) which corresponds to the experimental absorption maximum at $\lambda_{exp} = 451$ nm. This transition from (H-3) → L [78%] can be predominantly assigned to a ^{1}LC transition from π(**PySNBD**) → π*(**PySNBD**). Also, the transitions (1-13) calculated for **4** similarly constitute the sharp visible band with an shoulder that extends beyond 550 nm.
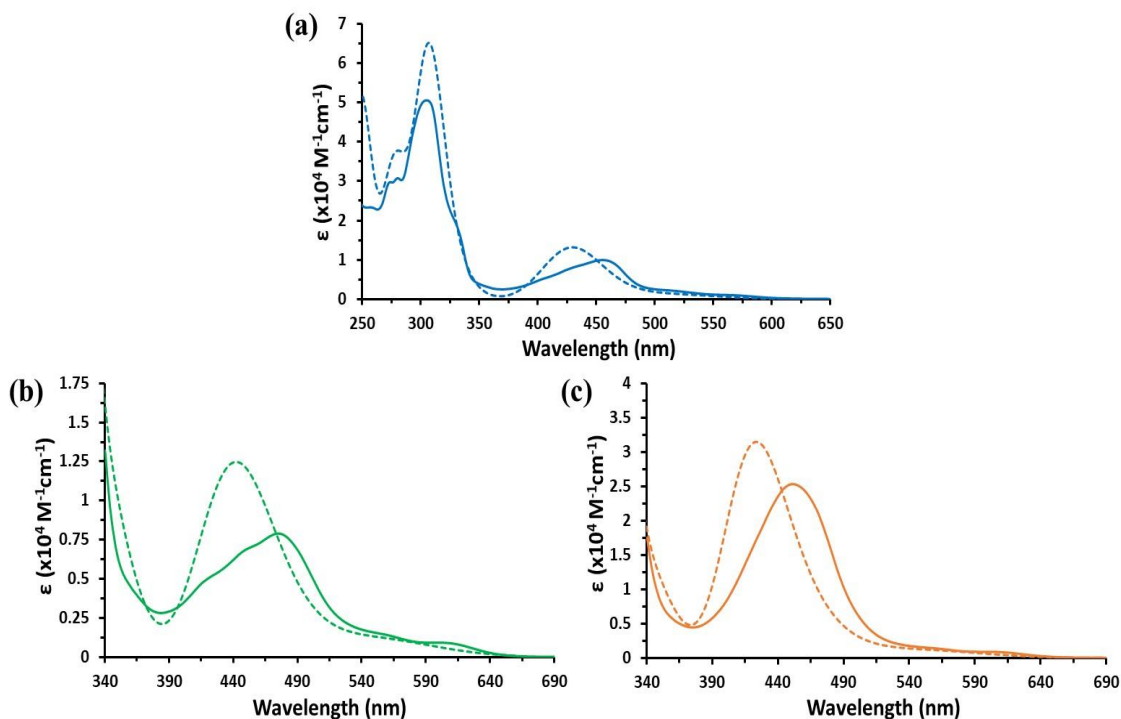
Figure 3.20. Experimental (solid line) and calculated (dotted line) electronic absorption spectra of (a) **2** in acetonitrile, (b) **3** and (c) **4** in acetone.

Table 3.15. TDDFT data of **2** in acetonitrile.

N^a	λ_{calc} (nm)	f^b	Major Contributions[c]	Assignment
1	529.7	0.011	H → L (94%), H-1 → L (4%)	MLCT
2	491.8	0.008	H-1 → L (93%), H → L (4%)	MLCT
3	472.6	0.003	H → L+1 (76%), H → L+2 (19%)	MLCT
4	459.3	0.004	H-2 → L (47%), H → L+2 (39%), H → L+1 (13%)	MLCT
5	439.4	0.062	H-2 → L (29%), H-1 → L+2 (24%), H → L+2 (23%), H-2 → L+1 (13%), H → L+1 (6%), H-1 → L+1 (2%)	MLCT
6	433.7	0.032	H-2 → L+1 (60%), H-2 → L+2 (17%), H-1 → L+2 (8%), H-1 → L+1 (7%), H-2 → L (2%)	MLCT
7	426.7	0.052	H-1→ L+1 (70%), H-1 →L+2 (25%)	MLCT
8	416.4	0.031	H-2 → L+2 (79%), H-2 → L+1 (17%)	MLCT
9	402.1	0.019	H-1→ L+2 (37%), H-2 →L (17%), H →L+2 (16%), H-1 → L+1 (13%), H-2 → L+1 (6%), H → L+6 (4%), H → L+3 (2%)	MLCT

[a] excited state number, [b] oscillator strength, [c] percent contribution = 2x(configuration coefficient)^{2}x100%.

Table 3.16. TDDFT data of **3** in acetone.

N^a	λ_{calc} (nm)	f^b	Major Contributions[c]	Assignment
1	562.6	0.013	H → L (94%), H-1 → L (3%)	MLCT
2	507.3	0.008	H-2 → L (50%), H-1 → L (44%), H → L (2%)	MLCT
3	491.8	0.003	H → L+2 (62%), H → L+1 (26%), H-2 → L (5%), H-1 → L (3%)	MLCT
4	481.4	0.006	H → L+1 (52%), H-2 → L (21%), H-1 → L (18%), H → L+2 (6%)	MLCT

Table 3.16. Continued

N^a	λ_{calc} (nm)	f^b	Major Contributions^c	Assignment
5	457.8	0.058	H-1 → L+2 (26%), H-1 → L (16%), H → L+2 (15%), H → L+1 (13%), H-2 → L (12%), H-1 → L+1 (11%), H-2 → L+1 (4%)	MLCT
6	449.7	0.025	H-2 → L+2 (46%), H-1 → L+2 (19%), H-1 → L+1 (9%), H-2 → L+1 (8%), H-2 → L (7%), H → L+1 (4%), H → L+2 (4%)	MLCT
7	440.1	0.021	H-1→ L+1 (60%), H-1 →L+2 (36%)	MLCT
8	431.3	0.067	H-2 → L+1 (85%), H-2 → L+2 (6%), H-1→ L+2 (3%), H-1→ L+1 (3%)	MLCT
9	414.9	0.021	H-2 → L+2 (39%), H-1 → L+1 (13%), H-1 → L+2 (11%), H → L+2 (10%), H-2 → L (7%), H-1 → L (5%), H → L+3 (5%), H → L+7 (4%)	MLCT

^{a} excited state number, ^{b} oscillator strength, ^{c} percent contribution = 2x(configuration coefficient)^{2}x100%.

Table 3.17. TDDFT data of **4** in acetone.

N^a	λ_{calc} (nm)	f^b	Major Contributions^c	Assignment
1	561.7	0.012	H → L+1 (94%), H-1 → L+1 (3%)	MLCT
2	507.1	0.008	H-2 → L+1 (61%), H-1 → L+1 (33%), H → L+1 (2%)	MLCT
4	490.4	0.003	H → L+3 (71%), H → L+2 (16%), H-1 → L+1 (6%), H-2 → L+1 (4%)	MLCT
5	481.9	0.005	H → L+2 (56%), H-1 → L+1 (23%), H-2 → L+1 (17%)	MLCT

Table 3.17. Continued

N^a	λ_{calc} (nm)	f^b	Major Contributions^c	Assignment
7	458.0	0.044	H-1 → L+3 (29%), H → L+2 (16%), H-1 → L+1 (16%), H → L+3 (12%), H-1 → L+1 (9%), H-2 → L+1 (7%), H-2 → L+2 (4%),. H-2 → L (3%)	MLCT
8	455.9	0.001	H-2 → L (95%)	MLCT
9	450.5	0.021	H-2 → L+3 (43%), H-1 → L+3 (25%), H-1 → L+1 (8%), H-1 → L+2 (8%), H → L+2 (6%), H → L+3 (4%), H-2 → L+2 (3%)	MLCT
10	441.4	0.023	H-1 → L+2 (69%), H-1 → L+3 (27%)	MLCT
11	432.0	0.064	H-2→ L+2 (91%), H-1 →L+3 (3%), H-2 →L+3 (2%)	MLCT
12	419.5	0.275	H-3→ L (78%), H-2 →L+3 (9%), H-3 →L+4 (3%)	LC/MLCT
13	413.4	0.051	H-2 → L+3 (36%), H-3 → L (17%), H-1 → L+3 (9%), H → L+3 (8%), H-1 → L+2 (7%), H-1 → L+1 (5%), H-2 → L+1 (5%), H → L+5 (4%), H → L+9 (3%), H → L+2 (2%)	LC/MLCT

^{a} excited state number, ^{b} oscillator strength, ^{c} percent contribution = 2x(configuration coefficient)^{2}x100%.

Dark Stability Evaluation

All three complexes were evaluated for their dark stability in the presence of CD_3CN using ^1H NMR technique. ^1H NMR spectra were obtained at variable times to monitor structural changes associated with **2**-**4** and are depicted in Figure (3.21-3.23). The result of the experiments demonstrate that all three compounds are unstable in the dark

which is evident from the facile exchange of monodentate nitrile/pyridyl functional groups by CD_3CN. Compound **2** exhibits very fast exchange of coordinated CH_3CN (δ = 1.37 ppm) with CD_3CN which can be followed by the diminishing intensity of the singlet peak at 1.37 ppm with a concomitant appearance of a free CH_3CN peak at 1.96 ppm (Figure 3.21).[128] The exchange reaction can be predicted to be complete within 2 h period but there is no change observed for the aromatic proton resonances of the [Ru(tpy)(pbpy)] framework during the course of the reaction. This observation further supports our hypothesis that the phenyl ring on the pbpy ligand provides sufficient steric bulk to render the photocage structure very unstable.

Unlike **2**, compounds **3** and **4** are more stable and exhibit much slower exchange of the monodentate pyridyl functional group by CD_3CN. In fact, the photorelease of the pyridyl functional group is significantly less efficient than the nitrile analogue due to the formation of a stronger bond with the Ru center under similar experimental conditions.[77] The argument of strong bond formation can be employed to justify the slow exchange of pyridyl group by nitrile functionality. Between **3** and **4**, the latter exhibits faster exchange of pyridyl moiety (**PySNBD**), which is consistent with the greater structural distortion displayed in its crystal structure. For **4**, the exchange reaction is monitored by the disappearance of the coordinated **PySNBD** ligand peaks at δ = 4.44 ppm and 5.95 ppm with concomitant appearance of the free **PySNBD** ligand resonances at δ = 4.77 ppm and 6.18 ppm (Figure 3.23). Dissociation of **4** can be observed within 10 minutes and the reaction is predicted to be complete within 72 h period. In the case of **3**, the pyridine molecule is released as a result of the exchange so the reaction was tracked by the

143

appearance of free pyridine peaks at δ = 8.58 ppm (ortho-H), 7.74 ppm (para-H) and 7.33 ppm (meta-H) (Figure 3.22). Unlike **4**, no dissociation was detected for **3** within 10 minutes.
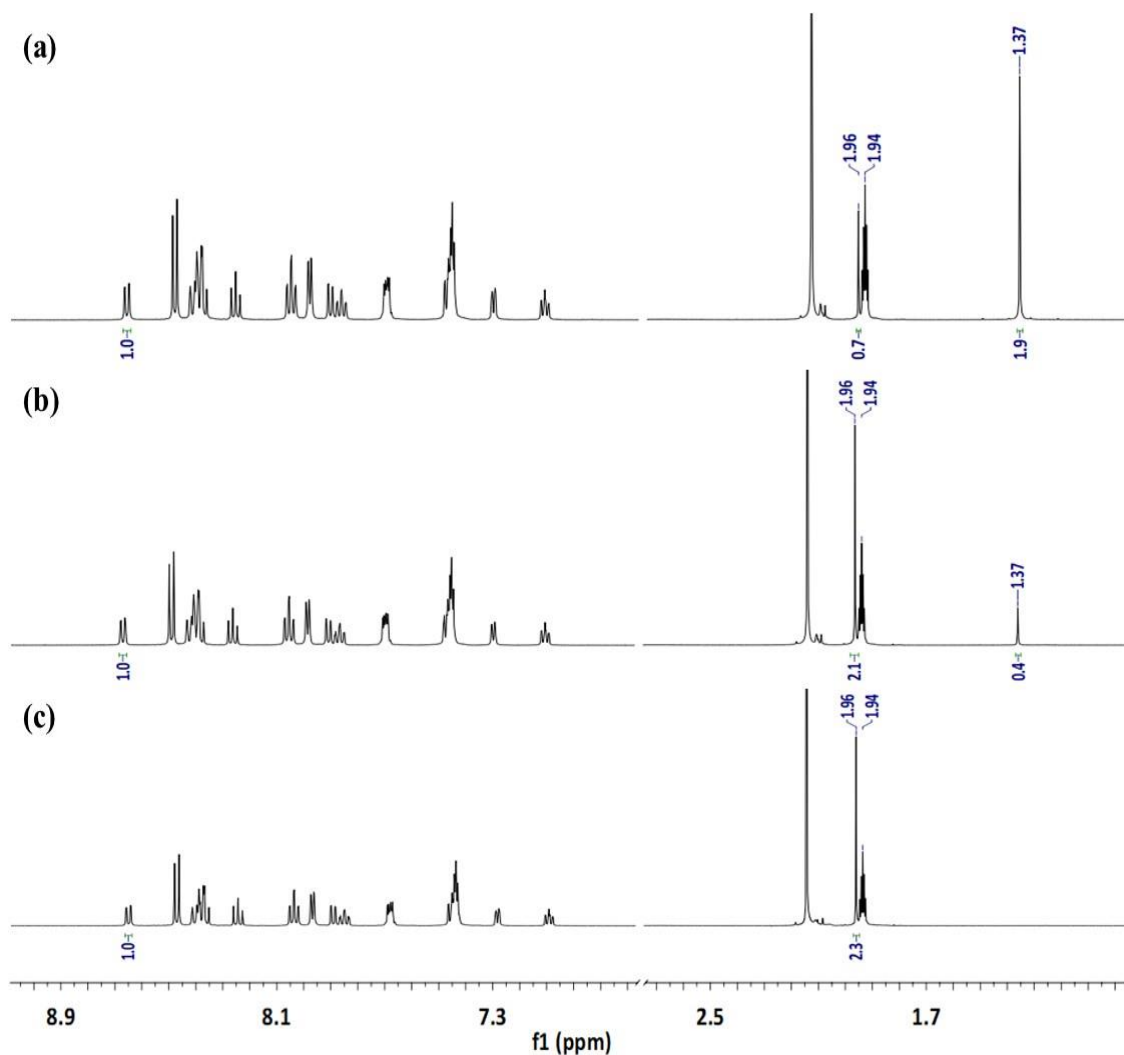
Figure 3.21. ^{1}H NMR spectra (CD$_3$CN, 500 MHz) of compound **2** in the dark after (a) 10 minutes, (b) 1 hour and (c) 24 hours.
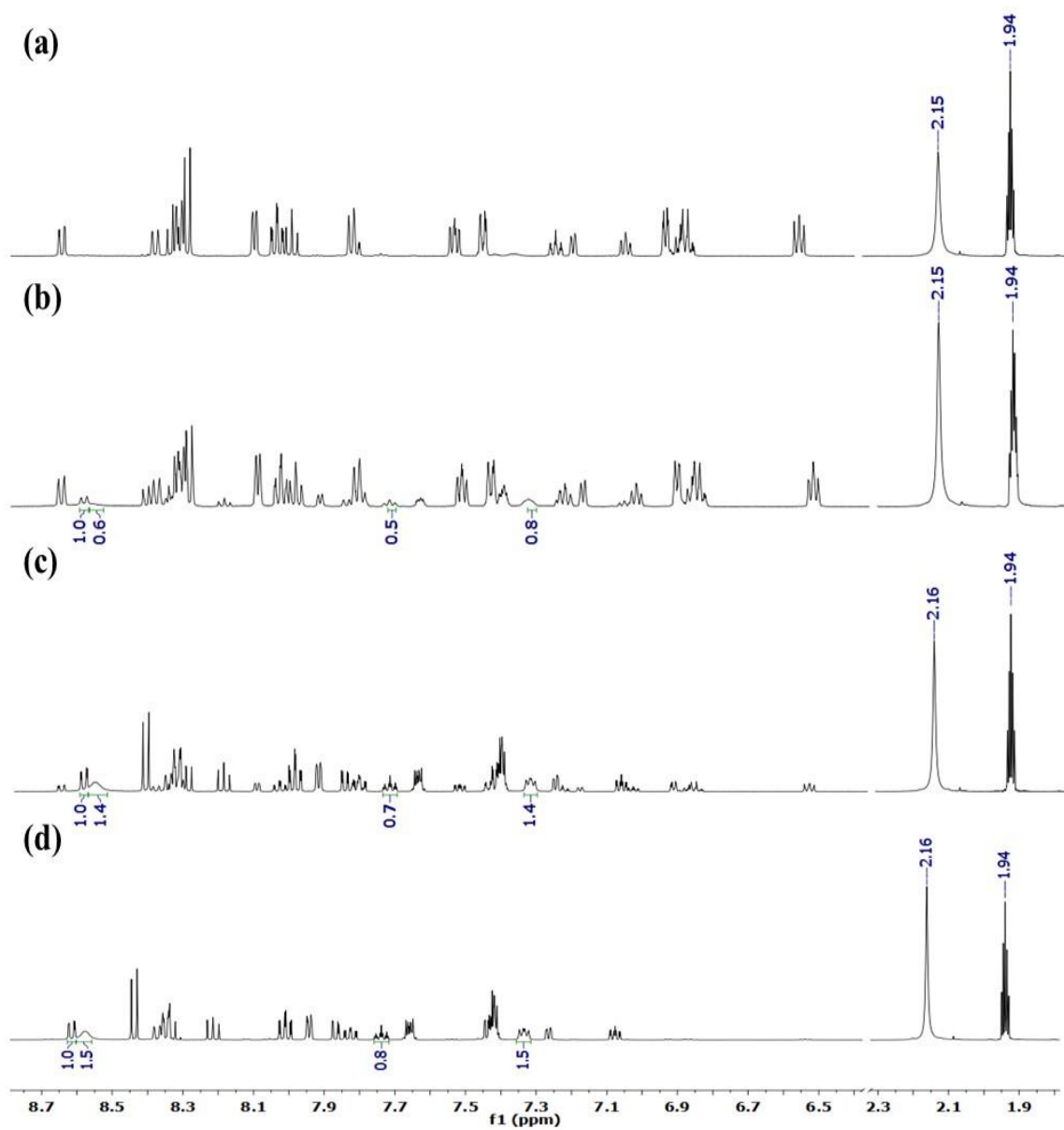
Figure 3.22. ^{1}H NMR spectra (CD$_3$CN, 500 MHz) of compound **3** in the dark after (a) 10 minutes, (b) 3 hours, (c) 24 hours and (d) 72 hours.
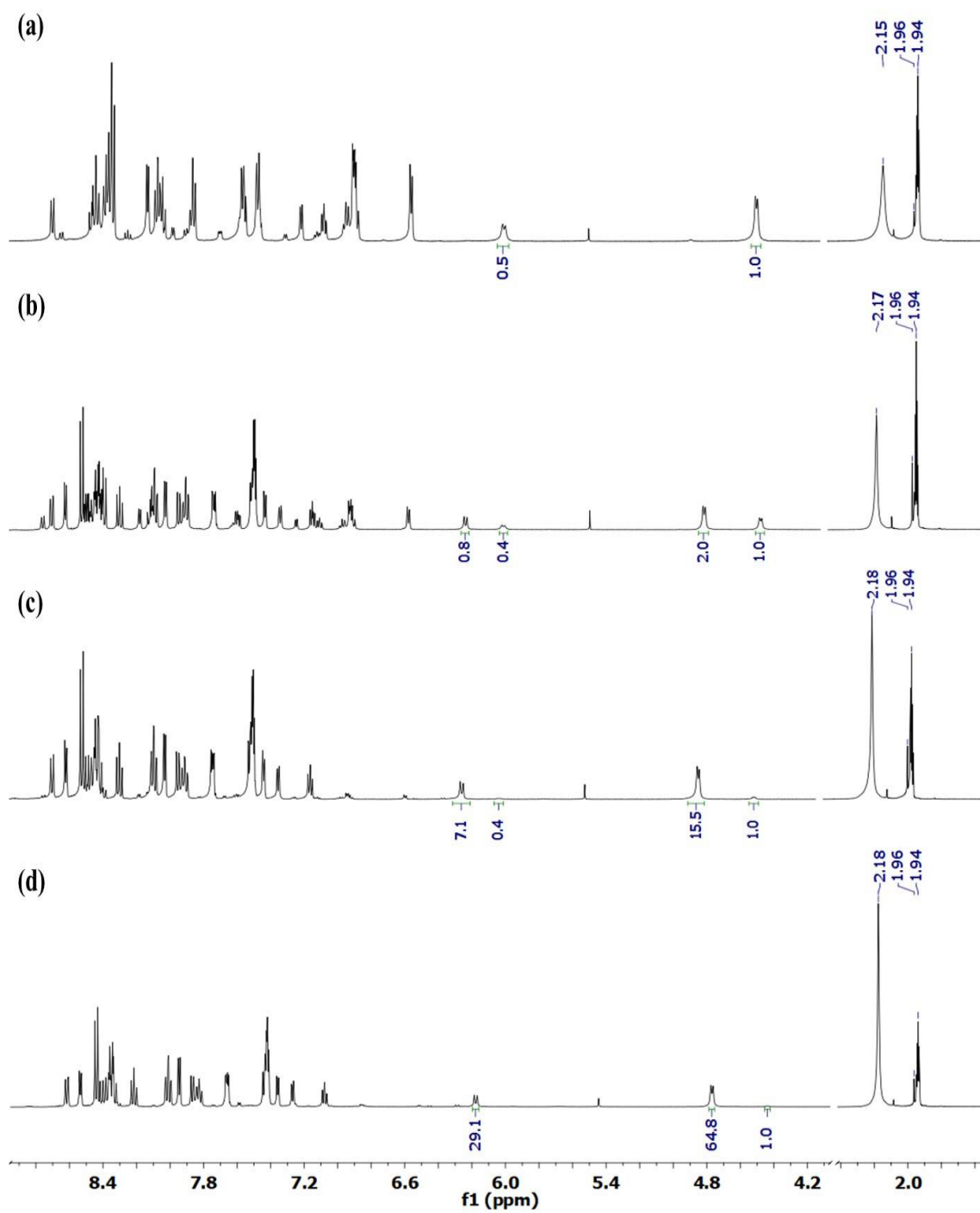
Figure 3.23. ^{1}H NMR spectra (CD$_3$CN, 500 MHz) of compound **4** in the dark after (a) 10 minutes, (b) 24 hours, (c) 72 hours and (d) 1 week.

146

Ethidium bromide stained agarose gel electrophoresis was used to demonstrate the covalent binding of cisplatin to double-stranded (ds) DNA which leads to noticeable decrease in the mobility of linearized pUC18 plasmid DNA.[93, 98] This technique is extensively employed to evaluate photoinduced DNA binding of Ru complexes possessing a photolabile moiety. When irradiated with a suitable visible light source, these complexes can release the photolabile moiety and the coordinately unsaturated metal fragment that is generated can bind to biomolecules in a manner akin to cisplatin.[68, 72-73, 75-76, 80] Compounds **2**-**4** were determined to be unstable in the dark with facile exchange of monodentate nitrile/pyridyl functional groups due to the steric effect of pbpy ligand. So, when dissolved in water/buffer during DNA binding evaluation, these complexes are predicted to be hydrolyzed even in the absence of light to form the mono-aqua species which is capable of covalently binding to ds DNA as in the case of cisplatin and also possibly π-stack with DNA using the phenyl ring on the pbpy ligand. Therefore, the interaction of **2**-**4** with ds DNA was assessed using ethidium bromide stained agarose gel electrophoresis with a linearized pUC18 plasmid DNA in the dark. Plasmid DNA was incubated in the dark with varying concentration of **2**-**4** for 24 h at 37°C as mentioned in the experimental section. Details of the lane distribution in each agarose gel can be found in Figure 3.24. As shown in Figure 3.24, **2** and **4** display lack of any covalent binding to DNA but the absence of a DNA signal shown by the loss of ethidium bromide staining at higher concentrations leads us to conclude that **2** and **4** demonstrate significant dose-

dependent DNA damage instead. In contrast, **3** exhibits strong binding with plasmid DNA by inducing a dose-dependent reduction in DNA mobility with less DNA damage detected at higher concentrations (Figure 3.24).
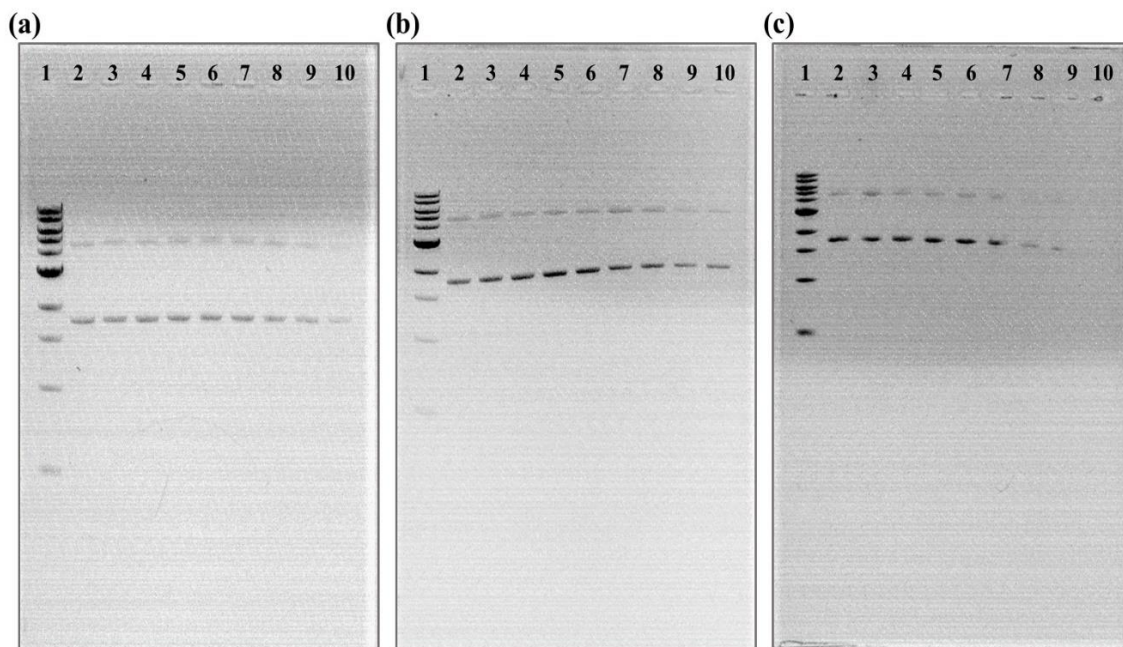
Figure 3.24. Imaged ethidium bromide stained agarose gels of linearized pUC18 plasmid DNA incubated for 24 h at 37°C with various concentrations of compounds **2-4** in the dark. (a) lane 1: 1kB DNA ladder; lane 2: linearized plasmid alone; lane 3: 1% DMSO; lanes 4-10: 2, 5, 10, 20, 50, 100, 200 μM of **2**; (b) lane 1: 1kB DNA ladder; lane 2: linearized plasmid alone; lane 3: 400 μM of pyridine; lanes 4-10: 2, 5, 10, 50, 100, 200, 400 μM of **3**; (c) lane 1: 1kB DNA ladder; lane 2: linearized plasmid alone; lane 3: 400 μM of **PySNBD** ligand; lanes 4-10: 2, 5, 10, 50, 100, 200, 400 μM of **4**.

Compound **3**, which is relatively more stable than the others, was chosen to further evaluate for its ability to photocleave DNA. Three working concentrations (5, 50, 200 μM) were selected to incubate with plasmid DNA in the dark ("Dark" sample) and in the presence of light ("Light" sample). The latter sample was irradiated with a Xe arc lamp source ($\lambda_{irr} \geq 395$ nm) for 1 h during which time the light orange-yellow color of **3** was

changed to pale purple, an indication of the formation of the parent cyclometallated complex **1**. As predicted for the Ru(II) photocage architecture, irradiation with visible light substantially facilitates the substitution of pyridine by water compared to its slow exchange in the dark. On the other hand, the pbpy ligand maintains its stereochemistry after the substitution which can favor the cyclometallation reaction upon losing a proton and substituting the weakly bound water to form **1**. So, **1** is likely the active species responsible for the DNA binding and DNA damage exhibited by the "Light" samples. Details of the lane distribution in each agarose gel are contained in Figure 3.25. Three assays were performed after irradiation at different incubation periods. In all three assays, the "Dark" samples in lanes (4-6) (Figure 3.25) displayed covalent binding with DNA similarly shown in Figure 3.24b. In contrast, the "Light" samples (Lanes 7-9) exhibit significant DNA damage at 50 µM and 200 µM range immediately after the irradiation which is evident from the partial or complete loss of DNA-ethidium bromide emission signal in Lanes 8 and 9 respectively. After incubation for 12 h and 24 h, there is not much change with respect to DNA damage other than the disappearance of the DNA signal in Lane 8 containing 50 µM of **3** in both assays (Figures 3.25b and 3.25c).
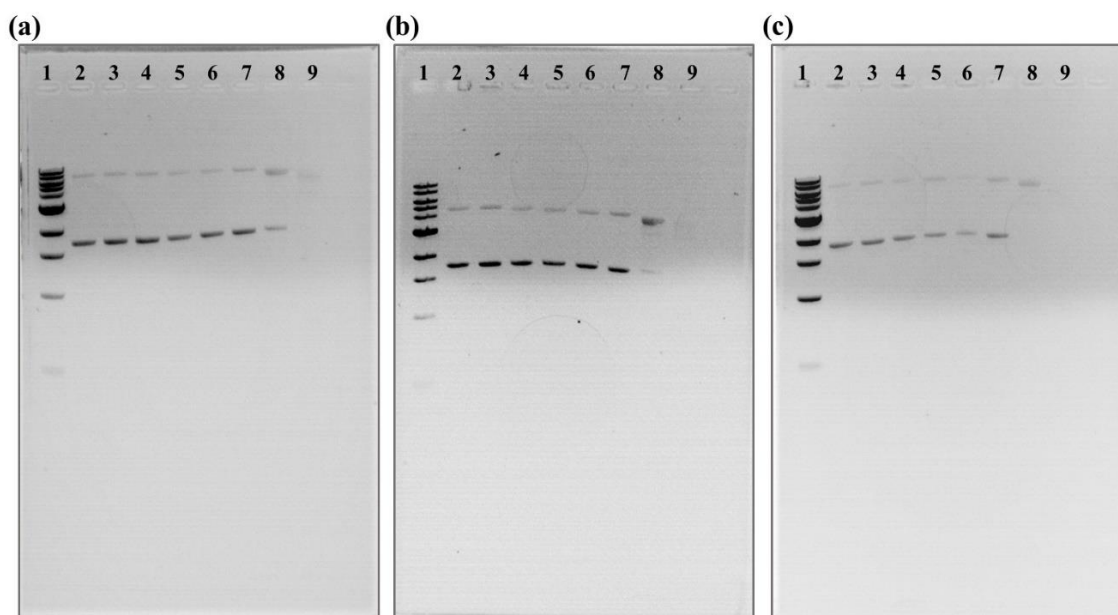
Figure 3.25. Imaged ethidium bromide stained agarose gels of linearized pUC18 plasmid DNA with various concentrations of compound **3** [lane 1: 1kB DNA ladder; lane 2: linearized plasmid alone; lane 3: 200 µM of pyridine; lanes 4-6: 5, 50, 200 µM of **3** without irradiation; lanes 7-9: 5, 50, 200 µM of **3** irradiated ($\lambda_{irr} \geq 395$ nm, 1 h)] after incubating for (a) 0 h (immediately after irradiation), (b) 12 h and (c) 24 h at 37°C.

Conclusions

The unusual bidentate coordination mode of pbpy ligand is utilized to design three new Ru(II) photocage structures possessing monodentate nitrile and pyridyl-functionalized caged molecules. All three complexes were synthesized in high yields and their purities were evaluated by ^{1}H NMR spectroscopy, mass spectrometry, elemental analyses and single crystal X-ray crystallography. The crystal structures reveal a distorted octahedral geometry around the Ru center with an unbound phenyl ring of the pbpy ligand pointing towards the metal center. This coordination motif generates steric congestion which facilitates the dissociation of the monodentate ligand even in absence of light as evidenced from ^{1}H NMR studies. The distorted solid-state structures are preserved in both gas and solvent phase optimized geometries as judged by DFT calculations. The electronic absorption spectra exhibit strong ^{1}MLCT bands between 400-500 nm with weak absorption tails that extend beyond 550 nm. The absorption profile of **4** is identical to the free fluorophore **PySNBD** in acetone. Due to lack of any conjugation, compound **4** retains its emissive property (λ_{ex} = 450 nm/ λ_{em} = 522 nm). The spectral properties and assignments were further verified by DFT and TDDFT calculations performed on the optimized geometries in the solvent phase. Due to severe steric effects, the coordinated monodentate ligand can be easily hydrolyzed in water/buffer to generate the mono-aqua species which can covalently bind with ds DNA akin to cisplatin. All three compounds display weak-to-moderate binding to plasmid DNA in a dose-dependent fashion as demonstrated by the reduction in DNA mobility in gel electrophoresis assays.

Additionally, **2** and **4** can potentially damage the DNA helical structure at higher concentrations. Compound **3**, when irradiated with visible light in the presence of plasmid DNA, exhibits photocleavage of DNA at 50μM as compared with dark samples. Light irradiation facilitates the formation of the cyclometallated starting material [Ru(tpy)(pbpy)]$^+$ (**1**), which is conceivably the active species responsible for the photocleavage of DNA. Although all three complexes demonstrate dissociation of the caged molecules even in absence of light, this unique coordination motif of the pbpy ligand constitutes a new architectural platform for designing sterically demanding Ru(II) photocage structures.

CHAPTER IV

ENHANCEMENT AND TUNING OF CYTOTOXIC PROPERTIES OF

CYCLOMETALLATED RUTHENIUM(II) COMPOUNDS

Introduction

Cancer is a disease characterized by uncontrolled cellular growth and is the second leading cause of death in the United States followed by heart related health issues. A drastic paradigm shift of cancer treatment occurred after the serendipitous discovery of cisplatin in the late 1960s, and, indeed, many current chemotherapeutic treatments rely on the administration of platinum chemotherapeutic drugs despite their detrimental side effects and tumor resistance.[7-8] To circumvent the limitations associated with these drugs, Ru compounds are being pursued as promising anticancer agents with lower systemic toxicity and effectiveness against Pt-resistant tumors. The initial success of NAMI-A and KP1019 in human clinical trials triggered further investigations of Ru compounds in cancer chemotherapy.[29-30, 173] Currently, most of the research is being focused on compounds with architectures similar to piano-stool Ru(II) arene scaffold pioneered by the Dyson and Sadler groups and the well-known Ru(II) polypyridyl complexes developed by a number of groups.[39, 67, 87, 95, 118, 124, 174-176]

More recently, cycloruthenated compounds, in which one nitrogen atom is replaced by a carbon anion, have emerged as an alternative to more traditional Ru(II) polypyridyl scaffolds. These compounds exhibit diverse applications ranging from

catalysis (C-H activation), to photosensitizers in dye sensitized solar cells (DSSC) and innovative anticancer therapies.[177-181]

The investigation of cyclometallated Ru complexes as anticancer agents was pioneered by Pfeffer and coworkers who demonstrated that they exhibit excellent antitumor properties with IC_{50} values surpassing the nanomolar barrier. It was found that the level of activity is directly correlated with the $Ru^{III/II}$ redox potentials and lipophilicity.[177, 182-183] Currently, octahedral heteroleptic cycloruthenated compounds are being explored for their applications as chemotherapeutic as well as PDT agents.[46, 60-61, 96-97, 175, 184-188] Chao *et al.* and Turro and Dunbar *et al.* explored this research by incorporating extended polypyridine ligands along with cyclometallating phpy ligand to further increase the lipophilicity of their compounds. The Chao group evaluated the anticancer activities of coordinatively unsaturated Ru(II) polypyridyl compounds with their cyclometallated analogues, [Ru(bpy)(CN)(NN)]$^+$ [CN = phpy and NN = imidazole, quinoxaline or phenazine-functionalized extended phenanthroline (phen) ligands], against both 2D cancer cell monolayers and 3D multicellular tumor spheroids (MCTSs). The study revealed that polypyridyl compounds are relatively inactive against most 2D cancer cell monolayers whereas all cyclometallated compounds exhibit higher activities than cisplatin as consequence of increased cellular uptake and higher lipophilicity.[185-186] The organometallic ruthenium dyes, [Ru(phpy)(NN)(N′N′)]$^+$ where NN and N′N′ = bpy, phendione (1,10-phenanthroline-5,6-dione), biq, dppn ligand, developed in the Dunbar laboratories are effective against HeLa cancer cells with similar or better cytotoxic properties than cisplatin at much shorter incubation periods. Additionally,

[Ru(phpy)(biq)$_2$]$^+$ exhibits enhanced activity upon irradiation with 633 nm light.[175] These studies support the hypothesis that the cytotoxic properties of cyclometallated Ru compounds can be further improved by tuning the lipophilicity of the ancillary ligands.

Specific to the topic of this chapter is the study of the versatile pbpy ligand which coordinates to ruthenium centers either as an anionic tridentate chelate to form the cyclometallated compound or in a bidentate neutral chelate fashion through the bipyridine moiety to form the non-cyclometallated compound.[163-164] The pbpy molecule and its substituted analogues have been used to prepare numerous cyclometallated compounds with applications as photosensitizers in DSSCs.[178, 180-181] Cyclometallated Ru scaffolds with coordinated pbpy ligands constitute a rich platform for the development of a variety of new drugs by modifications of the coordination environment through careful choice of ancillary ligands which can be used to tune their cytotoxicity and cellular uptake. Additionally, with bis-chelated Ru(II) complexes, geometrical isomers are possible which may have different activities against cancer cells. Chao *et al.* previously used the pbpy ligand to develop cyclometallated Ru(II) anthraquinone complexes that exhibit enhanced activities against hypoxic tumor cells. In these series of compounds, cyclometallation greatly increases the lipophilicity and the cellular uptake of the complexes by reducing the overall charge which is reflected in their much lower IC$_{50}$ values against both normoxic and hypoxic cancer cells as compared to their polypyridine analogues. The anthraquinone side-arm also imparts intercalating properties which leads to increased interactions with biomolecules.[187]

The efficacy of this class of compounds can be further enhanced by installing lipophilic moieties on the ancillary ligand, an effect that we explored by synthesizing four new cyclometallated Ru(II) complexes, *viz.*, [Ru(pbpy)(tpy)]$^+$ (**1**), [Ru(pbpy)(antpy)]$^+$ (**2**, antpy = 4′-(9-anthryl)-2,2′:6′,2″-terpyridine), [Ru(pbpy)(bpp)]$^+$ (**3**, bpp = 2,6-bis(N-pyrazolyl)pyridine) and [Ru(pbpy)(bdmpp)]$^+$ (**4**, bdmpp = 2,6-bis(3,5-dimethyl-N-pyrazolyl)pyridine) (Figure 4.1). The compounds were characterized by ^{1}H NMR spectroscopy, mass spectrometry, elemental analyses and single crystal X-ray crystallography. The electronic properties were investigated using electronic absorption spectroscopy and cyclic voltammetry and experimental observations were verified by DFT calculations. The compounds were evaluated for their cytotoxic properties against human lung adenocarcinoma (A549) cells and the mechanism of cell death was investigated with different biological assays.
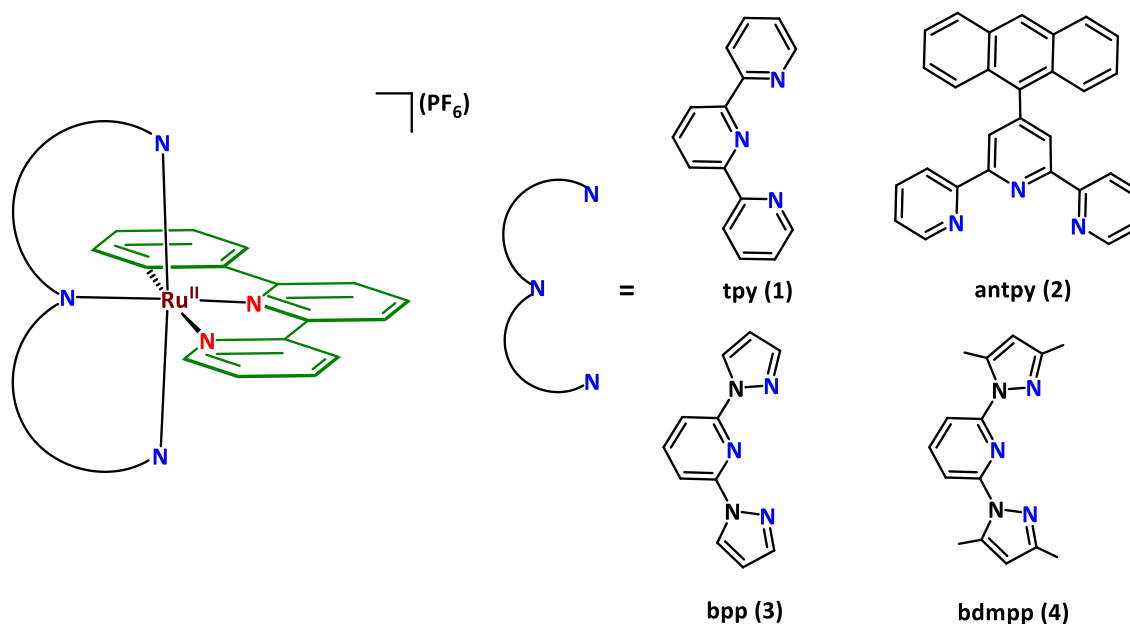
Figure 4.1. Schematic drawings of Ru(II) compounds with the cyclometallated pbpy ligand.

156

Experimental Section

General Methods

Reactions were conducted using standard Schlenk-line techniques to maintain anaerobic conditions in a N_2 atmosphere. All solvents were of reagent grade quality unless otherwise specified. Methanol, acetone, dichloromethane, diethyl ether, acetonitrile (Fisher Scientific) and ethanol (KOPTEC 200 proof) were used as received without further purification. Triethyl amine (EMD) was distilled and stored over KOH pellets (EMD). $RuCl_3 \cdot xH_2O$ (Pressure Chemicals Co.), 2,2′:6′,2′′-terpyridine (tpy, TCI and Beantown Chemicals) and NH_4PF_6 (Sigma Aldrich) were purchased and used as received. The ligands 6-phenyl-2,2′-bipyridine (pbpy),[164] 2,6-bis(N-pyrazolyl)pyridine (bpp),[189] 2,6-bis(3,5-dimethyl-N-pyrazolyl)pyridine (bdmpp)[189] and Ru(III)-precursor $[Ru(N_3)Cl_3]$ (N_3 = tpy, antpy, bpp, bdmpp)[166, 190-192] were synthesized in good yields following previously reported procedures. The 4′-(9-anthryl)-2,2′:6′,2′′-terpyridine (antpy) ligand was prepared by a modified literature procedure which produced improved yields.[193] For the synthesis of antpy ligand 2-acetylpyridine (Alfa Aesar), NaOH (EMD), aqueous NH_3 (EMD), PEG-300 (TCI) and 9-anthraldehyde (Sigma Aldrich) were used as received.

The ^{1}H NMR spectra were recorded on an Inova 500 MHz spectrometer. Chemical shifts are reported in δ (ppm) and coupling constants (J) in hertz (Hz). The residual solvent peaks were used as internal references ($\delta = 7.26$ for $CDCl_3$, $\delta = 2.05$ for $(CD_3)_2CO$, $\delta = 3.31$ for CD_3OD). Electrospray ionization (ESI) mass spectra were acquired on an Applied Biosystems PE SCIEX QSTAR mass spectrometer (MDS Sciex). Elemental analyses were performed by Atlantic Microlab, Inc. (Norcross, GA). Absorption spectra were recorded in acetonitrile on a Shimadzu UVPC-3001 spectrophotometer at room temperature. Electrochemical measurements were performed under anaerobic condition (N_2 atmosphere) with an HCH Electrochemical Analyzer model CH 1620A using a BAS Pt disk working electrode, a Pt wire auxiliary electrode, and a Ag/AgCl (3M $NaCl_{aq}$) reference electrode with 0.1 (M) tetra-*n*-butylammonium hexafluorophosphate ($[^nBu_4N](PF_6)$) in dry acetonitrile at a 0.1 V/s scan rate. The concentration of the Ru complexes for the electrochemical experiments was ~ 0.5 mM. Ferrocene was used as an internal standard and exhibited a $E_{1/2} = +0.44$ V *vs* Ag/AgCl for the Fc^+/Fc couple [ΔE_p for Fc^+/Fc couple= 80 mV] under the same experimental conditions. The $E_{1/2}$ values of the Ru complexes were referenced *vs* NHE using the following expression: $E_{1/2}$ *vs* NHE = [($E_{1/2}$ *vs* Ag/AgCl of Ru complex) + (0.64 − 0.44)] V, where 0.64 V = $E_{1/2}$ [Fc^+/Fc] *vs* NHE and 0.44 V = $E_{1/2}$ [Fc^+/Fc] *vs* Ag/AgCl.

Synthetic Details

4′-(9-anthryl)-2,2′:6′,2′′-terpyridine (antpy). 2-acetylpyridine (5g, 41.2 mmol) was added dropwise to a stirred suspension of crushed NaOH (1.65 g, 41.2 mmol) in PEG 300 (40 mL) at 0°C into which 9-anthraldehyde (4.249 g, 20.6 mmol) was added in portions followed by the addition of concentrated solution of aqueous NH_3 (25 mL). The reaction was stirred at room temperature for 1 h and then refluxed at 100°C for 24 h. The solution was cooled to room temperature and treated with water (100 mL) which yielded a dark yellow precipitate which was collected by filtration and washed with water until a neutral pH was achieved. The crude product was recrystallized from hot EtOH to obtain the antpy ligand as a pale white powder. Yield: 5.519 g (65%). ^1H NMR (500 MHz, $CDCl_3$): δ 8.81 – 8.77 (m, 2H), 8.63 (ddd, J = 4.7, 1.7, 0.8 Hz, 2H), 8.61 (s, 2H), 8.55 (s, 1H), 8.07 (d, J = 8.5 Hz, 2H), 7.92 (td, J = 7.8, 1.8 Hz, 2H), 7.71 (dd, J = 8.8, 0.7 Hz, 2H), 7.49 – 7.44 (m, 2H), 7.37 – 7.31 (m, 4H). ESI-MS(+): Calcd. for $C_{29}H_{19}N_3$ ([M+H]$^+$) 410.17, Found: 410.19.

[Ru(tpy)(pbpy)](Cl) (1). This compound was synthesized in higher yields by modifying a previously reported method.[163] [Ru(tpy)Cl₃] (257 mg, 0.583 mmol) and pbpy (136 mg, 0.583 mmol) were added to a Schlenk flask and treated with 32 mL of an EtOH:H_2O (3:1) mixture. Excess Et_3N (1 mL) was added to the mixture under N_2 which was refluxed for 15 h during which time the initial dark brown color slowly changed to dark purple. After cooling to room temperature, the solution was filtered through Celite® to remove unreacted [Ru(tpy)Cl₃] after which time the filtrate was reduced to dryness. The residue

159

was purified by flash column chromatography (Silica, MeOH/CH$_2$Cl$_2$, gradient 0% to 10% MeOH) and the dark purple band that was collected was reduced to ca. 10 mL. Upon addition of a hexane/diethyl ether mixture, a microcrystalline dark purple (almost black) solid was observed to form and the flask was stored in the refrigerator at 0°C for 1 h. The solid was collected by filtration, washed with hexane and diethyl ether and vacuum dried. Yield: 222 mg (63%). ^{1}H NMR (500 MHz, CD$_3$OD): δ 8.73 (d, J = 8.1 Hz, 2H), 8.57 (d, J = 8.2 Hz, 1H), 8.54 – 8.50 (m, 3H), 8.29 (d, J = 8.0 Hz, 1H), 8.12 – 8.06 (m, 2H), 7.88 (td, J = 8.1, 1.5 Hz, 1H), 7.82 (d, J = 7.1 Hz, 1H), 7.76 (td, J = 8.3, 1.4 Hz, 2H), 7.45 (d, J = 5.2 Hz, 1H), 7.42 (d, J = 5.6 Hz, 2H), 7.12 – 7.06 (m, 3H), 6.73 – 6.69 (m, 1H), 6.47 (td, J = 7.4, 1.1 Hz, 1H), 5.67 (d, J = 7.4 Hz, 1H). ESI-MS(+): Calcd. for [C$_{31}$H$_{22}$N$_5$Ru]$^+$ ([M − Cl]$^+$) 566.09. Found: 566.05. Single crystals suitable for X-ray diffraction were obtained by slow diffusion of diethyl ether into a dilute solution of **1** in (CHCl$_3$ and acetone). For further characterization and bio-evaluation studies, the Cl$^-$ anion was metathesized with PF$_6$$^-$ as the chloride salt is insoluble in PBS buffer even after the addition of 0.5% DMSO. Anal. Calcd. for C$_{31}$H$_{22}$F$_6$N$_5$PRu: C, 52.40; H, 3.12; N, 9.86. Found: C, 52.69; H, 3.07; N, 9.90.

[Ru(antpy)(pbpy)](Cl) (2). [Ru(antpy)Cl$_3$] (100 mg, 0.162 mmol) and pbpy (41.5 mg, 0.178 mmol) were suspended in 12 mL of MeOH:H$_2$O (5:1) mixture in a Schlenk flask. Excess Et$_3$N (1 mL) was added to the reaction mixture under N$_2$ and the solution was refluxed for 4 h which led to a gradual color change from the initial dark brown color to dark purple after 1 h. It was cooled to RT, filtered through Celite® to remove unreacted [Ru(antpy)Cl$_3$] and the filtrate was reduced to dryness. The residue was purified by flash

column chromatography (Silica, MeOH/CH$_2$Cl$_2$, gradient 0% to 10% MeOH) and a dark purple band was collected and reduced to ca. 5 mL, treated with a mixture of hexane and diethyl and refrigerated overnight. The resulting dark purple solid was collected by filtration, washed with hexane and diethyl ether and vacuum dried. Yield: 59 mg (47%). ^{1}H NMR (500 MHz, CD$_3$OD): δ 8.81 (s, 2H), 8.79 (s, 1H), 8.63 (d, J = 8.2 Hz, 1H), 8.55 (d, J = 7.8 Hz, 1H), 8.44 (d, J = 8.1 Hz, 2H), 8.28 (d, J = 7.9 Hz, 1H), 8.25 (dd, J = 6.4, 3.0 Hz, 2H), 8.13 – 8.09 (m, 2H), 7.97 – 7.93 (m, 2H), 7.84 (d, J = 7.2 Hz, 1H), 7.77 (d, J = 4.9 Hz, 1H), 7.69 – 7.65 (m, 2H), 7.63 – 7.60 (m, 4H), 7.49 (d, J = 5.3 Hz, 2H), 7.23 (ddd, J = 7.1, 5.4, 1.0 Hz, 1H), 7.11 – 7.07 (m, 2H), 6.80 – 6.76 (m, 1H), 6.65 (td, J = 7.3, 1.1 Hz, 1H), 5.97 (d, J = 6.8 Hz, 1H). ESI-MS(+): Calcd. for [C$_{45}$H$_{30}$N$_5$Ru]$^+$ ([M – Cl]$^+$) 742.15. Found: 742.15. Single crystals suitable for X-ray diffraction were obtained by slow diffusion of diethyl ether into a dilute solution of **2** in CHCl$_3$. For further characterization and bio-evaluation study, the Cl$^-$ anion was exchanged with PF$_6$$^-$ as the chloride salt is insoluble in PBS buffer even after the addition of 0.5% DMSO. Anal. Calcd. for C$_{45}$H$_{30}$F$_6$N$_5$PRu: C, 60.95; H, 3.41; N, 7.90. Found: C, 60.71; H, 3.41; N, 7.98.

[Ru(bpp)(pbpy)](PF$_6$) (3). [Ru(bpp)Cl$_3$] (170 mg, 0.406 mmol) and pbpy (95 mg, 0.406 mmol) were suspended in 24 mL of MeOH:H$_2$O (5:1) mixture in a Schlenk flask which led to a rapid color change from dark brown to dark green while purging with N$_2$. Upon addition of excess Et$_3$N (1 ml) the dark green color quickly turned to dark brown and the mixture was refluxed for 6 h. The solution was cooled to room temperature, filtered over Celite® to remove unreacted [Ru(bpp)Cl$_3$] and the filtrate was reduced to ca. 5 mL. The solution was added to a saturated aqueous solution of NH$_4$PF$_6$ which yielded a dark brown

precipitate which was collected by filtration, washed with water and diethyl ether and vacuum dried before purification. The crude product was purified by flash column chromatography (Basic Al_2O_3, MeCN/CH_2Cl_2, gradient 0% to 16% MeCN) and a dark reddish-brown band was collected and reduced to dryness. The residue was dissolved in acetone and, upon slow addition of diethyl ether, yielded a microcrystalline dark brown solid which was collected by filtration, washed with diethyl ether and vacuum dried. Yield: 109 mg (39%). ^{1}H NMR (500 MHz, $(CD_3)_2CO$): δ 9.06 (d, J = 3.1 Hz, 2H), 8.64 (d, J = 8.1 Hz, 1H), 8.48 (d, J = 7.8 Hz, 1H), 8.39 (d, J = 1.3 Hz, 1H), 8.38 (s, 1H), 8.32 (dd, J = 9.1, 7.1 Hz, 1H), 8.24 (d, J = 7.8 Hz, 1H), 8.09 – 8.04 (m, 2H), 8.00 (td, J = 7.8, 1.6 Hz, 1H), 7.84 (dd, J = 7.7, 1.0 Hz, 1H), 7.28 (ddd, J = 7.4, 5.3, 1.1 Hz, 1H), 7.02 (d, J = 2.1 Hz, 2H), 6.74 (td, J = 7.6, 1.2 Hz, 1H), 6.57 (dd, J = 7.3, 1.2 Hz, 1H), 6.54 (dd, J = 3.0, 2.1 Hz, 2H), 5.91 (dd, J = 7.4, 1.0 Hz, 1H). ESI-MS(+): Calcd. for $[C_{27}H_{20}N_7Ru]^+$ ($[M - PF_6]^+$) 544.08. Found: 544.06. Anal. Calcd. for $C_{27}H_{20}F_6N_7PRu$: C, 47.10; H, 2.93; N, 14.24. Found: C, 46.57; H, 2.97; N, 14.01. Single crystals suitable for X-ray diffraction were grown by the slow diffusion of diethyl ether into a dilute solution of **3** in acetone.

[Ru(bdmpp)(pbpy)](PF₆) (4). The compound was synthesized in a manner similar to **3** by using [Ru(bdmpp)Cl₃] (200 mg, 0.421 mmol) and pbpy (98 mg, 0.421 mmol). The crude product was purified by flash column chromatography (Basic Al_2O_3, MeCN/CH_2Cl_2, gradient 0% to 10% MeCN) and the dark reddish-brown band was collected and reduced to dryness. The residue was dissolved in acetone and slow addition of diethyl ether yielded a microcrystalline dark brown solid which was collected by filtration, washed with diethyl ether and vacuum dried. Yield: 157 mg (50%). ^{1}H NMR

(500 MHz, (CD$_3$)$_2$CO): δ 8.63 (d, J = 8.0 Hz, 1H), 8.53 (d, J = 7.9 Hz, 1H), 8.28 (d, J = 7.7 Hz, 1H), 8.22 – 8.14 (m, 3H), 8.08 – 8.05 (m, 1H), 8.05 – 8.01 (m, 2H), 7.86 (dd, J = 7.8, 1.1 Hz, 1H), 7.37 – 7.33 (m, 1H), 6.77 (td, J = 7.5, 1.2 Hz, 1H), 6.63 (td, J = 7.3, 1.3 Hz, 1H), 6.07 (s, 2H), 6.03 (dd, J = 7.4, 1.1 Hz, 1H), 2.92 (s, 6H), 1.30 (s, 6H). ESI-MS(+): Calcd. for [C$_{31}$H$_{28}$N$_7$Ru]$^+$ ([M–PF$_6$]$^+$) 600.14. Found: 600.12. Anal. Calcd. for C$_{31}$H$_{28}$F$_6$N$_7$PRu: C, 50.00; H, 3.79; N, 13.17. Found: C, 50.00; H, 3.77; N, 13.14. Single crystals suitable for X-ray diffraction were obtained by slow diffusion of diethyl ether into a dilute solution of **4** in an acetone/MeOH mixture.

X-Ray Crystallography

Single crystals of (**1**–**4**) were obtained as described in the experimental section. X-ray data of **1** were collected at 102.8 K on a Bruker D8-QUEST diffractometer equipped with a IμS Mo micro source (λ = 0.71073 Å). The data for **2**–**4** were collected at 110 K on a Bruker APEX II CCD X-ray diffractometer (Bruker-AXS, 2014) equipped with a graphite monochromated MoK$_\alpha$ radiation source (λ = 0.71073 Å). The data sets were integrated with the Bruker SAINT software package (SAINT v8.34A, Bruker, 2013).[136] Absorption corrections (SADABS)[137] were applied based on fitting a function to the empirical transmission surface as sampled by multiple equivalent measurements (SADABS-2012/1, Bruker, 2012). Solution and refinement of the crystal structures were carried out using the ShelX (2018/3) suite of programs [138-139] and the graphical interface OLEX 2.[140] All non-hydrogen atoms were refined with anisotropic displacement

parameters using full-matrix least-squares techniques on F^2. Hydrogen atoms were fixed to parent atoms and refined using the riding model. Idealized geometries were employed to model disordered $CHCl_3$ in **1** and **2**, the disordered diethyl ether solvent in **3**, and the disordered $(PF_6)^-$ anion and diethyl ether solvent in **4**.[141]

Structural Optimizations and TDDFT Calculations

The crystal structures of **1–4** were used as initial coordinates for the structural optimizations of the compounds in the gas phase with the Gaussian 09 program package[143] using the Becke's three -parameter exchange correlation functional and the Lee Yang and Parr correlation functional (B3LYP).[144,145] The Stuttgart RSC 1997 ECP basis set[146] was used for the Ru atoms and the 6-311G* basis set[147-148] was used for C, N and H atoms. The solvent phase geometry optimizations were performed by using SCRF calculations with SMD model (Truhlar's model)[149] in acetonitrile to incorporate solvent polarization effects with subsequent frequency analysis. The MOs were plotted with Ampac GUI 9 (Semichem, Inc; www.semichem.com) with an isovalue of 0.04. Fragment contributions to the MOs were calculated using the Chemissian v4.60 software (www.chemissian.com). TDDFT calculations were performed on the solvent optimized structures to compute electronic transitions from singlet ground states to singlet excited states using the SMD model with acetonitrile as the solvent.

Cell Culture Experiments

The human lung adenocarcinoma (A549) cell line, derived from type II pneumocytes (ATCC CCL-185), was obtained from American type culture collection (Manassas, VA). Cells were cultured in DMEM/F-12 medium (Dulbecco's Modified Eagle Medium/ Nutrient Mixture F-12, Sigma Aldrich) with 10% FBS and incubated in a humidified atmosphere containing 5% CO_2 at 37°C. They were approximately 80% confluent at the time of analysis.

In vitro *Cytotoxicity*

A549 cells were plated in a 96 well plate (Corning®) and pre-incubated in a humidified atmosphere containing 5% CO_2 at 37°C for 24 h. Solutions of the metal complexes in DMEM/F-12 medium (Sigma Aldrich) were added at different concentrations (final concentrations of compounds: 0–12.5 µM range, with less than 0.1 % DMSO) and the cells were incubated for another 48 h. After the incubation period, cells were then washed once with PBS and fixed with ethanol for 30 min. After fixation, Janus green B (1 mg/mL, Alfa Aesar) dissolved in PBS was added to each well and incubated at room temperature for 15 min. Cells were washed carefully with PBS (2 times) to remove any excess dye and 100 µL of ethanol was added to each well to extract the dye. The Janus Green B signal was then measured using a BioTek Synergy 4 plate reader set to an absorbance of 630 nm. Two experiments were conducted on different days with each

experiment having 8 replicates per concentration. The absorbance of Janus Green B is directly proportional to the number of living cells.

JC-1 Assay

Live cell imaging studies were performed using a Zeiss 510 META NLO multiphoton system consisting of an Axiovert 200 MOT inverted laser scanning confocal microscope (Carl Zeiss Microimaging, Thornwood, NY). A Zeiss Plan-Neofluar 40x/NA=1.3 oil immersion objective was used to acquire the images.

Cells were plated in Nunc Lab-Tek II chambered cover-glass slides (Thermo Scientific™) prior to treatment with compounds **1**–**4** and incubated for 48 h. Cells were then washed with PBS and labeled with the mitochondrial membrane potential probe, JC-1 (Invitrogen™) at a final concentration of 5 µg/mL for 30 min at 37°C and washed with PBS before cellular imaging. Excitation of JC-1 was performed using an Argon ion laser at 488 nm and emission data were collected using a dichroic 545 nm SP in combination with 2 filters 500–550 BP (green signal) and 565–615 BP (red signal). At least eight areas per well were scanned and two wells were analyzed per treatment. Two experiments were conducted on different days. The ratio of red signal/green signal was used as an indicator of cellular mitochondria membrane potential.

DCFH-DA Assay (2',7'-dichlorodihydrofluorescein diacetate Assay)

A549 cells were plated in a 96 well plate (Corning®) and pre-incubated in a humidified atmosphere containing 5% CO_2 at 37°C for 24 h. Solutions of the metal complexes in DMEM/F-12 medium (Sigma Aldrich) were added at different concentrations (final concentrations of compounds: 0–12.5 µM range, with less than 0.1 % DMSO) and the cells were incubated for another 48 h. After the incubation period, cells were washed once with PBS. A solution of DCFH-DA (10 µM, Life Technologies) in PBS was added to each well and incubated at 37°C for 30 min. The fluorescence signal of *in situ* generated DCF (2′,7′-dichlorofluorescein) was then measured at $\lambda_{em} = 530$ nm using a BioTek Synergy 4 plate reader set to excitation at $\lambda_{ex} = 485$ nm. Two experiments were conducted on different days with each experiment having 8 replicates per concentration. The fluorescence intensity of DCF is directly proportional to the level of ROS detected inside the cell.

ApoTox-Glo™ Triplex Assay

A549 cells were plated in a 96 well plate (Corning®) and pre-incubated in a humidified atmosphere containing 5% CO_2 at 37°C for 24 h. Solutions of the metal complexes in DMEM/F-12 medium (Sigma Aldrich) were added at different concentrations (final concentrations of compounds: 0–2 µM range, with less than 0.1 % DMSO) and the cells were incubated for another 48 h. Viability/Cytotoxicity Reagent and

Caspase-Glo® 3/7 Reagent (Promega) were prepared following the protocol. After the incubation period, cells were washed once with PBS and 100 µL of PBS was added to each well followed by addition of 20 µL of Viability/Cytotoxicity Reagent. The reagents were mixed briefly by orbital shaking and the plate was incubated at 37°C for 30 minutes. Fluorescence was measured at λ_{em} = 505 nm (for viability assay) and at λ_{em} = 520 nm (for cytotoxicity assay) using a BioTek Synergy 4 plate reader set to excitation at λ_{ex} = 400 nm and at λ_{ex} = 485 nm respectively. Then 100 µL of Caspase-Glo® 3/7 Reagent was added to each well, the reagents were mixed by orbital shaking and incubated at room temperature for 30 minutes. Luminescence was measured using a BioTek Synergy 4 plate reader. One experiment was conducted for each chemical with each experiment having 5 replicates per concentration. To further evaluate chemical **4**, temporal ApoTox-Glo™ Triplex Assay was performed with multiple exposure periods (8, 12, 24 and 48 h) following a similar protocol. One experiment was conducted for each exposure period with each experiment having 5 replicates per concentration. In an ideal case when a compound is cytotoxic and activates caspase-3/7 inside the cell, viability and cytotoxicity will be inversely correlated with a dose-dependent increase of apoptosis luminescence signal.

Results and Discussion

Synthesis and Characterization

pbpy ligand can coordinate to ruthenium ions either as an anionic tridentate chelate (**C^N^N**) to form cyclometallated compounds or in a bidentate neutral chelate (**N^N**) by utilizing the bipyridine moiety to form non-cyclometallated compounds.[163-164] The binding mode of the pbpy ligand is highly solvent dependent and the use of high dielectric solvents such as aqueous MeOH/EtOH or DMF favors the formation of cyclometallated compounds (Figure 4.2).[163] The synthesis of cyclometallated complexes **1**–**4** require longer reaction times than their polypyridyl congeners due to the required C-H bond activation step, but their preparation can nevertheless be achieved under relatively mild condition. A typical synthetic route for the preparation of bis-heteroleptic cyclometallated Ru(II) complexes commonly involves initial coordination of the ancillary polypyridyl ligand (**N^N^N**) to Ru in the first step followed by introduction of the cyclometallating ligand (**C^N^N**), often in presence of a base and a sacrificial reducing agent.[179, 194] For the synthesis of **1**–**4**, the Ru(III) precursors, *viz.*, [Ru^{III}(N$_3$)Cl$_3$] (N$_3$ = tpy, antpy, bpp, bdmpp)[166, 190-192], were isolated first by refluxing a 1:1 mixture of RuCl$_3$.3H$_2$O and the respective ancillary ligands (tpy, antpy, bpp, bdmpp) in EtOH (Figure 4.2). In the next step, cyclometallation of the pbpy ligand was achieved by refluxing a 1:1 molar ratio of the Ru(III) precursor:pbpy ligand in a refluxing (MeOH/EtOH+H$_2$O) solvent mixture. The Et$_3$N, which was used to deprotonate pbpy ligand, also acts as a sacrificial reductant to

facilitate the reduction of Ru(III) to Ru(II) under a N_2 environment (Figure 4.2). The yields of the cyclometallated complexes are considerably lower (**1**, 63%; **2**, 47%; **3**, 39%; **4**, 50%) compared to polypyridyl analogues, partly due to the additional chromatographic purification step to separate the desired compound from the byproduct bis-homoleptic analogues (*viz.* [Ru(N^N^N)$_2$]$^{2+}$) and non-cyclometallated derivatives.[163, 179] Compounds **1** and **2** were first isolated as the dark purple Cl$^-$ salt after chromatographic purification and later metathesized to the PF$_6$$^-$ salt after treatment with aqueous NH$_4$PF$_6$. Compounds **3** and **4** were precipitated with aqueous NH$_4$PF$_6$ and isolated as dark brown microcrystalline solids after chromatographic purification.
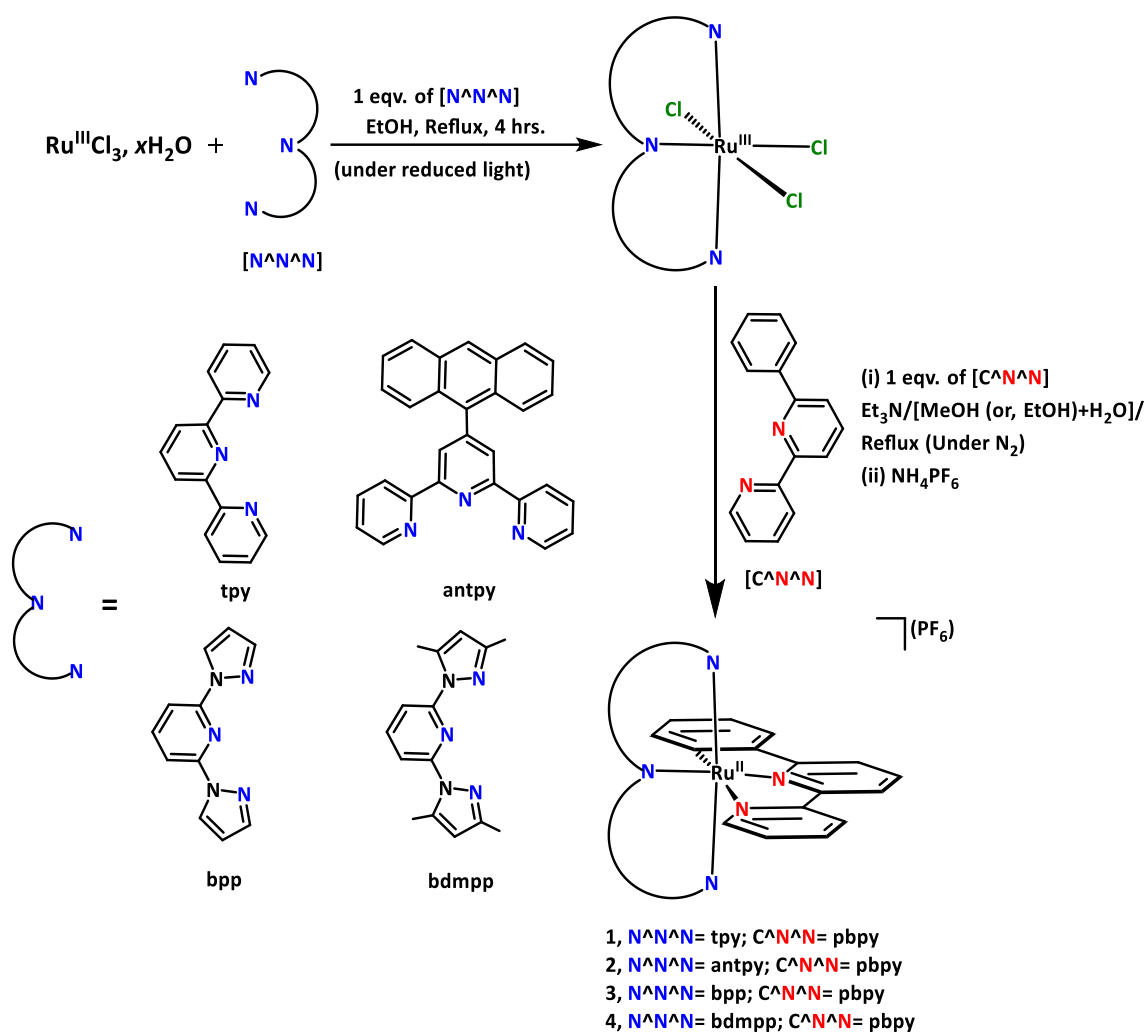
Figure 4.2. Reaction schemes for the syntheses of **1**–**4**.

The purity of the compounds was confirmed by ^{1}H NMR spectroscopy, ESI mass spectrometry and elemental analyses. The NMR spectra are consistent with C_{2v} molecular symmetry for all four compounds as one-half of the protons on the ancillary ligands (tpy[163, 194], antpy, bpp, bdmpp) are magnetically equivalent. Most importantly, cyclometallation has a dramatic influence on the resonance of the protons *ortho* and *para* to the C_{aryl} atom bound to Ru center.[179, 187] For example, the *ortho* proton in **1** is shifted upfield by 1.67 ppm (appears at 5.67 ppm, Figure 4.4) compared to its non-cyclometallating analogue

$[Ru(tpy)_2]^{2+,}$[179] which is ascribed to the decrease of positive charge on the metal center due to cyclometallation. The other compounds also exhibit significant shifts in the *ortho* proton resonances which appear close to 6 ppm (5.97 ppm for **2**; 5.91 ppm for **3**; 6.03 ppm for **4**) (Figure 4.5-4.7). The NMR spectra also confirm that all four complexes possess diamagnetic Ru(II) centers. The integration values of the peaks match the total proton count (**1**, 22H; **2**, 30H; **3**, 20H; **4**, 28H) for all compounds, indicating the formation of the desired molecules (Figure 4.4-4.7). In the ESI mass spectra, a single molecular ion peak corresponding to $[M–X]^+$ (where $X= Cl^-$ for compound **1** and **2** and $X= PF_6^-$ for compound **3** and **4**) cations is observed for all of the compounds (**1**, m/z=566.05; **2**, m/z=742.15; **3**, m/z=544.06; **1**, m/z=600.12) (Figure 4.8-4.11).

(a)
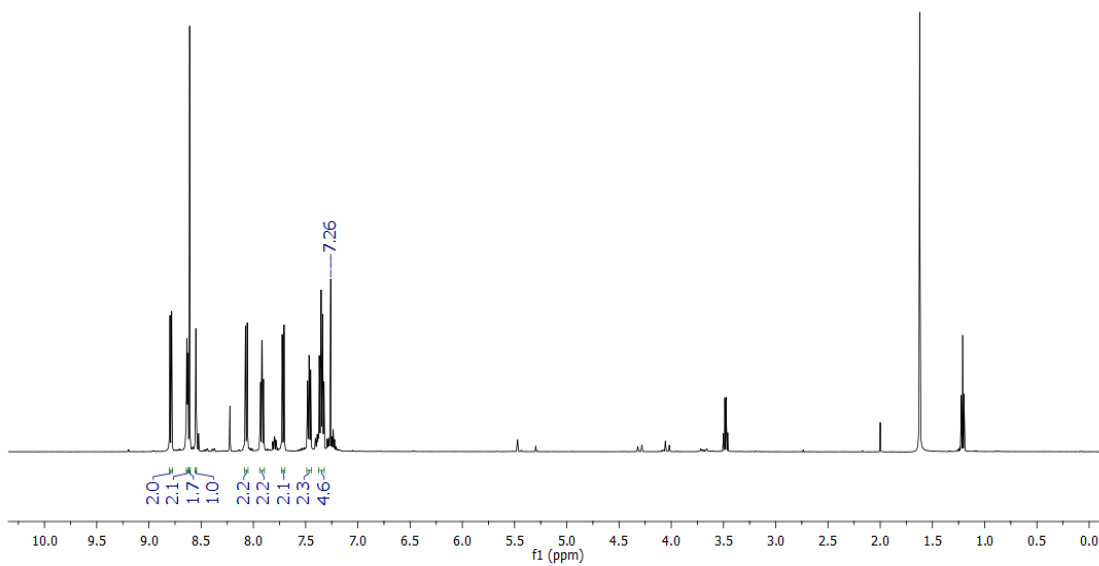
(b)
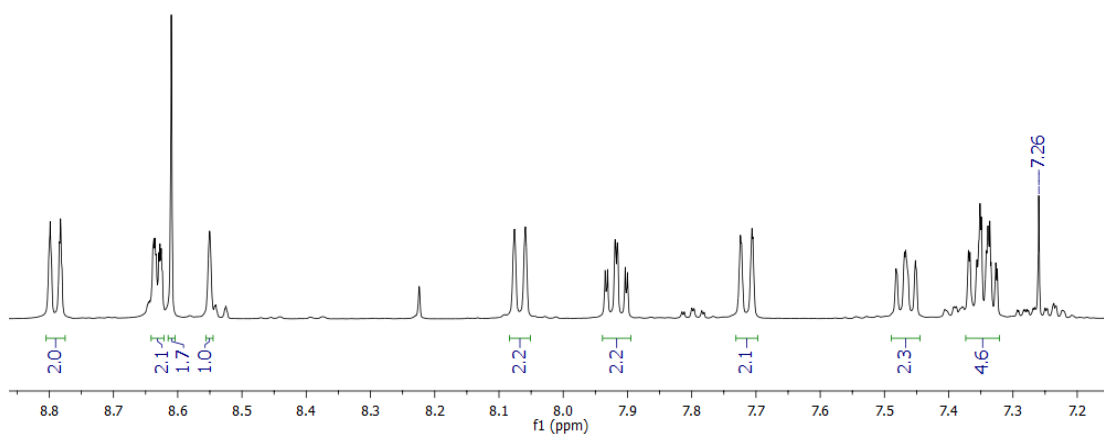
Figure 4.3. ^{1}H NMR spectra (CDCl$_3$, 500 MHz) of the **antpy** ligand (a) full spectrum, (b) enlarged aromatic region.
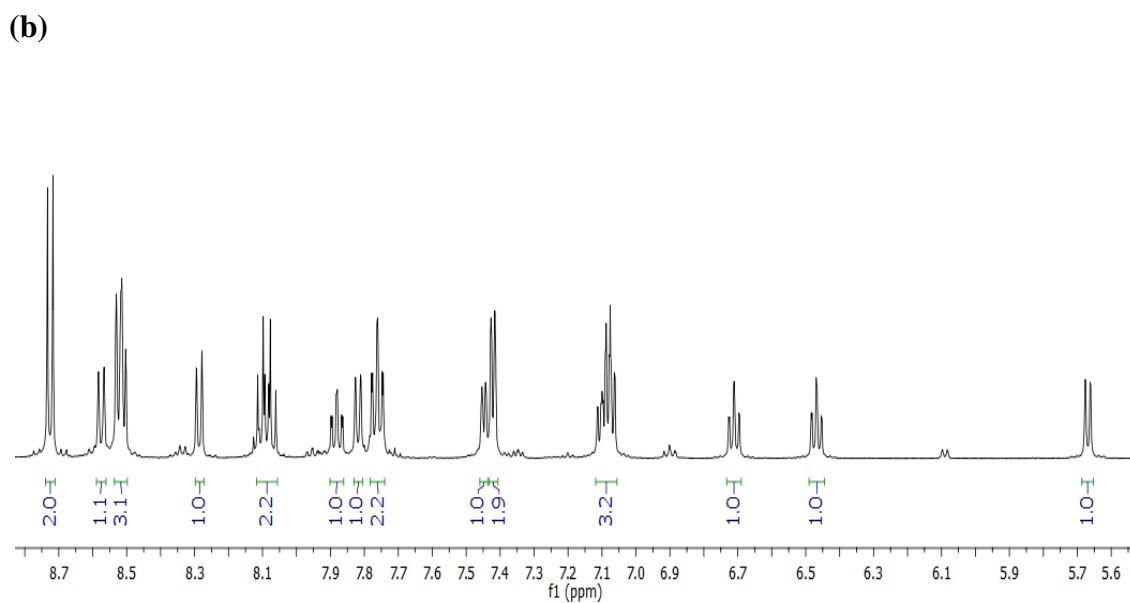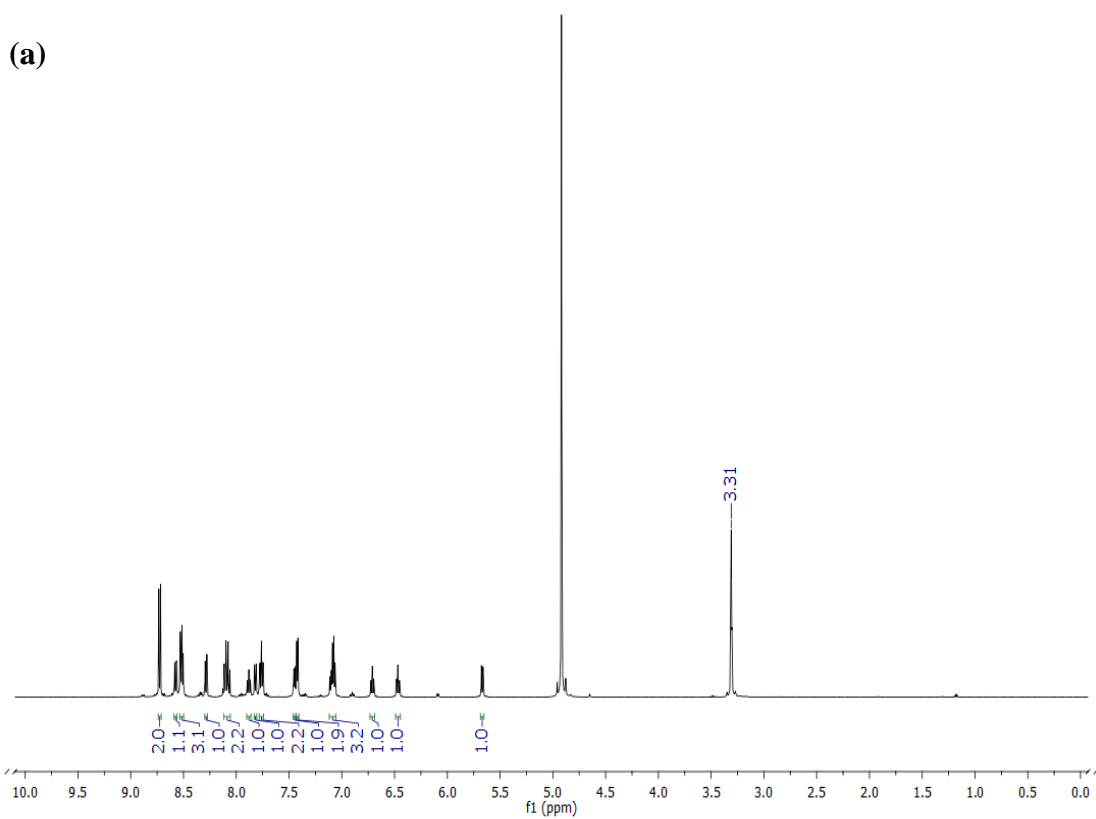
Figure 4.4. ^{1}H NMR spectra (CD$_3$OD, 500 MHz) of compound **1** (a) full spectrum, (b) enlarged aromatic region.
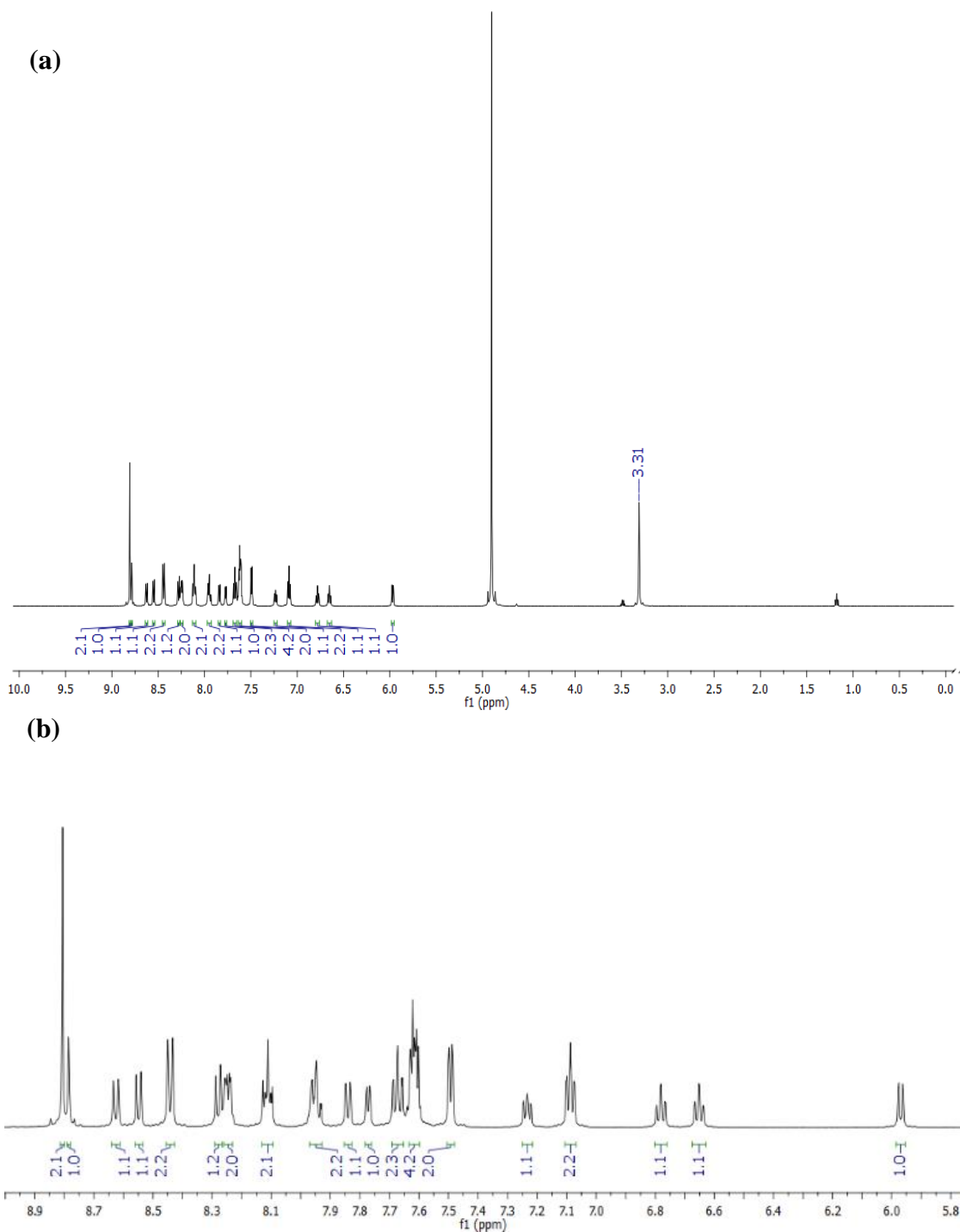
Figure 4.5. ^{1}H NMR spectra (CD$_3$OD, 500 MHz) of compound **2** (a) full spectrum, (b) enlarged aromatic region.
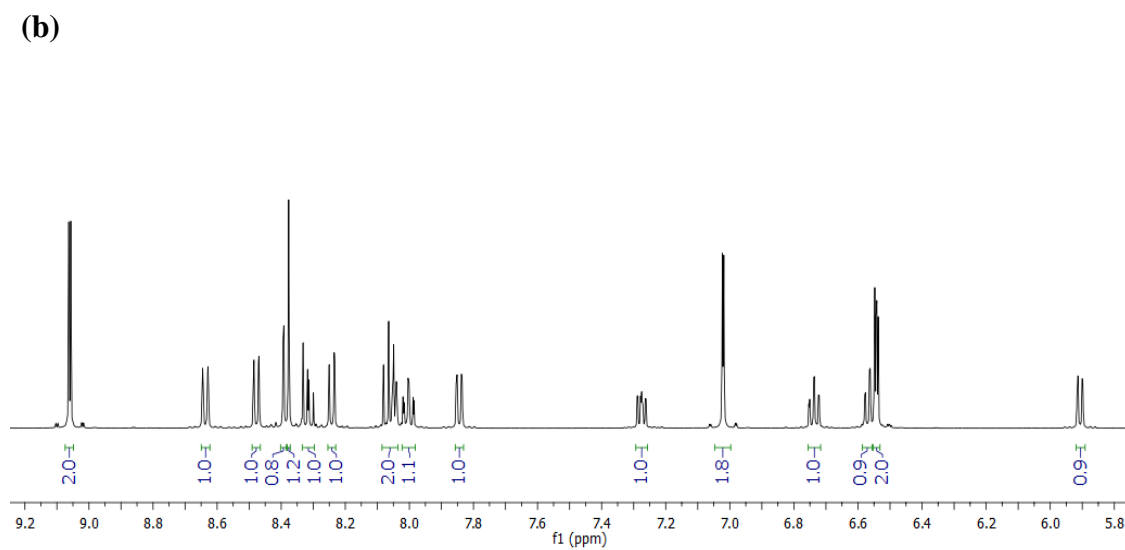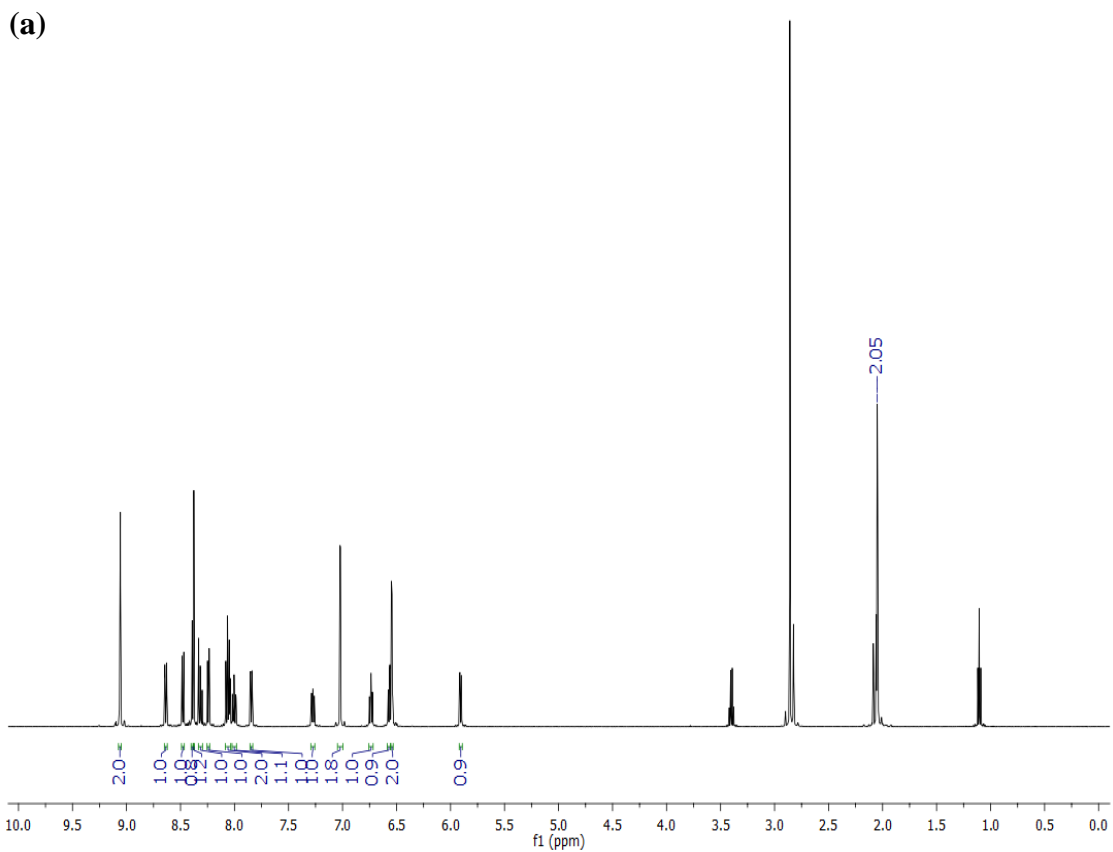
Figure 4.6. ^{1}H NMR spectra ($(CD_3)_2CO$, 500 MHz) of compound **3** (a) full spectrum, (b) enlarged aromatic region.
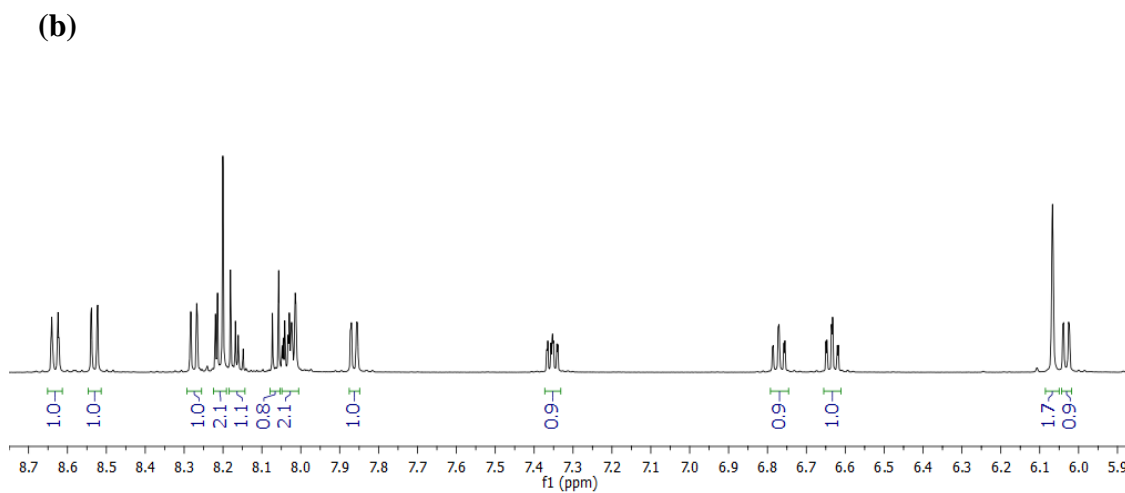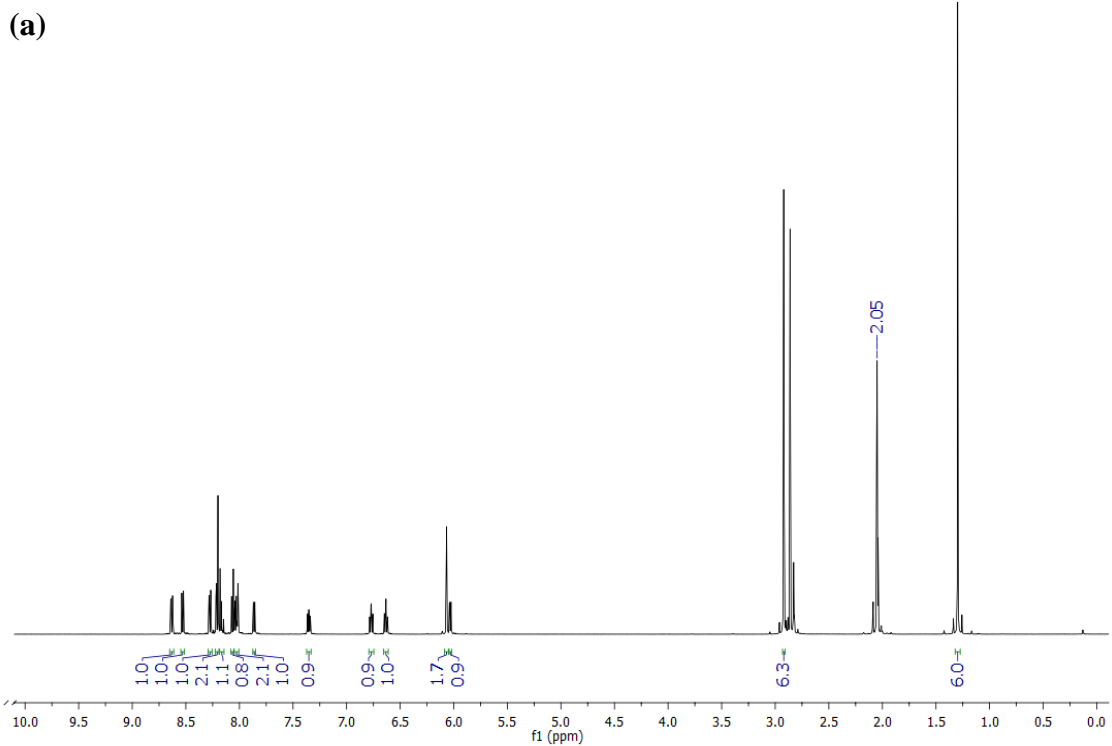
Figure 4.7. ¹H NMR spectra ((CD₃)₂CO, 500 MHz) of compound **4** (a) full spectrum, (b) enlarged aromatic region.
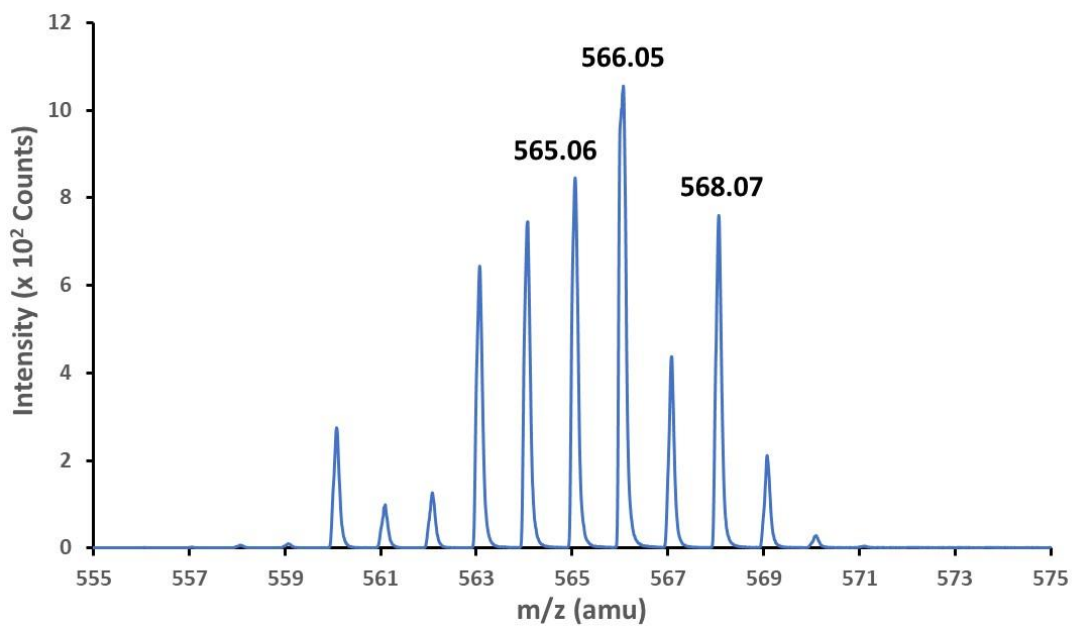
Figure 4.8. (+) ESI-MS spectrum of **1** showing the molecular ion peak of [Ru(tpy)(pbpy)]$^+$.
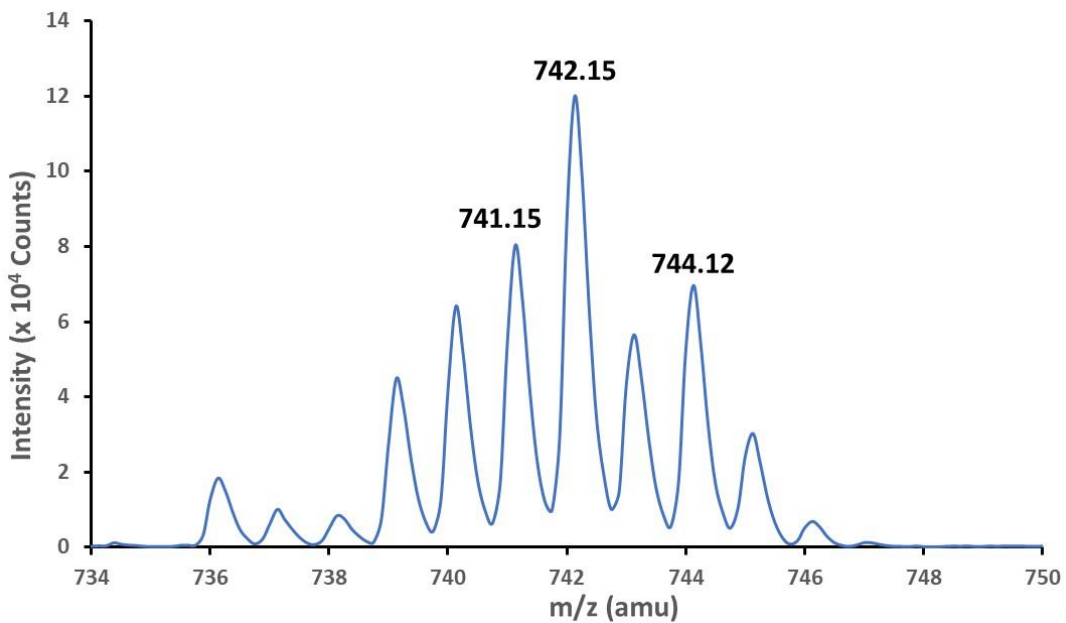
Figure 4.9. (+) ESI-MS spectrum of **2** showing the molecular ion peak of [Ru(antpy)(pbpy)]$^+$.
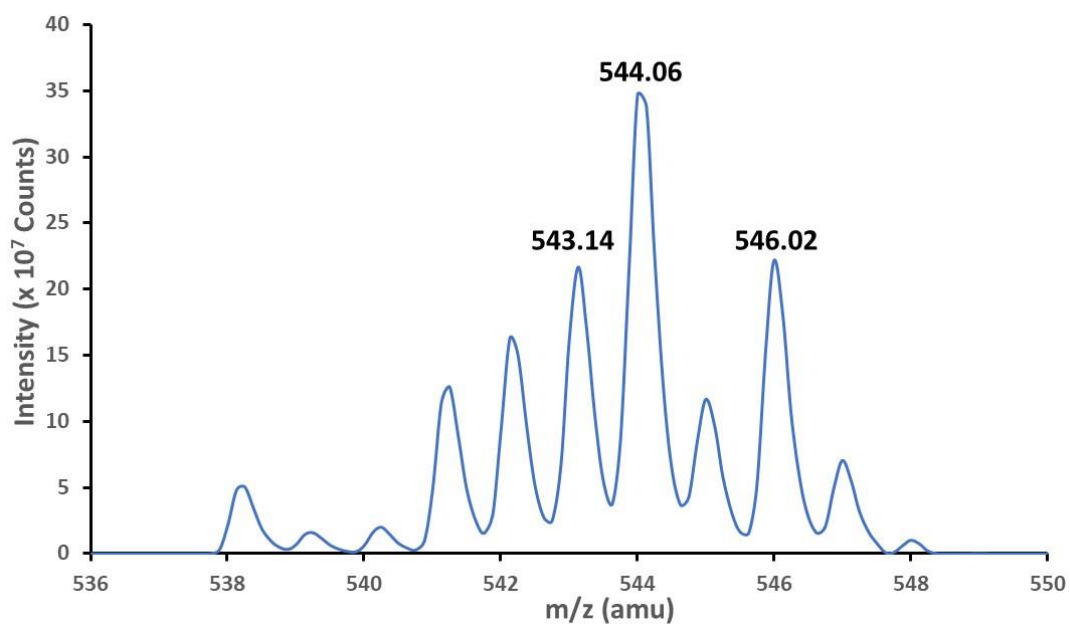
Figure 4.10. (+) ESI-MS spectrum of **3** showing the molecular ion peak of [Ru(bpp)(pbpy)]⁺.
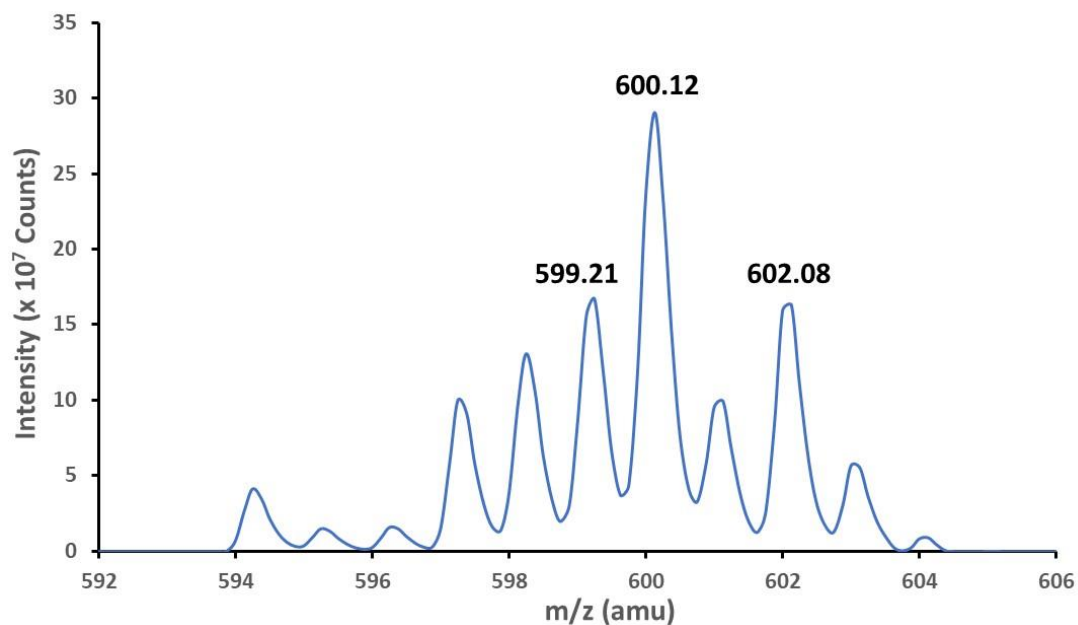
Figure 4.11. (+) ESI-MS spectrum of **4** showing the molecular ion peak of [Ru(bdmpp)(pbpy)]⁺.

Crystal Structure Determination

Single crystals suitable for X-ray diffraction were grown for all four compounds as described in the experimental section; the molecular structures are depicted in Figure (4.12-4.15). Compound **1** and **3** are structurally very similar and both crystallize in the orthorhombic *P*bca space group whereas compounds **2** and **4** crystallize in the monoclinic $P2_1$/c space group. Crystal data and refinement parameters along with all Ru-N(C) bond distances and some representative bond angles are compiled in Table (4.1-4.6). All four structures exhibit tridentate meridional binding of the ancillary ligands (tpy, antpy, bpp, bdmpp) and the cyclometallated pbpy ligand to form bis-chelates. Each planar ancillary ligand is oriented perpendicular to the plane of the coordinated pbpy ligand. The coordination sphere of each Ru center is surrounded by five N atoms and one anionic C atom in a distorted octahedral geometry, which is evident from the Ru-N(C) distances in Table (4.3-4.6). The Ru–N bond ranges from 1.937 (6) – 2.182 (4) Å whereas Ru–C bond ranges from 2.017 (6) – 2.034 (4) Å. Both bond distances are in good agreement with cyclometallated ruthenium (II) complexes containing pbpy ligands and its substituted analogues.[184, 194-196] The peripheral pyridyl/pyrazolyl rings on the ancillary ligands are distal from the metal center with longer Ru-N bonds (more than 2 Å) which result in a contraction of the central Ru-N bond (less than 2 Å). In fact, the bond between Ru and the central pyridine-N (Ru1-N2 for **1** and **2** and Ru1-N3 for compound **3** and **4**) of the ancillary ligands is the shortest (1.937(6) – 1.973(5) Å) among all Ru-N bonds in (**1-4**). In the case of the cyclometallated pbpy ligand, a pronounced trans influence of the anionic carbon

results in an elongation of the opposite Ru-N bond (2.146 (3) – 2.182 (4) Å).[184, 194-196] Overall, the shorter central nitrogen to ruthenium distance can be explained by the efficient overlap between the metal t_{2g} orbital with the π^*-orbital of the central pyridine ring.[197] The intra-ligand *trans* angles, *viz.*, N1-Ru1-N3(N5) and N4(N6)-Ru1-C for ancillary ligands and the pbpy ligand respectively are distorted significantly from linearity [156.61(16) – 159.1 (2)º], but are within the range of the corresponding angles reported for other cyclometallated Ru complexes.[184, 194-195] In compound **2**, the 9-anthracenyl subunit deviates from coplanarity with the attached terpyridine moiety. The twisted conformation about the inter-annular C-C bond (torsion angle = 65.8(9)º), alleviates non-bonded steric interactions between the H atoms at the 1-and 8-positions of the anthryl ring and those of the central pyridine ring on the terpyridine moiety but also diminishes the conjugation between the aromatic rings. Overall, the non-coplanar arrangement leads to the lowest conformational energy for the molecule.[198] Similar twisting of the 9-anthryl subunit is observed for antpy coordinated Ru(II) complexes.[190]

Table 4.1. Crystal data and refinement parameters for **1** and **2**.

Compound	1	2
Empirical Formula	$C_{32}H_{23}Cl_4N_5Ru$	$C_{48.03}H_{33.01}Cl_{10.02}N_5Ru$
Formula weight	720.42	1135.96
Temperature, K	102.79(2)	110(2)
Crystal system	Orthorhombic	Monoclinic
Space group	*P*bca	*P*2$_1$/c
Unit cell dimensions	$a = 13.4569(5)$ Å, $\alpha = 90°$ $b = 15.0703(5)$ Å, $\beta = 90°$ $c = 30.0154(10)$ Å, $\gamma = 90°$	$a = 21.187(6)$ Å, $\alpha = 90°$ $b = 14.966(4)$ Å, $\beta = 141.981(3)°$ $c = 24.636(7)$ Å, $\gamma = 90°$
Volume, Å^3	6087.1(4)	4811(2)
Z	8	4
Density, g/cm^3	1.572	1.568
Absorption coefficient, mm^{-1}	0.898	0.923
F(000)	2896	2281
Crystal color, morphology	dark purple, block	dark purple, plate
Crystal size, mm^3	$0.271 \times 0.225 \times 0.148$	$0.601 \times 0.215 \times 0.066$
Reflections collected	158618	39244
Independent reflections	6716 [$R_{int} = 0.0359$]	9104 [$R_{int} = 0.0837$]
Data/restraints/parameters	6716/0/379	9104/173/661
Goodness-of-fit on F^2	1.081	1.047
R indices [I>2sigma(I)][a,b]	$R_1 = 0.0433$, $wR_2 = 0.1165$	$R_1 = 0.0895$, $wR_2 = 0.2448$
R indices (all data)	$R_1 = 0.0499$, $wR_2 = 0.1223$	$R_1 = 0.1165$, $wR_2 = 0.2795$
Largest diff. peak/hole, e Å^3	1.59/–1.19	2.66/–1.14

[a] $R1 = \sum||F_o| - |F_c||/[\sum|F_o|]$. [b] $wR2 = [\sum[w(F_o^2 - F_c^2)^2]/\sum[w(F_o^2)^2]]^{1/2}$, $w = 1/\sigma^2 (F_o^2) + (aP)^2 +$

bP, where $P = [\max(0 \text{ or } F_o^2) + 2(F_c^2)]/3$.

Table 4.2. Crystal data and refinement parameters for **3** and **4**.

Compound	3	4
Empirical Formula	$C_{34.68}H_{35.36}F_6N_7O_{2.39}PRu$	$C_{66.44}H_{65.89}F_{12}N_{14}O_{1.31}P_2Ru_2$
Formula weight	834.58	1573.64
Temperature, K	110(2)	110(2)
Crystal system	Orthorhombic	Monoclinic
Space group	Pbca	$P2_1$/c
Unit cell dimensions	$a = 15.5779(19)$ Å, $\alpha = 90°$ $b = 18.142(2)$ Å, $\beta = 90°$ $c = 26.314(3)$ Å, $\gamma = 90°$	$a = 22.39(2)$ Å, $\alpha = 90°$ $b = 36.15(3)$ Å, $\beta = 157.928(12)°$ $c = 22.87(2)$ Å, $\gamma = 90°$
Volume, Å^3	7436.8(15)	6956(11)
Z	8	4
Density, g/cm^3	1.491	1.503
Absorption coefficient, mm^{-1}	0.537	0.566
F(000)	3397	3196
Crystal color, morphology	dark red, plate	dark red, plate
Crystal size, mm^3	$0.476 \times 0.176 \times 0.034$	$0.229 \times 0.107 \times 0.038$
Reflections collected	38066	45443
Independent reflections	7884 [$R_{int} = 0.0717$]	15318 [$R_{int} = 0.0764$]
Data/restraints/parameters	7884/206/562	15318/480/1022
Goodness-of-fit on F^2	1.043	1.017
R indices [I>2sigma(I)]^{a,b}	$R_1 = 0.0609$, $wR_2 = 0.1448$	$R_1 = 0.0806$, $wR_2 = 0.2167$
R indices (all data)	$R_1 = 0.1003$, $wR_2 = 0.1694$	$R_1 = 0.1160$, $wR_2 = 0.2594$
Largest diff. peak/hole, e Å^3	1.18/–0.78	2.19/–1.68

[a] $R1 = \sum||F_o| - |F_c||/[\sum|F_o|]$. [b] $wR2 = [\sum[w(F_o^2 - F_c^2)^2]/\sum[w(F_o^2)^2]]^{1/2}$, $w = 1/\sigma^2 (F_o^2)+(aP)^2+$

bP, where $P = [\max(0 \text{ or } F_o^2) + 2(F_c^2)]/3$.

Table 4.3. Selected bond distances and angles for **1**.

Bond lengths (Å)		Bond angles (°)	
Ru1–C31	2.032(3)	N1–Ru1–C31	92.31(11)
Ru1–N1	2.053(3)	N1–Ru1–N3	158.59(8)
Ru1–N2	1.961(3)	N3–Ru1–C31	91.02(11)
Ru1–N3	2.062(3)	N4–Ru1–C31	156.73(12)
Ru1–N4	2.146(3)	N5–Ru1–C31	79.97(12)
Ru1–N5	2.003(3)	N4–Ru1–N5	76.99(11)
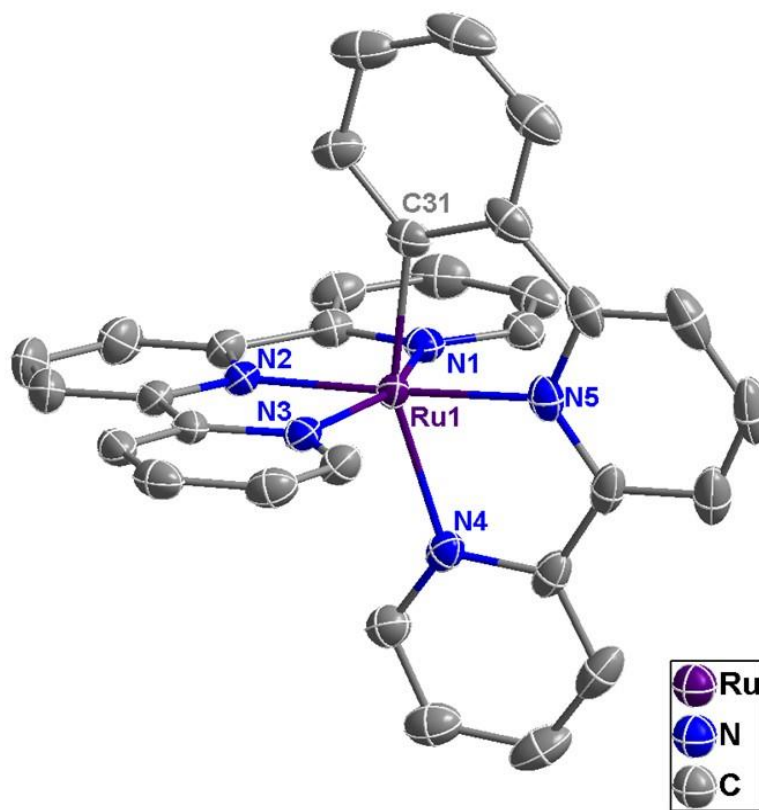
Figure 4.12. Thermal ellipsoid plot at the 50% probability level for the cation [Ru^{II}(tpy)(pbpy)]$^{+}$ in **1**. The (Cl)$^{-}$ counterion, solvent of crystallization (chloroform) and H atoms have been omitted for the sake of clarity.

Table 4.4. Selected bond distances and angles for **2**.

Bond lengths (Å)		Bond angles (°)	
Ru1–C45	2.021(7)	N1–Ru1–C45	93.4(2)
Ru1–N1	2.066(6)	N1–Ru1–N3	159.1(2)
Ru1–N2	1.937(6)	N3–Ru1–C45	90.1(2)
Ru1–N3	2.039(6)	N4–Ru1–C45	156.9(3)
Ru1–N4	2.156(6)	N5–Ru1–C45	79.7(3)
Ru1–N5	2.011(6)	N4–Ru1–N5	77.2(2)
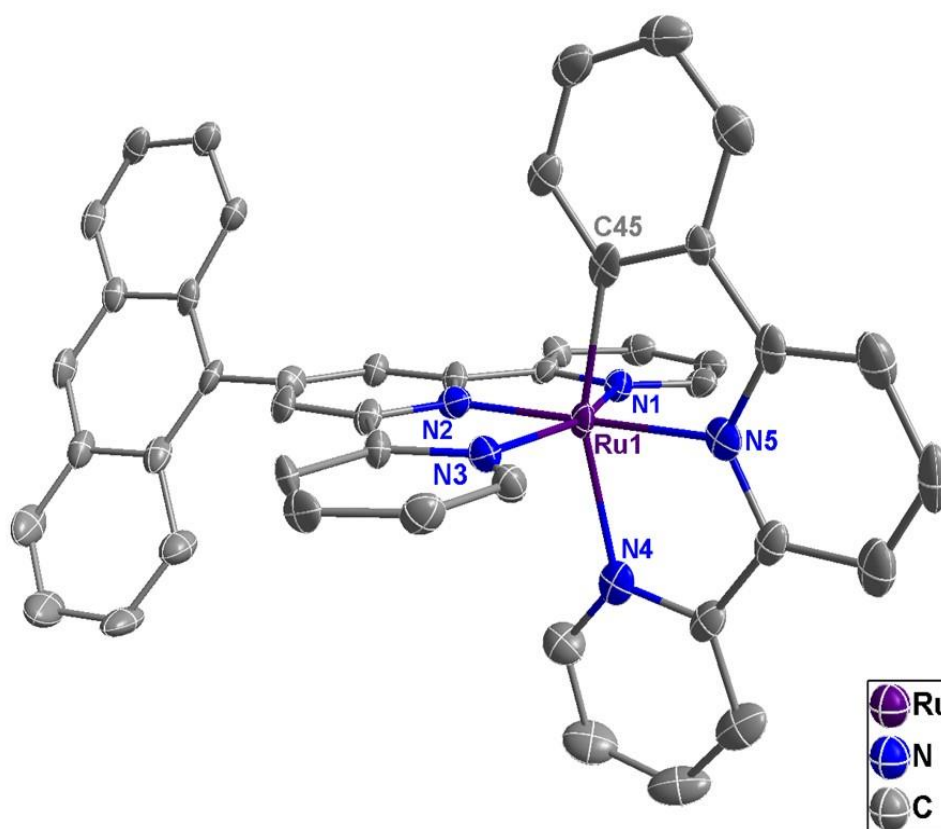
Figure 4.13. Thermal ellipsoid plot at the 50% probability level for the cation $[Ru^{II}(antpy)(pbpy)]^+$ in **2**. The $(Cl)^-$ counterion, solvent of crystallization (chloroform) and H atoms have been omitted for the sake of clarity.

185

Table 4.5. Selected bond distances and angles for **3**.

Bond lengths (Å)		Bond angles (°)	
Ru1–C27	2.034(4)	N1–Ru1–C27	92.60(16)
Ru1–N1	2.069(4)	N1–Ru1–N5	156.61(16)
Ru1–N3	1.965(4)	N5–Ru1–C27	89.52(16)
Ru1–N5	2.047(4)	N6–Ru1–C27	157.71(17)
Ru1–N6	2.182(4)	N7–Ru1–C27	81.00(17)
Ru1–N7	2.019(4)	N6–Ru1–N7	76.72(15)
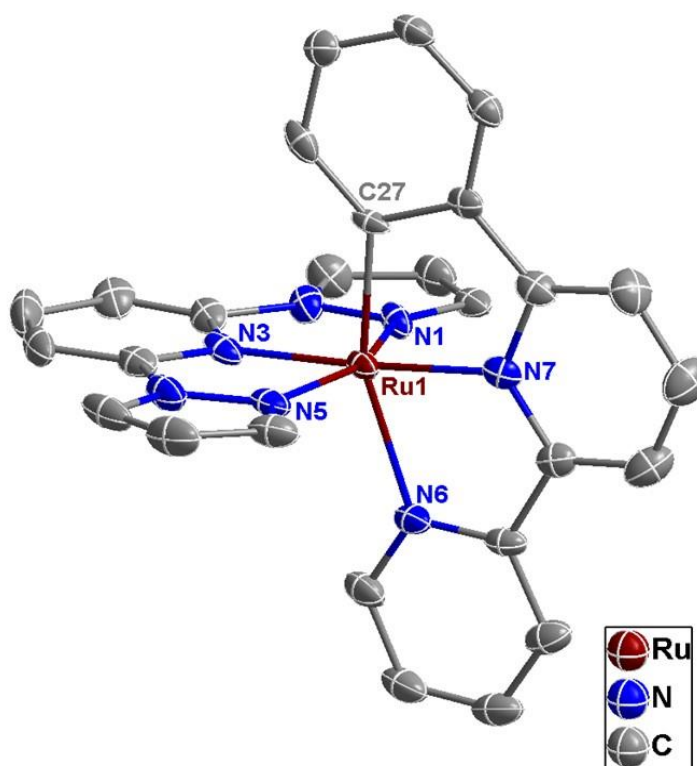
Figure 4.14. Thermal ellipsoid plot at the 50% probability level for the cation $[Ru^{II}(bpp)(pbpy)]^+$ in **3**. The $(PF_6)^-$ counterion, solvents of crystallization (acetone and diethyl ether) and H atoms have been omitted for the sake of clarity.

Table 4.6. Selected bond distances and angles for **4**.

Bond lengths (Å)		Bond angles (°)	
Ru1–C31	2.017(6)	N1–Ru1–C31	94.8(2)
Ru1–N1	2.058(6)	N1–Ru1–N5	157.0(2)
Ru1–N3	1.973(5)	N5–Ru1–C31	88.6(3)
Ru1–N5	2.055(6)	N6–Ru1–C31	157.7(2)
Ru1–N6	2.173(5)	N7–Ru1–C31	80.3(2)
Ru1–N7	2.001(5)	N6–Ru1–N7	77.4(2)
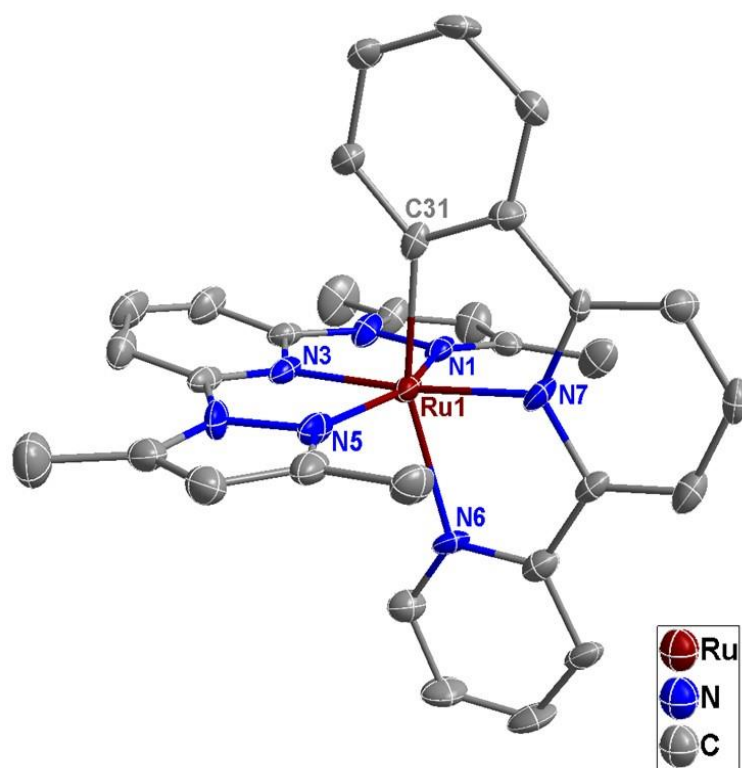
Figure 4.15. Thermal ellipsoid plot at the 50% probability level for the cation [Ru^{II}(bdmpp)(pbpy)]$^+$ in **4**. The (PF$_6$)$^-$ counterion, solvents of crystallization (acetone and diethyl ether) and H atoms have been omitted for the sake of clarity.

Geometry optimizations of **1**-**4** were performed in both the gas and acetonitrile solvent phases. The optimized geometries in acetonitrile are depicted in Figures 4.16 and 4.17 and are compared with the crystal structures vis-à-vis bond distances; Ru-N(C) bond distances are compiled in Table (4.7-4.10). From the bond distances, it can be concluded that the solid-state structure is essentially preserved in both the gas phase and solvent phase optimized geometries for all compounds. The solvent phase bond distances are slightly longer than those in the gas phase, except for the Ru-N bonds in the pbpy ligand for which the trend is opposite. Additionally, the optimized geometry of **2** (Figure 4.16) in acetonitrile similarly exhibits a twisted 9-anthryl moiety with a torsion angle of 77.1º which is larger than that found the solid-state structure.
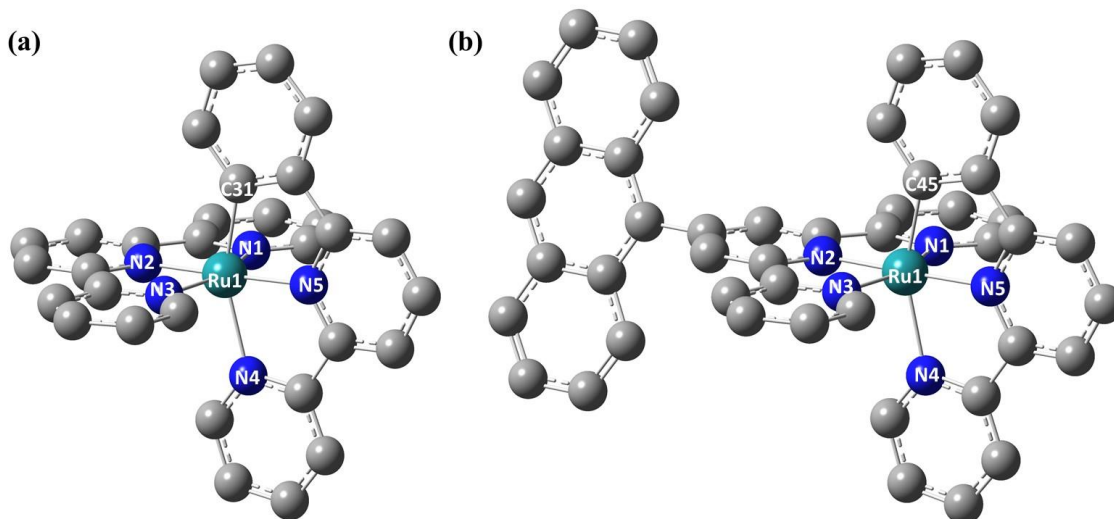
Figure 4.16. Optimized geometries of (a) [Ru(tpy)(pbpy)]$^+$ (**1**) and (b) [Ru(antpy)(pbpy)]$^+$ (**2**) in acetonitrile using the SMD Model. H atoms have been omitted for the sake of clarity.
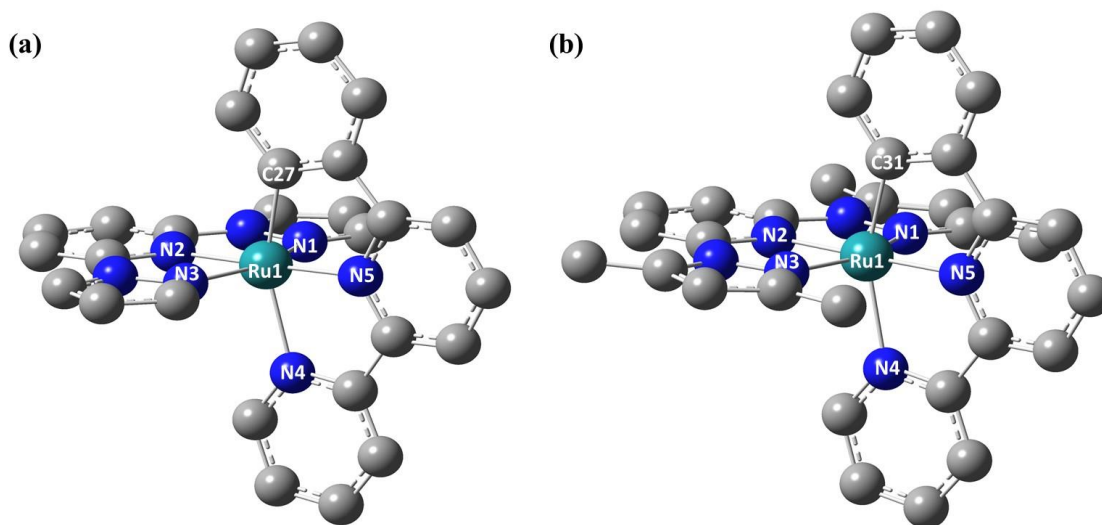
Figure 4.17. Optimized geometries of (a) [Ru(bpp)(pbpy)]⁺ (**3**) and (b) [Ru(bdmpp)(pbpy)]⁺ (**4**) in acetonitrile using the SMD Model. H atoms have been omitted for the sake of clarity.

Table 4.7. Comparison of bond distances for **1** from the crystal and the computationally optimized structures.[196]

Selected Bonds	Bond Distance (Å) [Crystal Structure]	Bond Distance (Å) [Gas Phase Optimized Structure]	Bond Distance (Å) [Solvent Phase Optimized Structure] ᵃ
Ru1–C31	2.032(3)	2.051	2.053
Ru1–N1	2.053(3)	2.094	2.100
Ru1–N2	1.961(3)	1.973	1.979
Ru1–N3	2.062(3)	2.095	2.098
Ru1–N4	2.146(3)	2.216	2.206
Ru1–N5	2.003(3)	2.053	2.047

ᵃ Acetonitrile as solvent.

Table 4.8. Comparison of bond distances for **2** from the crystal and the computationally optimized structures.

Selected Bonds	Bond Distance (Å) [Crystal Structure]	Bond Distance (Å) [Gas Phase Optimized Structure]	Bond Distance (Å) [Solvent Phase Optimized Structure] [a]
Ru1–C45	2.021(7)	2.049	2.052
Ru1–N1	2.066(6)	2.096	2.100
Ru1–N2	1.937(6)	1.976	1.978
Ru1–N3	2.039(6)	2.097	2.100
Ru1–N4	2.156(6)	2.215	2.204
Ru1–N5	2.011(6)	2.050	2.048

[a] Acetonitrile as solvent.

Table 4.9. Comparison of bond distances for **3** from the crystal and the computationally optimized structures.

Selected Bonds	Bond Distance (Å) [Crystal Structure]	Bond Distance (Å) [Gas Phase Optimized Structure]	Bond Distance (Å) [Solvent Phase Optimized Structure] [a]
Ru1–C27	2.034(4)	2.048	2.049
Ru1–N1	2.069(4)	2.088	2.091
Ru1–N3	1.965(4)	1.992	2.003
Ru1–N5	2.047(4)	2.089	2.091
Ru1–N6	2.182(4)	2.235	2.225
Ru1–N7	2.019(4)	2.044	2.037

[a] Acetonitrile as solvent.

Table 4.10. Comparison of bond distances for **4** from the crystal and the computationally optimized structures.

Selected Bonds	Bond Distance (Å) [Crystal Structure]	Bond Distance (Å) [Gas Phase Optimized Structure]	Bond Distance (Å) [Solvent Phase Optimized Structure] [a]
Ru1–C31	2.017(6)	2.047	2.050
Ru1–N1	2.058(6)	2.094	2.095
Ru1–N3	1.973(5)	1.996	2.006
Ru1–N5	2.055(6)	2.094	2.097
Ru1–N6	2.173(5)	2.231	2.224
Ru1–N7	2.001(5)	2.040	2.035

[a] Acetonitrile as solvent.

Electronic Absorption Spectroscopy and Electronic Structure Calculations

Electronic absorption spectra of **1**-**4** in acetonitrile are depicted in Figure 4.18; the absorption data are summarized in Table 4.11. The low-lying electronic transitions in the visible region are assigned to ^{1}MLCT charge transfer transitions from Ru(dπ) $\rightarrow$ L(π^*) (L = tpy, antpy, bpp, bdmpp, pbpy). Upon cyclometallation, the MLCT bands are bathochromically shifted due to destabilization of the Ru based t_{2g} orbitals by the π-donating anionic pbpy ligand.[184] Additionally, significant broadening of the peaks with the appearance of shoulders and a decrease of molar absorption coefficient (ϵ) also occurs in contrast to their polypyridyl analogues. [179, 184, 194, 198-199] Compounds **1** and **2** exhibits broad MLCT absorption bands with maxima at 513 nm (ϵ = 16,500 M^{-1}cm^{-1}) and 517 nm

(ε = 20,200 M^{-1}cm^{-1}) respectively with a broad shoulder extending beyond 650 nm. The MLCT maximum of **1** is red-shifted by ~ 37 nm compared to [Ru(tpy)$_2$]$^{2+}$ (λ_{max} = 476 nm in acetonitrile).[179] The introduction of the 9-anthracenyl moiety at the 4′-position of the tpy ligand in **2** gives rise to insignificant red-shifting (4 nm) of the MLCT band position compared to **1**. This observation can be explained by the lack of electronic communications between the anthracene moiety with the [Ru(tpy)(pbpy)] core owing to the twisted conformation in the optimized geometry of **2** in acetonitrile (Figure 4.16).[198] As a result, the absorption profiles of **1** and **2** in the visible region are nearly identical and reflect the absorption features of the [Ru(tpy)(pbpy)]$^+$ core. The MLCT maximum of **2** is red-shifted by ~35 nm compared to [Ru(antpy)(tpy)]$^{2+}$ (λ_{max}= 482 nm in acetonitrile).[190] Additional absorption features are noted for **1** and **2** in the 350-450 nm range which are ascribed to the population of excited sates involving the pbpy ligand.[179, 196]

When the pyridine rings on the ancillary ligands are replaced by pyrazole rings, the ^{1}MLCT transitions are blue-shifted to 473 nm (ε = 16,100 M^{-1}cm^{-1}) and 489 nm (ε = 16,000 M^{-1}cm^{-1}) for **3** and **4** respectively, owing to the fact that pyrazole containing ligands are poor π-acceptors. As reported in the literature, the π*(bpp) orbital is substantially higher in energy than π*(tpy), and, as a result, the Ru(dπ)-L(π*) (L=bpp, bdmpp) energy gap is significantly larger than that of Ru(dπ)-L(π*) (L=tpy, antpy) which results in a blue shift of the MLCT band.[199] It is noted, however, that there is an overall red-shift of the absorption maxima upon cyclometallation for **3** in the visible region compared to [Ru(bpp)(tpy)]$^{2+}$ (λ_{max} = 430 nm in acetonitrile).[199] Incorporation of four methyl substituents on the bpp ligand leads to red-shifting of the MLCT band in **4** to 489 nm

compared to **3** (473 nm), consistent with the stabilization of the π* (bdmpp) orbital due to the electron-donating methyl groups.

The UV-region of the spectra primarily consists of a manifold of intense ligand-centered π→π* transitions (Figure 4.18). Due to the asymmetry resulting from cyclometallation, the compounds exhibit more intra-ligand π→π* transitions in the UV-region compared to their symmetric polypyridine analogues.[194] The intense transition at 253 nm (ε = 178,400 $M^{-1}cm^{-1}$) exhibited by **2** is assigned to the anthracene based π→π* transition which is located at λ= 254 nm (ε = 104,600 $M^{-1}cm^{-1}$) in acetonitrile for $[Ru(antpy)(tpy)]^{2+}$.[190] The ^{1}MLCT transitions were further probed with TDDFT calculations which will be discussed in a later section.

Table 4.11. Electronic absorption data for **1**-**4** in acetonitrile at RT.

Compound	λ_{max} (nm) ($\varepsilon \times 10^4\ M^{-1}\ cm^{-1}$)
$[Ru(tpy)(pbpy)](PF_6)$ (**1**)	513 (1.65), 384 (1.24), 319 (5.14), 275 (5.05), 238 (5.65)[194]
$[Ru(antpy)(pbpy)](PF_6)$ (**2**)	517 (2.02), 386 (2.22), 367 (1.96), 319 (4.70), 284^a (4.80), 253 (17.84)
$[Ru(bpp)(pbpy)](PF_6)$ (**3**)	473 (1.61), 446^a (1.50), 331 (1.83), 292 (4.29), 267 (4.16), 237^a (3.36), 224 (3.56)
$[Ru(bdmpp)(pbpy)](PF_6)$ (**4**)	489 (1.60), 375 (0.45), 336 (1.46), 298 (4.43), 266 (4.44), 238^a (3.27), 227 (3.45)

^{a} Shoulder.
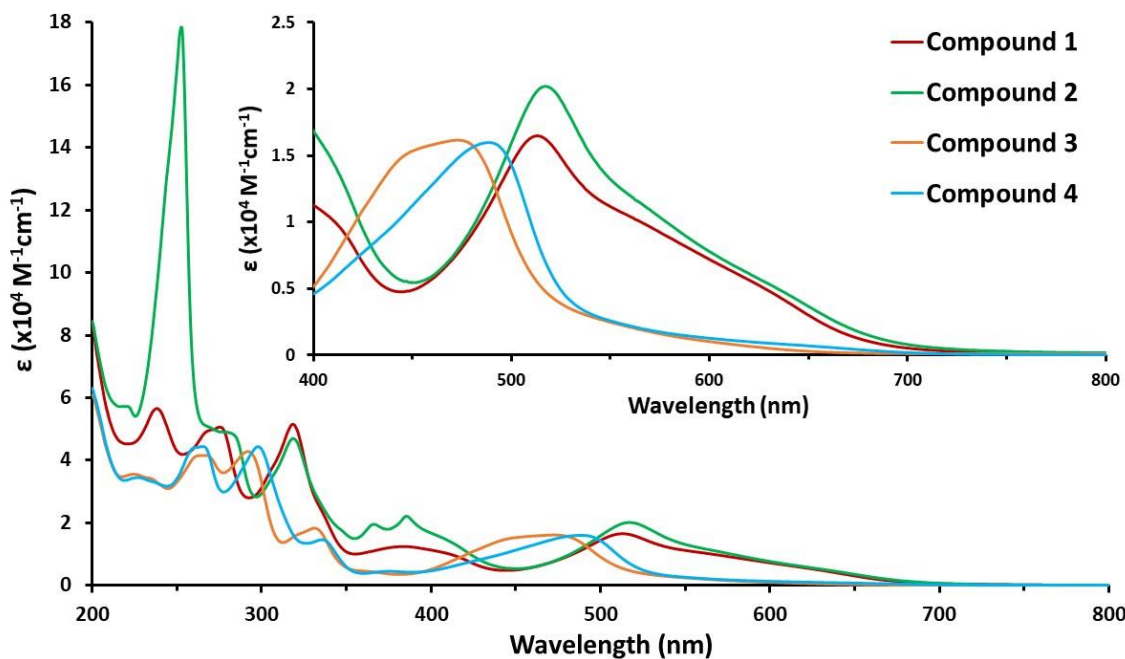
Figure 4.18. Electronic absorption spectra of **1**–**4** in acetonitrile at room temperature. Inset: [1]MLCT absorptions in the visible region.

The optimized geometries of the molecules in acetonitrile were analyzed to gain further insight into the electronic properties. Electron densities and energies of selected MOs along with the percentage contribution of the metal centers and coordinated ligands are tabulated in Table (4.12-4.17). In Ru(II) mononuclear complexes, (HOMO-2) to HOMO orbitals typically constitute the occupied "t_{2g}-type" Ru(dπ) orbitals in a pseudo-octahedral coordination environment. For compounds **1**-**4**, the (HOMO-2) to HOMO orbitals are primarily localized on the metal center with ligand mixing from both ancillary ligands and the pbpy ligand. Specifically, HOMOs possess considerable pbpy ligand contributions which indicates destabilization of the Ru based t_{2g} orbitals due to the π-donating pbpy ligand which results in the bathochromic shift of the absorption band compared to their polypyridine analogues. [179, 184, 194, 198-199] The LUMO to (LUMO+4)

194

orbitals are predominantly localized on both tridentate ligands in all complexes. For **1** and **2**, the LUMO orbital is centered on the terpyridine moiety of the ancillary ligands. In contrast, the LUMO is primarily localized on the bipyridine subunit of the pbpy ligand for **3** and **4**. As reported in the literature, the π^*(tpy) orbital is substantially lower in energy than π^*(bpp)[199], the predominant contribution of the pbpy ligand in LUMO of **3** and **4** leads to the conclusion that the π^*(pbpy) orbital is similarly lower in energy than π^*(bpp/bdmpp). Also, the (LUMO+3) on **2** is entirely localized on the anthracene moiety and constitutes one of the π^* orbitals. This observation further supports the lack of electronic communication between the aromatic rings due to the twisted conformation of the 9-anthracenyl subunit in the antpy ligand.[198]

Table 4.12. Frontier molecular orbitals (HOMO-2 to LUMO) of **1** and **2** (isovalue = 0.04).
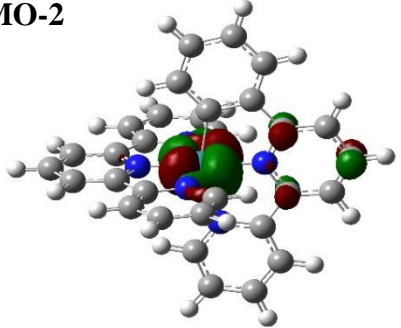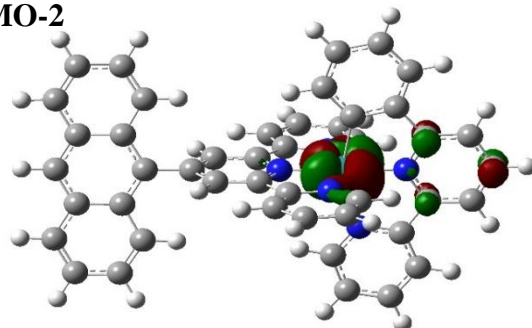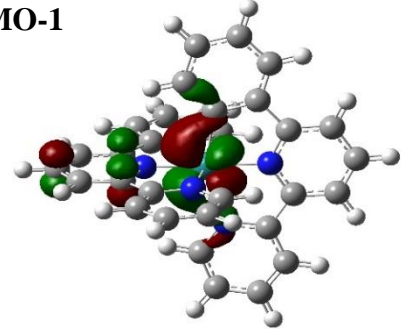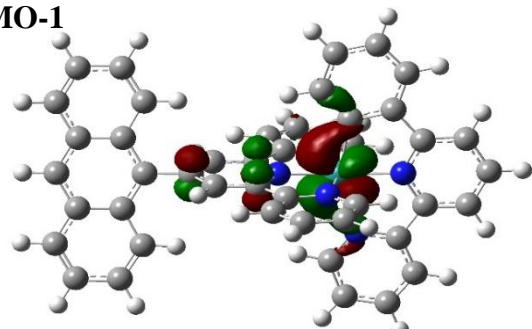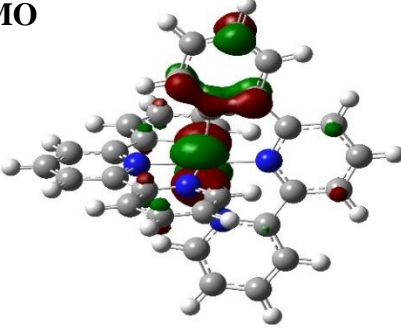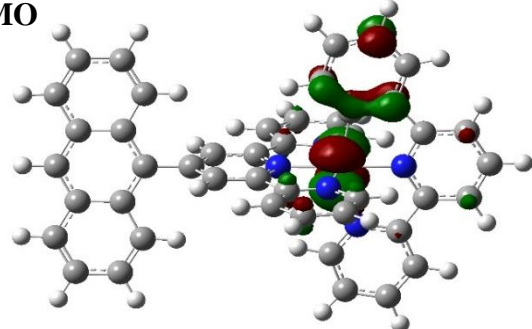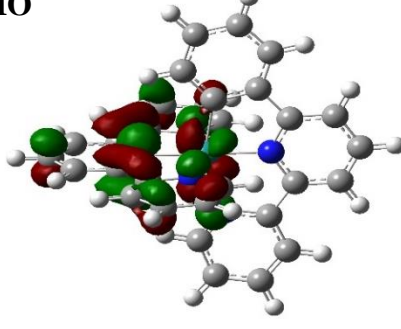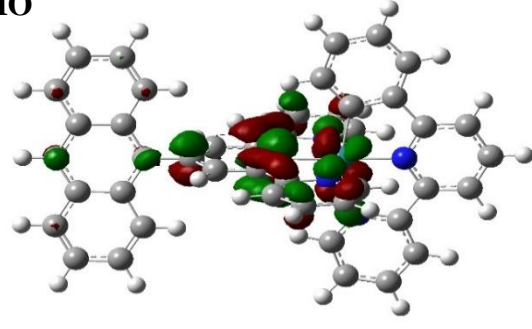
[Ru(tpy)(pbpy)]⁺ (1)	[Ru(antpy)(pbpy)]⁺ (2)
HOMO-2	HOMO-2
HOMO-1	HOMO-1
HOMO	HOMO
LUMO	LUMO

Table 4.13. Frontier molecular orbitals (LUMO+1 to LUMO+4) of **1** and **2** (isovalue = 0.04).
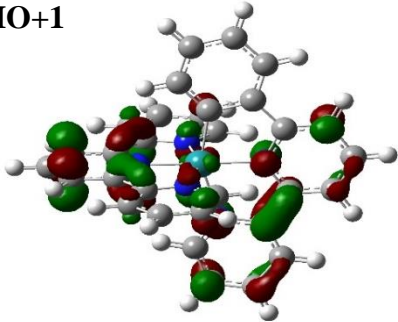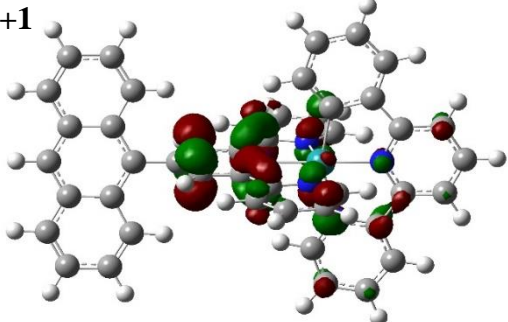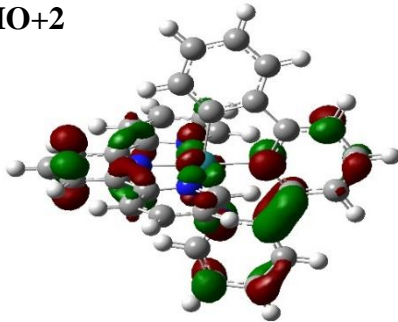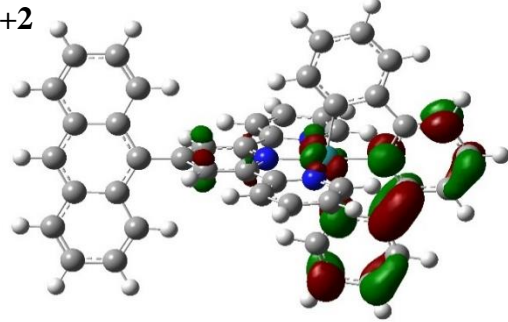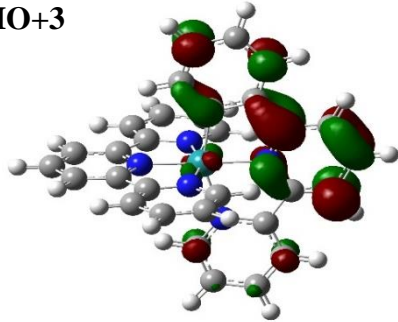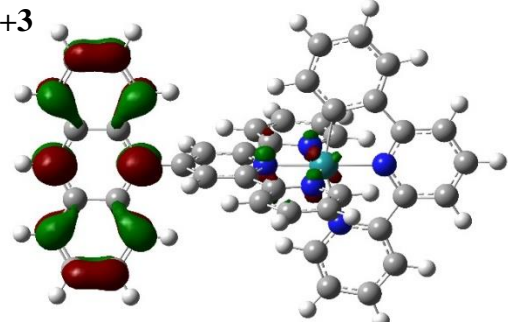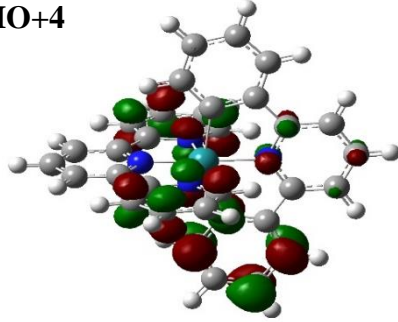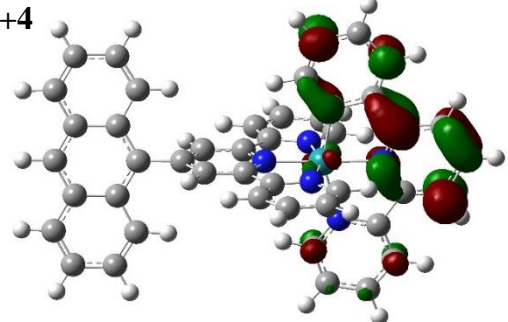
[Ru(tpy)(pbpy)]$^+$ (**1**)	[Ru(antpy)(pbpy)]$^+$ (**2**)
LUMO+1	LUMO+1
LUMO+2	LUMO+2
LUMO+3	LUMO+3
LUMO+4	LUMO+4

197

Table 4.14. Frontier molecular orbitals (HOMO-2 to LUMO) of **3** and **4** (isovalue = 0.04).
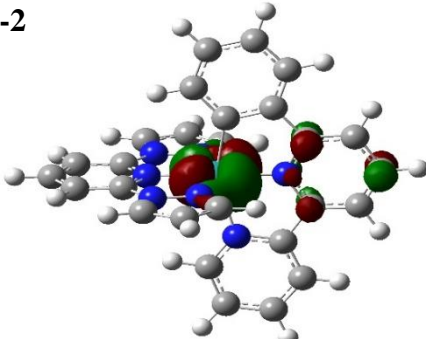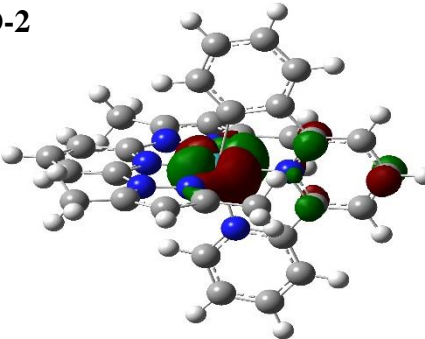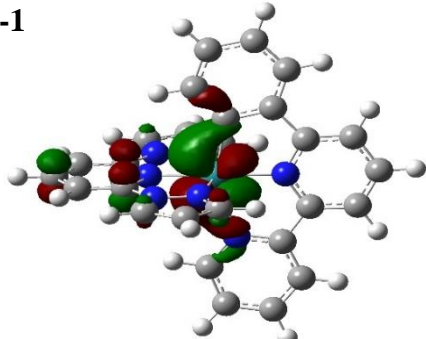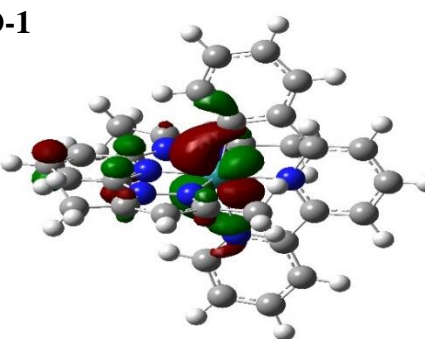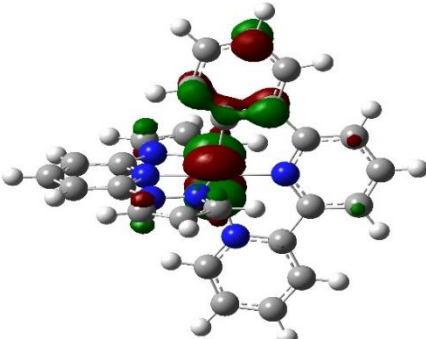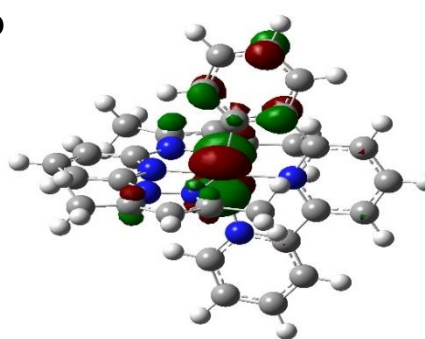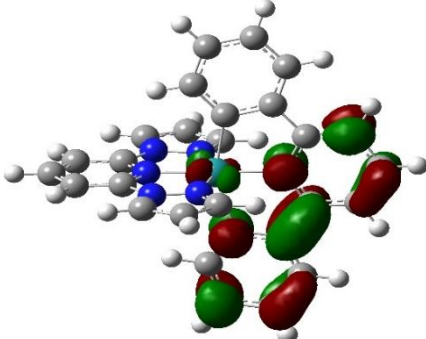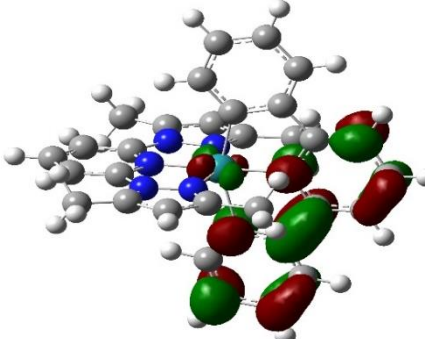
[Ru(bpp)(pbpy)]$^+$ (**3**)	[Ru(bdmpp)(pbpy)]$^+$ (**4**)
HOMO-2	HOMO-2
HOMO-1	HOMO-1
HOMO	HOMO
LUMO	LUMO

Table 4.15. Frontier molecular orbitals (LUMO+1 to LUMO+4) of **3** and **4** (isovalue = 0.04).
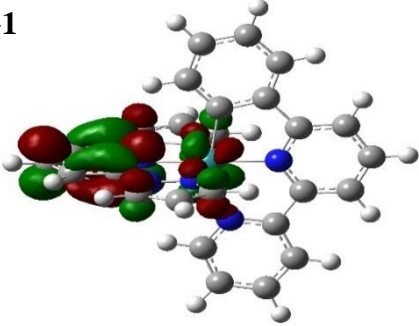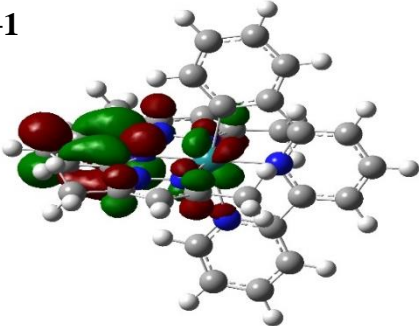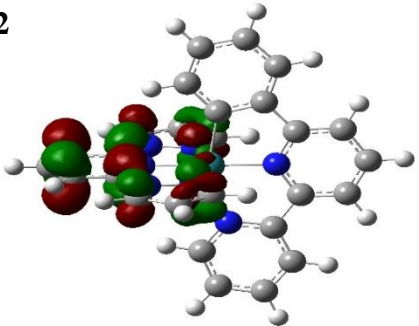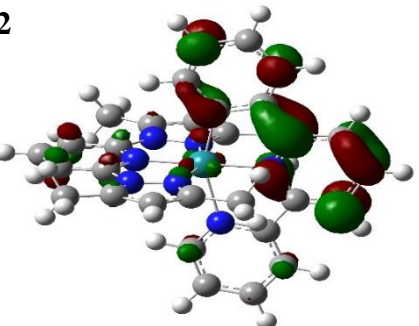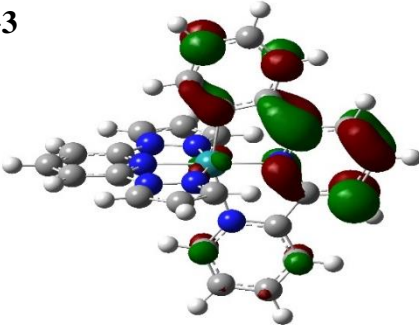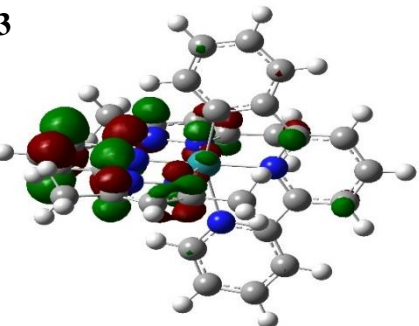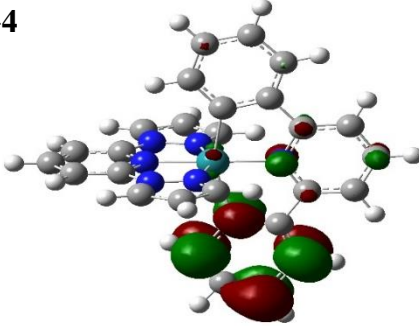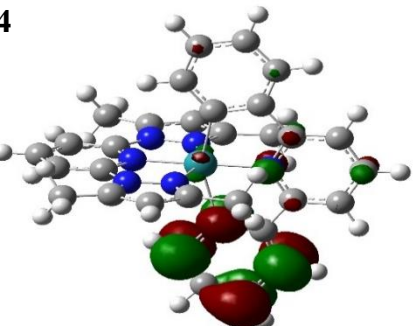
[Ru(bpp)(pbpy)]$^+$ (3)	[Ru(bdmpp)(pbpy)]$^+$ (4)
LUMO+1	**LUMO+1**
LUMO+2	**LUMO+2**
LUMO+3	**LUMO+3**
LUMO+4	**LUMO+4**

199

Table 4.16. Percent contributions of selected MOs and corresponding energies (E$_{MO}$) of **1** and **2**.

MO	[Ru(tpy)(pbpy)]$^+$ (1)				[Ru(antpy)(pbpy)]$^+$ (2)			
	% Contribution			E$_{MO}$	% Contribution			E$_{MO}$
	Ru	tpy	pbpy	(eV)	Ru	antpy	pbpy	(eV)
LUMO+4	1	50	49	-1.159	3	4	93	-1.558
LUMO+3	3	4	93	-1.553	2	96	2	-2.029
LUMO+2	5	44	51	-2.038	6	22	72	-2.053
LUMO+1	2	56	42	-2.088	2	80	18	-2.116
LUMO	12	76	12	-2.133	11	79	10	-2.176
HOMO	64	12	24	-5.160	64	12	24	-5.169
HOMO-1	60	20	20	-5.209	57	23	20	-5.203
HOMO-2	68	18	14	-5.474	68	19	13	-5.484

Table 4.17. Percent contributions of selected MOs and corresponding energies (E$_{MO}$) of **3** and **4**.

MO	[Ru(bpp)(pbpy)]$^+$ (3)				[Ru(bdmpp)(pbpy)]$^+$ (4)			
	% Contribution			E$_{MO}$	% Contribution			E$_{MO}$
	Ru	bpp	pbpy	(eV)	Ru	bdmpp	pbpy	(eV)
LUMO+4	2	1	96	-1.060	3	2	96	-1.033
LUMO+3	3	6	91	-1.541	2	83	15	-1.409
LUMO+2	2	94	4	-1.647	2	20	78	-1.534
LUMO+1	10	78	12	-1.734	9	80	11	-1.682
LUMO	5	5	90	-2.050	5	5	90	-2.019
HOMO	65	14	21	-5.058	65	16	19	-4.911
HOMO-1	62	17	21	-5.182	61	18	21	-5.045
HOMO-2	70	16	14	-5.550	70	15	15	-5.430

Electrochemical Properties

The redox properties of all four compounds were studied by cyclic voltammetry in dry deoxygenated acetonitrile at room temperature. The half-wave redox potential values ($E_{1/2}$) *vs* the Ag/AgCl reference electrode obtained from the cyclic voltammograms were further referenced to the NHE for the discussion of results as described in the experimental section and summarized in Table 4.18. Cyclic voltammograms of **1**-**4** are depicted in Figure 4.19. For all of the compounds, the oxidation event at the metal center observed between +0.63 V and + 0.80 V is assigned to a one-electron oxidation from Ru(II) to Ru(III) which is reversible as evidenced by the peak-to-peak separation (ΔE_{p}) values ranging (50–90) mV with respect to Fc^{+}/Fc couple (80 mV). Due to cyclometallation, the metal-based oxidation peaks are cathodically shifted by 720 mV – 890 mV compared to [Ru(tpy)$_2$]$^{2+}$.[194] The accessible reversible oxidation suggests that the Ru(dπ)-based HOMO is destabilized to higher energy by the π-donating ability of the anionic pbpy ligand.[184] The oxidation of the metal center occurs at +0.8 V for both **1** and **2**, which is shifted to less positive potentials for **3** and **4**, supporting the fact that pyrazole-containing ligands are poorer π-acceptors than pyridine analogues.[199] The introduction of four methyl groups on the bpp ligand leads to a shift of the Ru(II,III) oxidation couple from +0.72 V for **3** to +0.63 V for **4**. This decrease in the Ru(II,III) redox potential is consistent with the electron-donating ability of the methyl group which stabilizes the Ru(III) center. Also, the cathodic shift of 90 mV resulting from the replacement of the bpp ligand with the bdmpp ligand translates to an average potential change of 23 mV/methyl group which is close to

the reported value of 24 mV/methyl group.[199] In the case of **2**, the oxidation event is similarly cathodically shifted by 750 mV compared to its polypyridine analog [Ru(antpy)(tpy)]$^{2+}$ (+1.55 V *vs* NHE) owing to cyclometallation.[190]

For compounds **1** and **2**, multiple one-electron reduction events of the coordinated ligands are observed, whereas compound **3** and **4** exhibit only one ligand-based reduction event. The first reduction process located between -1.32 V and -1.47 V for all of the compounds are essentially quasi-reversible in nature with an irreversible reduction at potentials more negative than-1.6 V for **1** and **2**. All redox events occur at very similar potentials for **1** and **2** owing to the fact that there is lack of electronic communication between the anthracene moiety with the [Ru(tpy)(pbpy)] core due to the non-planar conformation of the 9-anthracenyl subunit. Both ligand-based reductions of **1** and **2** are shifted to more negative potentials compared to their polypyridyl analogues [Ru(tpy)$_2$]$^{2+}$ and [Ru(antpy)(tpy)]$^{2+}$ respectively as a consequence of enhanced π-backbonding to the ancillary tpy and antpy ligands due to an increase in electron density at the Ru(II) center due to cyclometallation.[179] In contrast, the ligand reduction event in **3** and **4** occurs at similar potential (~ 1.47 V) which can only be explained by reduction of the pbpy ligand instead of the ancillary ligands bpp and bdmpp. This conclusion is supported by the fact that the LUMO orbital on **3** and **4** is exclusively localized (90%) on the pbpy ligand (Table 4.17). Due to relatively high-lying π*(bpp/bdmpp) orbitals, the reduction of the ancillary ligands does not appear in the solvent window of +2 V to –2 V.

Table 4.18. Half-wave redox potentials ($E_{1/2}$) for **1**–**4** in acetonitrile.

Compound	$E_{1/2}$ (V) *vs* NHE ($\Delta E_p = E_{pa} - E_{pc}$ in mV)		
	$E_{1/2}$ [Ru$^{3+/2+}$]	$E_{1/2,red1}$	$E_{1/2,red2}$
[Ru(tpy)(pbpy)](PF$_6$) (**1**)[179, 194]	0.80 (80)	-1.35 (70)	-1.62 (90) [a]
[Ru(antpy)(pbpy)](PF$_6$) (**2**)	0.80 (90)	-1.32 (90)	-1.61 (80) [a]
[Ru(bpp)(pbpy)](PF$_6$) (**3**)	0.72 (50)	-1.47 (70)	–
[Ru(bdmpp)(pbpy)](PF$_6$) (**4**)	0.63 (70)	-1.46 (100) [a]	–

[a] irreversible.
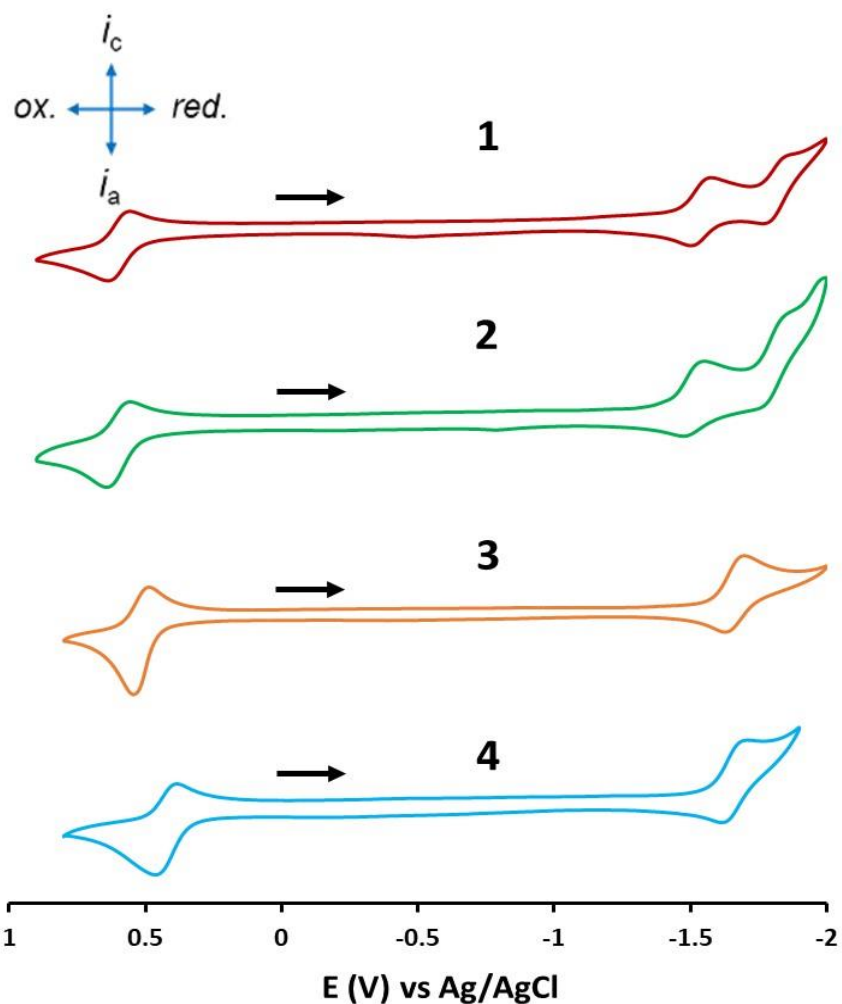
Figure 4.19. Cyclic voltammograms (*vs* Ag/AgCl) of compounds **1**–**4** in dry acetonitrile (0.1 M [^{n}Bu$_4$N](PF$_6$), 100 mV/s scan rate). i_c = cathodic current, i_a = anodic current, ox. = oxidation, red. = reduction. The black arrows indicate the direction of the scan.

TDDFT Calculations

TDDFT calculations were performed on the ground state optimized geometries of **1**–**4** in acetonitrile to substantiate the experimental electronic absorption spectra and to further interpret the visible electronic transitions. The most relevant ^{1}ES electronic

204

transitions calculated in acetonitrile (using the SMD model[149]) with $\lambda_{calc} \geq 400$ nm are listed in Table (4.19-4.22) along with their extinction coefficients in terms of oscillator strength (f) values, percent transition contributions, and nature of the transitions. The calculated absorption spectra qualitatively resemble the experimental absorption spectra of the complexes in the visible/near UV region (Figure 4.20-4.21) with visible absorption maxima shifted hypsochromically due to overestimation of orbital energies.[161] The computed singlet excited states in the visible region ($\lambda_{calc} \geq 400$ nm) are predominantly ^{1}MLCT in character whereas those in the UV region ($\lambda_{calc} \leq 400$ nm) possess ^{1}LC ($^1\pi\pi^*$) character, results that corroborate the experimental assignments. The calculated ^{1}MLCT transitions occur from Ru(dπ) $\rightarrow$ L(π^*) [L = tpy, antpy, bpp, bdmpp, pbpy] orbitals. For **1**, the most intense transition at $\lambda_{calc} = 483.1$ nm (f= 0.176) corresponds to the experimental absorption maximum at $\lambda_{exp} = 513$ nm and the transition at $\lambda_{calc} = 518.7$ nm (f = 0.071) along with the low energy visible transitions (1-4) constitute the experimental broad shoulder that extends beyond 650 nm.[179, 194] As predicted from the experimental MLCT band, the calculated spectrum of **2** also resembles that of **1** in the visible region, which further substantiates the lack of electronic communication between the 9-anthracenyl subunit and the [Ru(tpy)(pbpy)] core. Also, the calculated electronic transitions in the visible region (Table 4.19-4.20) closely match each other. For **2**, the most intense transition at $\lambda_{calc} = 487.5$ nm (f = 0.269) correlates to the experimental absorption maximum at $\lambda_{exp} = 517$ nm and the transition at $\lambda_{calc} = 525.9$ nm (f = 0.065) along with the low energy visible transitions (1-4) constitute the broad shoulder beyond 550 nm. Additionally, visible transitions from the (HOMO-3) orbital, which is a π-molecular

orbital centered on the anthracene moiety, can be assigned to a ^{1}LC ($^1\pi\pi^*$) transition. Due to structural similarities, the calculated absorption spectra of **3** and **4** are very similar but the energies are red-shifted for **4** dues to the relatively low-lying π^*-orbital of the bdmpp ligand compared to the bpp ligand. The most intense transitions at $\lambda_{calc} = 441.0$ nm (f = 0.200) for **3** and $\lambda_{calc} = 461.5$ nm (f = 0.106) for **4** correlates with their respective experimental absorption maxima at $\lambda_{exp} = 473$ nm and 489 nm.
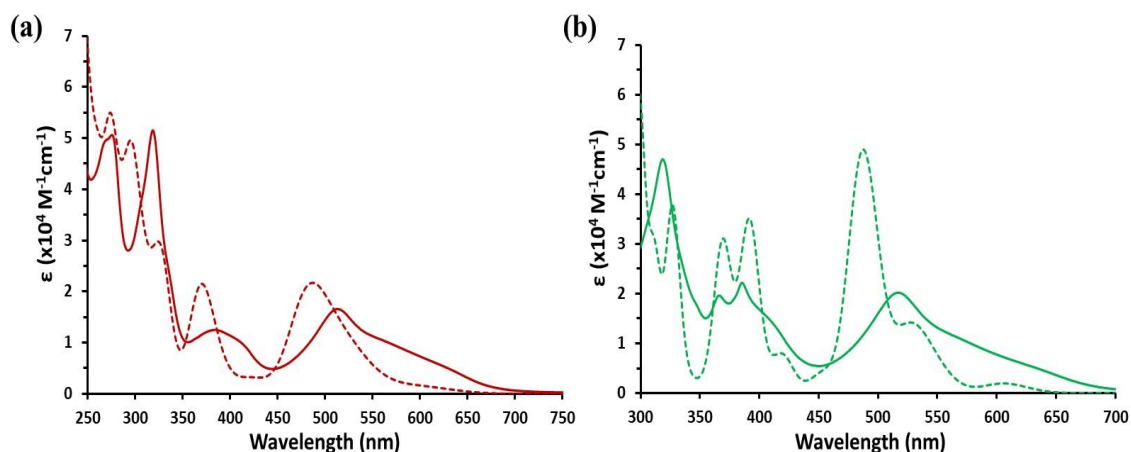
Figure 4.20. Experimental (solid line) and calculated (dotted line) electronic absorption spectra of (a) **1** and (b) **2** in acetonitrile.

Table 4.19. TDDFT data of **1**.

N^a	λ_{calc} (nm)	f^b	Major Contributions[c]	Assignment
1	602.4	0.012	H → L (94%), H-1 → L+2 (2%)	MLCT
3	547.1	0.014	H → L+2 (60%), H → L+1 (27%), H-1 → L (5%), H → L+3 (2%)	MLCT
4	537.4	0.003	H → L+1 (50%), H-1 → L (35%), H → L+2 (11%)	MLCT
6	518.7	0.071	H-1 → L+1 (50%), H-1 → L+2 (45%), H → L (2%)	MLCT
7	483.1	0.176	H-1 → L (36%), H-2 → L+2 (21%), H → L+1 (16%), H → L+2 (15%), H-2 → L+1 (8%)	MLCT
8	474.9	0.001	H-2 → L+1 (69%), H-2 → L+2 (29%)	MLCT
9	453.7	0.012	H-2→ L+2 (34%), H →L+3 (31%), H-2→L+1 (13%), H-1 → L (10%), H → L+6 (4%), H → L+1 (3%)	MLCT
10	429.7	0.002	H-1 → L+3 (96%)	MLCT
11	421.3	0.024	H→ L+3 (57%), H-2 →L+3 (12%), H-2→L+2 (8%), H-2 → L+1 (7%), H → L+2 (5%), H-1 → L (4%)	MLCT

[a] excited state number, [b] oscillator strength, [c] percent contribution = 2x(configuration coefficient)^{2}x100%.

Table 4.20. TDDFT data of **2**.

N^a	λ_{calc} (nm)	f^b	Major Contributions[c]	Assignment
1	606.0	0.011	H → L (83%), H → L+3 (9%), H-1 → L (2%)	MLCT
2	552.8	0.001	H-2 → L (55%), H-1 → L+2 (22%), H-1 → L+1 (9%), H-2 → L+3 (7%), H → L+2 (3%)	MLCT
3	546.7	0.023	H → L+2 (77%), H-1 → L (13%), H-1 → L+2 (2%)	MLCT
4	541.7	0.003	H → L+1 (69%), H-1 → L (22%), H → L+2 (2%)	MLCT
6	525.9	0.065	H-1 → L+1 (71%), H-1 → L+2 (22%), H → L (2%)	MLCT

Table 4.20. Continued

N^a	λ_{calc} (nm)	f^b	Major Contributions[c]	Assignment
7	487.5	0.269	H-1 → L (36%), H-2 → L+2 (24%), H → L+1 (24%), H → L+2 (8%)	MLCT
8	479.0	0.003	H-2→ L+1 (89%), H-2 → L+2 (8%)	MLCT
9	455.1	0.013	H-1 → L+3 (61%), H-2→ L+2 (12%), H-1→L (11%), H → L+3 (7%), H → L+4 (5%)	MLCT
10	453.0	0.007	H-2→ L+2 (35%), H →L+4 (24%), H-1→L+3 (22%), H-2 → L+1 (3%), H → L+1 (3%), H → L+7 (3%)	MLCT
11	448.2	0.002	H → L+3 (80%), H-1→ L+3 (9%), H→L (9%)	MLCT
12	429.9	0.002	H-1→ L+4 (92%), H→L+4 (4%)	MLCT
13	421.3	0.011	H→ L+4 (46%), H-3 →L (19%), H-2→L+2 (9%), H-2 → L+4 (9%), H → L+2 (3%), H-1 → L (3%)	MLCT/LC
14	418.8	0.003	H-3→ L+1 (85%), H-3 → L+2 (12%)	LC
15	417.9	0.029	H-3 → L (75%), H →L+4 (10%), H-2→L+4 (3%), H-2 → L+2 (2%)	LC/MLCT

[a] excited state number, [b] oscillator strength, [c] percent contribution = 2x(configuration coefficient)^{2}x100%.
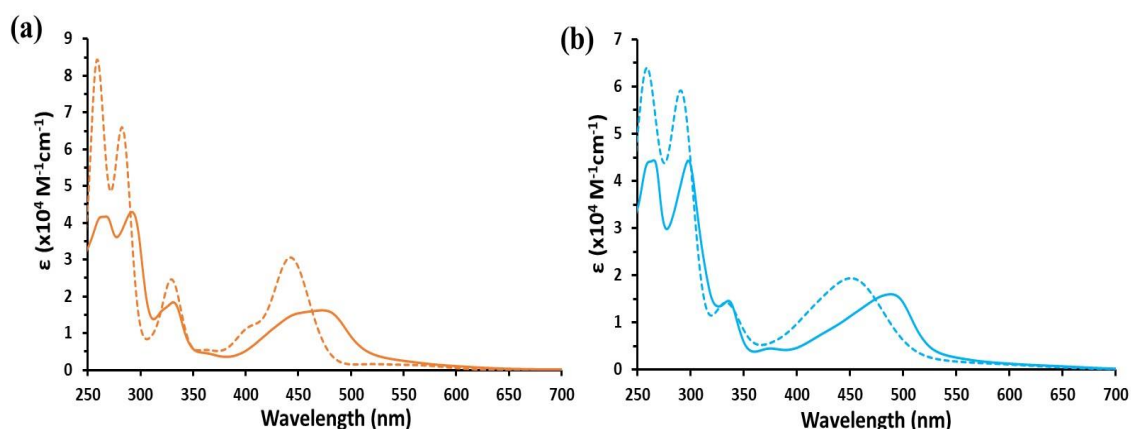
Figure 4.21. Experimental (solid line) and calculated (dotted line) electronic absorption spectra of (a) **3** and (b) **4** in acetonitrile.

Table 4.21. TDDFT data of **3**.

N^a	λ_{calc} (nm)	f^b	Major Contributions[c]	Assignment
1	568.1	0.011	H → L (95%), H → L+3 (3%)	MLCT
3	517.4	0.013	H → L+1 (95%)	MLCT
4	470.8	0.006	H → L+2 (68%), H-1 → L+1 (29%)	MLCT
5	455.7	0.017	H-2 → L (49%), H → L+3 (46%)	MLCT
6	447.8	0.055	H-1 → L+2 (91%), H-2 → L+1 (4%)	MLCT
7	443.7	0.002	H-2 → L+1 (83%), H-1 → L+3 (9%), H-1→L+2 (5%)	MLCT
8	441.0	0.200	H → L+3 (39%), H-2→ L (29%), H-1 → L+1 (15%), H → L+2 (13%), H → L (2%)	MLCT
9	433.1	0.002	H-1→ L+3 (87%), H-2 → L+1 (10%)	MLCT
10	404.6	0.088	H-1→ L+1 (40%), H →L+2 (14%), H-2→L+3 (11%), H-2 → L (10%), H → L+4 (9%), H → L+3 (7%)	MLCT

Table 4.21. Continued

N[a]	λ_{calc} (nm)	f[b]	Major Contributions[c]	Assignment
11	400.5	0.005	H-2 → L+2 (89%), H-2→L+3 (6%), H-1 → L+1 (2%)	MLCT

[a] excited state number, [b] oscillator strength, [c] percent contribution = 2x(configuration coefficient)^{2}x100%.

Table 4.22. TDDFT data of **4**.

N[a]	λ_{calc} (nm)	f[b]	Major Contributions[c]	Assignment
1	601.6	0.010	H → L (95%), H → L+2 (3%)	MLCT
3	534.3	0.017	H → L+1 (97%)	MLCT
4	477.2	0.010	H → L+2 (61%), H-2 → L (25%), H-1 → L+1 (11%)	MLCT
5	461.5	0.106	H-1 → L+1 (42%), H → L+3 (36%), H → L+2 (16%), H-2 → L (4%)	MLCT
6	457.8	0.076	H-2 → L (53%), H → L+3 (22%), H → L+2 (18%)	MLCT
7	454.9	0.006	H-1 → L+2 (76%), H-2 → L+1 (18%), H-1→L (2%)	MLCT
8	447.7	0.003	H-2 → L+1 (78%), H-1→ L+2 (19%)	MLCT
9	431.8	0.055	H-1→ L+3 (95%)	MLCT
10	414.7	0.083	H→ L+3 (33%), H-1 →L+1 (32%), H-2→L+2 (15%), H → L+4 (9%), H-2 → L (7%)	MLCT

[a] excited state number, [b] oscillator strength, [c] percent contribution = 2x(configuration coefficient)^{2}x100%.

Cytotoxic Properties

The *in vitro* cellular studies discussed in this section were performed in collaboration with Professor Robert C. Burghardt and Professor Rola Barhoumi Mouneimne in the College of Veterinary Medicine & Biomedical Sciences at Texas A&M University. The cytotoxic properties of all four cyclometallated Ru compounds were evaluated against human lung adenocarcinoma (A549) cells using the absorbance-based Janus Green B cell viability assay. Janus Green B [3-Diethylamino-7-(4-dimethylaminophenylazo)-5-phenylphenazinium chloride] is a cell penetrating dye which can accumulate inside the living cells upon treatment. In this assay, A549 cells were incubated with increasing concentrations of (**1**-**4**) (0-12.5 µM) for 48 h. The cells were subsequently washed with PBS buffer and fixed with ethanol. Following the cell fixation, the cells are stained with Janus Green B, and, after the removal of excess dye, the amount of dye trapped inside the living cells is dissolved in ethanol. The absorbance of Janus Green B (λ = 630 nm) measured in a microplate reader is directly proportional to the number of living cells.

The LC_{50} values (concentration of compound required to kill 50% of cell population) of the compounds were assessed from the % cell viability assays and are compiled in Table 4.23. All four compounds are more cytotoxic than cisplatin (LC_{50} = 6.2 µM)[32] and exhibit LC_{50} values in the low nanomolar range (Table 4.23). The low LC_{50} values are in good agreement with cyclometallated Ru(II) anthraquinone compounds with coordinated pbpy ligands evaluated against both hypoxic and normoxic A549 cells.[187] The

in vitro antiproliferative activities of **1**-**4** against A549 cells were found to follow the order: **4** >> **2** > **1** > **3** based on their LC_{50} values. Compounds **1** and **3**, lacking lipophilic side arms on ancillary ligands, exhibit moderate cytotoxicities compared to **2** and **4**. Due to incorporation of the anthracene moiety on the ancillary ligand, **2** demonstrates higher efficacy than compound **1** (~ 2.4 times), whereas, a much larger enhancement of the cytotoxicity is observed for **4** versus **3** dues to incorporation of four methyl groups on the bpp ligand, making **4** the most cytotoxic among the four (LC_{50} ~ 0.022 µM). By comparison to cisplatin, **4** is ~ 280 times more potent against A549 cells.[32, 188] This enhanced cytotoxicity for the four cyclometallated complexes is likely a consequence of their increased cellular uptake due to overall reduction of positive charge as in the case of other cyclometallated Ru compounds.[182-187] In support of this conclusion is the work of Chao *et al.* who demonstrated that non-cyclometallated Ru complexes bearing a 2+ charge are nearly non-toxic compare to their cyclometallated analogs.[185, 187] Hence, the strategy to incorporate the anionic cyclometallating pbpy ligand renders the compounds more lipophilic as a consequence of reduced positive charge and the lipophilicity and cytotoxic properties can be further tuned by incorporation of suitable ancillary ligands.[183]

Table 4.23. Cytotoxicity data for complex **1**-**4** against A549 cells using the Janus Green B cell viability assay. Values in parentheses represent the standard deviation.

Compound	LC$_{50}$, µM
[Ru(tpy)(pbpy)](PF$_6$) (**1**)	0.261 (0.102)
[Ru(antpy)(pbpy)](PF$_6$) (**2**)	0.107 (0.032)
[Ru(bpp)(pbpy)](PF$_6$) (**3**)	0.455 (0.056)
[Ru(bdmpp)(pbpy)](PF$_6$) (**4**)	0.022 (0.020)

Investigation of the Mechanism of Cell Death

Mitochondria are known as the cellular power house and govern the metabolism of the cell. The mitochondrial membrane potential (MMP) is a vital component of a respiring cell and, when compromised, can lead to cellular death. Disruption of the MMP leads to mitochondrial dysfunction and is an event associated with the intrinsic pathway of apoptosis.[32] It is well established that positively charged Ru(II) polypyridyl compounds tend to accumulate inside the mitochondria due to the negative potential of the inner mitochondrial membrane and can induce cell death by disrupting the MMP.[32, 200-208] To measure the changes in the MMP ($\Delta\Psi_m$), the lipophilic cationic fluorescent probe JC-1 (5′,6,6′-tetrachloro-1,1′,3,3′-tetraethylbenzimidazolylcarbocyanine iodide) was used which also accumulates inside the mitochondria; its emission characteristics are highly sensitive to membrane potential changes. At high mitochondrial membrane potential, the dye tends to aggregate to form "J-aggregates" and emits a red fluorescence (590 nm). In contrast, at low mitochondrial membrane potentials which occur due to mitochondrial depolarization, the dye exists as monomer and emits a green fluorescence (527 nm).[175]

Therefore, changes from red to green fluorescence signify a decrease in MMP or depolarization of the mitochondria and is measured by the red/green emission intensity ratio (R).[32]

During the assay, A549 cells were incubated with compounds **1**-**4** at different concentrations for 48 h followed by treatment of the cells with JC-1. Upon calculation of R-values (Figure 4.22-4.23), the results indicate that all four compounds are capable of inducing mitochondrial depolarization and disrupting the MMP near their respective LC_{50} values; a progressive decrease of R values are noted after surpassing their LC_{50} dose limit. Compounds **1** and **3** behave differently at lower concentrations, exhibiting apparent hyperpolarization of mitochondria which cannot be explained on the basis their structures (Figure 4.22). When the cells are treated with a dose of the compounds greater than their LC_{50} values (0.261 µM for **1** and 0.455 µM for **3**), mitochondrial depolarization is triggered. In contrast, **2** and **4** exhibit steady dose-dependent decrease of R values over all concentration ranges (Figure 2.23) which further supports their superb cytotoxic efficacy against A549 cells. Among the four compounds, **4** proved to be most efficient with a drastic decrease in R-values in the lower nanomolar range (Figure 4.23b). It can be concluded from these results that mitochondrial dysfunction as a consequence of mitochondrial depolarization and disruption of the MMP is directly related to the cytotoxicity of the complexes which leads to PCD via the intrinsic pathway of apoptosis.[14]
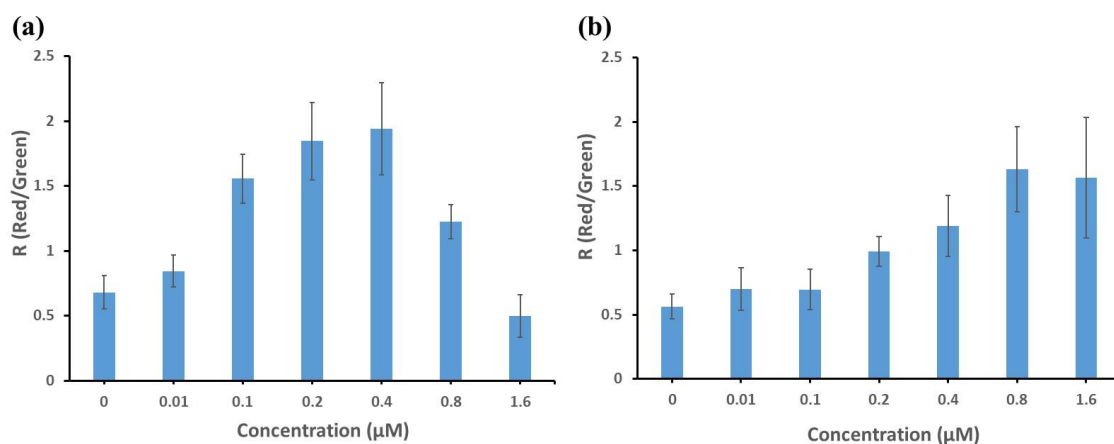
Figure 4.22. R values from the JC-1 assay at different concentration of (a) **1** and (b) **3** after 48 h of incubation against A549 cells. The graphs represent mean R values with standard deviations.
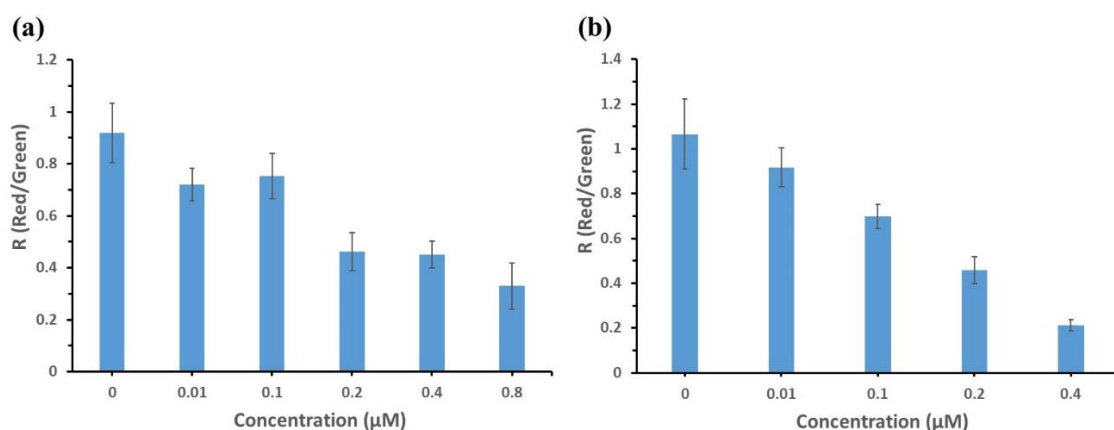
Figure 4.23. R values from the JC-1 assay at different concentration of (a) **2** and (b) **4** after 48 h of incubation against A549 cells. The graphs represent mean R values with standard deviations.

The ApoTox-Glo™ Triplex Assay combines three different assay chemistries to determine viability, cytotoxicity and caspase activation events within a single assay well. The first part of the assay assesses two protease activities, one of which is a marker for viable cells and the other of which is for dead cells. In the viability assay, a cell permeable coumarin-based fluorophore-peptide substrate, GF-AFC, is cleaved upon entering the live

cell by protease to generate fluorogenic AFC. The fluorescence intensity of the *in situ* generated fluorophore is directly proportional to the number of viable cells. Simultaneously, live cell proteases become inactive upon loss of cell membrane integrity. A second rhodamine-based fluorophore-peptide substrate, bis-AAF-R110, interacts with dead cell proteases and generate fluorogenic R110 upon cleavage of the peptide side chain. Similarly, the fluorescence intensity of the *in situ* generated fluorophore is directly proportional to the number of dead cells. Because bis-AAF-R110 is cell impermeable, essentially no signal is generated from the live cells. Since, both live and dead cell proteases produce different fluorophores, viz. AFC (λ_{ex}= 400 nm and λ_{em}= 505 nm) and R110 (λ_{ex}= 485 nm and λ_{em}= 520 nm), which have different excitation and emission wavelengths, they can be detected simultaneously inside the same well.[209] The second part of the assay assesses the activity of caspase-3/7 activity inside the cell. Caspases are a class of cysteine proteases involved in both the initiation and execution phases of apoptosis and activation of caspases are considered a hallmark of cellular death via the intrinsic pathway of apoptosis. Particularly, the activity of caspase-3/7, which are considered to be executioner caspases, can be monitored using the Caspase-Glo® assay kit. The kit contains a caspase-3/7 substrate, a tetra-peptide (DEVD) tethered luciferin (DEVD-NH-luciferin) and a luciferase enzyme. Caspase-3/7 generated during apoptotic cell death cleaves the peptide chain to form luminogenic aminoluciferin and the intensity of luminescence can be directly compared to caspase-3/7 activity.[210] Thus, in an ideal case when a compound is cytotoxic and activates caspase-3/7 inside the cell, viability and

cytotoxicity will be inversely correlated with a dose-dependent increase of the apoptosis luminescence signal.

During the assay, A549 cells were treated with various concentrations of compound **1**-**4** and incubated for 48 h. After the incubation period, the assay was performed on each plate following the ApoTox-Glo™ Triplex Assay protocol supplied with the kit and each plate was read using a microplate reader. For the viability and cytotoxicity assay, fluorescence intensity was measured at the given emission wavelength of the fluorophores, and, for the apoptosis detection assay, luminescence intensity was measured for each well. It was found that there is an apparent lack of correlation between the cytotoxicity and the viability assay results for the compounds. Nevertheless, a dose-dependent increase in apoptosis luminescence intensity/cell was detected after surpassing the LC_{50} values of **1**-**4** (Figure 4.24). It can be concluded that the cytotoxic properties of the compounds can be correlated with the activation of caspase-3/7 pathway inside the cell, which ultimately leads to PCD via apoptosis.[14, 32, 187]
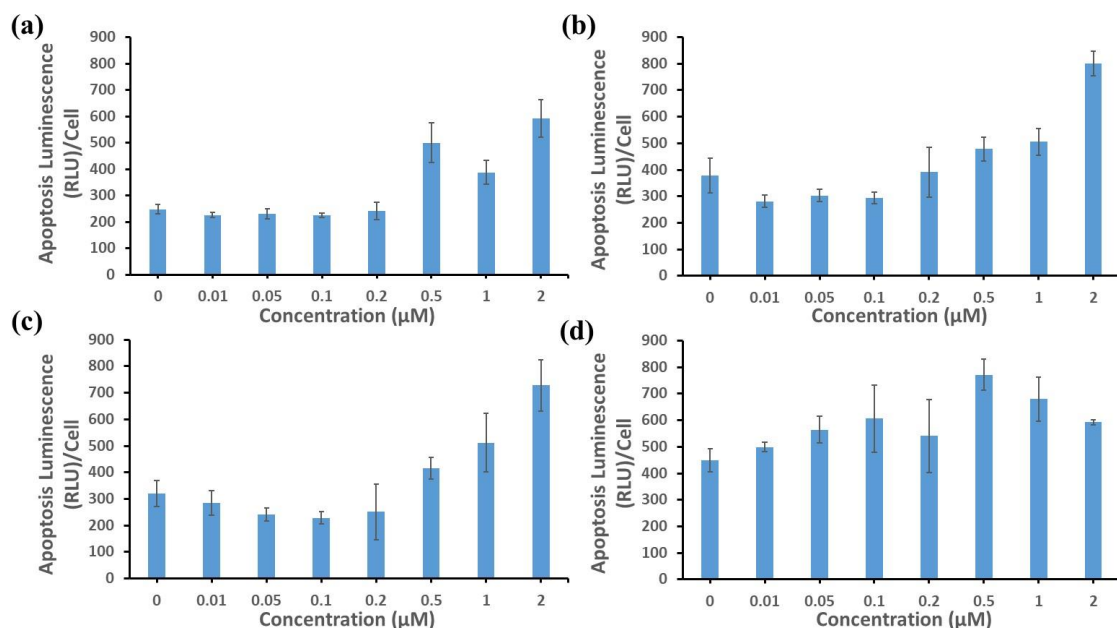
Figure 4.24. Apoptosis luminescence/cell values from the dose dependent ApoTox-Glo™ Triplex Assay of (a) **1**, (b) **2**, (c) **3** and (d) **4** after 48 h of incubation against A549 cells. The graphs represent mean luminescence intensity with standard deviations.

For compound **4**, noticeable changes in the luminescence intensity were observed at concentrations comparable to its LC_{50} value of ~ 0.022 µM (Figure 4.24d). After surpassing the 0.1 µM concentration, which is ~ 5 times the value of its LC_{50} concentration, most of the cells are dead and a correlation between caspase activity with concentration would be unreasonable. Being the most cytotoxic in the series, compound **4** was further evaluated using the temporal ApoTox-Glo™ Triplex Assay with multiple exposure periods (8, 12, 24 and 48 h). An increase in the apoptosis luminescence intensity/cell is noted going from 8 h to 12 h period followed by a gradual decrease in the value (Figure 4.25). The assay results display an early activation of caspase-3/7 inside the cell due to the cytotoxicity of **4** leading to apoptotic cell death at its LC_{50} dose.[14]
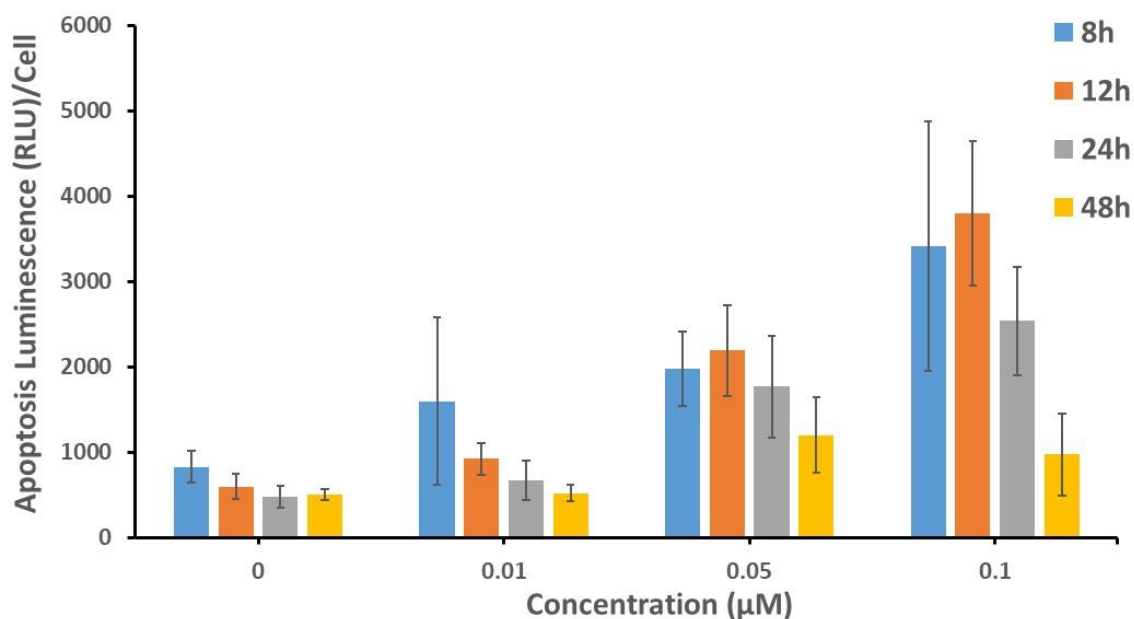
Figure 4.25. Apoptosis luminescence/cell values from the dose dependent ApoTox-Glo™ Triplex Assay of **4** at different incubation periods against A549 cells. The graphs represent mean luminescence intensity with standard deviations.

Development of oxidative stress inside the cell through the generation of intracellular ROS are well known to trigger apoptosis. ROS such as superoxide anion, hydroxyl radical, hydrogen peroxide are reportedly involved in the anticancer activity of many metal based compounds including those of Ru.[200-201, 205, 207-208, 211] Increased levels of ROS in the cell can irreversibly damage DNA and other cell organelles and proteins involved in cellular metabolism thus initiating various apoptotic signaling pathways.[211] To measure the cellular ROS generation, a fluorescence-based assay involving DCFH-DA was used. DCFH-DA is hydrolyzed by intracellular esterase enzymes to generate non-fluorescent DCFH (2′,7′-dichlorodihydrofluorescein) which is subsequently oxidized by cellular ROS to form fluorescent DCF. Thus, the fluorescence intensity of *in situ* generated

DCF (λ_{ex}= 485 nm and λ_{em}= 530 nm), which is measured using a microplate reader, can be directly related to the quantity of ROS generated inside the cell.[200]

A549 cells were treated with various concentrations of **1**-**4** and incubated for 48 h. After the incubation period, the cells were treated with DCFH-DA and incubated at 37°C for 30 minutes followed by measurement of the fluorescence intensity using a microplate reader. It is evident from the normalized fluorescence intensity graph (Figures 4.26) that all four compounds increase the level of intracellular ROS in a concentration dependent fashion after a dose that is close to their respective LC_{50} values as compared to the control (normalized fluorescence intensity of control = 1). Compounds **1**, **2** and **4** generate more oxidative stress inside the cell than does **3** which is reflected in its lower cytotoxicity.

Overall, the generation of ROS was unable to shed light on the differences in cytotoxic behavior of **2** and **4** compared to **1** and **3** but it can be concluded that formation of ROS can possibly increase the oxidative stress inside the cell which can act as a stimulus to trigger ROS mediated apoptosis via mitochondrial dysfunction in a manner akin to mixed ligand Ru polypyridyl complexes.[14, 200, 207, 212]
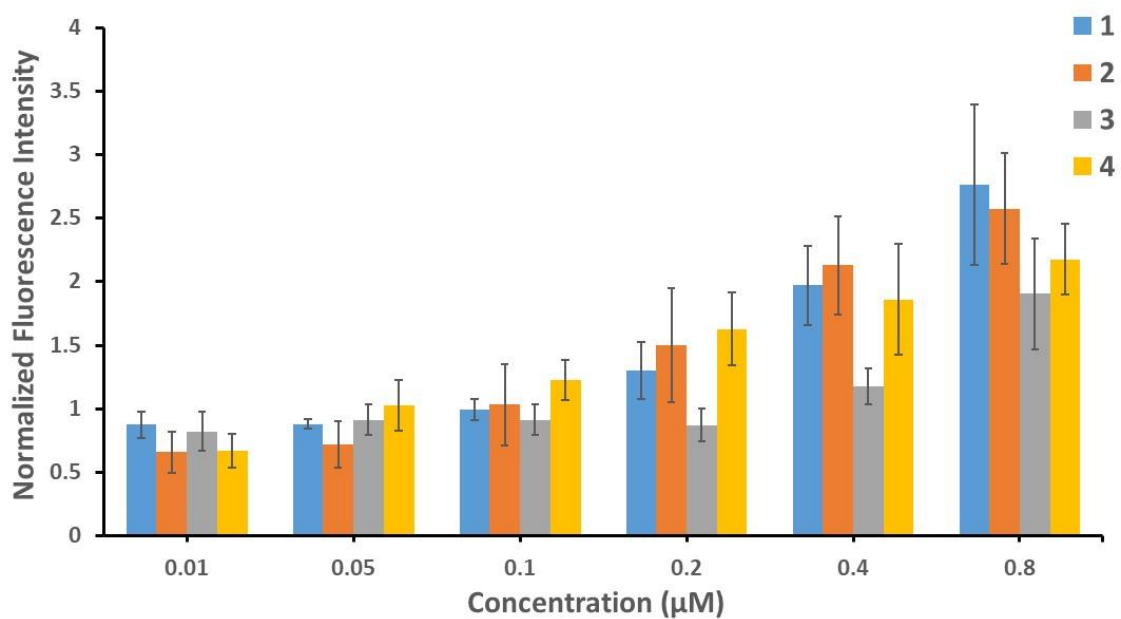
Figure 4.26. Dose dependent DCFH-DA assay of **1**-**4** after 48 h of incubation against A549 cells. The graphs represent normalized fluorescence intensity of DCF with standard deviations.

Conclusions

Cyclometallated bis-heteroleptic Ru complexes have been increasingly used as photosensitizers in DSSC applications, but *in vitro* antiproliferative properties of these families of complexes have been much less explored which prompted us to design and synthesize four Ru(II) complexes with the cyclometallated pbpy ligand with suitable ancillary ligands. All four complexes were characterized by ^{1}H NMR spectroscopy, mass spectrometry, elemental analyses and single crystal X-ray crystallography. The crystal structures exhibit tridentate meridional binding of the ligands to form bis-chelates in a distorted octahedral geometry. A pronounced trans influence of the anionic carbon resulted in elongation of the opposite Ru-N bond as is typically found with cyclometallated Ru compounds. The ^{1}MLCT bands are bathochromically shifted due to destabilization of the Ru(dπ) HOMO due to the π-donating ability of the anionic pbpy ligand. Additionally, significant broadening of the peaks with shoulders are also observed due to cyclometallation compared to polypyridyl analogues. The optimized geometries in acetonitrile, which closely mimic the solid-state structures, were analyzed to gain further insight into the electronic properties of the molecules. The results indicate that the HOMO is localized on Ru with significant pbpy ligand contributions. Due to differences in the π*-orbital energies of the ancillary ligands, the LUMO is centered on the tpy moiety for **1** and **2** in contrast to **3** and **4** for which the LUMO is localized on the pbpy ligand. All four compounds exhibit a reversible metal-based oxidation with one or more quasi-reversible ligand reductions. Due to cyclometallation, the metal-based oxidations are cathodically

shifted by 720 mV – 890 mV compared to their polypyridine analogues. Conversely, the ligand-based reductions are shifted to more negative potentials for **1** and **2** as a result of enhanced π-back-bonding to ancillary ligands, whereas the reduction appears at ~ 1.47 V for both **3** and **4** as a consequence of localization of the LUMO on the pbpy ligand. The calculated absorption spectra from TDDFT calculations qualitatively resemble the experimental absorption spectra of the complexes in the visible/near UV region with the absorption maxima being shifted hypsochromically due to overestimation of the orbital energies. The computed singlet excited states in the visible region ($\lambda_{calc} \geq 400$ nm) are predominantly ^{1}MLCT in nature whereas those in the UV region ($\lambda_{calc} \leq 400$ nm) are ^{1}LC ($^1\pi\pi^*$) in character, results that corroborate the experimental assignments.

All four compounds are highly cytotoxic against human lung adenocarcinoma (A549) cells with LC_{50} values in the low micromolar range (0.022 – 0.455 µM), which is much lower than cisplatin. The *in vitro* antiproliferative activities of (**1-4**) are found to follow the order: **4** >> **2** > **1** > **3**. Compound **4,** the most active of the series, is ~ 280 times more potent compare to cisplatin against A549 cells. This enhanced cytotoxicity of all four cyclometallated complexes can only be explained by their higher cellular uptake due to overall reduction of positive charge. Additionally, all four complexes are capable of inducing mitochondrial depolarization and disrupting the MMP near their respective LC_{50} values; a progressive decrease of R values are noted after surpassing the LC_{50} dose limit. Therefore, mitochondrial dysfunction can be directly correlated with the cytotoxic behavior which leads to PCD via the intrinsic pathway of apoptosis similar to other Ru polypyridine compounds. A dose-dependent increase in caspase-3/7 activity is detected

after surpassing the LC$_{50}$ values of **1**-**4** using the ApoTox-Glo™ Triplex Assay. The cytotoxic properties of the compounds can be correlated with the activation of caspase-3/7 pathway inside the cell, which ultimately leads to PCD following the apoptosis. The Temporal ApoTox-Glo™ Triplex Assay of **4** with multiple exposure periods revealed an early activation of caspase-3/7 inside the cell. Moreover, all four compounds have the ability to facilitate the generation of intracellular ROS levels which can stimulate oxidative stress inside the cell and trigger ROS mediated apoptosis via mitochondrial dysfunction. To summarize, compounds **1**-**4** serve as a new family of pro-apoptotic Ru anticancer compounds that are capable of killing A549 cells following the intrinsic pathway of apoptosis leading to PCD. The incorporation of the anionic cyclometallated pbpy ligands enhances the cellular uptake of these Ru compounds due to increased lipophilicity as a consequence of reduced positive charge. In addition, their lipophilicities and cytotoxicities can be further tuned by the careful choice of ancillary ligands. These promising results clearly indicate that further exploration of Ru cyclometallated compounds in cancer chemotherapy are warranted.

CHAPTER V

FUTURE WORKS AND CONCLUSIONS

Cancer is a medical condition characterized by uncontrolled cellular growth in a part of the body, which is becoming an epidemic worldwide. The serendipitous discovery of cisplatin, which revolutionized the field of cancer chemotherapy, motivated medicinal inorganic chemists to explore metal-based chemotherapeutic drugs. The dose-limiting side effects along with increased tumor resistance associated with Pt-based chemotherapy encouraged the development of new metal based anticancer drugs. In that vein, Ru-based compounds are promising platforms for tackling cancer with lower systemic toxicities and greater selectivity. Apart from their investigation as anticancer chemotherapeutics, Ru(II) complexes with light accessible excited states are increasingly being evaluated as photosensitizers in PDT, in which a pro-drug is activated by irradiation with visible light with complete spatiotemporal control. The efficacy of PDT relies on the presence of cellular oxygen which makes it ineffective against most hypoxic tumors. To circumvent the oxygen dependence, a new promising field of therapeutics is under development called PCT. Upon irradiation, photochemotherapeutic agents can attack the cancer cells via multiple mechanisms which combine to help in killing cancer cells and overcoming tumor resistance. To develop novel Ru(II) pro-drug candidates for PCT, "photocaging" strategies are being sought by various research groups where caging a drug/inhibitor to a Ru center that is stable in the absence of light and then triggering controlled release or uncaging of the molecule with visible light irradiation which leads to cytotoxicity. In this dissertation,

new architectural platforms are explored to design novel Ru(II) photocages. In addition, a new series of organometallic Ru(II) compounds with cyclometallated ligand was evaluated for enhanced cytotoxicity that can be regulated by modifying the ligand environment. The results discussed in the previous chapters will help to expand ongoing research in Ru-based chemotherapeutics for cancer therapy.

In Chapter II, three new partially solvated dinuclear Ru(II) photocages with pyrazine and quinoxaline-functionalized bridging ligands were synthesized and characterized to improve the absorption profile of the photocages at the lower energy regime of the visible light necessary for their PCT application. The electronic absorption spectra exhibit sufficiently red-shifted MLCT bands between 490-550 nm which extend into the red region ($\lambda \geq 620$ nm) of the visible spectrum which is part of the therapeutic window (600-900 nm) for PCT. The structural distortion around the metal centers engenders selective photocleavage of the caged solvent molecules from both metal centers of the dinuclear Ru-tppz complex upon irradiation with red light ($\lambda > 610$ nm). The remaining two complexes, *viz.*, dinuclear Ru-dpq and Ru-dpb, failed to display appreciable photodissociation. When evaluated against human cervical carcinoma (HeLa) cells for their potential phototoxic properties, all three compounds exhibited high LC_{50} values ($LC_{50} \gg 200$ µM) both in the dark and under irradiated conditions despite the fact that one complex is highly photoactive. It was concluded that low solubility in buffer in addition to high positive charge (+4) are likely to be the reasons for their inactivity and lack of cellular uptake.

To improve photodissociation, one could modify the cage design by installing bulky polypyridine ancillary ligands such as dmbpy, dmphen (2,9-dimethyl-1,10-phenanthroline) (Figure 5.1) which will impose distortion around the coordination environment to lower the energy of the dissociative ^{3}LF state to facilitate the process. This should also improve solubility and increase the likelihood of cell penetration due to the presence of alkyl side chains on the ancillary ligand. Coordination of anionic ligands such as phpy ligand can help to lower the overall positive charge is another viable option. Although the new compounds do not exhibit promising phototoxic properties for use as PCT agents, the strategy of bridging two Ru(II) centers with pyrazine and quinoxaline-based bridging ligands is found to be a successful design strategy for the synthesis of dinuclear Ru(II) photocage prototypes that are capable of absorbing low energy visible light.
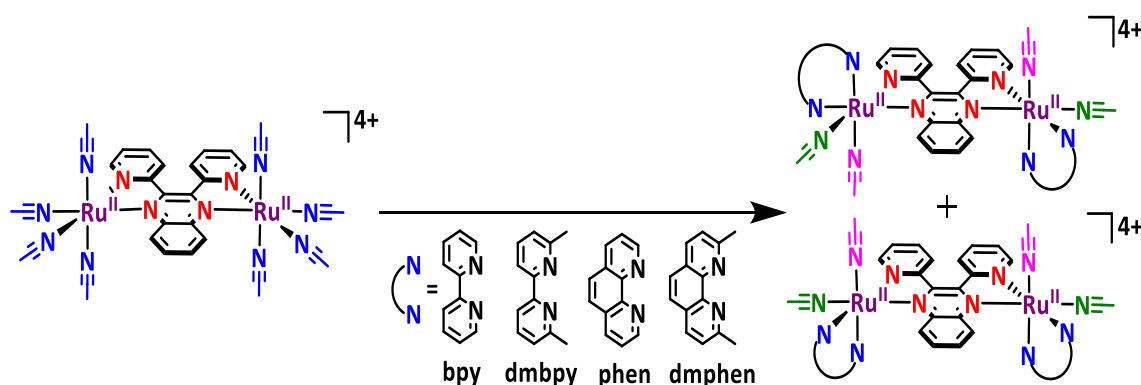
Figure 5.1. Molecular structures of proposed dinuclear Ru(II) photocages.

In an effort to reduce the overall positive charge on the Ru(II) photocages, the work in Chapter III focused on a more common mononuclear Ru(II) photocage design. An unusual bidentate coordination mode of the pbpy ligand is targeted in which the phenyl ring is directed towards the Ru center. By employing this novel architecture, three new Ru(II) photocage structures possessing monodentate nitrile and pyridyl-functionalized caged molecules were synthesized and thoroughly characterized. The crystal structures revealed a distorted octahedral geometry around the Ru center and it was found that this coordination motif generates sufficient steric congestion to facilitate the dissociation of the monodentate ligand even in the absence of light as evidenced from ^{1}H NMR spectral studies. Substitution of the nitrile ligand with pyridyl-based ligands improves the dark stability as predicted from literature reports. Thermal hydrolysis of the monodentate ligands in water/buffer can lead to the formation of active mono-aqua species which are known to covalently bind with ds DNA akin to cisplatin. As a result, all complexes were evaluated for their potential DNA binding properties and were found to exhibit weak-to-moderate binding to plasmid DNA in a dose-dependent fashion as demonstrated by the reduction in DNA mobility in gel electrophoresis assays. Two of the compounds can potentially damage the DNA helical structure at higher concentrations. The pyridine coordinated complex, when irradiated with visible light in the presence of plasmid DNA, exhibits photocleavage of DNA at 50µM as compared to dark samples. Light irradiation facilitates the formation of the cyclometallated starting material [Ru(tpy)(pbpy)]$^+$, which is conceivably the active species responsible for the photocleavage of DNA and studies are ongoing to support this hypothesis. Although all three complexes demonstrate

228

dissociation of the caged molecules even in the absence of light, this unique coordination motif of the pbpy ligand constitutes a new architectural platform for designing sterically demanding Ru(II) photocage structures.

As evidenced from the aforementioned study, introduction of an electron donating methyl amine substituent at the *p*-position of the coordinated pyridine moiety renders the thermal substitution more facile due to partial decrease in π-back-bonding interactions. Instead, incorporation of strong electron withdrawing substituents such as nitro or aldehyde groups at the *p*-position could improve the back-bonding interaction which might lead to improved dark stability relative to the unsubstituted pyridine moiety. Also, instead of tethering the fluorophore onto the monodentate ligand which is eventually substituted, it would be more prudent to attach it to the spectator tpy ligand at the 4′-position of the central pyridine ring with a suitable linker (Figure 5.2). This situation can facilitate charge transfer from metal to fluorophore through the tpy ligand and photoactivation can occur at much lower energies depending on the fluorophore moiety. A similar strategy was demonstrated by Bonnet *et al.* who incorporated the rhodamine B moiety into tpy ligand to prepare a photocage that is capable of absorbing yellow light to undergo ligand dissociation.[113]

[L = -NO$_2$, -CHO]
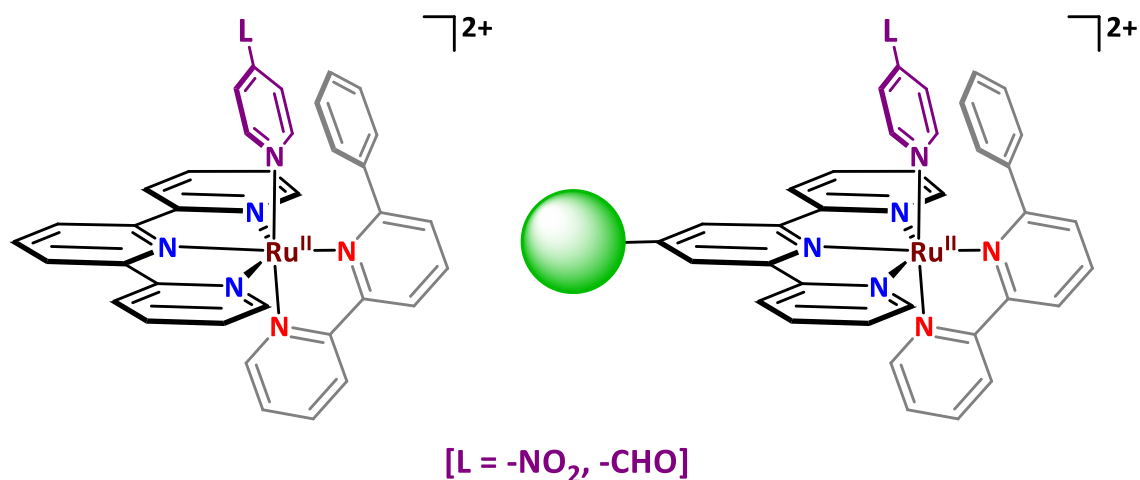
Figure 5.2. Molecular structures of proposed mononuclear Ru(II) photocages with pbpy ligand.

Unlike the previous two chapters, Chapter IV describes the enhancement and tuning of cytotoxic properties of a series of cyclometallated Ru(II)-dyads. It was demonstrated in the literature that cyclometallation drastically enhances the cytotoxicity of Ru(II) complexes due to overall reduction of positive charge which is reflected in their improved cellular uptake. In this work, in addition to incorporation of the cyclometallating pbpy ligand to synthesize four bis-heteroleptic Ru(II) complexes, the electronic properties were also tuned by choosing a suitable ancillary ligand environment which was shown to immensely alter their anticancer properties. All four compounds were structurally characterized and their electronic properties were investigated using electronic absorption spectroscopy and cyclic voltammetry in addition to verification of experimental observations by DFT calculations. The compounds were found to be highly cytotoxic when evaluated *in vitro* against human lung adenocarcinoma (A549) cells with LC$_{50}$ values in the low micromolar range (0.022 – 0.455 µM), which is much lower than

230

cisplatin and consistent with higher cellular uptake due to reduction of positive charge. All of the compounds are capable of inducing mitochondrial depolarization and disrupting MMP near their respective LC_{50} values which eventually triggers the activation of caspase 3/7 leading to PCD via the intrinsic pathway of apoptosis. Additionally, it was found that these complexes are efficient at enhancing the intracellular ROS levels which can stimulate oxidative stress inside the cell and ultimately trigger ROS mediated apoptosis via mitochondrial dysfunction. Therefore, this investigation showcases a new family of pro-apoptotic Ru anticancer compounds whose lipophilicities and cytotoxicities can be further tuned by the careful choice of ancillary ligands. These promising results clearly indicate that further exploration of Ru(II) cyclometallated compounds in cancer chemotherapy is warranted.

The non-emissive/weak emissive nature of these compounds prevented us from effectively deciphering their cellular localization using confocal microscopy which is absolutely necessary for the investigation of *in vitro* cell death mechanism. Although inductively coupled plasma mass spectrometry (ICP-MS) can interpret the cell colocalization, modification of the complexes by tethering a fluorophore moiety on the ancillary ligand provides another way to track the compounds in the cells using confocal microscopy more accurately. To prevent the quenching of the fluorescence, a less flexible linker needs to be introduced between the ancillary ligand and the fluorophore (Figure 5.3). Future work with this fluorophore is currently underway to elucidate more accurate cell death mechanisms.
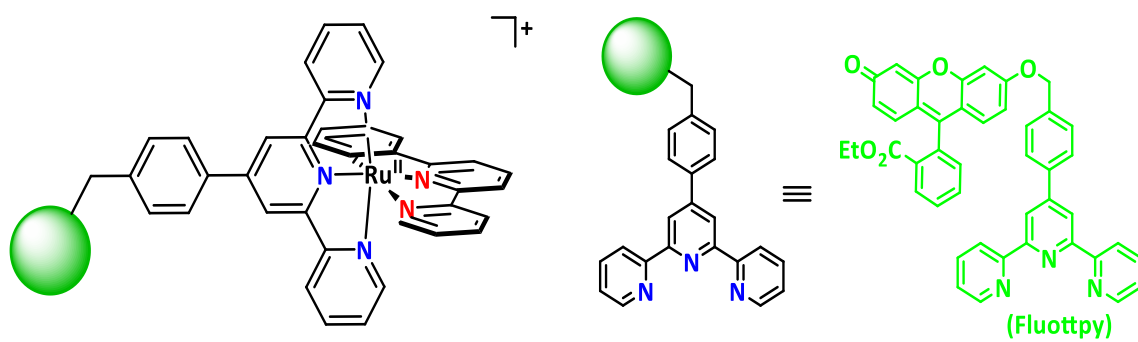
Figure 5.3. Molecular structure of proposed fluorophore tethered cyclometallated Ru(II) complex.

Taken together as a body of work, the research described in this dissertation expands the understanding of new ligand platforms that serve to introduce desired properties into Ru(II) complexes for their potential applications in photoactivated chemotherapy (PCT) and chemotherapy of cancer in general.

REFERENCES

1.   American   Cancer   Society   Cancer   Facts   &   Figures   2019.
http://www.cancer.org/content/dam/cancer-org/research/cancer-facts-and-
statistics/annual-cancer-facts-and-figures/2019/cancer-facts-and-figures-2019.pdf
(accessed July 7, 2019).

2.   Ruddon, R. W., *Cancer Biology*. 4th ed.; Oxford University Press: New York, NY,
2007.

3.   Clark, W. H. Tumour progression and the nature of cancer. *Br. J. Cancer.* **1991,**
64 (4), 631-644.

4.   World   Health   Organization   https://www.who.int/news-room/fact-
sheets/detail/cancer (accessed August 13, 2019).

5.   Rosenberg, B.; Van Camp, L.; Krigas, T. Inhibition of Cell Division in Escherichia
coli by Electrolysis Products from a Platinum Electrode. *Nature* **1965,** *205* (4972), 698-
699.

6.   Rosenberg, B.; Vancamp, L.; Trosko, J. E.; Mansour, V. H. Platinum Compounds:
a New Class of Potent Antitumour Agents. *Nature* **1969,** *222* (5191), 385-386.

7.   Kelland, L. The resurgence of platinum-based cancer chemotherapy. *Nat. Rev.
Cancer* **2007,** *7* (8), 573-584.

8.   Wheate, N. J.; Walker, S.; Craig, G. E.; Oun, R. The status of platinum anticancer
drugs in the clinic and in clinical trials. *Dalton Trans.* **2010,** *39* (35), 8113-8127.

9.   Takahara, P. M.; Rosenzweig, A. C.; Frederick, C. A.; Lippard, S. J. Crystal structure of double-stranded DNA containing the major adduct of the anticancer drug cisplatin. *Nature* **1995,** *377* (6550), 649-652.

10.   Jamieson, E. R.; Lippard, S. J. Structure, Recognition, and Processing of Cisplatin−DNA Adducts. *Chem. Rev.* **1999,** *99* (9), 2467-2498.

11.   Johnstone, T. C.; Suntharalingam, K.; Lippard, S. J. The Next Generation of Platinum Drugs: Targeted Pt(II) Agents, Nanoparticle Delivery, and Pt(IV) Prodrugs. *Chem. Rev.* **2016,** *116* (5), 3436-3486.

12.   Mjos, K. D.; Orvig, C. Metallodrugs in Medicinal Inorganic Chemistry. *Chem. Rev.* **2014,** *114* (8), 4540-4563.

13.   Barry, N. P. E.; Sadler, P. J. Exploration of the medical periodic table: towards new targets. *Chem. Commun.* **2013,** *49* (45), 5106-5131.

14.   Tan, C.-P.; Lu, Y.-Y.; Ji, L.-N.; Mao, Z.-W. Metallomics insights into the programmed cell death induced by metal-based anticancer compounds. *Metallomics* **2014,** *6* (5), 978-995.

15.   Kenny, R. G.; Marmion, C. J. Toward Multi-Targeted Platinum and Ruthenium Drugs—A New Paradigm in Cancer Drug Treatment Regimens? *Chem. Rev.* **2019,** *119* (2), 1058-1137.

16.   Barry, N. P. E.; Sadler, P. J. Challenges for Metals in Medicine: How Nanotechnology May Help To Shape the Future. *ACS Nano* **2013,** *7* (7), 5654-5659.

17.   Shi, H.; Wang, Q.; Venkatesh, V.; Feng, G.; Young, L. S.; Romero-Canelón, I.; Zeng, M.; Sadler, P. J. Photoactive platinum(iv) complex conjugated to a cancer-cell-targeting cyclic peptide. *Dalton Trans.* **2019,** *48* (24), 8560-8564.

18.   Bratsos, I.; Jedner, S.; Gianferrara, T.; Alessio, E. Ruthenium Anticancer Compounds: Challenges and Expectations. *CHIMIA* **2007,** *61* (11), 692-697.

19.   Depenbrock, H.; Schmelcher, S.; Peter, R.; Keppler, B. K.; Weirich, G.; Block, T.; Rastetter, J.; Hanauske, A. R. Preclinical activity of *trans*-indazolium [tetrachlorobisindazoleruthenate(III)] (NSC 666158; IndCR; KP 1019) against tumour colony-forming units and haematopoietic progenitor cells. *Eur. J. Cancer* **1997,** *33* (14), 2404-2410.

20.   Hartinger, C. G.; Jakupec, M. A.; Zorbas-Seifried, S.; Groessl, M.; Egger, A.; Berger, W.; Zorbas, H.; Dyson, P. J.; Keppler, B. K. KP1019, A New Redox-Active Anticancer Agent – Preclinical Development and Results of a Clinical Phase I Study in Tumor Patients. *Chem. Biodivers.* **2008,** *5* (10), 2140-2155.

21.   Hartinger, C. G.; Zorbas-Seifried, S.; Jakupec, M. A.; Kynast, B.; Zorbas, H.; Keppler, B. K. From bench to bedside – preclinical and early clinical development of the anticancer agent indazolium trans-[tetrachlorobis(1H-indazole)ruthenate(III)] (KP1019 or FFC14A). *J. Inorg. Biochem.* **2006,** *100* (5), 891-904.

22.   Trondl, R.; Heffeter, P.; Kowol, C. R.; Jakupec, M. A.; Berger, W.; Keppler, B. K. NKP-1339, the first ruthenium-based anticancer drug on the edge to clinical application. *Chem. Sci.* **2014,** *5* (8), 2925-2932.

23.   Timerbaev, A. R. Advances in developing tris(8-quinolinolato)gallium(iii) as an anticancer drug: critical appraisal and prospects. *Metallomics* **2009,** *1* (3), 193-198.

24.   Rudnev, A. V.; Foteeva, L. S.; Kowol, C.; Berger, R.; Jakupec, M. A.; Arion, V. B.; Timerbaev, A. R.; Keppler, B. K. Preclinical characterization of anticancer gallium(III) complexes: solubility, stability, lipophilicity and binding to serum proteins. *J. Inorg. Biochem.* **2006,** *100* (11), 1819-1826.

25.   Zhang, P.; Sadler, P. J. Redox-Active Metal Complexes for Anticancer Therapy. *Eur. J. Inorg. Chem.* **2017,** *2017* (12), 1541-1548.

26.   Groessl, M.; Reisner, E.; Hartinger, C. G.; Eichinger, R.; Semenova, O.; Timerbaev, A. R.; Jakupec, M. A.; Arion, V. B.; Keppler, B. K. Structure−Activity Relationships for NAMI-A-type Complexes (HL)[trans-RuCl4L(S-dmso)ruthenate(III)] (L = Imidazole, Indazole, 1,2,4-Triazole, 4-Amino-1,2,4-triazole, and 1-Methyl-1,2,4-triazole): Aquation, Redox Properties, Protein Binding, and Antiproliferative Activity. *J. Med. Chem.* **2007,** *50* (9), 2185-2193.

27.   Bergamo, A.; Sava, G. Ruthenium anticancer compounds: myths and realities of the emerging metal-based drugs. *Dalton Trans.* **2011,** *40* (31), 7817-7823.

28.   Bergamo, A.; Sava, G. Linking the future of anticancer metal-complexes to the therapy of tumour metastases. *Chem. Soc. Rev.* **2015**.

29.   Leijen, S.; Burgers, S. A.; Baas, P.; Pluim, D.; Tibben, M.; van Werkhoven, E.; Alessio, E.; Sava, G.; Beijnen, J. H.; Schellens, J. H. M. Phase I/II study with ruthenium compound NAMI-A and gemcitabine in patients with non-small cell lung cancer after first line therapy. *Invest. New Drugs* **2015,** *33* (1), 201-214.

30.   Gransbury, G. K.; Kappen, P.; Glover, C. J.; Hughes, J. N.; Levina, A.; Lay, P. A.; Musgrave, I. F.; Harris, H. H. Comparison of KP1019 and NAMI-A in tumour-mimetic environments. *Metallomics* **2016,** *8* (8), 762-773.

31.   Havrylyuk, D.; Heidary, D. K.; Nease, L.; Parkin, S.; Glazer, E. C. Photochemical Properties and Structure–Activity Relationships of RuII Complexes with Pyridylbenzazole Ligands as Promising Anticancer Agents. *Eur. J. Inorg. Chem.* **2017,** *2017* (12), 1687-1694.

32.   Peña, B.; Saha, S.; Barhoumi, R.; Burghardt, R. C.; Dunbar, K. R. Ruthenium(II)-Polypyridyl Compounds with π-Extended Nitrogen Donor Ligands Induce Apoptosis in Human Lung Adenocarcinoma (A549) Cells by Triggering Caspase-3/7 Pathway. *Inorg. Chem.* **2018,** *57* (20), 12777-12786.

33.   Notaro, A.; Gasser, G. Monomeric and dimeric coordinatively saturated and substitutionally inert Ru(ii) polypyridyl complexes as anticancer drug candidates. *Chem. Soc. Rev.* **2017,** *46* (23), 7317-7337.

34.   Gasser, G.; Ott, I.; Metzler-Nolte, N. Organometallic Anticancer Compounds. *J. Med. Chem.* **2011,** *54* (1), 3-25.

35.   Morris, R. E.; Aird, R. E.; del Socorro Murdoch, P.; Chen, H.; Cummings, J.; Hughes, N. D.; Parsons, S.; Parkin, A.; Boyd, G.; Jodrell, D. I.; Sadler, P. J. Inhibition of Cancer Cell Growth by Ruthenium(II) Arene Complexes. *J. Med. Chem.* **2001,** *44* (22), 3616-3621.

36.   Bruijnincx, P. C. A.; Sadler, P. J., Controlling platinum, ruthenium, and osmium reactivity for anticancer drug design. In *Adv. Inorg. Chem.*, van Eldik, R.; Hubbard, C. D., Eds. Academic Press: 2009; Vol. 61, pp 1-62.

37.   Zhang, P.; Sadler, P. J. Advances in the design of organometallic anticancer complexes. *Journal of Organometallic Chemistry* **2017,** *839*, 5-14.

38.   Scolaro, C.; Bergamo, A.; Brescacin, L.; Delfino, R.; Cocchietto, M.; Laurenczy, G.; Geldbach, T. J.; Sava, G.; Dyson, P. J. In Vitro and in Vivo Evaluation of Ruthenium(II)−Arene PTA Complexes. *J. Med. Chem.* **2005,** *48* (12), 4161-4171.

39.   Murray, B. S.; Babak, M. V.; Hartinger, C. G.; Dyson, P. J. The development of RAPTA compounds for the treatment of tumors. *Coord. Chem. Rev.* **2016,** *306*, 86-114.

40.   Renfrew, A. K.; Karges, J.; Scopelliti, R.; Bobbink, F. D.; Nowak-Sliwinska, P.; Gasser, G.; Dyson, P. J. Towards Light-Activated Ruthenium-Arene (RAPTA-Type) Prodrug Candidates. *Chembiochem* **2019**.

41.   Feng, L.; Geisselbrecht, Y.; Blanck, S.; Wilbuer, A.; Atilla-Gokcumen, G. E.; Filippakopoulos, P.; Kräling, K.; Celik, M. A.; Harms, K.; Maksimoska, J.; Marmorstein, R.; Frenking, G.; Knapp, S.; Essen, L.-O.; Meggers, E. Structurally Sophisticated Octahedral Metal Complexes as Highly Selective Protein Kinase Inhibitors. *J. Am. Chem. Soc.* **2011,** *133* (15), 5976-5986.

42.   Blanck, S.; Maksimoska, J.; Baumeister, J.; Harms, K.; Marmorstein, R.; Meggers, E. The Art of Filling Protein Pockets Efficiently with Octahedral Metal Complexes. *Angew. Chem. Int. Ed.* **2012,** *51* (21), 5244-5246.

43.   Smalley, K. S. M.; Contractor, R.; Haass, N. K.; Kulp, A. N.; Atilla-Gokcumen, G. E.; Williams, D. S.; Bregman, H.; Flaherty, K. T.; Soengas, M. S.; Meggers, E.; Herlyn, M. An Organometallic Protein Kinase Inhibitor Pharmacologically Activates p53 and Induces Apoptosis in Human Melanoma Cells. *Cancer Res.* **2007,** *67* (1), 209.

44.   Brabec, V.; Kasparkova, J. Ruthenium coordination compounds of biological and biomedical significance. DNA binding agents. *Coord. Chem. Rev.* **2018,** *376*, 75-94.

45.   Mital, M.; Ziora, Z. Biological applications of Ru(II) polypyridyl complexes. *Coord. Chem. Rev.* **2018,** *375*, 434-458.

46.   Zeng, L.; Gupta, P.; Chen, Y.; Wang, E.; Ji, L.; Chao, H.; Chen, Z.-S. The development of anticancer ruthenium(ii) complexes: from single molecule compounds to nanomaterials. *Chem. Soc. Rev.* **2017,** *46* (19), 5771-5804.

47.   van Niekerk, A.; Chellan, P.; Mapolie, S. F. Heterometallic Multinuclear Complexes as Anti-Cancer Agents-An Overview of Recent Developments. *Eur. J. Inorg. Chem.* **2019,** *2019* (30), 3432-3455.

48.   Mari, C.; Pierroz, V.; Ferrari, S.; Gasser, G. Combination of Ru(ii) complexes and light: new frontiers in cancer therapy. *Chem. Sci.* **2015,** *6* (5), 2660-2686.

49.   Imberti, C.; Zhang, P.; Huang, H.; Sadler, P. J. New Designs for Phototherapeutic Transition Metal Complexes. *Angew. Chem. Int. Ed.* **2019**.

50.   Villemin, E.; Ong, Y.; Thomas, C.; Gasser, G. Polymer encapsulation of ruthenium complexes for biological and medicinal applications. *Nat. Rev. Chem.* **2019,** *3* (4), 261-282.

51.   National Cancer Institute Photodynamic Therapy for Cancer. https://www.cancer.gov/about-cancer/treatment/types/surgery/photodynamic-fact-sheet (accessed August 18, 2019).

52.   Dolmans, D. E. J. G. J.; Fukumura, D.; Jain, R. K. Photodynamic therapy for cancer. *Nat. Rev. Cancer* **2003,** *3* (5), 380-387.

53.   Agostinis, P.; Berg, K.; Cengel, K. A.; Foster, T. H.; Girotti, A. W.; Gollnick, S. O.; Hahn, S. M.; Hamblin, M. R.; Juzeniene, A.; Kessel, D.; Korbelik, M.; Moan, J.; Mroz, P.; Nowis, D.; Piette, J.; Wilson, B. C.; Golab, J. Photodynamic therapy of cancer: An update. *CA: Cancer J. Clin.* **2011,** *61* (4), 250-281.

54.   Juarranz, Á.; Jaén, P.; Sanz-Rodríguez, F.; Cuevas, J.; González, S. Photodynamic therapy of cancer. Basic principles and applications. *Clin. Transl. Oncol.* **2008,** *10* (3), 148-154.

55.   Smith, N. A.; Sadler, P. J. Photoactivatable metal complexes: from theory to applications in biotechnology and medicine. *Philos. Trans. Royal Soc. A* **2013,** *371* (1995).

56.   Bonnet, S. Shifting the Light Activation of Metallodrugs to the Red and Near-Infrared Region in Anticancer Phototherapy. *Comments Inorg. Chem.* **2015,** *35* (4), 179-213.

57.   Monro, S.; Colón, K. L.; Yin, H.; Roque, J.; Konda, P.; Gujar, S.; Thummel, R. P.; Lilge, L.; Cameron, C. G.; McFarland, S. A. Transition Metal Complexes and Photodynamic Therapy from a Tumor-Centered Approach: Challenges, Opportunities, and Highlights from the Development of TLD1433. *Chem. Rev.* **2019,** *119* (2), 797-828.

58.   Tanielian, C.; Schweitzer, C.; Mechin, R.; Wolff, C. Quantum yield of singlet oxygen production by monomeric and aggregated forms of hematoporphyrin derivative. *Free Radic. Biol. Med.* **2001,** *30* (2), 208-212.

59.   Champeau, M.; Vignoud, S.; Mortier, L.; Mordon, S. Photodynamic therapy for skin cancer: How to enhance drug penetration? *J. Photochem. Photobiol. B: Biol.* **2019,** *197*, 111544.

60.   Ghosh, G.; Colón, K. L.; Fuller, A.; Sainuddin, T.; Bradner, E.; McCain, J.; Monro, S. M. A.; Yin, H.; Hetu, M. W.; Cameron, C. G.; McFarland, S. A. Cyclometalated Ruthenium(II) Complexes Derived from α-Oligothiophenes as Highly Selective Cytotoxic or Photocytotoxic Agents. *Inorg. Chem.* **2018,** *57* (13), 7694-7712.

61.   McCain, J.; Colon, K. L.; Barrett, P. C.; Monro, S. M. A.; Sainuddin, T.; Roque Iii, J.; Pinto, M.; Yin, H.; Cameron, C. G.; McFarland, S. A. Photophysical Properties and Photobiological Activities of Ruthenium(II) Complexes Bearing pi-Expansive Cyclometalating Ligands with Thienyl Groups. *Inorg. Chem.* **2019,** *58* (16), 10778-10790.

62.   Liu, J.; Zhang, C.; Rees, T. W.; Ke, L.; Ji, L.; Chao, H. Harnessing ruthenium(II) as photodynamic agents: Encouraging advances in cancer therapy. *Coord. Chem. Rev.* **2018,** *363*, 17-28.

63.   Jakubaszek, M.; Goud, B.; Ferrari, S.; Gasser, G. Mechanisms of action of Ru(ii) polypyridyl complexes in living cells upon light irradiation. *Chem. Commun.* **2018,** *54* (93), 13040-13059.

64.   Bonnet, S. Why develop photoactivated chemotherapy? *Dalton Trans.* **2018,** *47* (31), 10330-10343.

65.   Knoll, J. D.; Albani, B. A.; Turro, C. New Ru(II) Complexes for Dual Photoreactivity: Ligand Exchange and 1O2 Generation. *Acc. Chem. Res.* **2015,** *48* (8), 2280-2287.

66.   Loftus, L. M.; White, J. K.; Albani, B. A.; Kohler, L.; Kodanko, J. J.; Thummel, R. P.; Dunbar, K. R.; Turro, C. New RuII Complex for Dual Activity: Photoinduced Ligand Release and 1O2 Production. *Chem. Eur. J.* **2016,** *22* (11), 3704-3708.

67.   Rohrbaugh, T. N.; Collins, K. A.; Xue, C.; White, J. K.; Kodanko, J. J.; Turro, C. New Ru(ii) complex for dual photochemotherapy: release of cathepsin K inhibitor and 1O2 production. *Dalton Trans.* **2018,** *47* (34), 11851-11858.

68.   Knoll, J. D.; Turro, C. Control and utilization of ruthenium and rhodium metal complex excited states for photoactivated cancer therapy. *Coord. Chem. Rev.* **2015,** *282– 283*, 110-126.

69.   Mari, C.; Gasser, G. Lightening up Ruthenium Complexes to Fight Cancer? *CHIMIA* **2015,** *69* (4), 176-181.

70.   Li, A.; Turro, C.; Kodanko, J. J. Ru(ii) polypyridyl complexes as photocages for bioactive compounds containing nitriles and aromatic heterocycles. *Chem. Commun.* **2018,** *54* (11), 1280-1290.

71.   Cuello-Garibo, J.-A.; Meijer, M. S.; Bonnet, S. To cage or to be caged? The cytotoxic species in ruthenium-based photoactivated chemotherapy is not always the metal. *Chem. Commun.* **2017,** *53* (50), 6768-6771.

72.   Garner, R. N.; Gallucci, J. C.; Dunbar, K. R.; Turro, C. [Ru(bpy)$_2$(5-cyanouracil)$_2$]$^{2+}$ as a Potential Light-Activated Dual-Action Therapeutic Agent. *Inorg. Chem.* **2011,** *50*, 9213-9215.

73.   Sgambellone, M. A.; David, A.; Garner, R. N.; Dunbar, K. R.; Turro, C. Cellular Toxicity Induced by the Photorelease of a Caged Bioactive Molecule: Design of a Potential Dual-Action Ru(II) Complex. *J. Am. Chem. Soc.* **2013,** *135*, 11274-11282.

74.   Respondek, T.; Garner, R. N.; Herroon, M. K.; Podgorski, I.; Turro, C.; Kodanko, J. J. Light Activation of a Cysteine Protease Inhibitor: Caging of a Peptidomimetic Nitrile with RuII(bpy)2. *J. Am. Chem. Soc.* **2011,** *133*, 17164-17167.

75.   Wachter, E.; Heidary, D. K.; Howerton, B. S.; Parkin, S.; Glazer, E. C. Light-activated ruthenium complexes photobind DNA and are cytotoxic in the photodynamic therapy window. *Chem. Commun.* **2012,** *48* (77), 9649-9651.

76.   Havrylyuk, D.; Deshpande, M.; Parkin, S.; Glazer, E. C. Ru(ii) complexes with diazine ligands: electronic modulation of the coordinating group is key to the design of "dual action" photoactivated agents. *Chem. Commun.* **2018,** *54* (88), 12487-12490.

77.   Knoll, J. D.; Albani, B. A.; Durr, C. B.; Turro, C. Unusually efficient pyridine photodissociation from Ru(II) complexes with sterically bulky bidentate ancillary ligands. *J. Phys. Chem. A* **2014,** *118* (45), 10603-10610.

78.   Albani, B. A.; Durr, C. B.; Turro, C. Selective Photoinduced Ligand Exchange in a New Tris–Heteroleptic Ru(II) Complex. *J. Phys. Chem. A* **2013,** *117* (50), 13885-13892.

79.   Göttle, A. J.; Alary, F.; Boggio-Pasqua, M.; Dixon, I. M.; Heully, J.-L.; Bahreman, A.; Askes, S. H. C.; Bonnet, S. Pivotal Role of a Pentacoordinate 3MC State on the

Photocleavage Efficiency of a Thioether Ligand in Ruthenium(II) Complexes: A Theoretical Mechanistic Study. *Inorg. Chem.* **2016,** *55* (9), 4448-4456.

80.   Garner, R. N.; Joyce, L. E.; Turro, C. Effect of Electronic Structure on the Photoinduced Ligand Exchange of Ru(II) Polypyridine Complexes. *Inorg. Chem.* **2011,** *50*, 4384-4391.

81.   Nisbett, K.; Tu, Y.-J.; Turro, C.; Kodanko, J. J.; Schlegel, H. B. DFT Investigation of Ligand Photodissociation in [RuII(tpy)(bpy)(py)]2+ and [RuII(tpy)(Me2bpy)(py)]2+ Complexes. *Inorg. Chem.* **2018,** *57* (1), 231-240.

82.   Bonnet, S.; Collin, J.-P.; Sauvage, J.-P.; Schofield, E. Photochemical Expulsion of the Neutral Monodentate Ligand L in Ru(Terpy*)(Diimine)(L)2+: A Dramatic Effect of the Steric Properties of the Spectator Diimine Ligand. *Inorg. Chem.* **2004,** *43* (26), 8346-8354.

83.   Cuello-Garibo, J.-A.; Pérez-Gallent, E.; van der Boon, L.; Siegler, M. A.; Bonnet, S. Influence of the Steric Bulk and Solvent on the Photoreactivity of Ruthenium Polypyridyl Complexes Coordinated to l-Proline. *Inorg. Chem.* **2017,** *56* (9), 4818-4828.

84.   Huisman, M.; White, J. K.; Lewalski, V. G.; Podgorski, I.; Turro, C.; Kodanko, J. J. Caging the uncageable: using metal complex release for photochemical control over irreversible inhibition. *Chem. Commun.* **2016,** *52* (85), 12590-12593.

85.   Arora, K.; Herroon, M.; Al-Afyouni, M. H.; Toupin, N. P.; Rohrabaugh, T. N.; Loftus, L. M.; Podgorski, I.; Turro, C.; Kodanko, J. J. Catch and Release Photosensitizers: Combining Dual-Action Ruthenium Complexes with Protease Inactivation for Targeting Invasive Cancers. *J. Am. Chem. Soc.* **2018,** *140* (43), 14367-14380.

86.   Rohrabaugh, T. N.; Rohrabaugh, A. M.; Kodanko, J. J.; White, J. K.; Turro, C. Photoactivation of imatinib-antibody conjugate using low-energy visible light from Ru(ii)-polypyridyl cages. *Chem. Commun.* **2018,** *54* (41), 5193-5196.

87.   Li, A.; Turro, C.; Kodanko, J. J. Ru(II) Polypyridyl Complexes Derived from Tetradentate Ancillary Ligands for Effective Photocaging. *Acc. Chem. Res.* **2018,** *51* (6), 1415-1421.

88.   Engels, J.; Schlaeger, E. J. Synthesis, structure, and reactivity of adenosine cyclic 3',5'-phosphate-benzyltriesters. *J. Med. Chem.* **1977,** *20* (7), 907-911.

89.   Kaplan, J. H.; Forbush, B.; Hoffman, J. F. Rapid photolytic release of adenosine 5'-triphosphate from a protected analog: utilization by the sodium:potassium pump of human red blood cell ghosts. *Biochemistry* **1978,** *17* (10), 1929-1935.

90.   Zayat, L.; Calero, C.; Alborés, P.; Baraldo, L.; Etchenique, R. A New Strategy for Neurochemical Photodelivery: Metal−Ligand Heterolytic Cleavage. *J. Am. Chem. Soc.* **2003,** *125* (4), 882-883.

91.   Zayat, L.; Noval, M. G.; Campi, J.; Calero, C. I.; Calvo, D. J.; Etchenique, R. A New Inorganic Photolabile Protecting Group for Highly Efficient Visible Light GABA Uncaging. *ChemBioChem* **2007,** *8* (17), 2035-2038.

92.   Salierno, M.; Fameli, C.; Etchenique, R. Caged Amino Acids for Visible-Light Photodelivery. *Eur. J. Inorg. Chem.* **2008,** *2008* (7), 1125-1128.

93.   Singh, T. N.; Turro, C. Photoinitiated DNA Binding by *cis*-[Ru(bpy)$_2$(NH$_3$)$_2$]$^{2+}$. *Inorg. Chem.* **2004,** *43*, 7260-7262.

94.   Liu, Y.; Turner, D. B.; Singh, T. N.; Angeles-Boza, A. M.; Chouai, A.; Dunbar, K. R.; Turro, C. Ultrafast Ligand Exchange: Detection of a Pentacoordinate Ru(II) Intermediate and Product Formation. *J. Am. Chem. Soc.* **2009,** *131*, 26-27.

95.   Albani, B. A.; Peña, B.; Leed, N. A.; de Paula, N. A. B. G.; Pavani, C.; Baptista, M. S.; Dunbar, K. R.; Turro, C. Marked Improvement in Photoinduced Cell Death by a New Tris-heteroleptic Complex with Dual Action: Singlet Oxygen Sensitization and Ligand Dissociation. *J. Am. Chem. Soc.* **2014,** *136* (49), 17095-17101.

96.   Palmer, A. M.; Peña, B.; Sears, R. B.; Chen, O.; Ojaimi, M. E.; Thummel, R. P.; Dunbar, K. R.; Turro, C. Cytotoxicity of cyclometallated ruthenium complexes: the role of ligand exchange on the activity. *Philos. Trans. R. Soc. A* **2013,** *371*, 20120135.

97.   Albani, B. A.; Peña, B.; Dunbar, K. R.; Turro, C. New cyclometallated Ru(II) complex for potential application in photochemotherapy? *Photochem. Photobiol. Sci.* **2014,** *13*, 272-280.

98.   Sears, R. B.; Joyce, L. E.; Ojaimi, M.; Gallucci, J. C.; Thummel, R. P.; Turro, C. Photoinduced ligand exchange and DNA binding of cis-[Ru(phpy)(phen)(CH$_3$CN)$_2$]$^+$ with long wavelength visible light. *J. Inorg. Biochem.* **2013,** *121*, 77-87.

99.   Al-Afyouni, M. H.; Rohrabaugh, T. N.; Al-Afyouni, K. F.; Turro, C. New Ru(ii) photocages operative with near-IR light: new platform for drug delivery in the PDT window. *Chem. Sci.* **2018,** *9* (32), 6711-6720.

100.   Knoll, J. D.; Albani, B. A.; Turro, C. Excited state investigation of a new Ru(ii) complex for dual reactivity with low energy light. *Chem. Commun.* **2015,** *51* (42), 8777-8780.

101.   Loftus, L. M.; Al-Afyouni, K. F.; Rohrabaugh, T. N.; Gallucci, J. C.; Moore, C. E.; Rack, J. J.; Turro, C. Unexpected Role of Ru(II) Orbital and Spin Contribution on Photoinduced Ligand Exchange: New Mechanism To Access the Photodynamic Therapy Window. *J. Phys. Chem. C* **2019,** *123* (16), 10291-10299.

102.   Loftus, L. M.; Al-Afyouni, K. F.; Turro, C. New RuII Scaffold for Photoinduced Ligand Release with Red Light in the Photodynamic Therapy (PDT) Window. *Chem. Eur. J.* **2018,** *24* (45), 11550-11553.

103.   Loftus, L. M.; Li, A.; Fillman, K. L.; Martin, P. D.; Kodanko, J. J.; Turro, C. Unusual Role of Excited State Mixing in the Enhancement of Photoinduced Ligand Exchange in Ru(II) Complexes. *J. Am. Chem. Soc.* **2017,** *139* (50), 18295-18306.

104.   Respondek, T.; Sharma, R.; Herroon, M. K.; Garner, R. N.; Knoll, J. D.; Cueny, E.; Turro, C.; Podgorski, I.; Kodanko, J. J. Inhibition of Cathepsin Activity in a Cell-Based Assay by a Light-Activated Ruthenium Compound. *ChemMedChem* **2014,** *9* (6), 1306-1315.

105.   Herroon Mackenzie, K.; Sharma, R.; Rajagurubandara, E.; Turro, C.; Kodanko Jeremy, J.; Podgorski, I. Photoactivated inhibition of cathepsin K in a 3D tumor model. *Biol. Chem.* **2016,** *397* (6), 571.

106.   van Rixel, V. H. S.; Busemann, A.; Göttle, A. J.; Bonnet, S. Preparation, stability, and photoreactivity of thiolato ruthenium polypyridyl complexes: Can cysteine derivatives protect ruthenium-based anticancer complexes? *J. Inorg. Biochem.* **2015,** *150*, 174-181.

107.	Goldbach, R. E.; Rodriguez-Garcia, I.; van Lenthe, J. H.; Siegler, M. A.; Bonnet, S. N-Acetylmethionine and Biotin as Photocleavable Protective Groups for Ruthenium Polypyridyl Complexes. *Chem. Eur. J.* **2011,** *17* (36), 9924-9929.

108.	Bianka, S.; S., v. R. V. H.; J., v. R. E.; L., H. S.; B., M. M. J.; Freek, A.; A., S. M.; Sylvestre, B. Chemical Swarming: Depending on Concentration, an Amphiphilic Ruthenium Polypyridyl Complex Induces Cell Death via Two Different Mechanisms. *Chem. Eur. J.* **2016,** *22* (31), 10960-10968.

109.	Lameijer, L. N.; Brevé, T. G.; van Rixel, V. H. S.; Askes, S. H. C.; Siegler, M. A.; Bonnet, S. Effects of the Bidentate Ligand on the Photophysical Properties, Cellular Uptake, and (Photo)cytotoxicity of Glycoconjugates Based on the [Ru(tpy)(NN)(L)]2+ Scaffold. *Chem. Eur. J.* **2018,** *24* (11), 2709-2717.

110.	N., L. L.; L., H. S.; G., B. T.; C., A. S. H.; Sylvestre, B. d- Versus l-Glucose Conjugation: Mitochondrial Targeting of a Light-Activated Dual-Mode-of-Action Ruthenium-Based Anticancer Prodrug. *Chem. Eur. J.* **2016,** *22* (51), 18484-18491.

111.	Bahreman, A.; Rabe, M.; Kros, A.; Bruylants, G.; Bonnet, S. Binding of a Ruthenium Complex to a Thioether Ligand Embedded in a Negatively Charged Lipid Bilayer: A Two-Step Mechanism. *Chem. Eur. J.* **2014,** *20* (24), 7429-7438.

112.	Bonnet, S.; Limburg, B.; Meeldijk, J. D.; Klein Gebbink, R. J. M.; Killian, J. A. Ruthenium-Decorated Lipid Vesicles: Light-Induced Release of [Ru(terpy)(bpy)(OH2)]2+ and Thermal Back Coordination. *J. Am. Chem. Soc.* **2011,** *133* (2), 252-261.

113.   Bahreman, A.; Cuello-Garibo, J.-A.; Bonnet, S. Yellow-light sensitization of a ligand photosubstitution reaction in a ruthenium polypyridyl complex covalently bound to a rhodamine dye. *Dalton Trans.* **2014,** *43* (11), 4494-4505.

114.   Lameijer, L. N.; Ernst, D.; Hopkins, S. L.; Meijer, M. S.; Askes, S. H. C.; Le Dévédec, S. E.; Bonnet, S. A Red-Light-Activated Ruthenium-Caged NAMPT Inhibitor Remains Phototoxic in Hypoxic Cancer Cells. *Angew. Chem. Int. Ed.* **2017,** *56* (38), 11549-11553.

115.   Sun, W.; Wen, Y.; Thiramanas, R.; Chen, M.; Han, J.; Gong, N.; Wagner, M.; Jiang, S.; Meijer, M. S.; Bonnet, S.; Butt, H.-J.; Mailänder, V.; Liang, X.-J.; Wu, S. Red-Light-Controlled Release of Drug–Ru Complex Conjugates from Metallopolymer Micelles for Phototherapy in Hypoxic Tumor Environments. *Adv. Funct. Mater.* **2018,** *28* (39), 1804227.

116.   Hopkins, S. L.; Siewert, B.; Askes, S. H. C.; Veldhuizen, P.; Zwier, R.; Heger, M.; Bonnet, S. An in vitro cell irradiation protocol for testing photopharmaceuticals and the effect of blue, green, and red light on human cancer cell lines. *Photochemical & Photobiological Sciences* **2016,** *15* (5), 644-653.

117.   Karaoun, N.; Renfrew, A. K. A luminescent ruthenium(II) complex for light-triggered drug release and live cell imaging. *Chem. Commun.* **2015,** *51* (74), 14038-14041.

118.   Chan, H.; Ghrayche, J. B.; Wei, J.; Renfrew, A. K. Photolabile Ruthenium(II)–Purine Complexes: Phototoxicity, DNA Binding, and Light-Triggered Drug Release. *Eur. J. Inorg. Chem.* **2017,** *2017* (12), 1679-1686.

119. Howerton, B. S.; Heidary, D. K.; Glazer, E. C. Strained Ruthenium Complexes Are Potent Light-Activated Anticancer Agents. *J. Am. Chem. Soc.* **2012,** *134* (20), 8324-8327.

120. Wei, J.; Renfrew, A. K. Photolabile ruthenium complexes to cage and release a highly cytotoxic anticancer agent. *J. Inorg. Biochem.* **2018,** *179*, 146-153.

121. Hidayatullah, A. N.; Wachter, E.; Heidary, D. K.; Parkin, S.; Glazer, E. C. Photoactive Ru(II) Complexes With Dioxinophenanthroline Ligands Are Potent Cytotoxic Agents. *Inorg. Chem.* **2014,** *53* (19), 10030-10032.

122. Joshi, T.; Pierroz, V.; Mari, C.; Gemperle, L.; Ferrari, S.; Gasser, G. A Bis(dipyridophenazine)(2-(2-pyridyl)pyrimidine-4-carboxylic acid)ruthenium(II) Complex with Anticancer Action upon Photodeprotection. *Angew. Chem.* **2014,** *126* (11), 3004-3007.

123. Pierroz, V.; Joshi, T.; Leonidova, A.; Mari, C.; Schur, J.; Ott, I.; Spiccia, L.; Ferrari, S.; Gasser, G. Molecular and Cellular Characterization of the Biological Effects of Ruthenium(II) Complexes Incorporating 2-Pyridyl-2-pyrimidine-4-carboxylic Acid. *J. Am. Chem. Soc.* **2012,** *134* (50), 20376-20387.

124. Mari, C.; Pierroz, V.; Leonidova, A.; Ferrari, S.; Gasser, G. Towards Selective Light-Activated RuII-Based Prodrug Candidates. *Eur. J. Inorg. Chem.* **2015,** *2015* (23), 3879-3891.

125. Siewert, B.; Langerman, M.; Pannwitz, A.; Bonnet, S. Synthesis and Avidin Binding of Ruthenium Complexes Functionalized with a Light-Cleavable Free Biotin Moiety. *Eur. J. Inorg. Chem.* **2018,** *2018* (37), 4117-4124.

126.   van Rixel, V. H. S.; Siewert, B.; Hopkins, S. L.; Askes, S. H. C.; Busemann, A.; Siegler, M. A.; Bonnet, S. Green light-induced apoptosis in cancer cells by a tetrapyridyl ruthenium prodrug offering two trans coordination sites. *Chem. Sci.* **2016,** *7* (8), 4922-4929.

127.   Garner, R. N.; Pierce, C. G.; Reed, C. R.; Brennessel, W. W. Photoinitiated treatment of Mycobacterium using Ru(II) isoniazid complexes. *Inorg. Chim. Acta* **2017,** *461*, 261-266.

128.   Albani, B. A.; Pena, B.; Saha, S.; White, J. K.; Schaeffer, A. M.; Dunbar, K. R.; Turro, C. A dinuclear Ru(ii) complex capable of photoinduced ligand exchange at both metal centers. *Chem. Commun.* **2015,** *51* (92), 16522-16525.

129.   Wadman, S. H.; Havenith, R. W. A.; Hartl, F.; Lutz, M.; Spek, A. L.; van Klink, G. P. M.; van Koten, G. Redox Chemistry and Electronic Properties of 2,3,5,6-Tetrakis(2-pyridyl)pyrazine-Bridged   Diruthenium   Complexes   Controlled   by   N,C,N′-BisCyclometalated Ligands. *Inorg. Chem.* **2009,** *48* (13), 5685-5696.

130.   Wallace, A. W.; Rorer Murphy Jr, W.; Petersen, J. D. Electrochemical and photophysical properties of mono- and bimetallic ruthenium(II) complexes. *Inorg. Chim. Acta* **1989,** *166* (1), 47-54.

131.   Rillema, D. P.; Mack, K. B. The low-lying excited state in ligand .pi.-donor complexes of ruthenium(II): mononuclear and binuclear species. *Inorg. Chem.* **1982,** *21* (10), 3849-3854.

132.   Molnar, S. M.; Neville, K. R.; Jensen, G. E.; Brewer, K. J. Utilization of substituted polyazine bridging ligands to tune the spectroscopic and electrochemical properties of bimetallic ruthenium complexes. *Inorg. Chim. Acta* **1993,** *206* (1), 69-76.

133.   Goodwin, H. A.; Lions, F. Tridentate Chelate Compounds. II1. *J. Am. Chem. Soc.* **1959,** *81* (24), 6415-6422.

134.   Baiano, J. A.; Carlson, D. L.; Wolosh, G. M.; DeJesus, D. E.; Knowles, C. F.; Szabo, E. G.; Murphy, W. R. Bimetallic complexes of rhenium(I). Preparation of Re(BL)(CO)3Cl and [Re(CO)3Cl]2(BL) (BL = 2,3-bis(2-pyridyl)pyrazine, 2,3-bis(2-pyridyl)quinoxaline, and 2,3-bis(2-pyridyl)benzo[g]quinoxaline). *Inorg. Chem.* **1990,** *29* (12), 2327-2332.

135.   Bennett, M. A.; Smith, A. K. Arene ruthenium(II) complexes formed by dehydrogenation of cyclohexadienes with ruthenium(III) trichloride. *J. Chem. Soc., Dalton Trans.* **1974,** (2), 233-241.

136.   *SMART and SAINT*. Siemens Analytical X-ray Instruments Inc.: Madison, WI, 1996.

137.   Sheldrick, G. M., *SADABS*. University of Gottinggen: Gottingen, Germany, 1996.

138.   Sheldrick, G. A short history of SHELX. *Acta Crystallogr. A* **2008,** *64* (1), 112-122.

139.   Sheldrick, G. Crystal structure refinement with SHELXL. *Acta Crystallogr. C* **2015,** *71* (1), 3-8.

140.   Dolomanov, O. V.; Bourhis, L. J.; Gildea, R. J.; Howard, J. A. K.; Puschmann, H. OLEX2: a complete structure solution, refinement and analysis program. *J. Appl. Crystallogr.* **2009,** *42* (2), 339-341.

141.   Guzei, I. An idealized molecular geometry library for refinement of poorly behaved molecular fragments with constraints. *J. Appl. Crystallogr.* **2014,** *47* (2), 806-809.

142.   Spek, A. PLATON SQUEEZE: a tool for the calculation of the disordered solvent contribution to the calculated structure factors. *Acta Crystallogr. C* **2015,** *71* (1), 9-18.

143.   Gaussian 09, Revision B.01, Frisch, M. J.; Trucks, G. W.; Schlegel, H. B.; Scuseria, G. E.; Robb, M. A.; Cheeseman, J. R.; Scalmani, G.; Barone, V.; Mennucci, B.; Petersson, G. A.; Nakatsuji, H.; Caricato, M.; Li, X.; Hratchian, H. P.; Izmaylov, A. F.; Bloino, J.; Zheng, G.; Sonnenberg, J. L.; Hada, M.; Ehara, M.; Toyota, K.; Fukuda, R.; Hasegawa, J.; Ishida, M.; Nakajima, T.; Honda, Y.; Kitao, O.; Nakai, H.; Vreven, T.; Montgomery, Jr., J. A.; Peralta, J. E.; Ogliaro, F.; Bearpark, M.; Heyd, J. J.; Brothers, E.; Kudin, K. N.; Staroverov, V. N.; Kobayashi, R.; Normand, J.; Raghavachari, K.; Rendell, A.; Burant, J. C.; Iyengar, S. S.; Tomasi, J.; Cossi, M.; Rega, N.; Millam, N. J.; Klene, M.; Knox, J. E.; Cross, J. B.; Bakken, V.; Adamo, C.; Jaramillo, J.; Gomperts, R.; Stratmann, R. E.; Yazyev, O.; Austin, A. J.; Cammi, R.; Pomelli, C.; Ochterski, J. W.; Martin, R. L.; Morokuma, K.; Zakrzewski, V. G.; Voth, G. A.; Salvador, P.; Dannenberg, J. J.; Dapprich, S.; Daniels, A. D.; Farkas, Ö.; Foresman, J. B.; Ortiz, J. V.; Cioslowski, J.; Fox, D. J. Gaussian, Inc., Wallingford, CT, 2009.

144.   Lee, C.; Yang, W.; Parr, R. G. *Phys. Rev. B* **1998,** *37*, 785-789.

145.   Becke, A. D. *J. Chem. Phys.* **1993,** *98*, 5648-5652.

146.   Andrae, D.; Häußermann, U.; Dolg, M.; Stoll, H.; Preuß, H. Energy-adjustedab initio pseudopotentials for the second and third row transition elements. *Theor. Chem. Acc.* **1990,** *77* (2), 123-141.

147.   Krishnan, R.; Binkley, J. S.; Seeger, R.; Pople, J. A. Self-consistent molecular orbital methods. XX. A basis set for correlated wave functions. *J. Chem. Phys.* **1980,** *72* (1), 650-654.

148.   Frisch, M. J.; Pople, J. A.; Binkley, J. S. Self-consistent molecular orbital methods 25. Supplementary functions for Gaussian basis sets. *J. Chem. Phys.* **1984,** *80* (7), 3265-3269.

149.   Marenich, A. V.; Cramer, C. J.; Truhlar, D. G. Universal Solvation Model Based on Solute Electron Density and on a Continuum Model of the Solvent Defined by the Bulk Dielectric Constant and Atomic Surface Tensions. *J. Phys. Chem. B* **2009,** *113* (18), 6378-6396.

150.   Fantacci, S.; De Angelis, F.; Wang, J.; Bernhard, S.; Selloni, A. A Combined Computational and Experimental Study of Polynuclear Ru−TPPZ Complexes: Insight into the Electronic and Optical Properties of Coordination Polymers. *J. Am. Chem. Soc.* **2004,** *126* (31), 9715-9723.

151.   Yao, C.-J.; Zheng, R.-H.; Nie, H.-J.; Cui, B.-B.; Shi, Q.; Yao, J.; Zhong, Y.-W. A Combined Experimental and Computational Study of Linear Ruthenium(II) Coordination Oligomers with End-Capping Organic Redox Sites: Insight into the Light Absorption and Charge Delocalization. *Chem. Eur. J.* **2013,** *19* (37), 12376-12387.

152.   Schulze, B.; Escudero, D.; Friebe, C.; Siebert, R.; Görls, H.; Sinn, S.; Thomas, M.; Mai, S.; Popp, J.; Dietzek, B.; González, L.; Schubert, U. S. Ruthenium(II) Photosensitizers of Tridentate Click-Derived Cyclometalating Ligands: A Joint Experimental and Computational Study. *Chem. Eur. J.* **2012,** *18* (13), 4010-4025.

153.   Lackner, W.; Standfest-Hauser, C. M.; Mereiter, K.; Schmid, R.; Kirchner, K. Photochemical displacement of the benzene ligand in [(η6-C6H6)Ru(CH3CN)2(L)]2+ and [(η6-C6H6)Ru(CH3CN)(L2)]2+ (L=CH3CN, PPh3, L2=dppe, bipy). *Inorg. Chim. Acta* **2004,** *357* (9), 2721-2727.

154.   Petroni, A.; Slep, L. D.; Etchenique, R. Ruthenium(II) 2,2'-Bipyridyl Tetrakis Acetonitrile Undergoes Selective Axial Photocleavage. *Inorg. Chem.* **2008,** *47* (3), 951-956.

155.   Ypsilantis, K.; Plakatouras, J. C.; Manos, M. J.; Kourtellaris, A.; Markopoulos, G.; Kolettas, E.; Garoufis, A. Stepwise synthesis, characterization, DNA binding properties and cytotoxicity of diruthenium oligopyridine compounds conjugated with peptides. *Dalton Trans.* **2018,** *47* (10), 3549-3567.

156.   Hartshorn, C. M.; Daire, N.; Tondreau, V.; Loeb, B.; Meyer, T. J.; White, P. S. Synthesis and Characterization of Dinuclear Ruthenium Complexes with Tetra-2-pyridylpyrazine as a Bridge. *Inorg. Chem.* **1999,** *38* (13), 3200-3206.

157.   Coe, B. J.; Meyer, T. J.; White, P. S. Synthetic and Structural Studies on trans-Tetrapyridine Complexes of Ruthenium(II). *Inorg. Chem.* **1995,** *34* (3), 593-602.

158.   Rillema, D. P.; Taghdiri, D. G.; Jones, D. S.; Worl, L. A.; Meyer, T. J.; Levy, H. A.; Keller, C. D. Structure and redox and photophysical properties of a series of ruthenium

heterocycles based on the ligand 2,3-bis(2-pyridyl)quinoxaline. *Inorg. Chem.* **1987,** *26* (4), 578-585.

159.   Arana, C. R.; Abruna, H. D. Monomeric and oligomeric complexes of ruthenium and osmium with tetra-2-pyridyl-1,4-pyrazine (TPPZ). *Inorg. Chem.* **1993,** *32* (2), 194-203.

160.   Cooper, J. B.; MacQueen, D. B.; Petersen, J. D.; Wertz, D. W. Role of the LUMO in determining redox stability for 2,3-dipyridylpyrazine and 2,3-dipyridylquinoxaline-bridged ruthenium(II) bimetallic complexes. *Inorg. Chem.* **1990,** *29* (19), 3701-3705.

161.   Sun, Y.; El Ojaimi, M.; Hammitt, R.; Thummel, R. P.; Turro, C. Effect of Ligands with Extended π-System on the Photophysical Properties of Ru(II) Complexes. *J. Phys. Chem. B* **2010,** *114*, 14664-14670.

162.   Kuete, V.; Karaosmanoğlu, O.; Sivas, H., Chapter 10 - Anticancer Activities of African Medicinal Spices and Vegetables. In *Medicinal Spices and Vegetables from Africa*, Kuete, V., Ed. Academic Press: 2017; pp 271-297.

163.   Constable, E. C.; Hannon, M. J. Solvent effects in the reactions of 6-phenyl-2,2′-bipyridine with ruthenium(II). *Inorg. Chim. Acta* **1993,** *211* (1), 101-110.

164.   Constable, E. C.; Henney, R. P. G.; Leese, T. A.; Tocher, D. A. Cyclometallation reactions of 6-phenyl-2,2[prime or minute]-bipyridine; a potential C,N,N-donor analogue of 2,2[prime or minute]: 6[prime or minute],2[double prime]-terpyridine. Crystal and molecular structure of dichlorobis(6-phenyl-2,2[prime or minute]-bipyridine)ruthenium(II). *J. Chem. Soc., Dalton Trans.* **1990,** (2), 443-449.

256

165.   Carrone, G.; Gantov, F.; Slep, L. D.; Etchenique, R. Fluorescent Ligands and Energy Transfer in Photoactive Ruthenium–Bipyridine Complexes. *J. Phys. Chem. A* **2014,** *118* (45), 10416-10424.

166.   Sullivan, B. P.; Calvert, J. M.; Meyer, T. J. Cis-trans isomerism in (trpy)(PPh3)RuC12. Comparisons between the chemical and physical properties of a cis-trans isomeric pair. *Inorg. Chem.* **1980,** *19* (5), 1404-1407.

167.   Sheldrick, G. M. *TWINABS*, Version 2012/1, Georg-August-Universität Göttingen, Göttingen, Germany, 2012.

168.   Dennington, R.; Keith, T. A.; Millam, J. M. *GaussView*, Version 6, Semichem Inc., Shawnee Mission, KS, 2016.

169.   A., J. B.; Hemlata, A.; A., W. T.; Edgar, M.; Somnath, M.; Sascha, O. Judicious Ligand Design in Ruthenium Polypyridyl CO2 Reduction Catalysts to Enhance Reactivity by Steric and Electronic Effects. *Chem. Eur. J.* **2016,** *22* (42), 14870-14880.

170.   Bossert, J.; Daniel, C. Electronic absorption spectroscopy of [Ru(phen)2(bpy)]2+, [Ru(phen)2(dmbp)]2+, [Ru(tpy)(phen)(CH3CN)]2+ and [Ru(tpy)(dmp)(CH3CN)]2+: A theoretical study. *Coord. Chem. Rev.* **2008,** *252* (23), 2493-2503.

171.   Rasmussen, S. C.; Ronco, S. E.; Mlsna, D. A.; Billadeau, M. A.; Pennington, W. T.; Kolis, J. W.; Petersen, J. D. Ground- and Excited-State Properties of Ruthenium(II) Complexes Containing Tridentate Azine Ligands, Ru(tpy)(bpy)L2+, Where L Is a Polymerizable Acetylene. *Inorg. Chem.* **1995,** *34* (4), 821-829.

172.   Hecker, C. R.; Fanwick, P. E.; McMillin, D. R. Evidence for dissociative photosubstitution reactions of (acetonitrile)(bipyridine)(terpyridine)ruthenium(2+).

Crystal and molecular structure of [Ru(trpy)(bpy)(py)](PF6)2.cntdot.(CH3)2CO. *Inorg. Chem.* **1991,** *30* (4), 659-666.

173. Bergamo, A.; Sava, G. Linking the future of anticancer metal-complexes to the therapy of tumour metastases. *Chem. Soc. Rev.* **2015,** *44* (24), 8818-8835.

174. Dougan, S. J.; Sadler, P. J. The Design of Organometallic Ruthenium Arene Anticancer Agents. *CHIMIA* **2007,** *61* (11), 704-715.

175. Peña, B.; David, A.; Pavani, C.; Baptista, M. S.; Pellois, J.-P.; Turro, C.; Dunbar, K. R. Cytotoxicity Studies of Cyclometallated Ruthenium(II) Compounds: New Applications for Ruthenium Dyes. *Organometallics* **2014,** *33* (5), 1100-1103.

176. Kohler, L.; Nease, L.; Vo, P.; Garofolo, J.; Heidary, D. K.; Thummel, R. P.; Glazer, E. C. Photochemical and Photobiological Activity of Ru(II) Homoleptic and Heteroleptic Complexes Containing Methylated Bipyridyl-type Ligands. *Inorg. Chem.* **2017,** *56* (20), 12214-12223.

177. Gaiddon, C.; Pfeffer, M. The Fate of Cycloruthenated Compounds: From C–H Activation to Innovative Anticancer Therapy. *Eur. J. Inorg. Chem.* **2017,** *2017* (12), 1639-1654.

178. Bomben, P. G.; Robson, K. C. D.; Koivisto, B. D.; Berlinguette, C. P. Cyclometalated ruthenium chromophores for the dye-sensitized solar cell. *Coord. Chem. Rev.* **2012,** *256* (15), 1438-1450.

179. Bomben, P. G.; Robson, K. C. D.; Sedach, P. A.; Berlinguette, C. P. On the Viability of Cyclometalated Ru(II) Complexes for Light-Harvesting Applications. *Inorg. Chem.* **2009,** *48* (20), 9631-9643.

180. Kim, J.-J.; Choi, H.; Paek, S.; Kim, C.; Lim, K.; Ju, M.-J.; Kang, H. S.; Kang, M.-S.; Ko, J. A New Class of Cyclometalated Ruthenium Sensitizers of the Type ĈN̂N for Efficient Dye-Sensitized Solar Cells. *Inorg. Chem.* **2011,** *50* (22), 11340-11347.

181. Wadman, S. H.; Kroon, J. M.; Bakker, K.; Havenith, R. W. A.; van Klink, G. P. M.; van Koten, G. Cyclometalated Organoruthenium Complexes for Application in Dye-Sensitized Solar Cells. *Organometallics* **2010,** *29* (7), 1569-1579.

182. Leyva, L.; Sirlin, C.; Rubio, L.; Franco, C.; Le Lagadec, R.; Spencer, J.; Bischoff, P.; Gaiddon, C.; Loeffler, J.-P.; Pfeffer, M. Synthesis of Cycloruthenated Compounds as Potential Anticancer Agents. *Eur. J. Inorg. Chem.* **2007,** *2007* (19), 3055-3066.

183. Fetzer, L.; Boff, B.; Ali, M.; Xiangjun, M.; Collin, J.-P.; Sirlin, C.; Gaiddon, C.; Pfeffer, M. Library of second-generation cycloruthenated compounds and evaluation of their biological properties as potential anticancer drugs: Passing the nanomolar barrier. *Dalton Trans.* **2011,** *40* (35), 8869-8878.

184. Lameijer, L. N.; van de Griend, C.; Hopkins, S. L.; Volbeda, A.-G.; Askes, S. H. C.; Siegler, M. A.; Bonnet, S. Photochemical Resolution of a Thermally Inert Cyclometalated Ru(phbpy)(N–N)(Sulfoxide)+ Complex. *J. Am. Chem. Soc.* **2019,** *141* (1), 352-362.

185. Huang, H.; Zhang, P.; Chen, H.; Ji, L.; Chao, H. Comparison Between Polypyridyl and Cyclometalated Ruthenium(II) Complexes: Anticancer Activities Against 2D and 3D Cancer Models. *Chem. Eur. J.* **2015,** *21* (2), 715-725.

186.   Huang, H.; Zhang, P.; Yu, B.; Chen, Y.; Wang, J.; Ji, L.; Chao, H. Targeting Nucleus DNA with a Cyclometalated Dipyridophenazineruthenium(II) Complex. *J. Med. Chem.* **2014,** *57* (21), 8971-8983.

187.   Zeng, L.; Chen, Y.; Huang, H.; Wang, J.; Zhao, D.; Ji, L.; Chao, H. Cyclometalated Ruthenium(II) Anthraquinone Complexes Exhibit Strong Anticancer Activity in Hypoxic Tumor Cells. *Chem. Eur. J.* **2015,** *21* (43), 15308-15319.

188.   Vojtech, N.; Jyoti, Y.; Olga, S.; Dolores, S. M.; Hana, K.; Gorakh, Y.; Jana, K.; Delia, B.; José, R.; Viktor, B. Organoruthenium Complexes with C^N Ligands are Highly Potent Cytotoxic Agents that Act by a New Mechanism of Action. *Chem. Eur. J.* **2017,** *23* (61), 15294-15299.

189.   Jameson, D. L.; Goldsby, K. A. 2,6-bis(N-pyrazolyl)pyridines: the convenient synthesis of a family of planar tridentate N3 ligands that are terpyridine analogs. *J. Org. Chem.* **1990,** *55* (17), 4992-4994.

190.   Wang, J.; Medlycott, E. A.; Hanan, G. S.; Loiseau, F.; Campagna, S. The multichromophore approach: A case of temperature controlled switching between single and dual emission in Ru(II) polypyridyl complexes. *Inorg. Chim. Acta* **2007,** *360* (3), 876-884.

191.   Philippopoulos, A. I.; Terzis, A.; Raptopoulou, C. P.; Catalano, V. J.; Falaras, P. Synthesis, Characterization, and Sensitizing Properties of Heteroleptic RuII Complexes Based on 2,6-Bis(1-pyrazolyl)pyridine and 2,2′-Bipyridine-4,4′-dicarboxylic Acid Ligands. *Eur. J. Inorg. Chem.* **2007,** *2007* (36), 5633-5644.

192.   Catalano, V. J.; Kurtaran, R.; Heck, R. A.; Öhman, A.; Hill, M. G. Bdmpp complexes of Ru(II) as structural analogs for Ru(II)-2,2′:6′,2″-terpyridine species (where bdmpp is 2,6-bis(3,5-dimethyl-N-pyrazoyl)pyridine). *Inorg. Chim. Acta* **1999,** *286* (2), 181-188.

193.   Winter, A.; van den Berg, A. M. J.; Hoogenboom, R.; Kickelbick, G.; Schubert, U. S. A Green and Straightforward Synthesis of 4′-Substituted Terpyridines. *Synthesis* **2006,** *2006* (17), 2873-2878.

194.   Wadman, S. H.; Lutz, M.; Tooke, D. M.; Spek, A. L.; Hartl, F.; Havenith, R. W. A.; van Klink, G. P. M.; van Koten, G. Consequences of N,C,N′- and C,N,N′-Coordination Modes on Electronic and Photophysical Properties of Cyclometalated Aryl Ruthenium(II) Complexes. *Inorg. Chem.* **2009,** *48* (5), 1887-1900.

195.   Wadman, S. H.; Kroon, J. M.; Bakker, K.; Lutz, M.; Spek, A. L.; van Klink, G. P. M.; van Koten, G. Cyclometalated ruthenium complexes for sensitizing nanocrystalline TiO2 solar cells. *Chem. Commun.* **2007,** (19), 1907-1909.

196.   Kreitner, C.; Heinze, K. Excited state decay of cyclometalated polypyridine ruthenium complexes: insight from theory and experiment. *Dalton Trans.* **2016,** *45* (35), 13631-13647.

197.   Maity, D.; Das, S.; Mardanya, S.; Baitalik, S. Synthesis, Structural Characterization, and Photophysical, Spectroelectrochemical, and Anion-Sensing Studies of Heteroleptic Ruthenium(II) Complexes Derived from 4′-Polyaromatic-Substituted Terpyridine Derivatives and 2,6-Bis(benzimidazol-2-yl)pyridine. *Inorg. Chem.* **2013,** *52* (12), 6820-6838.

198.   Ding, H.-Y.; Wang, X.-S.; Song, L.-Q.; Chen, J.-R.; Yu, J.-H.; Chao, L.; Zhang, B.-W. Aryl-modified ruthenium bis(terpyridine) complexes: Quantum yield of 1O2 generation and photocleavage on DNA. *J. Photochem. Photobiol. A* **2006,** *177* (2–3), 286-294.

199.   Jameson, D. L.; Blaho, J. K.; Kruger, K. T.; Goldsby, K. A. Redox regulation in ruthenium(II) complexes of 2,6-bis(N-pyrazolyl)pyridine ligands: synthetically versatile analogs of 2,2':6',2''-terpyridine. *Inorg. Chem.* **1989,** *28* (24), 4312-4314.

200.   Lai, S.-H.; Jiang, G.-B.; Yao, J.-H.; Li, W.; Han, B.-J.; Zhang, C.; Zeng, C.-C.; Liu, Y.-J. Cytotoxic activity, DNA damage, cellular uptake, apoptosis and western blot analysis of ruthenium(II) polypyridyl complex against human lung decarcinoma A549 cell. *J. Inorg. Biochem.* **2015,** *152*, 1-9.

201.   Zeng, C.-C.; Lai, S.-H.; Yao, J.-H.; Zhang, C.; Yin, H.; Li, W.; Han, B.-J.; Liu, Y.-J. The induction of apoptosis in HepG-2 cells by ruthenium(II) complexes through an intrinsic ROS-mediated mitochondrial dysfunction pathway. *Eur. J. Med. Chem.* **2016,** *122*, 118-126.

202.   Xie, Y.-Y.; Li, Z.-Z.; Lin, G.-J.; Huang, H.-L.; Wang, X.-Z.; Liang, Z.-H.; Jiang, G.-B.; Liu, Y.-J. DNA interaction, cytotoxicity, apoptotic activity, cell cycle arrest, reactive oxygen species and mitochondrial membrane potential assay induced by ruthenium(II) polypyridyl complexes. *Inorg. Chim. Acta* **2013,** *405*, 228-234.

203.   Tang, B.; Shen, F.; Wan, D.; Guo, B.-H.; Wang, Y.-J.; Yi, Q.-Y.; Liu, Y.-J. DNA-binding, molecular docking studies and biological activity studies of ruthenium(ii) polypyridyl complexes. *RSC Adv.* **2017,** *7* (56), 34945-34958.

204.   Chen, T.; Mei, W.-J.; Wong, Y.-S.; Liu, J.; Liu, Y.; Xie, H.-S.; Zheng, W.-J. Chiral ruthenium polypyridyl complexes as mitochondria-targeted apoptosis inducers. *MedChemComm* **2010,** *1* (1), 73-75.

205.   Qian, C.; Wang, J.-Q.; Song, C.-L.; Wang, L.-L.; Ji, L.-N.; Chao, H. The induction of mitochondria-mediated apoptosis in cancer cells by ruthenium(ii) asymmetric complexes. *Metallomics* **2013,** *5* (7), 844-854.

206.   Chen, T.; Liu, Y.; Zheng, W.-J.; Liu, J.; Wong, Y.-S. Ruthenium Polypyridyl Complexes That Induce Mitochondria-Mediated Apoptosis in Cancer Cells. *Inorg. Chem.* **2010,** *49* (14), 6366-6368.

207.   Zhao, Z.; Luo, Z.; Wu, Q.; Zheng, W.; Feng, Y.; Chen, T. Mixed-ligand ruthenium polypyridyl complexes as apoptosis inducers in cancer cells, the cellular translocation and the important role of ROS-mediated signaling. *Dalton Trans.* **2014,** *43* (45), 17017-17028.

208.   Wan, D.; Tang, B.; Wang, Y.-J.; Guo, B.-H.; Yin, H.; Yi, Q.-Y.; Liu, Y.-J. Synthesis and anticancer properties of ruthenium (II) complexes as potent apoptosis inducers through mitochondrial disruption. *Eur. J. Med. Chem.* **2017,** *139*, 180-190.

209.   Niles, A. L.; Moravec, R. A.; Eric Hesselberth, P.; Scurria, M. A.; Daily, W. J.; Riss, T. L. A homogeneous assay to measure live and dead cells in the same sample by detecting different protease markers. *Anal. Biochem.* **2007,** *366* (2), 197-206.

210.   O'Brien, M. A.; Daily, W. J.; Hesselberth, P. E.; Moravec, R. A.; Scurria, M. A.; Klaubert, D. H.; Bulleit, R. F.; Wood, K. V. Homogeneous, Bioluminescent Protease Assays: Caspase-3 as a Model. *J. Biomol. Screen.* **2005,** *10* (2), 137-148.

211.   Luo, Z.; Yu, L.; Yang, F.; Zhao, Z.; Yu, B.; Lai, H.; Wong, K.-H.; Ngai, S.-M.; Zheng, W.; Chen, T. Ruthenium polypyridyl complexes as inducer of ROS-mediated apoptosis in cancer cells by targeting thioredoxin reductase. *Metallomics* **2014,** *6* (8), 1480-1490.

212.   Chen, J.-c.; Zhang, Y.; Jie, X.-m.; She, J.; Dongye, G.-z.; Zhong, Y.; Deng, Y.-y.; Wang, J.; Guo, B.-y.; Chen, L.-m. Ruthenium(II) salicylate complexes inducing ROS-mediated apoptosis by targeting thioredoxin reductase. *J. Inorg. Biochem.* **2019,** *193*, 112-123.

APPENDIX A

NOMENCLATURE

WHO	World Health Organization
US	United States
FDA	Food and Drug Administration
NSCLC	Non-small cell lung cancer
SCLC	Small cell lung cancer
DNA	Deoxyribonucleic acid
CTR1	Copper transporter-1
MOF	Metal organic framework
DMSO	Dimethylsulfoxide
ROS	Reactive oxygen species
en	Ethylenediamine
PTA	1,3,5-triaza-7-phosphaadamantane
RAPTA	Ruthenium-arene-PTA
GSK3β	Glycogen synthase kinase 3β
PCT	Photoactivated chemotherapy
ER	Endoplasmic reticulum
PDT	Photodynamic therapy
PCD	Programmed cell death
PS	Photosensitizer

LED	Light-emitting diode
^{1}GS	Singlet ground state
^{1}ES	Singlet excited state
^{3}ES	Triplet excited state
ISC	Intersystem crossing
^{3}O$_2$	Triplet oxygen or, molecular oxygen
^{1}O$_2$	Singlet oxygen
SAR	Structure activity relationship
EC$_{50}$	Half maximal effective concentration
^{3}MLCT	Triplet metal-to-ligand charge transfer
^{3}IL	Triplet intra-ligand
^{1}MLCT	Singlet metal-to-ligand charge transfer
^{3}LF	Triplet ligand field
cAMP	Cyclic adenosine monophosphate
ATP	Adenosine triphosphate
GABA	γ-aminobutyric acid
NH$_3$	Ammonia
MeCN (CH$_3$CN)	Acetonitrile
bpy	2,2′-bipyridine
9-EtG	9-ethylguanine
5-CNU	5-cyanouracil
dppn	Benzo[*i*]dipyrido[3,2- a:2′,3′-c]phenazine

IC$_{50}$	Half maximal inhibitory concentration
PI	Phototoxicity index
phpy	2-phenylpyridine
biq	2,2′-biquinoline
phen	1,10-phenanthroline
CTSK	Cathepsin K
CTSL	Cathepsin L
tpy	2,2′;6′,2″-terpyridine
dmbpy	6,6′-dimethyl-2,2′-bipyridine
CTSB	Cathepsin B
dmdppn	3,6-dimethylbenzo[i]dipyrido[3,2-a:2′,3′-c]phenazine
H$_2$O	Water
CDC	Critical aggregate concentration
NAMPT	Nicotinamide phosphoribosyltransferase
NAD$^+$	Oxidized nicotinamide adenine dinucleotide
Ec	Econazole
6-MP	6-mercaptopurine
dmdpq	7,10-dimethylpyrazino[2,3-f][1,10]phenanthroline
GSH	Glutathione
dop	2,3-dihydro-1,4-dioxino[2,3-f]-1,10-phenanthroline
PLPG	Photo-labile protecting group
acac	Acetylacetonate

dqpy	2,6-di(quinoline-2-yl)pyridine
HOMO	Highest occupied molecular orbital
LUMO	Lowest unoccupied molecular orbital
tppz	Tetra-2-pyridinylpyrazine
dpq	2,3-di(pyridin-2-yl)quinoxaline
dpb	2,3-di(pyridin-2-yl)benzo[*g*]quinoxaline
DFT	Density functional theory
ECP	Effective core potential
SCRF	Self-consistent reaction field
MO	Molecular orbital
TDDFT	Time-dependent density functional theory
ATCC	American type culture collection
DMEM	Dulbecco's modified Eagle medium
DPBS	Dulbecco's phosphate-buffered saline
FBS	Fetal bovine serum
PBS	Phosphate-buffered saline
^{1}LC	Singlet ligand centered
RT	Room temperature
NHE	Normal hydrogen electrode
NADH	Reduced nicotinamide adenine dinucleotide
LC_{50}	Half maximal lethal concentration
pbpy	6-phenyl-2,2′-bipyridine

EtOH	Ethanol
MeOH	Methanol
THF	Tetrahydrofuran
EtOAc	Ethyl acetate
Py	Pyridine
PySNBD	7-nitro-N-(pyridine-4-ylmethyl)-2,1,3-benzoxadiazole
EDTA	Ethylenediaminetetraacetic acid
PCR	Polymerase chain reaction
DMF	Dimethyl formamide
ds DNA	Double-stranded DNA
DSSC	Dye sensitized solar cells
MCTSs	Multicellular tumor spheroids
phendione	1,10-phenanthroline-5,6-dione
antpy	4′-(9-anthryl)-2,2′:6′,2″-terpyridine
bpp	2,6-bis(N-pyrazolyl)pyridine
bdmpp	2,6-bis(3,5-dimethyl-N-pyrazolyl)pyridine
PEG 300	Polyethylene glycol 300
Et_3N	Triethyl amine
DCFH-DA	2′,7′-dichlorodihydrofluorescein diacetate
DCFH	2′,7′-dichlorodihydrofluorescein
DCF	2′,7′-dichlorofluorescein
MMP	Mitochondrial membrane potential

dmphen	2,9-dimethyl-1,10-phenanthroline
ΔE_p	peak-to-peak separation
CD_3CN	Deuterated acetonitrile
CD_3OD	Deuterated methanol
dmso-d_6	Deuterated dimethylsulfoxide
acetone-d_6	Deuterated acetone
$CDCl_3$	Deuterated chloroform